2015

Behaviour of blended waste materials for land reclamation for port extension

Seyed Mohammad Ali Tasalloti
University of Wollongong

UNIVERSITY OF WOLLONGONG

Department of Engineering and Information Sciences,

School of Civil, Mining and Environmental Engineering

Behaviour of Blended Waste Materials for Land Reclamation for Port Extension

Seyed Mohammad Ali Tasalloti

(BSc, MSc)

This thesis is presented as part of the requirement for the award of the Degree of Doctor of Philosophy of the University of Wollongong

January 2015

CERTIFICATION

I, Seyed Mohammad Ali Tasalloti, declare that this thesis, submitted in fulfilment of the requirements for the award of Doctor of Philosophy, in the School of Civil, Mining, and Environmental Engineering, University of Wollongong, is wholly my own work unless otherwise referenced or acknowledged. The document has not been submitted for qualifications at any other academic institution.

S.M. Ali Tasalloti
January 2015

ABSTRACT

In Australia, a large amount of industrial byproducts are produced annually, mainly coal wash (CW) and steel furnace slag (SFS) from coal mining and steel making, respectively. The effective reuse and recycling of these materials rather than their disposal are the preferred and sustainable methods from the waste management perspective and these are economically beneficial. In recent years, the need for more land to accommodate new infrastructures such as expansion of existing ports has been increased significantly. The use of industrial waste as structural fill material is considered relevant for these types of projects. However, due to the lack of information on the geotechnical behaviour of waste materials, specifically mixtures of coal wash and steel furnace slag, they have been used in limited quantities. Individual CW and SFS can pose serious problems due to the swelling potential in SFS and particle degradation in CW that can cause differential settlements. However, the adverse effect of individual materials might be minimised by blending them together. Therefore, an in-depth study on the geotechnical behaviour of CW-SFS mixtures is essential.

This doctoral thesis is part of an industrial project for the expansion of Port Kembla Outer Harbour near Wollongong, Australia. For this project, mixtures of CW-SFS (five mixtures in total) were considered for the fill material. The suitability of different CW-SFS mixtures in terms of geotechnical characteristics to be used as structural fill is investigated through extensive laboratory tests. A comprehensive range of geotechnical parameters of CW-SFS blends was determined in order to establish the relationship between them and the CW percentage. These parameters include specific gravity, compaction characteristics and degradation due to the compaction energy, permeability of the mixtures compacted to the maximum dry density, California Bearing Ratio (CBR) both for as compacted and soaked condition, the Unconfined Compressive Strength (UCS), the swelling (free swelling and swelling pressure) characteristics and in-depth study on the stress-strain behaviour under monotonic triaxial conditions.

In order to investigate the effect of CW (or SFS) content in the mechanical behaviour of CW-SFS blends, series of drained triaxial tests on 100mm diameter and 200mm height specimens were carried out. Confining pressure was varied between 30kPa to 220kPa to mimic port loading conditions. Based on these tests, an empirical equation was proposed to predict the peak deviatoric stress for different CW-SFS blends and confining pressure. Furthermore, the ultimate adoption of CW-SFS mixtures as structural fill was supported by establishing a mathematical model for the stress-strain behaviour based on generalised plasticity and critical state concept. It was shown that within a unique framework, the model was capable of capturing the mechanical behaviour of different CW-SFS mixtures.

Based on the laboratory results, an optimisation method for the CW-SFS mixtures was suggested. Following this method, the most suitable blends can be identified by considering the required properties for site condition. The performance of the CW-SFS mixtures on a large scale was assessed through field investigation, with the results confirming the suitability of the optimum mixture as structural fill.

The constitutive model proposed for the CW-SFS blends was implemented into the finite element software (ABAQUS) by developing the user-defined program (known as the UMAT subroutine). The numerical model was initially calibrated using the drained triaxial results from the laboratory and then verified and assessed by comparing them to the field trial investigation. The numerical model is capable of being used under different loading conditions for a range of CW-SFS mixtures, enabling practicing engineers and designers to evaluate the performance of a given blend for site conditions.

ACKNOWLEDGEMENTS

I wish to express my gratitude to all who contributed to the completion of this research study. First and foremost I would like to kindly express my sincerest thanks to my supervisor, Prof. Buddhima Indraratna, for his motivation, valuable suggestions, encouraging comments, constructive criticisms, proofreading, and amazing patience in completing my research at the University of Wollongong. I also thank my co-supervisors, A/Prof. Cholachat Rujikiatkamjorn and Dr. Ana Heitor for their inspiring guidance and assistance throughout this research.

The assistance provided by Dr. Gabriele Chiaro, the Research Fellow in this project, in sharing his experience on problems involved, in laboratory testing, as well as his aid in field trial investigation, is greatly appreciated. I appreciate not only his technical assistance, but also the fact that he is one of the best friends I have found in Australia.

Financial assistance given by the Australian Research Council (ARC) Linkage project, University of Wollongong, and other industrial partners including Port Kembla Port Corporation, Coffey Geotechnics, Douglas Partners, Menard Bachy, BHP Billiton-Illawarra Coal and Australian Steel Mill Services to carry out this research is gratefully acknowledged.

Some parts of the thesis have been published earlier in Canadian Geotechnical Journal and Proceedings of the ICE - Ground Improvement. They have been reproduced in this thesis with kind permission from "© Canadian Science Publishing or its licensors" and "ICE Publishing", respectively.

My special appreciation goes to all technical staff at the School of Civil, Mining, and Environmental Engineering, especially the dedicated efforts of Mr. Alan Grant for his continuous support and for troubleshooting the problems in the laboratory apparatus. The assistance from other technical officers including Mr. Ritchie McLean, Mr. Ian Laird, Mr. Cameron Neilson, and Mr. Fernando Escribano, is also gratefully acknowledged. I also thank Mr. Jordan Peterson and Mr. Michael Lofts for their kind assistance in conducting parts of the laboratory tests.

I would like to thank all my friends in Iran, Australia, and all around the world for their continuous friendship and contacts, especially all of the students in the Centre for Geomechanics and Railway Engineering.

Thanks to my family members, especially to my parents for their constant support and encouragement throughout my life, without whom I would not able to understand the value of knowledge and start my PhD in Australia.

Last but not least, none of this would have been possible without the love and patience of my lovely wife, Zahra Shahnazzadeh who unconditionally assisted me throughout the long journey. She has been a constant source of love, support and strength throughout these years. Her encouragements, especially at the critical moments, provided me more confidence and hope to continue my research.

LIST OF PUBLICATIONS

The following award and publications are related with this PhD thesis.

a. Award

First Prize in Young Professional Geotechnical Award (2014), Australian Geomechanics Society (AGS), *Sydney Chapter, the Institution of Engineers Australia, Sydney* (9th July 2014)

b. Journal papers

Tasalloti, S.M.A., Indraratna, B., Rujikiatkamjorn, C., and Heitor, A. "A laboratory study on the shear behaviour of mixtures of coal wash and steel furnace slag as potential structural fill", *Geotechnical Testing Journal* (under review)

Chiaro, G., Indraratna, B., Tasalloti, S.M.A.,(2014) "Predicting the behaviour of coal wash and steel slag mixtures under triaxial conditions", *Canadian Geotechnical Journal* (in press, available online).

Chiaro, G., Indraratna, B., Tasalloti, S.M.A., and Rujikiatkamjorn, C.,(2013) "Optimisation of coal wash – BOS slag fines blend as a structural fill for port reclamation", *Journal of ICE, Ground Improvement* (in press, available online).

Tasalloti, S.M.A., Indraratna, B., Heitor, A, Rujikiatkamjorn, C., and Chiaro, G. "Geotechnical assessment on the behavior of coal wash-steel furnace slag as a structural fill", *Australian Geomechanics Journal* (under review)

c. Conference papers

Tasalloti, S.M.A., Indraratna, B., Chiaro, G., and Heitor, A. "Field investigation on compaction and strength performance of two coal wash-BOS slag mixtures", to be submitted to The 2015 International Foundations Congress. & Equipment Exposition, San Antonio, Texas, USA (accepted)

Heitor, A., Indraratna, B., Rujikiatkamjorn, C., Chiaro, G., and Tasalloti, S.M.A. "Evaluation of the coal wash and steel furnace slag blends as effective reclamation fill for port expansion", In A. Bouazza, S. T. S. Yuen, & B. Brown, (Eds.), 7th International Congress on Environmental Geotechnics (pp. 972-979), 10-14 November 2014, Melbourne, Australia.

Rujikiatkamjorn, C., Indraratna, B., Chiaro, G., Naeeni, S. and Tasalloti, S.M.A.,(2012) "Compaction and strength testing of industrial waste blends as potential port reclamation fill", In G. A. Narsilio, A. Arulrajah & J. Kodikara (Eds.), 11th Australia - New Zealand Conference on Geomechanics: Ground Engineering in a Changing World (pp. 973-978). Australia. Engineers Australia.

LIST OF SYMBOLS

Letters

A	area between initial and final particle size distribution
A_L	cross-sectional area of a given applied axial load
A_c	cross-sectional area of specimen after consolidation
B	area between final particle size distribution and arbitrary boundary of maximum breakage
$B_{Skempton}$	Skempton's B-value
B_r	breakage using Hardin's method
C_c	coefficient of compression
C_s	coefficient of swelling
CP	collapse potential
D_c	degree of compaction
D^e	elastic stiffness matrix
D^{ep}	elasto-plastic stiffness matrix
d_{95}	diameter for 95% fine by weight
d_f	loading direction component
d_g	dilatancy ratio
d_{max}	maximum particle size
dp'	effective mean stress increment
dq	deviatoric stress increment
E	modulus of elasticity or Young's modulus
E_i	initial deformation modulus
E_{sec}	secant deformation modulus
e_0	initial void ratio/void ratio after isotropic consolidation
e	current void ratio
e^*_{cs}	void ratio at critical state for mixtures
e_f	final void ratio
e_w	water ratio
f	yield surface
f_{CW}	coal wash content
g	plastic potential
G	shear modulus
G_i	initial shear modulus
G_s	specific gravity
G_{sec}	secant shear modulus
Δe	change in void ratio
H	plastic modulus
h_0	model parameter for hardening
H_0	initial height of specimen
H_c	height of specimen after consolidation
ΔH	change in height of specimen during loading
ΔH_0	change in height of specimen in consolidation
ΔH_ε	change in height of specimen from start of shearing to any strain

ΔH_s	change in height of specimen during saturation
I	parameter for adjusting size of the sub-step algorithm
J_2	second deviatoric stress invariant
k	permeability
K_s	moduli of reaction
M	slope of critical state line in the p'-q plot
M^*_{cs}	slope of critical state line in the p'-q plot for mixtures
M_R	resilient modulus
m	plastic flow direction vector
m_{pk}	model parameter for hardening corresponding to the deviator peak stress state
m_v , m_q	components of plastic flow direction vectors
n	loading direction vector
n_v , n_q	components of loading direction vectors
P	axial load on specimen
p_{atm}	atmospheric pressure (=100 kPa)
p'	effective mean stress
p'_0	confining pressure
p'_{peak}	peak effective mean stress
p^*	equivalent past stress
q	deviatoric stress
q_{peak}	peak deviatoric stress
q_u	unconfined compressive stress
$q_{u,\max}$	unconfined compressive strength
q/p	stress ratio
$(q/p)_{peak}$	peak stress ratio
R	relative error in sub-step algorithm
S_f	free swelling/swelling potential
S_p	swelling pressure
S_u	undrained shear strength
t_{90}	time to 90% consolidation
T	sub-step dimensionless parameter
ΔT	increment of sub-step dimensionless parameter
Δu	increment of pore water pressure
V_0	initial volume of specimen
V_c	volume of specimen after consolidation
V_{SFS}	volume of steel furnace slag in mixture
V_t	volume of specimen
ΔV_c	change in volume of specimen during consolidation
ΔV_ε	change in volume of specimen from start of shearing to any strain
ΔV_{sat}	change in volume of specimen during saturation
w	moisture content

Greek Letters

α	value of coal wash content in percentage
Γ	specific volume on CSL corresponding to p'=1kPa on critical state line
Γ^*	specific volume on CSL corresponding to p'=1kPa on critical state line for mixtures
γ_d	dry unit weight
$\gamma_{d,in-situ}$	*in-situ* dry unit weight
$\gamma_{d,\max}$	maximum dry unit weight
γ_w	unit weight of water
ε	strain tensor
$\dot{\varepsilon}$	rate of strain in triaxial drained shearing
ε_1	axial strain/major principal strain
ε_2	intermediate principal strain
ε_3	lateral strain/minor principal strain
ε_v	volumetric strain
ε_{v-cs}	volumetric strain at critical state
ε_s	shear strain
$d\varepsilon$	strain increments
$d\sigma$	stress increments
$\Delta\sigma_3$	increment of confining pressure
$\Delta\sigma_e$	elastic stress increment/elastic stress predictor
$d\varepsilon_e$	elastic strain increment
$d\varepsilon_p$	plastic strain increment
$d\varepsilon_s$	shear strain increment
$d\varepsilon_v$	volumetric strain increment
η_{pk} , η_{pt}	stress ratio at deviator peak state and stress ratio at PT state, respectively
K	bulk modulus
κ	unloading-reloading slope
κ^*	swelling-recompression index for mixtures
λ	Lame parameter
λ_{CSL}	slope of critical state line in the p'-e plot
λ_{ISO}	slope of isotropic compression line
λ^*	slope of critical state line in the p'-e plot for mixtures
$d\lambda$	plastic multiplier
μ_f , ξ_f , η_f	model parameters for plastic potential
μ_g , ξ_g	model parameters for dilatancy
μ_{pk}	model parameter for hardening
N	specific volume on ICL corresponding to p'=1kPa

σ	stress invariant/stress tensor
σ'_1	effective major principal stress
σ'_2	effective intermediate principal stress
σ'_3	effective confining pressure/effective minor principal stress
σ_v	vertical stress
σ'_n	normal stress
$d\sigma_v$	increment of vertical stress
τ	shear stress
v	specific volume
v_0	initial specific volume
v^*_{cs}	critical specific volume for mixtures
ν_i	initial Poisson's ratio
ϕ'	friction angle
ϕ'_p	peak friction angle
ϕ'_{cs}	critical state friction angle
ψ	state parameter
ψ^*	state parameter for mixtures
ψ_{pk}	state parameter at peak stress state
ψ_{pt}	state parameter at PT state

Abbreviations

ASMS	Australian Steel Mill Services
BI	Breakage Index
BOS	Basic Oxygen System
CBR	California Bearing Ratio
CH	Constant Head
CID	Consolidated Isotropic Drained
CL	Centre Line
CS	Critical State
CSL	Critical State Line
CU	Consolidated Undrained
CV	Constant Volume
CW	Coal Wash
DCPT	Dynamic Cone Penetration Test
ETOL	Error Tolerance
FE	Finite Element
ICL	Isotropic Compression Line
ISO	Improved Swell Oedometer
LVDT	Linear Variable Differential Transformer
MDD	Maximum Dry Density
MDUW	Maximum Dry Unit Weight
ND	Nuclear Densometer

OMC	Optimum Moisture Content
PKPC	Port Kembla Port Corporation
PLT	Plate Load Test
PT	Phase Transformation
PSD	Particle Size Distribution
RC	Relative Compaction
SCR	Sand Cone Replacement
SFS	Steel Furnace Slag
SPT	Standard Penetration Test
STATEV	State Variable
UCS	Unconfined Compression Strength
UMAT	User-defined Material subroutine
USCS	Unified Soil Classification System
XRF	X-Ray Fluorescence
ZAV	Zero Air Void

TABLE OF CONTENTS

LIST OF FIGURES

LIST OF TABLES

CHAPTER ONE

1 INTRODUCTION

1.1 BACKGROUND

Due to the worldwide increase in urbanisation and population density, the need for more land to accommodate new infrastructure, including the expansion of the existing ports, has increased substantially in recent years. In many countries where there is no shortage of conventional fill materials (e.g. sand and gravel) and the cost of using quarries is relatively small, these natural materials are largely used for embankments and land reclamation projects (Massarsch, 1991, Watts and Cooper, 2011, Zekkos and Flanagan, 2011). However, the use of fresh aggregates is often uneconomical, and environmentally unfavourable. Since the production of industrial waste materials such as coal wash and steel furnace slag from mining activities and steel making has been rapidly increasing (Leventhal, 1996, Geiseler, 1996), effective recycling of these byproducts is both economically beneficial and environmentally sustainable, and certainly an utmost priority from a waste management perspective. Industrial byproducts can be classified as coarse grained or fine grained depending on the processing mechanisms by which they are produced, and it is the coarser particle fraction that carries the potential for effective use as a structural fill (Indraratna, 1994a, Indraratna *et al.*, 1994b, Leventhal, 1996).

There are many examples where industrial byproducts such as steel slag and coal washery rejects have been used in civil engineering projects such as road embankments, reclamation fill, asphalt aggregates, concrete aggregate, and subgrade fill (Indraratna *et al.*, 1994b, Rai *et al.*, 2002, Dippenaar, 2005, Lim and Chu, 2006, Okogbue and Ezeajugh, 1991, Safiuddin *et al.*, 2010, Malasavage *et al.*, 2012, Indraratna *et al.*, 2013a). Most of these applications and subsequent studies have only focused on one type of waste material, not as a mixture. It is already known that

using steel slag on its own can pose a serious problem because of its potential to swell (Wang, 2010; Wang *et al.*, 2010). In contrast, although not expansive, coal washery rejects can cause differential settlement due to particle degradation or collapse (Pusadkar and Ramasamy, 2005). On the basis that the adverse effects of both materials might be diminished by mixing them together, an in-depth study of the geotechnical behaviour of blended waste materials on coal wash and steel furnace slag was therefore most beneficial.

In this thesis, the geotechnical behaviour of coal wash and steel furnace slag mixtures was studied through extensive laboratory and field investigations. A framework to establish the effectiveness of granular waste fills and to optimise these mixtures as a suitable reclamation fill is proposed.

1.2 RESEARCH MOTIVATION

The main motivation of this study is directly linked to an industrial project for the extension of Port Kembla Outer Harbour 10km south of the city of Wollongong. Port Kembla is located on the east coast of Australia and is one of the major commercial ports in NSW. It consists of an inner harbour (which has been commissioning for about 30 years) and an outer harbour. To provide additional land and berthing facilities to cater for future trade growth, Port Kembla Port Corporation (PKPC) is developing the outer harbour. This development includes approximately 42 hectares of land and construction of 7 new berths. Most of the land reclamation to date within inner harbour have been constructed using blast furnace slag for underwater and coal wash above tidal level. Generally, the dredged material from surrounding area is considered as fill material but since the dredged fills in Port Kembla area are contaminated by pyrites that produce sulphuric acid upon excavation (oxidation) and can threaten marine species and the surrounding coastal environment and also since blast furnace slag is in short supply, PKPC decided to use a mixture of industrial wastes (i.e. coal wash and steel furnace slag) for reclamation. However, the behaviour of these two materials and their mixtures is not clearly understood.

In order to assess the suitability of these industrial wastes as a structural fill, extensive laboratory and field investigation is necessary. This study characterized the geotechnical behaviour of these materials and provided recommendations for industry on the optimum blended material for site condition by establishing design aids (charts and guides) which relate the geotechnical properties of different mixtures with various parameters such as shear strength, permeability and breakage.

1.3 OBJECTIVES AND SCOPE OF THE RESEARCH

This research aims to study the geotechnical characterization of blended industrial wastes (i.e. coal wash and steel furnace slag) and provide the optimum mixture to be used as a structural fill for land reclamation above the water table in a port environment. Within the scope of this study, only the monotonic loading under saturated drained condition was considered. A range of effective confining pressures (i.e. 30 to 220kPa) was adopted to represent the expected field loading conditions. The specific objectives are as follows:

1. Conducting extensive laboratory tests to evaluate the basic geotechnical parameters for coal wash (CW) and steel furnace slag (SFS) individually as well as different mixtures. These geotechnical properties include specific gravity, compaction characteristics, permeability, unconfined compression strength, and California bearing ratio. The swelling behaviour of the mixtures at various degree of compaction under two conditions; (i) free swelling (i.e. no surcharge applied on the specimen) and (ii) swelling pressure in the constant volume condition was also considered.
2. Conducting comprehensive isotropic compression and static triaxial tests in drain condition on CW-SFS mixtures. Different parameters will be varied such as the confining pressure and percentage of coal wash to steel furnace slag to investigate stress strain and degradation behaviour of the mixtures. The failure envelopes and the governing empirical equation for all mixtures will be provided. An analytical model will be developed to predict the

stress-strain behaviour of CW-SFS mixtures. The model will provide a generalised plasticity formulation appropriate for the mixtures.

3. Assessing the behaviour of CW-SFS mixtures in the field and formulating guidelines to optimise CW and SFS mixtures, for the benefit of practising engineers.

4. Implementation of the constitutive model into the finite element code (ABAQUS) by developing UMAT subroutine.

1.4 THESIS ORGANISATION

The thesis will be divided into 8 chapters (including this Introduction), which are organised as follows:

This Chapter 1 has given the background of this research study. It has highlighted the objectives and the scope of research.

In Chapter 2 (Literature Review), the current and past studies on the use of waste materials and waste management in civil engineering practice are discussed. It contains an overview of the characteristics of the two industrial byproducts that are used in this research (coal wash and steel furnace slag). It outlines the production process, the physical and chemical characteristics, the geotechnical properties such as compaction characteristics, permeability, strength, swell/collapse potential.

Chapter 3 describes the experimental and testing programs. Firstly, the testing materials are identified through their particle size distribution and index properties. Then, the testing methods and corresponding equipment are described in detail. Subsequently, the specimen preparation for the triaxial and swelling tests is explained.

Chapter 4 presents the tests results and discussion on basic geotechnical characteristics of CW, SFS, and their mixtures. These tests include specific gravity, compaction characteristics and degradation due to the compaction energy,

permeability of the mixtures compacted to the maximum dry density, California Bearing Ratio (CBR) both for as compacted and soaked condition and the Unconfined Compressive Strength (UCS). This chapter also covers the experimental results on the swelling behaviour of the mixtures. The effect of CW content and the degree of compaction on free swelling and swelling pressure of the mixtures is presented and discussed.

In Chapter 5, firstly the laboratory results from the study of CW content on the compressibility of the different mixtures through isotropic compression tests are presented. Then, the stress-strain behaviour of CW-SFS mixtures in drained condition under various confining pressures is presented and discussed. The effect of CW percentage on the shear behaviour (i.e. peak friction angle, failure envelopes, volumetric response, stress-dilatancy, and particle degradation) is illustrated and discussed, and an empirical equation for the failure envelopes of CW-SFS mixtures is provided. Subsequently, based on the experimental findings, an elasto-plastic analytical model is developed to predict the stress-strain behaviour of the CW-SFS mixtures. The model is based on the generalised plasticity, and the modification made to make it appropriate for the mixtures in the current study is presented and discussed. A comparison between model prediction and experimental results is also given.

Chapter 6 describes the details of the performance of the mixtures in the field. Firstly, an acceptance criterion for granular waste material is proposed to identify a suitable waste material as structural fill. Additionally, an optimisation method for the CW-SFS mixtures is suggested. Then, the Port Kembla Outer Harbour extension project is described and the field testing program and the results are presented.

Chapter 7 presents the numerical analysis of the behaviour of CW-SFS mixtures. Firstly, the implementation of the developed constitutive model into finite element code (ABAQUS) by developing UMAT subroutine is described. Then, the verification of the numerical model using the drained triaxial results on the different CW-SFS mixtures is covered. This chapter also highlights how the constitutive

governing equations developed for the CW-SFS mixture are applied to the field trial. While, recognising the limited field data, the applicability of theory to practice is elucidated in this chapter.

Chapter 8 summarises the main findings of this research in reference to the application of these mixtures in the field and then provides some recommendations for future work. A list of References and Appendices follow Chapter 8.

CHAPTER TWO

2 LITERATURE REVIEW

2.1 INTRODUCTION

In this chapter, current and past research studies on industrial waste materials, namely coal wash (CW) and steel furnace slag (SFS) in relation to their properties and practical applications are discussed. It begins with the management of waste materials all around the world and covers specifically waste classification and recycling in Australia. Then, the two byproducts considered in this study (i.e. CW and SFS) are explored. The production process, physical and chemical properties, geotechnical properties, and engineering application of these two byproducts are explained. Finally, a summary of this chapter, along with the contribution of this study, is provided.

2.2 MANAGEMENT OF WASTE MATERIALS

2.2.1 Classification of waste materials

The generation of waste materials, especially industrial by-products, has increased recently due to rapid urbanization and population growth. The production of any kind of waste can be harmful for the environment and public health. However, the effective reuse and recycling of these materials would be economically beneficial and environmentally friendly. Classification and management of these materials are the first steps toward reduction of the volume of waste materials. Classifying wastes into groups that pose risks to the environment and human health facilitates their management and appropriate disposal or recycling (Hogland and Stenis, 2000, Aiban, 2006, Wei and Huang, 2001).

In Australia, each territory has its own classification and waste management criteria. Since the current study is conducted within New South Wales State, the relevant state regulations about waste materials are addressed here. In this regard, waste materials are classified into six groups (Department of Environment, 2009):

1. Special wastes: is a class of waste that has unique regulatory requirements, such as clinical and related waste, asbestos waste, and waste tyres.
2. Liquid wastes: corresponds to any waste that has an angle of repose of less than 5 degrees, becomes free-flowing at or below 60°C, or is generally not capable of being picked up by a spade or shovel.
3. Hazardous waste: such as lead-acid or nickel-cadmium batteries, coal tar or coal tar pitch, lead paint waste, etc.
4. Restricted solid waste.
5. General solid waste (putrescibles): such as household waste, food waste, animal waste, etc.
6. General solid waste (non-putrescible): glass, plastic, ceramics, bricks, concrete or metal, wood waste, garden waste, virgin excavated natural material, building and demolition waste, asphalt waste, and industrial waste such as coal wash and steel furnace slag.

Those groups are pre-classified waste materials by the EPA (Environment Protection Authority). When the waste is not within those groups, the waste generators should chemically assess their waste to determine its classification. In this case, there are two measurable properties of chemical contaminants used to classify wastes, which are (Department of Environment, 2009):

1. the specific contaminant concentration (SCC) of any chemical contaminant in the waste, expressed as milligrams per kilogram (mg/kg)
2. the leachable concentration of any chemical contaminant using the toxicity characteristics leaching procedure (TCLP), expressed as milligrams per litre (mg/L)

When these two tests are conducted, the waste can be classified using the criteria provided in "Waste Classification Guidelines" by the Department of Environment, Climate Change and Water (NSW). Currently, there are levy exemptions for coal washery reject as well as steel furnace slag to be used in open areas if the percentage of any chemical containment in the waste and its leachable concentration of any chemical contaminants are within the range specified in Tables 2.1 and 2.2, for coal washery reject and steel furnace slag, respectively. This provides an opportunity to use these two waste materials as a structural fill in construction.

Table 2.1 Chemical and other material property requirement for exemption of coal washery reject (Department of Environment, 2009)

Chemicals and other attributes	Maximum average concentration for characterisation (mg/kg)	Maximum average concentration for routine testing (mg/kg)	Absolute maximum concentration (mg/kg)
Mercury	0.5	Not required	1
Cadmium	0.5	Not required	1
Lead	50	50	100
Arsenic	10	Not required	20
Chromium	75	75	150
Copper	50	50	100
Nickel	40	40	80
Selenium	2	Not required	5
Zinc	100	100	200
Electrical Conductivity	1 dS/m	1 dS/m	2 dS/m
pH	8 to 11	Not required	7 to 12
Combustible content	30%	30%	40%
Sulphur %	0.5%	0.5%	1%

The waste management hierarchy is shown in Figure 2.1. This Figure shows that the production and use of a waste should be an alternative to disposal (the least preferable option) but should not be at the expense of more preferable options. However, waste material should only be used where it is safe and sustainable to do so (Environment Protection Authority , 2010).

Table 2.2 Chemical and other material property requirement for exemption of steel furnace slag (Department of Environment, 2009)

Chemicals and other attributes	Maximum average concentration for characterisation (mg/kg)	Maximum average concentration for routine testing (mg/kg)	Absolute maximum concentration (mg/kg)
Mercury	0.5	Not required	1
Cadmium	0.5	0.5	1
Lead	10	10	20
Arsenic	5	Not required	10
Beryllium	10	Not required	20
Boron	NA	NA	NA
Chromium (total)	1000	Not required	2000
Copper	20	Not required	40
Molybdenum	15	15	30
Nickel	30	30	60
Selenium	2	Not required	5
Zinc	50	50	100
Leachable concentration (TCLP) of Chromium	0.1 mg/L	0.1 mg/L	0.2 mg/L
Leachable concentration (TCLP) of Zinc	0.5 mg/L	0.5 mg/L	1.0 mg/L
Electrical Conductivity	NA	NA	NA
pH	7.5 to 12.5	Not required	7 to 13

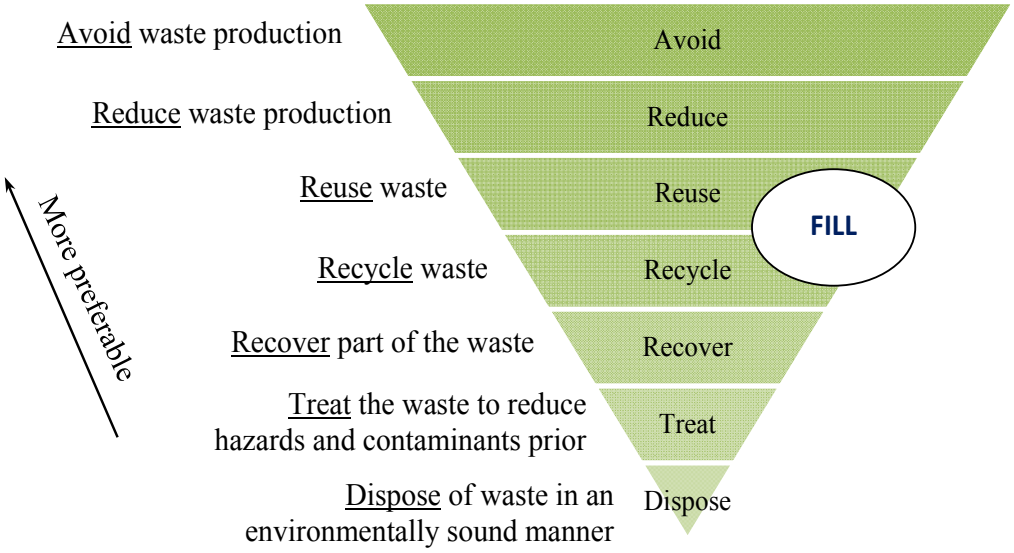

Figure 2.1 Waste material hierarchy (after Environment Protection Authority, 2010)

2.2.2 Recycled aggregates

With respect to recycled aggregates in Australia, they are classified into three groups and their source regions are shown in Figure 2.2 (Cement concrete & aggregates Australia, 2008):

1. Manufactured aggregates: aggregates manufactured from selected naturally-occurring materials, byproducts of industrial processes or a combination of these such as fly ash, manufactured sand, polystyrene aggregate.
2. Recycled aggregates: aggregates derived from the processing of materials previously used in a product and/or in construction such as recycled concrete aggregate, reclaimed aggregate, reclaimed asphalt pavement, crushed brick, crushed concrete, scrap tyres.
3. Reused byproduct: aggregates produced from byproducts of industrial processes such as air-cooled blast furnace slag, granulated blast furnace slag, electric arc furnace slag, steel furnace slag, coal washery reject.

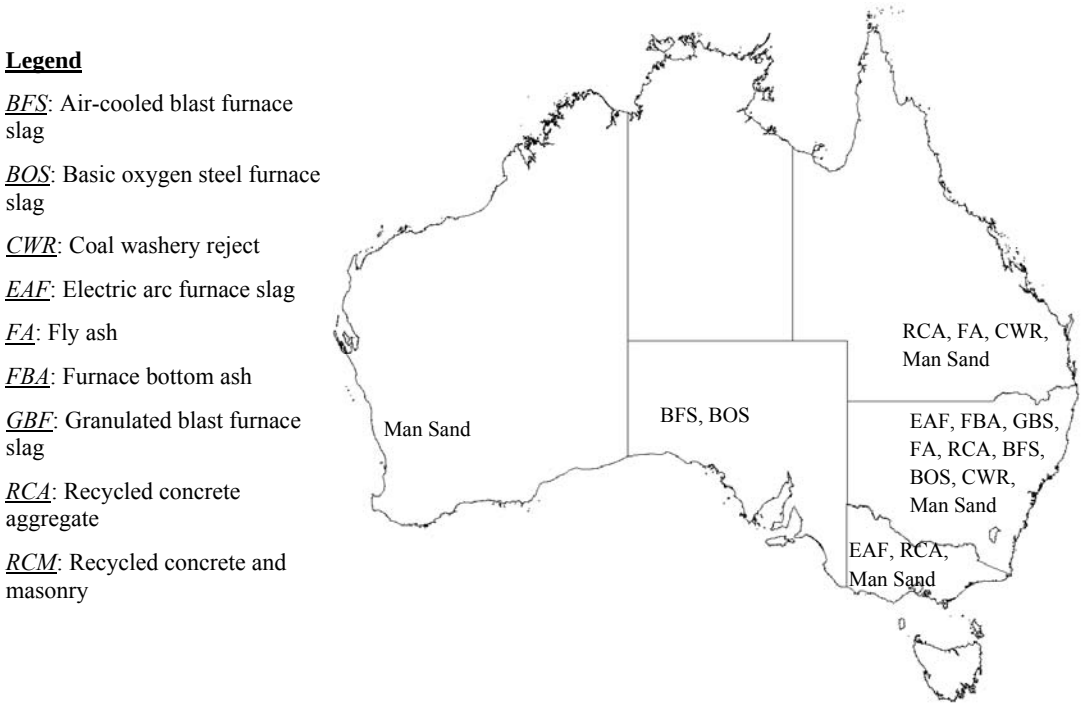

Figure 2.2 Source of recycled aggregates in Australia (after Cement concrete & aggregates Australia, 2008)

2.3 COAL WASH AND STEEL FURNACE SLAGE

Coal wash (CW) and steel furnace slag (SFS) are two industrial waste materials produced in large volume in Australia annually. The production of these two byproducts has been rapidly increasing recently, due to mining activities and steel production (Leventhal and de Ambrosis, 1985, Leventhal, 1996, Geiseler, 1996). It has been recognised that disposal and land filling of industrial waste materials such as CW and SFS can pose an environmental concerns. Approximately 180 million tons of coal mine refuse is produced yearly in the US and most of it is disposed of in the environment (Roth *et al.*, 1977). In New South Wales (Australia), more than 2 million tons of coal wash is produced annually, which is around 25-40% in weight of the total run-of-mine coal (Lu and Do, 1992, Rujikiatkamjorn *et al.*, 2012)

Furthermore, although the annual amount of aggregates worldwide (13 billion tonnes) is much higher than the amount of steel making slag (around 53 million tonnes), the bulk landfilling of this byproduct poses considerable environmental

issues (Emery, 1982). It was estimated that 12 million tonnes of steel slag are produced annually in Europe, and only 65% of this amount is used in different applications and the remnant is just dumped in the environment (Motz and Geiseler, 2001). In Table 2.3, the annual amount of SFS production in different countries is provided. It can be seen that this quantity is relatively great and the recycling reuse of SFS in different applications is both environmentally and economically interesting.

Table 2.3 Annual amount steel slag production in different countries

Country	Steel slag (Million ton)	Reference
Europe	12	Motz and Geiseler, 2001
USA	8-13 (in 2000)	Proctor *et al.*, 2000, Shi, 2004, Wang *et al.*, 2010
Germany	4.1 (in 1971)	Wachsmuth *et al.*, 1981

2.3.1 Production process

2.3.1.1 Coal Wash

The raw coal extracted from the mining industries has many impurities such as shale, sandstone, mudstone, particles from parent rock, and non-carbonaceous material within the coal seam (Figure 2.3). For extracting the pure coal free of impurities, the raw material goes through four stages of separation processes which include comminution (i.e. crushing the bigger particles to smaller ones), sizing, concentration, and dewatering. These operations are very important in the mining industry, because a suitable coal with specified physical and chemical properties should be produced by removing the high ash material. The coal wash waste is produced at the stage of concentration where the refuse is separated from clean coal. There are different methods for this concentration, and one of the conventional methods is gravity separation. In this method, since the specific gravity of pure coal is much less than that of other materials, pure coal floats on top of the other materials in the bath and the coarse fraction impurities known as coal wash (or coal washery

reject) settles on the bottom of the bath enabling their separation. The fine fraction is usually produced in the second stage of flotation and disposed in the form of slurry in tailing ponds (Holubec, 1976, Albrecht, 1980, Leventhal and de Ambrosis, 1985, Mackinnon and Swanson, 2010).

The washery reject can be classified into fine-grained (less than 0.5mm or 0.1mm) or coarse-grained (75mm to 30mm) depending on the processing mechanisms by which they are produced, and the coarse fraction is the one usually considered to be used as fill material (Indraratna, 1994a). In a coal mining plant, around 80% of coal washery reject is in the form of coarse-grained particles and the remaining is fine-grained sizes known as coal tailing (Leventhal, 1996).

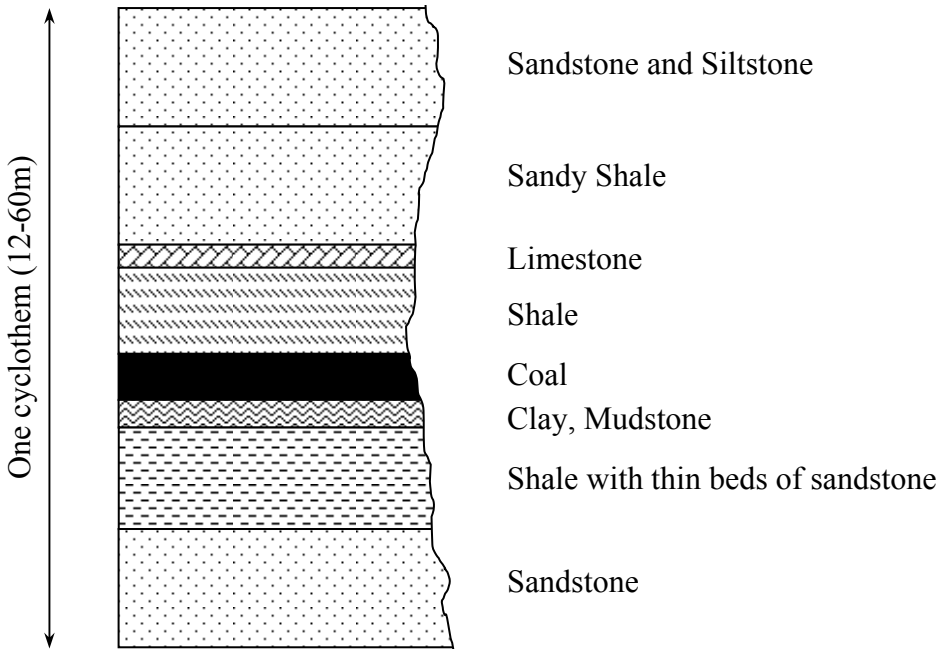

Figure 2.3 Typical coal seam in a cyclothem (after Holubec, 1976)

The quantity of CW in Australia, is evenly divided between the two principal coal producing states, New South Wales and Queensland. In Figure 2.4, the main coal plants areas in Australia are shown (Rujikiatkamjorn *et al.*, 2013).

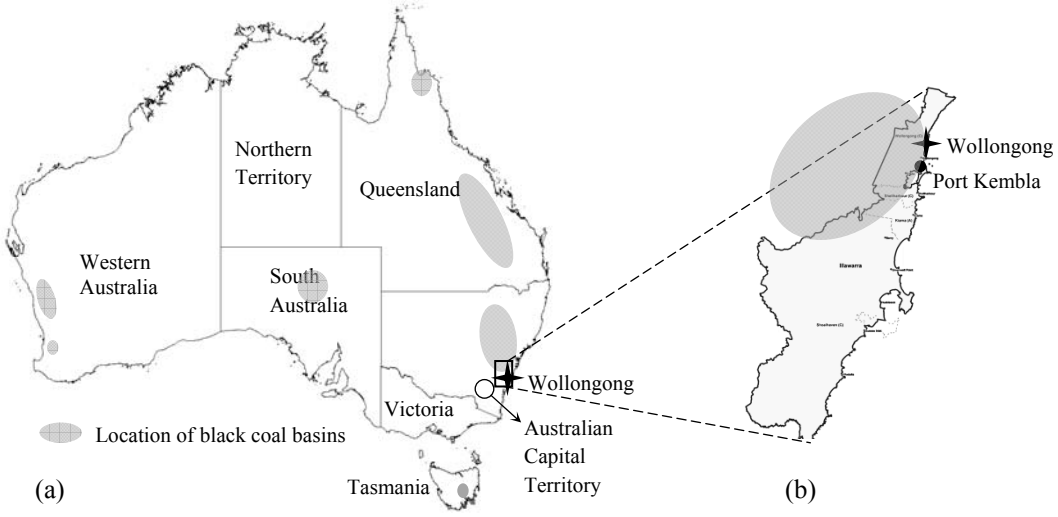

Figure 2.4 Location of Black coal basins in (a) Australia and (b) Illawarra region (after Rujikiatkamjorn *et al.*, 2013)

2.3.1.2 Steel Furnace Slag

In the steel industry, blast furnace slag (BFS) and steel furnace slag (SFS) are the largest portion of byproducts in the conversion of iron ore or scrap iron to steel, which is around 10-15% by weight of the steel output (Proctor *et al.*, 2000). There are two methods being used for steel making as shown in Figure 2.5; (a) conversion of iron to steel in a basic oxygen furnace (BOF) and (b) melting of scrap to make steel in an electric arc furnace (EAF). In the BOF method, scarp, hot metal and flux are charged to a furnace and then for removing the impurities, high pressure oxygen is injected into the converter. These impurities are combined with lime and dolomitic lime and form steel slag. On the other hand, in the EAF method, cold steel scrap is used (rather than hot metal). By passing electric current through electrodes, an arc is formed and melts the scrap. Then, in order to reach the required chemical composition, other metals are added. Therefore, steel slag forms and floats on the surface (Shi, 2004).

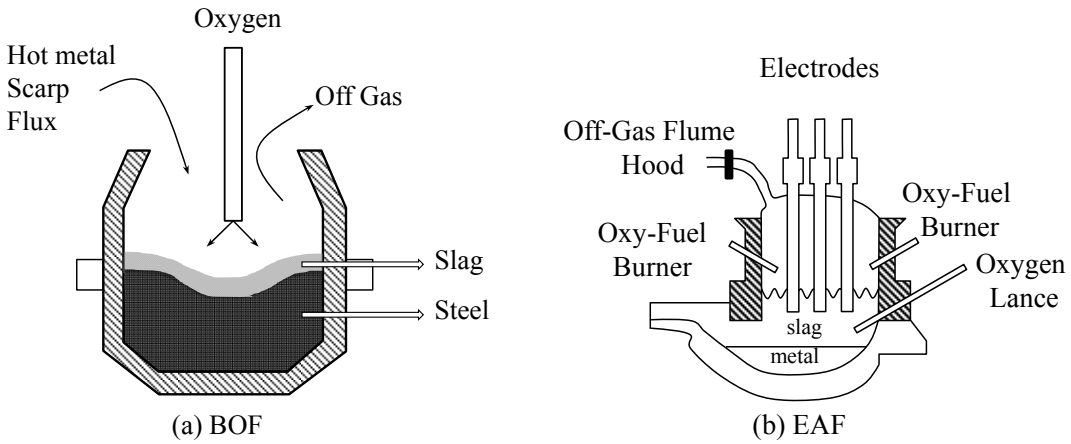

Figure 2.5 Schematic illustration of steel furnace slag production in (a) basic oxygen furnace and (b) electric arc furnace (after Shi, 2004)

After the formation of SFS, several methods are used for cooling. These methods include natural air, water spray, water quenching, air quenching, and shallow box chilling. By cooling down the steel slag, the particle sizes will be in the range of 3-12mm. It should be noted that the chemical properties of SFS are influenced by the cooling method (Zhu *et al.*, 1989).

Around 31% of slag production in Australia and New Zealand in the year 2000 was steel furnace slag (Dippenaar, 2005). The total slag production in these countries is summarised in Table 2.4.

Table 2.4 Total slag production in Australia and New Zealand in the year 2000 (Dippenaar, 2005)

Origin	Blast furnace slag		Steel furnace slag		
	Air cooled slag	Granulated slag	BOF slag	EAF slag	Other
Mass produced (t)	1 050 000	700 000	800 000	155 000	360 000
% Produced	34	23	26	5	12

2.3.2 Physical and chemical properties

2.3.2.1 Coal Wash

Coal wash contains residues of fine-grained carbonaceous parent rocks with small amounts of coal, fragments of shale, and sandstone (Leventhal and de Ambrosis, 1985, Okagbue and Ochulor, 2007). Particles are usually in a plate-shaped elongated form and the length to thickness ratio is more than 3 (Holubec, 1976). The typical chemical composition of coal wash is presented in Table 2.5.

Table 2.5 Chemical composition in coal wash (Leventhal and de Ambrosis, 1985)

Component	Percentage
Ash (mainly SiO_2 and Al_2O_3)	40-66
Carbon	19-32
Sulphur (maximum)	0.4

The specific gravity of coal wash varies from one location to another. This variation is affected by the large difference in specific gravities of coal and shale or clay minerals and their associated percentages in the washery reject (i.e. the two main solid components of coal). The percentage of carbonaceous content in the coal wash has the largest influence on the G_s value (e.g. G_s value changes from 2.05-2.45 once the percentage of this component increases from 20% to 40%). Some G_s values reported in literature are provided in Tables 2.9 and 2.10. Generally, the specific gravity of fine waste is lower than that of the coarse fraction (Holubec, 1976). It is evident that the G_s of coal wash is significantly lower than conventional materials. Due to the internal porosity of CW particles, the bulk specific gravity (i.e. without crushing the bigger particles) is usually lower than actual values. Saxena *et al.* (1984) suggested that the CW particles should be pulverized down to fine fractions to obtain accurate values of G_s.

The values for plastic limit and liquid limit of finer fractions depend on the type of parent rock, the processing method, the clay content, and the type of clay minerals. Table 2.6 provides a summary of Atterberg limits for coal wash. It can be seen that a wide range of limits are available in the literature similar to other engineering properties of coal wash. These values indicate that coal wash is in the range of low to medium plasticity.

Table 2.6 Atterberg limits for coal wash (fine fraction)

Reference	Liquid Limit (LL)	Plastic Limit (PL)	Plasticity Index (PI)
Okogbue and Ezeajugh, 1991	37.1	25.8	11.3
Saxena *et al.*, 1984	27	15	12
Indraratna *et al.*, 2012	27.2	17.7	9.5

2.3.2.2 Steel Furnace Slag

SFS is a high-porosity, honeycomb-shaped material, and mainly consists of CaO, MgO, SiO_2, and FeO. The concentration of these components is around 88% to 92%. Therefore, SFS is usually represented as a CaO-MgO-SiO_2-FeO quaternary system. XRD analysis on the SFS revealed that its composition is similar to the Portland cement clinker (Wang *et al.*, 2010). The chemical composition of SFS depends on the method of steelmaking (whether it is BOS or EAF), type of steel made, and the source material.

Table 2.7 shows an example for the percentage of each chemical constituent for the SFS produced in different countries. The main components in SFS are CaO, Fe, SiO_2, MgO and MnO (Shen and Forssberg, 2003, Setién *et al.*, 2009).

The source of free lime present in the SFS is residual free lime from raw material and precipitated lime from the molten slag. It was observed that when the free lime content is less than 3%, the precipitated lime is the main source, and in case of more than 3% free lime in the SFS, the precipitated lime contribution in the total lime is insignificant and the residual lime makes the major contribution. The variation of

total, residual, and precipitated lime is plotted in Figure 2.6 (Wachsmuth *et al.*, 1981).

Table 2.7 Chemical composition of different types of steel slag (Shen and Forssberg, 2003)

Country	Slag	Fe_{total}	CaO	MnO	MgO	SiO_2	P_2O_5	Al_2O_3	S
Europe	BOF slag low MgO content	14-20	45-55	<5	<3	12-18	<2	<3	NR
	BOF slag high MgO content	15-20	42-55	<5	5-8	12-15	<2	<3	NR
	EAF slag low MgO content	18-28	30-40	<6	4-8	12-17	<1.5	4-7	NR
	EAF slag high MgO content	20-29	25-35	<6	8-15	10-15	<1.5	4-7	NR
Japan	BOF slag (converter)	17.5	44.3	5.3	6.4	13.8	NR	1.5	0.07
	EAF slag	15.2	38.0	6.0	6.0	19.0	NR	7.0	0.38
China	BOF slag	17-27	34-48	1.5-6	2.5-10	9-15	0.9	0.9-2.8	0.2
USA	BOF slag	15-30	40-50	5-10	5-10	10-15	1-3	2	NR

NR=no report

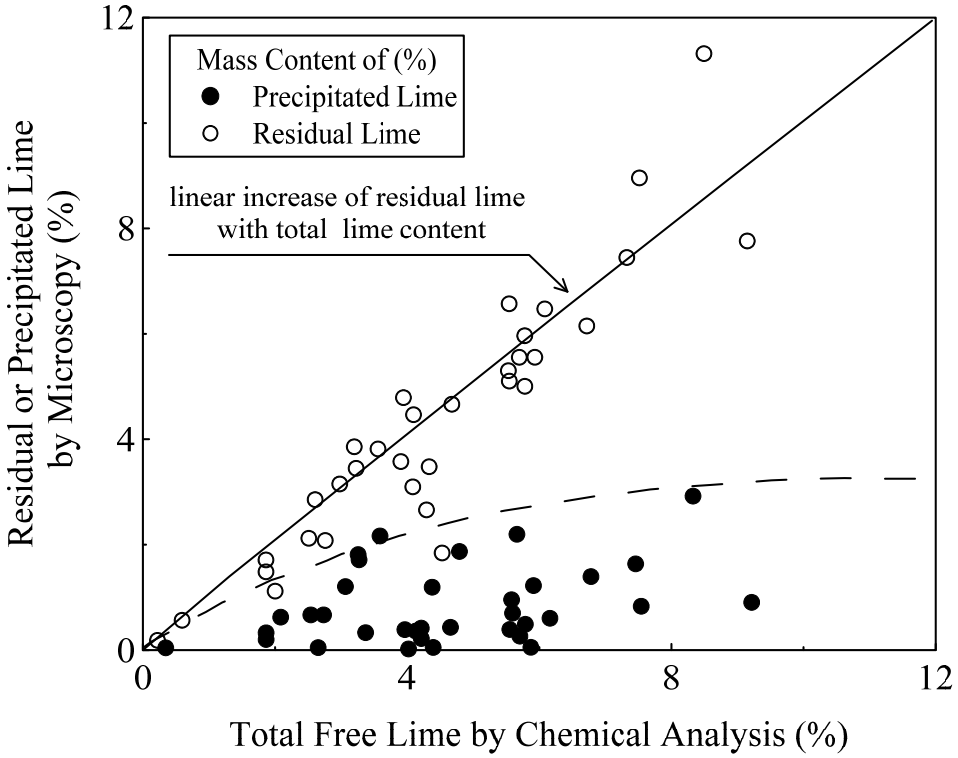

Figure 2.6 Contribution of residual and precipitated lime in steel slag (after Wachsmuth *et al.*, 1981)

Steel furnace slag can be compared with other natural aggregates. In a study conducted by Geiseler (1996), the physical properties of SFS were compared with natural aggregates which are summarised in Table 2.8. It is evident that the density of SFS is much higher than conventional aggregates, the compressive strength is close to that of granite, and the high value of Los Angeles Abrasion test implies that SFS particles are hard to grind.

Table 2.8 Physical properties of steel slags in comparison with natural aggregates (Geiseler, 1996)

Property	Unit	BOF slag	EAF slag	Basalt	Granite
Bulk density	g/cm^3	3.1-3.7	3.2-3.8	2.8-3.1	2.6-2.8
Absorption of water	wt. %	0.2-1.0	0.2-1.0	<0.5	0.3-1.2
Los Angeles test	wt. %	9-18	8-15	-	15-20
Compressive strength	`N/mm^2	>100	>100	>250	>120

2.3.3 Geotechnical properties

2.3.3.1 Coal Wash

Particle size distribution (PSD)

The particle size of coal mine refuse can be divided into fine and coarse fractions. The particle size for the fine fraction is in the range of 0.001-1mm, whereas for the coarse fraction is 0.075-100mm. In Figure 2.7, the PSD of the coal wash used in different studies is shown. It can be seen that there is a wide variation of particle sizes for this material, due to the different procedure being used in mining plants. Therefore, the geotechnical properties of coal wash can vary significantly depending on the coal wash type and the gradation.

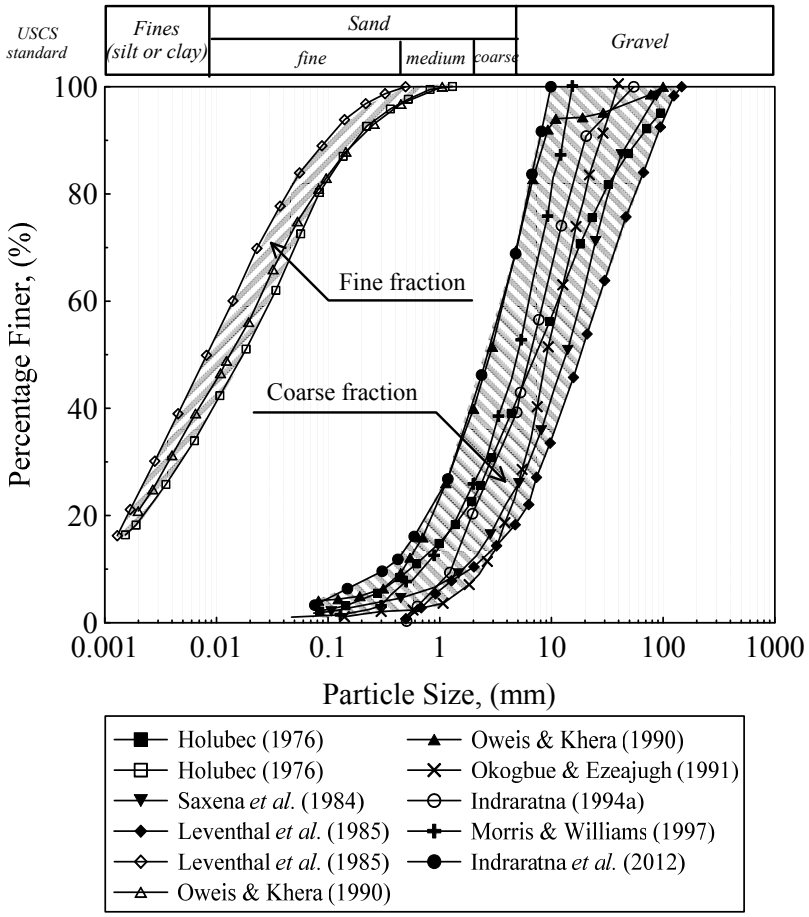

Figure 2.7 PSD curves for both coarse and fine fraction coal wash reported by different researchers

Compaction characteristics

Compaction characteristics of coal washery rejects have been investigated in several studies, and the compaction curve for the coal wash was not identical. Similar to other properties of CW, the maximum dry unit weight (MDUW) depends on the type of CW, chemical composition, and coarse and fine percentage.

The dry unit weight of CW typically ranges between 12.5-21 kN/m^3, whereas the associated optimum moisture content (OMC) is between 6-20% (Oweis and Khera, 1990). A summary of MDUW, OMC, and the G_s is given in Table 2.9. Figure 2.8 shows the compaction curves of CW obtained from different sources.

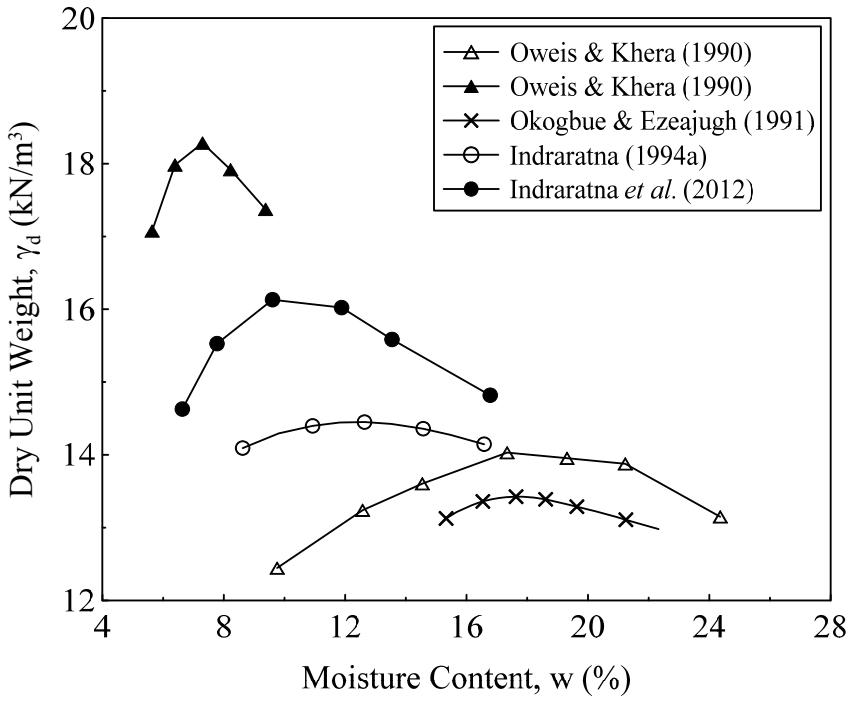

Figure 2.8 Compaction curve for different coal wash

Table 2.9 Summary of compaction characteristics of coal wash

Investigator	Source	G_s	OMC	MDUW (kN/m^3)
Holubec, 1976	US	1.75-2.5	9-21	14.5-18.9
Chen *et al.*, 1976	UK	1.8-2.7	4-16	14.8-20.4
Okogbue and Ezeajugh, 1991	Nigeria	1.72-1.99	15.8-17.7	13.2-13.8
Thomson and Rodin, 1972	UK	1.8-2.7	4-16	14.7-20.6
Indraratna *et al.*, 2012	Australia	2.04	10.4	16.13

OMC, optimum moisture content; MDUW, maximum dry unit weight; G_s, specific gravity

Permeability

Similar to other geotechnical properties, the permeability of coal wash varies based on the particle size distribution, void ratio (or density), fine content, and chemical composition. Furthermore, for the compacted specimens, the compaction energy along with the moisture content also influences permeability. Generally, the permeability of a specimen compacted at optimum moisture content is two to three times lower than for a specimen compacted at dry of optimum moisture content (Mitchell and Soga, 2005, Saxena *et al.*, 1984). In Table 2.10 permeability values of coal wash reported in several references are provided.

Shear Strength

Coal wash (coarse particles) is a cohesionless granular material that exhibits a curved failure envelope. The peak friction angle of coal wash depends on the initial void ratio and the confining pressure (in triaxial condition) or vertical stress (in direct shear). Figure 2.9 shows a range of friction angle against void ratios. It can be seen that there is a curvilinear relationship between internal friction and void ratio (or density). Similar to any granular material, the strength properties of the coal wash depends on the size and the shape of particles. Furthermore, the washery process and the chemical properties of parent rock influences the strength properties of coal

wash. This implies that the range of shear strength for coal wash is significantly wide (Leventhal and de Ambrosis, 1985)

Table 2.10 Summary of permeability properties of coal wash

Investigator	Description of coal wash	G_s	Permeability (m/s)
Leventhal and de Ambrosis, 1985)	Coarse refuse (D_{max}=100mm, D_{50}=10mm) and Fine refuse (D_{max}=0.1mm, D_{50}=0.005mm)	1.75-2.15	$1\times10^{-6}-1\times10^{-4}$ for coarse and $1\times10^{-9}-1\times10^{-8}$ for fine
Williams and Morris, 1990	Coal tailings (D_{max}=1mm, D_{50}=0.01mm)	1.25-2.20	3.0×10^{-9}
Indraratna, 1994a	Coarse fraction (D_{max}=10mm) Fine fraction (D_{max}=1.2mm)	2.10-2.14	4.5×10^{-2} 5.0×10^{-3}
Indraratna *et al.*, 1994b	D_{max}=0.2mm, D_{50}=0.0015mm, e=0.34	1.83-2.19	6.0×10^{-8}
Qiu and Sego, 2001	Coal wash tailing, D_{max}=2mm, D_{50}=0.029mm	1.94	$4.0\times10^{-9}-1.1\times10^{-7}$
Rujikiatkamjorn *et al.*, 2013	D_{max}=10mm, D_{50}=2.5mm, e=0.304-0.428	2.13	$6.0\times10^{-10}-1.0\times10^{-8}$
Indraratna *et al.*, 2013a	D_{max}=10mm, D_{50}=2.5mm	2.04	$1.0\times10^{-9}-1.1\times10^{-8}$ depending on e_0 and moisture content
Holubec, 1976	Fresh uncompacted Well compacted coarse fraction Compacted fine fraction	1.4-2.22	1.0×10^{-3} $1.0\times10^{-5}-1.0\times10^{-9}$ $1.0\times10^{-5}-1.0\times10^{-6}$
Thomson and Rodin, 1972	Coarse fraction	1.8-2.7	$1.0\times10^{-5}-1.0\times10^{-6}$
Saxena *et al.*, 1984	Coarse fraction (D_{max}=50mm, D_{50}=14mm)	2.24-2.57	$3.6\times10^{-8}-1.1\times10^{-4}$

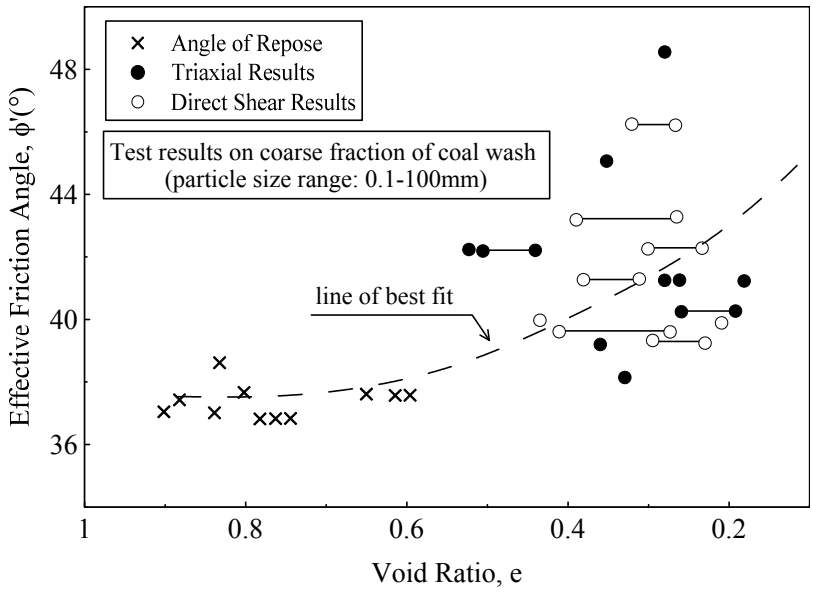

Figure 2.9 Effect of void ratio on friction angle of coal wash (after Leventhal, 1996)

Indraratna (1994a) investigated the geotechnical behaviour of coal tailing and its improvement by adding 2-5% cement. The most notable findings of this study are that an optimum mixture of 55% coarse particles with 45% coal tailing shows higher CBR value compared to the individual components, and that a small addition of cement (around 5%) can increase the unconfined compressive strength (UCS) of an optimum blend significantly. The addition of cement increases the cohesion of coal tailing from almost zero to 600kPa, while there is insignificant change in the internal friction angle. Figure 2.10 shows the UCS of blended optimum coal with different percentages of lime and cement are plotted against curing time. It is evident that there is only a small influence of lime on the coal wash shear strength, while the effect of cement is noticeable.

In another study by Indraratna *et al.* (1994b), the shear strength of the coal tailing was improved by using an internal reinforcement such as layers of geotextile. It was shown that the apparent friction angle of coal tailing increased from 30˚ (for specimen without reinforcement) to 45˚ (with three layers of geotextile). Moreover, the mode of shearing was mainly influenced by the initial moisture content rather than the fabric inclusion. For instance, the failure mode for coal tailing specimen with lower moisture content was tensile cracking, whereas for specimens with higher

percentage of moisture content, bulging failure was observed. For the reinforced specimens, bulging failure was detected between geotextile layers, and strain-hardening behaviour on elevated confining pressure was observed.

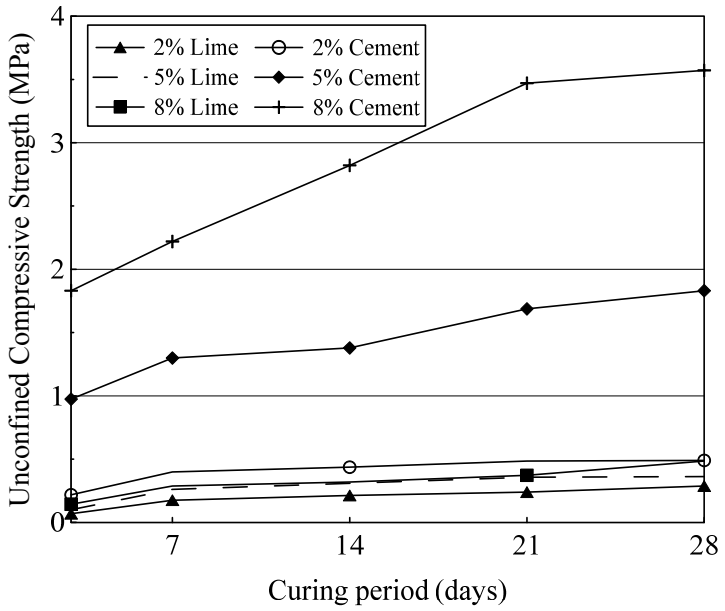

Figure 2.10 Effect of cement and lime on the strength of coal wash (after Indraratna, 1994a)

The secant modulus of coal mine spoil for a stress range higher than 100kPa is approximately 7.2MPa (Koutsoftas and Kiefer, 1990). The strength of the compacted coal waste under unconfined compression testing depends on the moisture content of the specimen. Generally, the higher the moisture content, the lower the shear strength, and the behaviour transforms from brittle to a relatively more ductile response. The cohesion of the coarse fraction coal refuse is insignificant and usually ignored for the shear strength. However, the effective friction angle under undrained triaxial test was reported in the range of 25-43° (Saxena *et al.*, 1984).

The California Bearing Ratio (CBR) test result is another indicator for compressive strength of any material. The soaked and unsoaked CBR values for the compacted coal wash specimens under standard Proctor energy were 12-14% and 11-13%, respectively (Okogbue and Ezeajugh, 1991). In Table 2.11, a summary of the shear strength properties of coal wash available in literature is provided. Similar to other

coal wash properties, there is a wide variation in friction angle and cohesion values. The percentage of fine fraction, particle size distribution, density, confining pressure, and the chemical composition are the main parameters affecting the strength properties.

Table 2.11 Summary of strength properties of coal wash

Investigator	Description of coal wash	Friction angle (°)	Cohesion (kPa)
Holubec, 1976	Coarse fraction (US)	28-41	0-24
Thomson and Rodin, 1972	Coarse fraction (UK)	0	23-42
Saxena *et al.*, 1984	Coarse fraction	27-4	0-45
Leventhal and de Ambrosis, 1985	Coarse fraction (AUS)	37-45	0
Okogbue and Ezeajugh, 1991	Coarse fraction (Nigeria)	39-58	13-15
Indraratna *et al.*, 1994b	Fine fraction (AUS)	17-30	21-29

Collapse Potential

Certain type of soils may exhibit large settlement when subjected to a wetting process with no additional increase in stress. The wetting process may be caused either by a sudden change of the groundwater table or heavy rainfall. The additional settlement caused due to wetting and consequent collapse of soil structure, is termed as collapse settlement. For a given compacted soil, the most important factors that determine its collapse potential are pre-wetting moisture condition, dry density and stress state (El-Ehwany and Houston, 1990, Charles and Watts, 1996, Auriol *et al.*, 2008). The collapse potential is expressed as a change in void ratio upon wetting compared to the pre-wetting volume of the soil at any stress level (Indraratna *et al.*, 1994b). The collapse potential (*CP*) is expressed in percentage and defined by Eq. 2-1 (ASTM D5333-03).

$$CP = \frac{\Delta e}{1 + e_0} \times 100\% \tag{2.1}$$

where Δe is change in void ratio on inundation and e_0 is initial void ratio.

For assessing the severity of collapse potential, the collapse potential is determined under a vertical stress of 200kPa in accordance with the ASTM D5333-03 and then the value of *CP* is compared with those tabulated in Table 2.12.

Table 2.12 Classification of collapse index (ASTM D5333-03)

Degree of Collapse	Collapse Potential (*CP*) %
None	0
Slight	0.1-2.0
Moderate	2.1-6.0
Moderately severe	6.1-10.0
severe	>10

In a study by Indraratna *et al.*(2012), it was shown that the collapse potential of coal wash in non-compacted specimens was much higher compared to compacted specimens. In addition, by increasing the vertical load on a specimen before inundation, the collapse potential increases linearly for a non-compacted specimen whereas, for the compacted specimens, the rate of collapse potential over vertical stress decreased gradually. The results of this investigation are shown in Figure 2.11. Similarly, Leventhal and de Ambrosis (1985) investigated the collapse potential of the loose coal wash specimens by conducting two series of tests; first series on the dry samples and the second series on the inundated samples (Figure 2.12). This study revealed that not only the inundation caused the sudden change in the void ratio, but also it influenced on the stiffness of the specimens in a way that the stiffness of the inundated specimen was lower that the dry specimen.

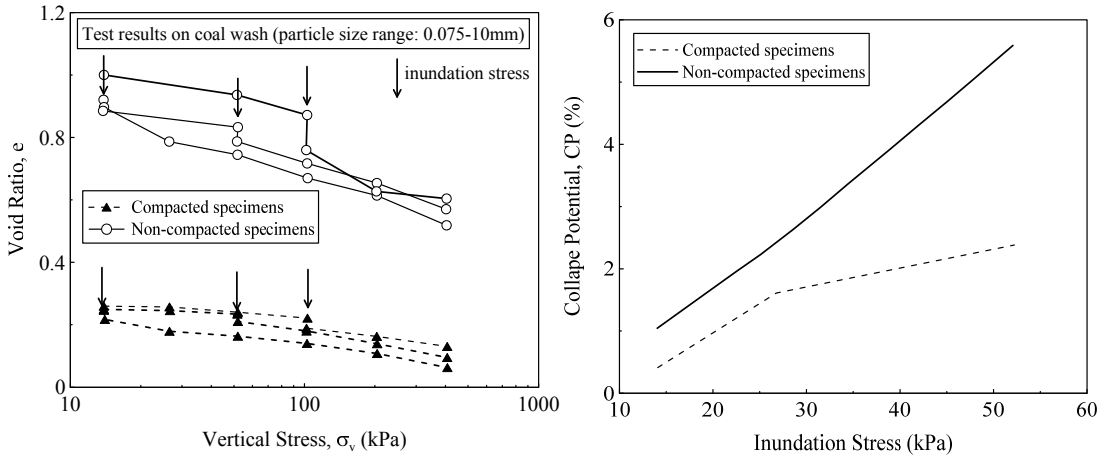

Figure 2.11 Collapse potential for coal wash: (a) collapse settlement under varied vertical stress and (b) variation of collapse potential against vertical stress for compacted and non-compacted specimen (after Indraratna *et al.*, 2012)

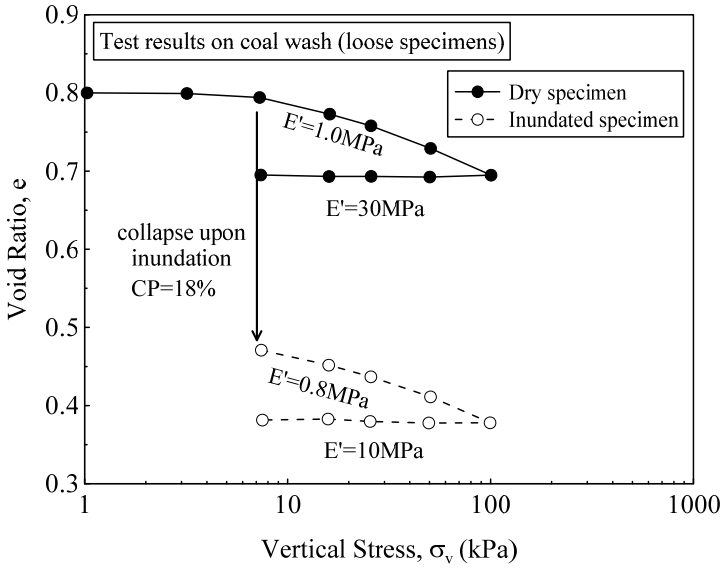

Figure 2.12 Collapse settlement of loose coal wash (after Leventhal and de Ambrosis, 1985)

Particle Breakage

One of the main drawbacks of the coal wash is particle degradation upon loading. Two factors can cause particle breakage in coal wash; physical weathering and chemical weathering. Physical weathering usually happens during handling, disposal, compaction, and under monotonic or repetitive loading condition like access roads. In contrast, the oxidation of pyrite (that is presented in shale and carbonaceous

particles) causes chemical weathering, and the extent of weathering may be significant (e.g. few meters below the surface). The particle breakage process is usually observed for coarser fraction of particles (2-20mm). An example of particle size degradation influenced by chemical weathering is plotted in Figure 2.13 (Holubec, 1976). It is evident that particle degradation causes an increase in fine fraction and subsequently influences material properties such as reduction in permeability and shear strength.

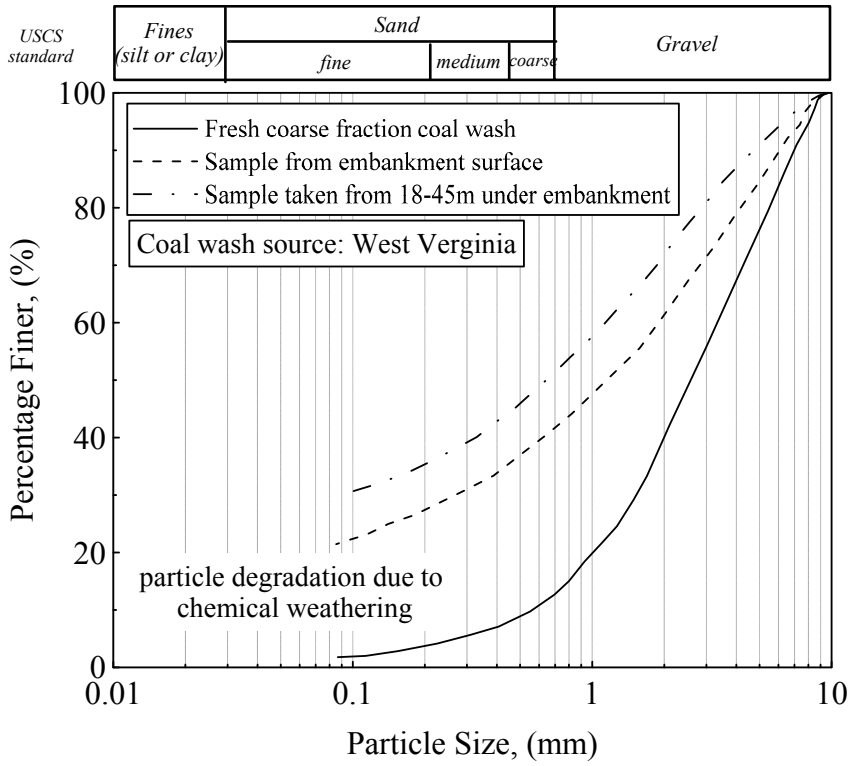

Figure 2.13 Particle degradation in coal wash due to the chemical weathering (after Holubec, 1976)

2.3.3.2 Steel Furnace Slag

Particle size distribution (PSD)

Similar to coal wash, the particle size distribution of steel furnace slag depends on the source material, the steelmaking process, and the cooling process. During the cooling process, different sizes of steel slag (i.e. from large particles as boulder size

to smaller sizes as silt-size) are generated. After the cooling process, the steel furnace slag is screened to three gradation sizes; coarse gradation (i.e. particles in the range of 64mm to 200mm), medium gradation (i.e. particle sizes up to 64mm) and fine gradation for particles smaller than 64mm (Yildirim and Prezzi, 2009). In Figure 2.14, the PSD of the steel furnace slag used in different studies is shown. It can be seen that there is a wide variation of particle sizes for this material. Therefore, the geotechnical properties of steel furnace slag can vary significantly depending on the gradation.

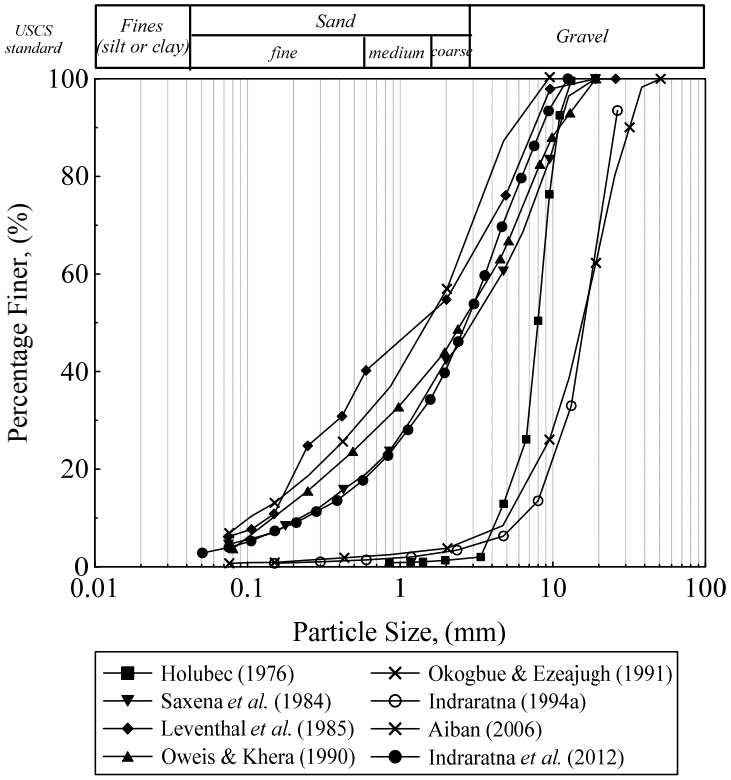

Figure 2.14 PSD curves for steel furnace slag reported by different researchers

Compaction

Similar to CW, the specific gravity of SFS depends on gradation and chemical composition. The generation of steel slag cannot be controlled precisely, and therefore any variation on the percentage of components in SFS influences the G_s

(Yildirim and Prezzi, 2009). A clear example is blast furnace slag (from iron making) and SFS (from steelmaking). Although the chemical components for these two byproducts are similar, the percentage of each constituent is quite different (the manganese and iron contents in SFS are significantly higher). Therefore, the G_s for blast furnace slag is in the range of 2.2-2.5, whereas for SFS it is around 3.2 to 3.5 (Emery, 1982). A summary of compaction characteristics of SFS reported in past studies is provided in Table 2.13. Due to the high G_s values of steel slag, the maximum dry unit weight of steel slag is typically higher than the natural aggregates.

Table 2.13 Summary of compaction properties of steel furnace slag

Investigator	Type	G_s	OMC	MDUW (kN/m^3)
Malasavage *et al.*, 2012	US	3.45	9-10	25
Montenegro *et al.*, 2012	Ladle furnace slag (<2mm)	N/A	19	16.9
Lee, 1974	Steel slag	3.1-3.6	N/A	15.7-18.9
Ghionna *et al.*, 1996	N/A	N/A	4-6	26
Rohde *et al.*, 2003	EAF slag	3.4-3.5	3-6	23-26
Andreas *et al.*, 2005	35%EAF slag+65% Ladle slag	N/A	13	22
Yildirim and Prezzi, 2009	BOF slag	3.29-3.34	4-8	19-22

Shear Strength

Steel furnace slag is a cohesionless granular material and usually shows a relatively high strength and friction angle due to the roughness of the particles. The strength characteristics depend on the type of steel slag, density, and the particle size (Faraone

et al., 2009). In a study by Malasavage *et al.* (2012), the strength characteristics of SFS was determined through a series of consolidated undrained (CU) triaxial tests and the friction angle of 46° was recorded in the laboratory. In addition, the CPT results in the field was observed to increase with depth from 10MPa to the maximum 80MPa (corresponding to the depth of 0.2m to 3m, respectively). It was observed that the shear strength of steel byproducts increases with time due to their cementitious properties. Shi (2002) conducted a series of compression tests on three different ladle slag fines and observed that the compressive strength of the specimens increased in a range of 50% to 250% during 28 days curing.

Furthermore, Yildirim and Prezzi (2009) conducted extensive direct shear and triaxial tests on fresh and aged BOF slag. In direct shear tests, for a range of 30-70kPa vertical stresses, peak friction angles of 50-53° were observed. It was shown that the friction angle of an aged steel slag was lower than a fresh slag. The results of consolidated isotropic drained (CID) triaxial tests on aged steel slag revealed that the friction angle was 43.5-47.3° under 200-50kPa confining pressures.

Swelling Potential

One of the key issues in utilizing SFS in practical application is the volume stability of SFS. The existence of free lime (unhydrated lime) and/or free MgO causes volume expansion in contact with water which cause disintegration of the slag particles and thus loss of strength (Motz and Geiseler, 2001, Montenegro *et al.*, 2012, Juckes, 2003). The main reason for swelling of the SFS is the reaction of free lime with water. Once the free lime reacts with water, the specific gravity changes from 3.34 to 2.23 which results in volume expansion. Due to the denser structure of free lime in the SFS, the hydration rate is quite slow (Wang *et al.*, 2010).

Unlike some byproducts such as coal wash and blast furnace slag, steel slag has expansive potential up to 10% due to the hydration of calcium and magnesium oxides (mostly the free CaO and MgO). This can cause serious problems if SFS is

used in confined applications. Even if used as a base or sub-base material SFS can cause damage to the superstructure (Crawford and Burn, 1969). Figure 2.15 shows an example of expansive potential for different type of SFS and it shows that ageing SFS (e.g. acidic treatment, use of coarser particles) results in reduced percentage of expansion. Since the water is involved in the steelmaking process, it is expected that part of hydration and SFS ageing would occure before being used (Emery, 1982).

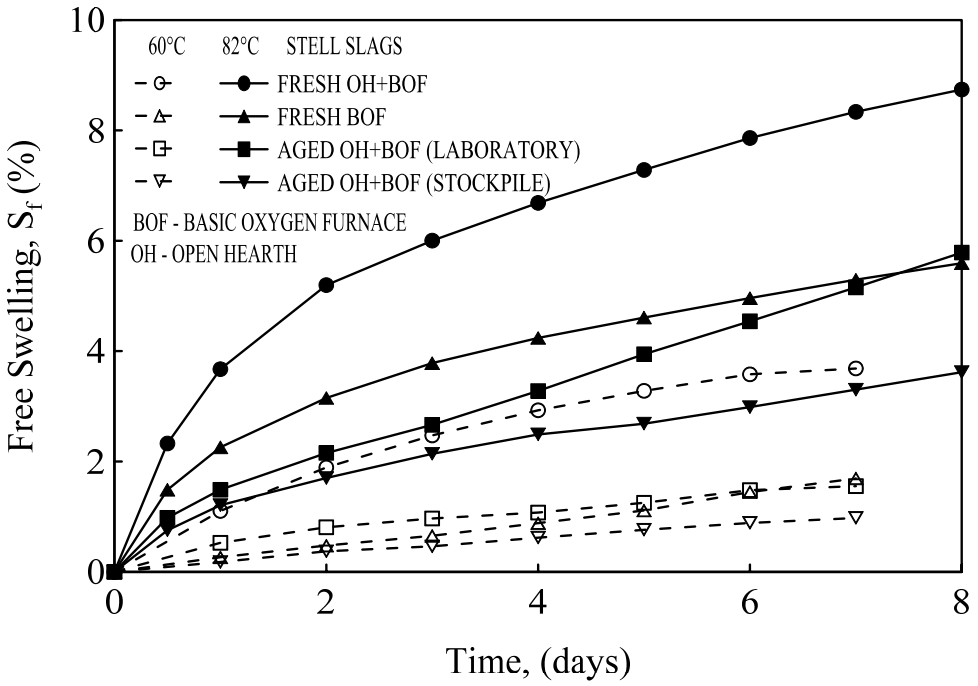

Figure 2.15 Expansion of fresh and aged steel slag with time under two different temperatures (after Emery, 1982)

Motz and Geiseler (2001) studied the volume expansion characteristic of different types of SFS, using two conditions: bituminous bound and unbound mixture. In this study, the steam method was adopted for volume expansion measurements. The values of the volume expansion are presented in Table 2.14.

.

Table 2.14 Results of expansion test on BOF/EAF slags in two different conditions (after Motz and Geiseler, 2001)

Type of steel slag	Maximum expansion (%)		Testing time (hr)
	Aggregates for bituminous bound mixture	Aggregates for unbound mixture	
BOF/EAF slag (MgO<5%)	3.5	5	24
BOF/EAF slag (MgO>5%)	3.5	5	168
BOF/EAF slag (MgO<5%)	6.5	7.5	24
BOF/EAF slag (MgO>5%)	6.5	7.5	168
BOF/EAF slag (MgO<5%)	10	10	24
BOF/EAF slag (MgO>5%)	10	10	168

Wachsmuth *et al.* (1981) conducted an investigation on the volume stability of 30 different samples of SFS under the two conditions of bituminous bound or unbound. For the bituminous bound condition, the specimens were mixed with bitumen and compacted in a cylindrical shape and then kept under water at 40˚C for 42 days. For the unbound condition, the specimens (1-3.15 mm particle size) were tested in the autoclave chamber. In Figure 2.16a, the volume expansion of unbound specimens is presented. It can be seen that the volume expansion of SFS depends on the percentage of pores and free lime. As these two parameters increased, the volume expansion was increased. In addition, Wachsmuth *et al.* (1981) graphically demonstrated the effect of the volume content of pores and the percentage of free lime on the volume expansion of SFS (Figure 2.16b).

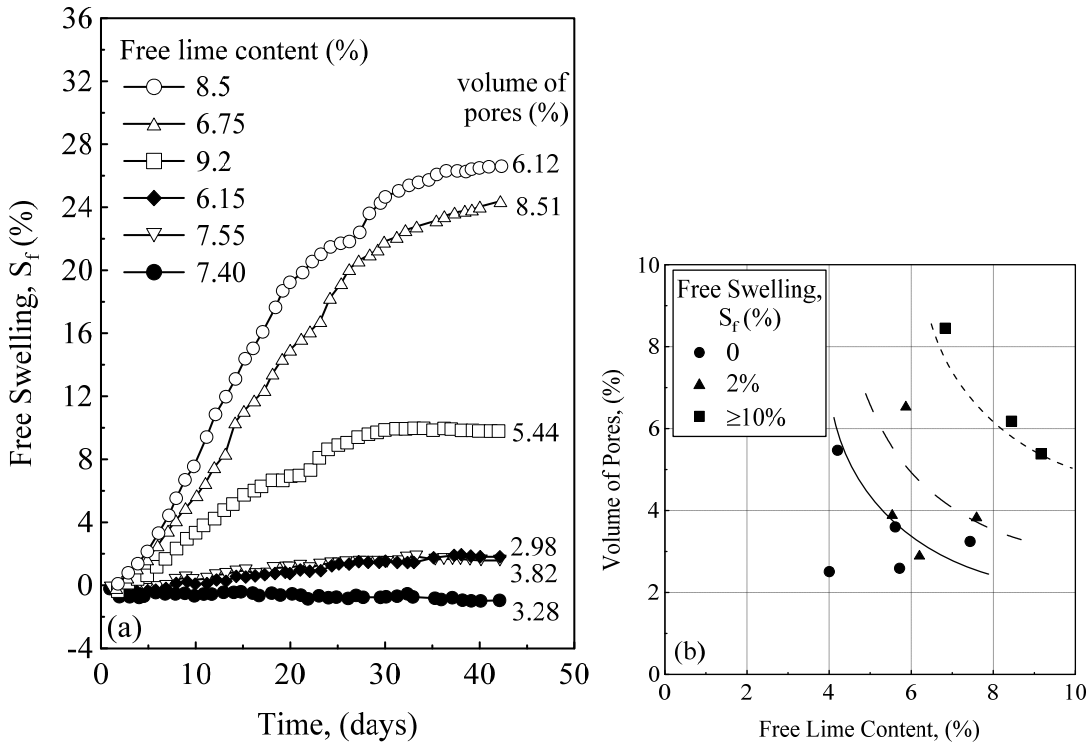

Figure 2.16 (a) Volume expansion of unbound bituminous BOF slag and (b) effect of porosity and free lime on the volume expansion (after Wachsmuth *et al.*, 1981)

Wang *et al.* (2010) suggested that the total SFS volume expansion could be determined considering the expansion mechanism due to physical change. This mechanism can be elaborated through Figure 2.17. Once the hydration of SFS occurs, the void volume within the SFS bulk is accompanied by the increase of the solid phase. By assuming a spherical shape of particles, the volume of voids and solids accounts for 26% and 74% of total volume, respectively. Although the absolute volume of the system increases, the volume ratio of solids to voids does not change. It was reported that the volume of solid phase increases by 97.92% during hydration, so the void volume increases by 26/74×97.92%=34.40%. Therefore, the combination of volume increase in both voids and solids is 34.40%+97.92%=132.23%. Since the absolute volume change for lime-water systems is -4.54%, the actual volume expansion of free lime in SFS is 132.23%-

4.54%=127.78%. Then, the SFS volume expansion can be expressed by the following equation:

$$E_{SFS} = \frac{1}{V_0 D} \times \frac{V_0 D \gamma_s F}{\gamma_1} \times \frac{E_1}{100} \tag{2.2}$$

where E_s is the volume expansion of SFS, V_0 is the apparent volume of SFS (cm^3), D is the denseness of steel slag (γ_0/γ_s), γ_0 is the bulk density of SFS samples with voids (g/cm^3), γ_s is the specific gravity of steel slag (g/cm^3), F is the free lime content (%), γ_1 is the compacted density of lime (g/cm^3), and E_1 is the volume expansion of lime (127.78%).

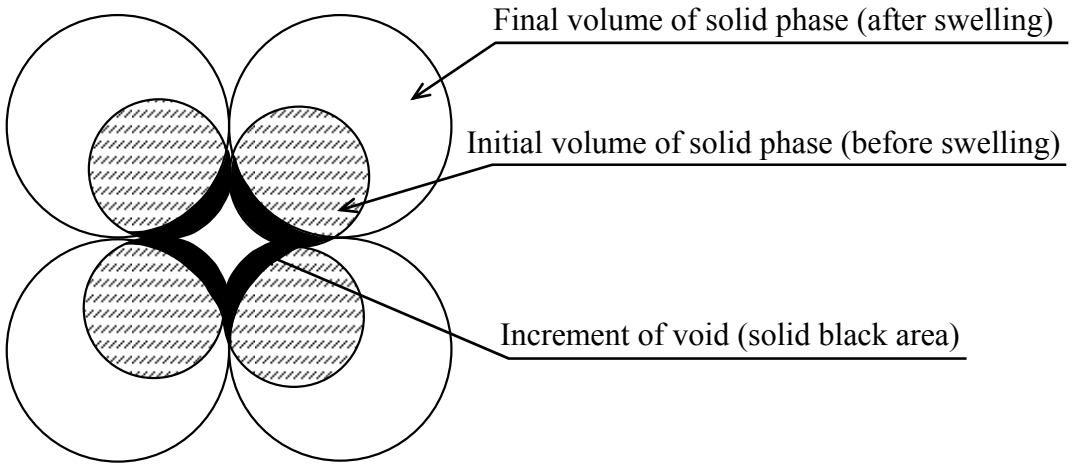

Figure 2.17 Simplified expansion mechanism of SFS (after Wang *et al.*, 2010)

2.3.4 Engineering applications

As discussed in the previous section, waste management plays a significant role in reducing the issues related to industrial wastes (e.g. recycling and reusing of wastes rather than disposal in landfills). One of the options to reduce this problem is to use these materials in different fields of application such as cement production (Maslehuddin *et al.*, 2003, Shi and Qian, 2000), civil and road construction work (Maslehuddin *et al.*, 2003), and soil reclamation and water treatment (Ortiz *et al.*, 2001). In Table 2.15, the field application for different types of solid waste along with the source of solid is provided.

Table 2.15 Different types and sources of solid wastes and their recycling and utilization potentials for construction materials (adapted from Pappu *et al.*, 2007)

Type of solid wastes	Source details	Recycling and utilization potentials
Agro-waste (organic)	Rice, wheat, saw mill waste, ground nut shell, cotton stalk, vegetable residues	Cement boards, boards, wall panels, fibrous building panels, bricks, acid-proof cement, polymer composites
Industrial waste (inorganic)	Coal combustion residues, steel slag, construction debris	Fine and coarse aggregates, bricks, blocks, tiles, cement, paint, concrete, ceramic products
Mining/mineral waste	Coal washeries waste; mining waste tailing from iron, copper, zinc, gold and aluminium industries	Bricks, fine and coarse lightweight aggregates, tiles
Non-hazardous waste	Waste gypsum, lime sludge, limestone waste, broken glass and ceramics	Blocks, bricks, cement clinker, hydraulic binder, fibrous gypsum boards, gypsum plaster
Hazardous waste	Contaminated blasting materials, galvanizing waste, metallurgical residues, sludge from waste water and waste treatment plants	Boards, bricks, cement, ceramics, tiles

2.3.4.1 Coal Wash

The application of coal wash in civil engineering depends on the particle size. Coarse fractions of coal wash can be utilized in the construction of tailing dams, mine access roads and fill embankments (Indraratna, 1994a). Haibin and Zhenling (2010) provides a flow chart for the utilization and recycling of coal mine waster (or coal gangue) which is shown in Figure 2.18. It can be seen that this byproduct can be mainly used for power generation, land reclamation, brick and cement production.

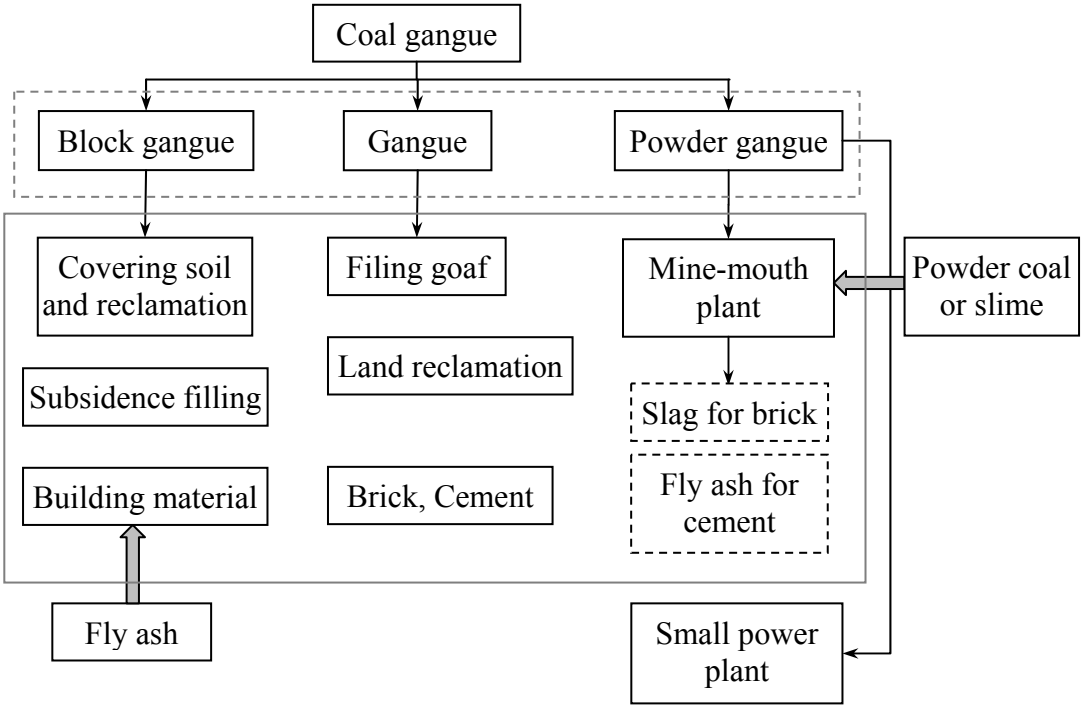

Figure 2.18 Utilization of coal mine residue (after Haibin and Zhenling, 2010)

2.3.4.2 Steel Furnace Slag

Since the percentage of Fe in SFS is quite large, the first step of processing of SFS is the iron recovery. Therefore, the utilization of SFS can be divided into two stages. The first stage is the direct application in the iron and steel-making process, and the second stage is the application outside the steel-making process. A summary of the SFS application is shown in Figure 2.19 (Shen and Forssberg, 2003).

For many years, SFS has been used in many applications such as road construction, fill material, cement additive, and landfill cover material. Proctor *et al.* (2000) provided a list of application where steel furnace slag can be used. These applications are given in Table 2.16.

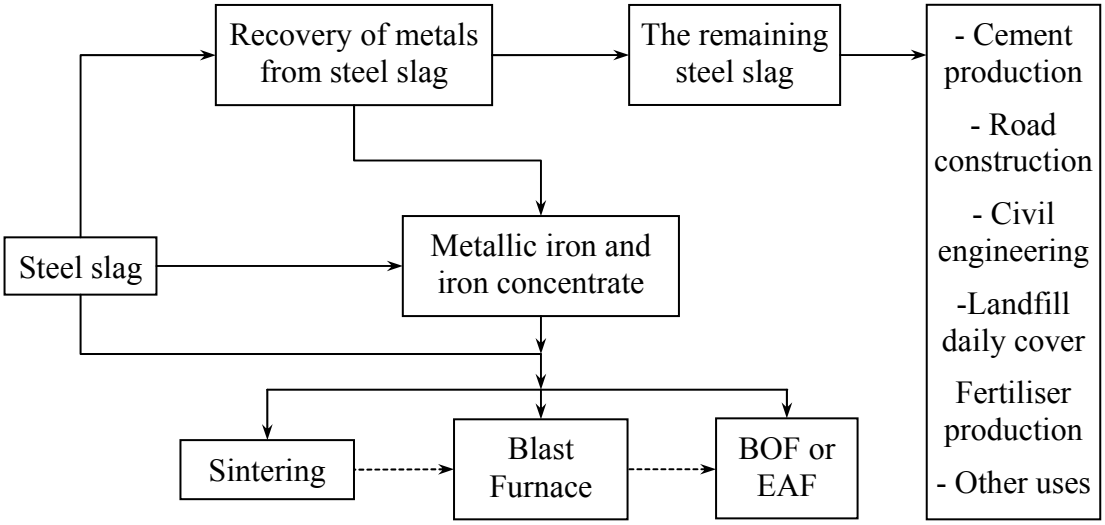

Figure 2.19 Utilization of steel slag (after Shen and Forssberg, 2003)

Table 2.16 Application of steel slag in different condition (Proctor *et al.*, 2000)

Typical iron and steel slag uses	Application					
	Applied to land surface	Applied to land subsurface	Placed in water	Encapsulated uses	Agricultural uses	Landfill uses
Aggregate in bituminous mixes (pavement)				×		
Concrete aggregate				×		
Surfacing stabilised shoulders	×		×	×		
Bank stabilisation (erosion control)	×		×			
Gabions and riprap	×		×			
Base and sub-base aggregate	×	×		×		
Unpaved driveways	×					
Railroad ballast	×					
Landfill cover						×
fill	×	×	×			×

It is noticeable that around 40% of total steel slag produced in China has been used in cement production commercially for more than 20 years (Shen and Forssberg,

2003). In contrast, although SFS shows cementitious properties, only a small amount of it is used in concrete production. For example, out of 5.1 million tonnes annual production of SFS in US, no steel slag is used in the cementing component because of its expansion potential (Shi and Qian, 2000).

Emery *et al.* (1973) reported that in most countries, steel furnace slag is used as an aggregate in asphalt. For instance, the production and utilisation of iron and steel-making slag are outlined in Table 2.17. It can be seen that more than 50% of steel slag is used in various applications (Dippenaar, 2005).

Table 2.17 Production and utilisation of blast furnace and steel-making slag in Australia and New Zealand in the year 2000 (Dippenaar, 2005)

Slag type	Blast furnace	Granulated blast furnace	BOF slag	EAF slag
Production (t)	1 050 000	700 000	800 000	155 000
Utilisation (t)	750 000	700 000	510 000	84 000
Utilisation (%)	71	100	64	54
Production technique	Air cooled	Molten slag quenched with high pressure water sprays	Air cooled and watered	Air cooled and watered
Typical applications	Base, sub-base, Concrete aggregate, Filter aggregate, Construction fill	Sub-base, Construction fill, Construction sand, Cement manufacture, Reinforced earth wall infill	Sealing aggregate, Asphalt aggregate, Base, Sub-base, Subsoil drain, Construction fill	Sealing aggregate, Asphalt aggregate, Base, Sub-base, Subsoil drain, Construction fill

Emery (1982) studied the application of SFS in the asphalt mixes and reported that excellent performance could be reached by eliminating the expansive behaviour of SFS through usage of asphalt cement coating. Furthermore, this study showed that due to the great resistance of this type of asphalt mix to stripping, this asphalt could be used in places subject to heavy axle loads, such as industrial roads and parking spaces.

Wang *et al.* (2010) proposed a criterion in regards to the application of SFS considering its volume expansion. The use of Eqs. (2.3) and (2.4) could provide an indication to whether a particular SFS could be used in the field based on the free lime content in the SFS.

$$F_{all} < 2.0\% + \frac{K_{25}\left(\gamma_s - \gamma_0\right)}{0.38\gamma_s^2} + 100 \quad \text{for free lime} \leq 4\% \tag{2.3}$$

$$F_{all} < 2.8\% + \frac{K_{25}\left(\gamma_s - \gamma_0\right)}{0.38\gamma_s^2} + 100 \quad \text{for free lime} > 4\% \tag{2.4}$$

where F_{all} is the allowable free lime content, K_{25} is the differentials in volume expansion caused with the application of surcharge (%), γ_s is the specific gravity of steel slag (g/cm^3), and γ_0 is the bulk density of SFS samples with voids (g/cm^3).

In essence, SFS can be utilized in different fields of application. In Table 2.18, the fields of application where SFS can be used are provided. There is a wide range of applications for SFS but some properties of SFS such as volume expansion prevent its use as individual aggregate.

Table 2.18 Summary of utilization of SFS in different application

Investigator	Type of SFS	Application
Motz and Geiseler, 2001	BOF, EAF with different percentage of MgO	• Road construction material such as unbound layers (base, sub-base) or for bituminous bound layers (surface layer) • Hydraulic structures (dams, dikes, stabilisation of river banks)
Emery, 1982	All types of SFS	• Returning it to blast furnace slag • Road construction • Use in asphalt mixes • Use as fertilizer
Shi and Qian, 2000	Several types of SFS	• Activated steel slag cement decreases both the time of initial and final setting and increases the strength of concrete
Shen and Forssberg, 2003	BOF and EAF	• Iron recovery • Cement production, fertilizer, road construction
Shi, 2004	BOF and EAF	• Use in different cementing systems as a cementing component

2.4 SUMMARY

In this chapter, the past studies relevant to the topic of this research were the focus. These topics include: the management approach to the different waste materials, presenting two industrial byproducts considered in this study (i.e. coal wash and steel furnace slag) in terms of the production process, physical and chemical compositions for different type of CW and SFS, geotechnical characteristics and finally their utilization and application in the field.

It was shown that geotechnical properties (i.e. internal friction angle, compaction characteristics, and permeability) of individual CW and SFS were comparable with the conventional fill material. Therefore, they have been used in many areas of civil engineering. However, most of these applications and subsequent studies only focused on one type of waste material, not as a mixture. It is already known that

using steel slag on its own can pose a serious problem with infrastructure because of its high swelling potential (Wang, 2010; Wang *et al.*, 2010), and although not expansive, coal washery rejects can cause differential settlement due to particle degradation or collapse (Pusadkar and Ramasamy, 2005). On the basis that the adverse effects of both materials might be diminished by mixing the two materials, an in-depth study of the behaviour of blended waste materials on coal wash and steel furnace slag was therefore essential.

The main objective of this study is to firstly evaluate the geotechnical behaviour of CW and SFS mixtures (preliminary parameters as well as stress-strain behaviour) and then, based on their characteristics, a framework to establish the effectiveness of granular waste fills and to optimise CW-SFS blend as a suitable reclamation fill. This is then proposed for the Port Kembla Outer Harbour expansion in the following chapters.

CHAPTER THREE

3 EXPERIMENTAL TESTING PROGRAM

3.1 INTRODUCTION

Two industrial byproducts (i.e. coal wash and steel furnace slag which are in abundance in the Illawarra region, NSW, Australia) were considered in this investigation. For establishing the design guidelines for the use of CW-SFS mixtures, the accurate determination of the engineering properties of the blended mixtures is essential. However, limited studies have reported the detailed properties of CW and SFS. Therefore, to address this knowledge gap in the current state of practice, the suitability of CW, SFS and their mixtures for use as a structural fill, was evaluated through both laboratory and field investigations. The preliminary stage of the laboratory tests was conducted to evaluate the geotechnical properties of the individual CW and SFS material and their mixtures. These tests included specific gravity (G_s), compaction characteristics, California Bearing Ratio (CBR), permeability, Unconfined Compression Strength (UCS), and volume stability or swelling potential. Subsequently, the stress-strain behaviour was examined through a series of triaxial tests. Finally, a field investigation was carried out to analyse the performance of two selected CW-SFS mixtures in a field trial. The performance of the two blends employed on site was evaluated through *in-situ* density testing, Dynamic Cone Penetration Tests (DCPT), and Plate Load Tests (PLT) and the swell potential was monitored using surface marks. The summary of this program is shown in Figure 3.1.

This chapter initially describes the materials used in this study (i.e. chemical composition and particle size distribution). Then, the laboratory program for triaxial testing, including the isotropic compression tests and drained shearing, over a range

of effective confining pressure, is outlined. The aspects of triaxial equipment are explained briefly. Afterwards, the details of the tests conducted to evaluate the swell potential and swell pressure are described. Subsequently, the procedures adopted in the specimen preparation including compaction and saturation are explained.

3.2 TEST MATERIALS

Blended mixtures of two industrial byproducts were investigated in this study i.e. Coal Wash (CW) and Steel Furnace Slag (SFS). These materials are byproducts or wastes produced from the coal mining and steel making industries, and they are typically disposed of in stockpiles occupying otherwise usable land. The CW used in this study was produced at the Dendrobium colliery and supplied by BHP Billiton-Illawarra Coal. This mine is one of the largest coal mines in the region (Figure 3.2), and it is located approximately 8km west of Wollongong. CW is a well-graded, dark-coloured and heterogeneous material with varying constituents including coal residuals, ash, and carbon. As CW results from mining operations, extraction at different levels inevitability results in some degree of material variability. The index properties (e.g. specific gravity) were observed to vary from batch to batch. Therefore, all tests were performed on a particular batch of CW and SFS for consistency. The chemical components of the CW determined in the XRF technique are provided in Table 3.1.

The SFS supplied by Australian Steel Mill Services (ASMS) is produced in a basic oxygen system (BOS) as explained in Chapter 2. Table 3.2 provides the chemical composition of SFS (determined in the XRF technique), and it can be seen that it mainly consists of heavy oxides (e.g. Fe_2O_3, SiO_2). The visual appearance of CW and SFS is shown in Figure 3.3.

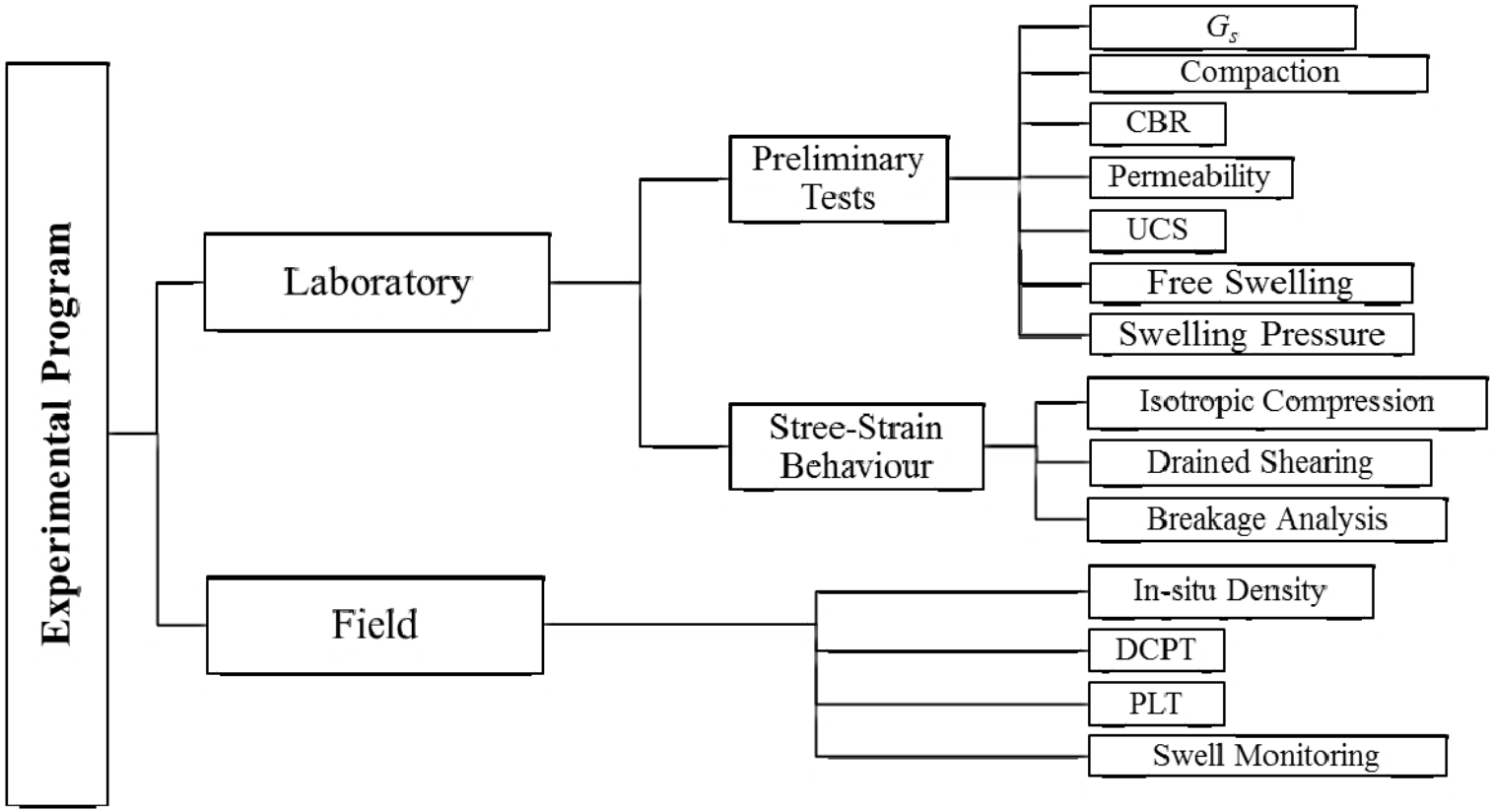

Figure 3.1 Summary of laboratory and field testing programs

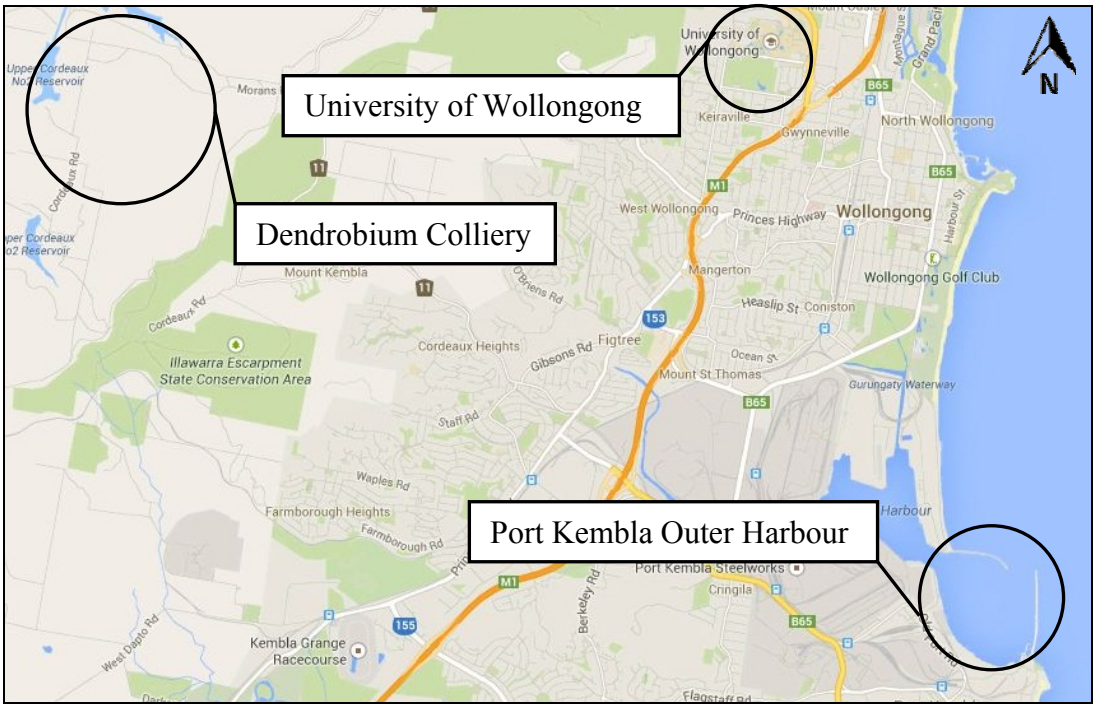

Figure 3.2 Location of the coal wash colliery in this study

Table 3.1 Chemical composition of Dendrobium CW in this study

Components	Proportion (%)*
Ash	65.6
Carbon	24.3
Volatiles	14.4
Hydrogen	1.90
Nitrogen	0.55
Sulphur	0.23
Phosphor	0.02

* Provided by the supplier BHP Illawarra Coal.

Table 3.2 Chemical composition of SFS in this study

Components	SiO_2	Al_2O_3	CaO	MgO	Fe_2O_3	MnO	TiO_2	Others
Proportion (%)*	12.5	2.8	38.3	9.9	30	3.7	1.2	1.6

* McCallum, 2005

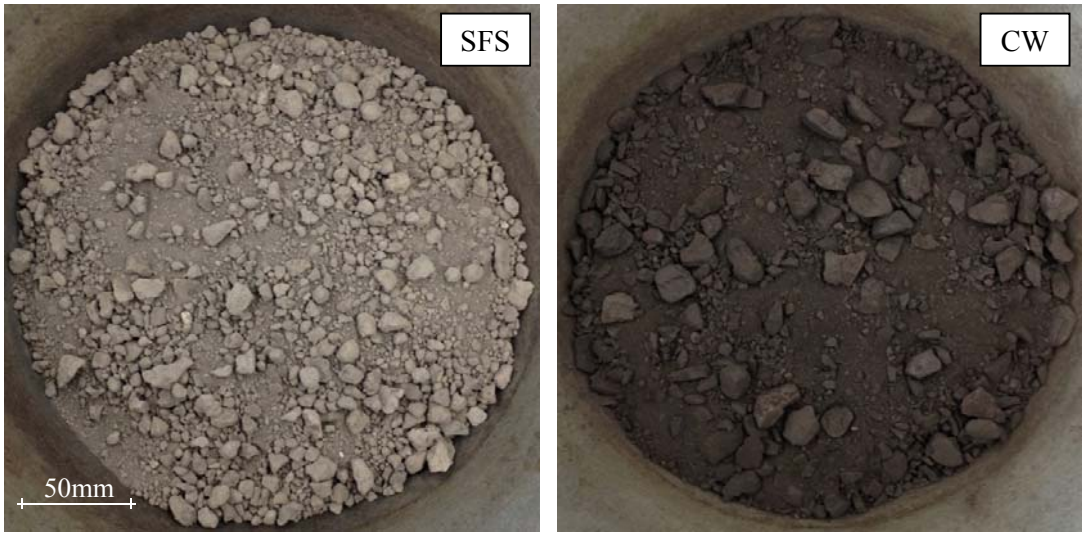

Figure 3.3 Typical appearance of steel furnace slag (SFS) and coal wash (CW)

The original particle size distributions (PSD) of individual CW and SFS materials as received in the laboratory are plotted in Figure 3.4. Due to some cohesion between the coarse and fine particles of CW, the wet sieving method was used (ASTM D1140, 2000). In terms of particle size distribution alone, CW and SFS can be classified as equivalent to materials conforming to GW-GM and SW, respectively, according to the Unified Soil Classification System (USCS). The liquid limit of CW fines was 27.7% and a plasticity index of 10.7%, whereas SFS fines were generally very low to non-plastic.

Since the shear behaviour of granular material is influenced by the initial PSD, all the mixtures were prepared with the same initial PSD (Figure 3.4) to exclude the effect of initial gradation on its behaviour, as was observed in other studies (Indraratna *et al.*, 1998, Ni *et al.*, 2000, Suiker *et al.*, 2005, Cho *et al.*, 2006, Cerato and Lutenegger, 2006). The PSD adopted for triaxial testing was adjusted to meet the PSD obtained upon compaction in a field trial at Port Kembla. It was observed that the larger particles (>16mm) of CW were easily degraded into smaller sizes during compaction. Much of the particle breakage appeared to be split across the main body of the particle rather than just abrading the angular edges and corners, and this was mainly the result of the compaction process.

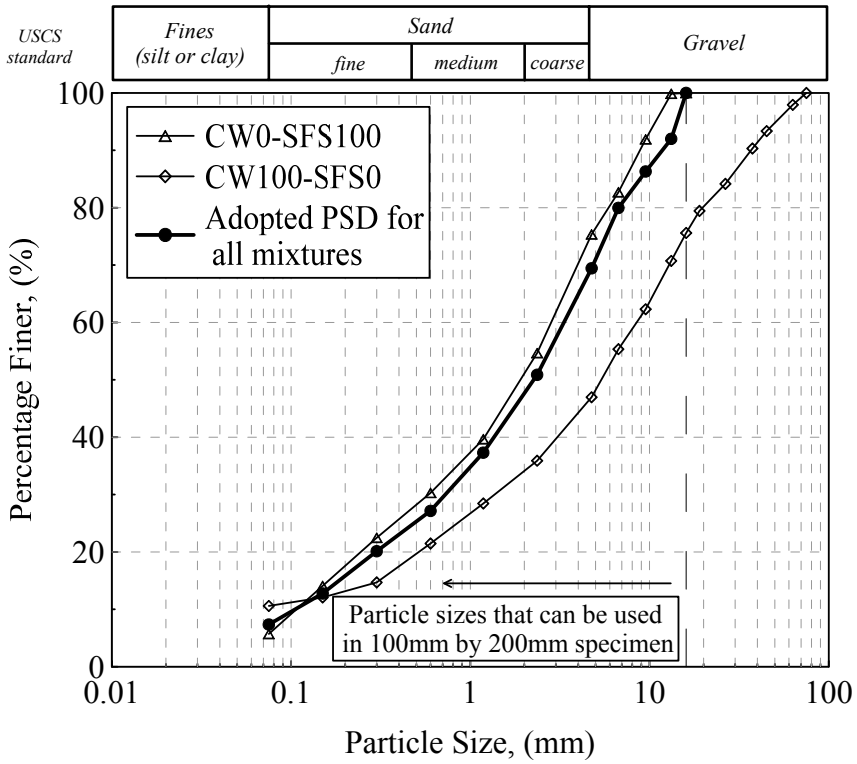

Figure 3.4 Particle size distribution curves for CW and SFS as received in the laboratory and adopted one for this study

3.3 LABORATORY TESTING PROGRAMME

The details of the apparatus and the testing conditions adopted to evaluate the stress-strain behaviour (i.e. triaxial testing) and volume instability (i.e. swell potential) of the CW-SFS mixtures are described in the following sub-sections.

3.3.1 Triaxial testing

This study involved isotropic compression and shear behaviour of CW-SFS mixtures and the evaluation of the role of CW percentage and confining pressure. For this purpose, a series of isotropic compression and consolidated drained triaxial tests was conducted under various confining pressures and CW content. All specimens were prepared to 90% Standard Proctor compaction. The triaxial testing program is summarized in Table 3.3. Five isotropic compression tests and 20 consolidated

drained triaxial tests were conducted on five different mixtures. The mixtures are expressed as CW-SFS, and the numbers after CW and SFS are the percentages of coal wash and steel furnace slag corresponding to the oven-dried weight in the mixtures, respectively. An effective confining pressure in the range of 30-220 kPa was applied to mimic typical port loading conditions (Lai *et al.*, 2011). The lower limit of confining pressure (i.e. 30kPa) was considered for the shallow areas in the port where only a small surcharge load is applied on the pavements, while the upper limit of confining pressure (i.e. 220kPa) would be larger than the maximum live load that is expected during the design life of the port owing to heavy infrastructure including container warehouses. To avoid any boundary effects related to the largest particle size, the drained triaxial tests were performed on specimens that were 100mm in diameter and 200mm in height as suggested in ASTM D7181 (2011).

For the triaxial tests, test procedure was in accordance with ASTM D7181. The triaxial apparatus used is illustrated in Figure 3.5 and this equipment consisted of the following parts:

- a frame that provided reaction forces
- a loading rig to apply vertical displacement from the bottom of the specimen
- a load cell for measuring vertical load on the specimen
- an outer chamber
- two pressure/volume controllers (accuracy of 0.1kPa and 1mm^3) for applying cell and back pressure as well as measuring volume change
- a LVDT (linear variable differential transformer, accuracy 0.001mm) displacement for strain measurements
- Pore water pressure transducers (accuracy 0.01kPa)
- Data acquisition

The system was connected to a computer which allowed the user to control the test and monitor the plots displayed using the GDSLab software.

Table 3.3 Triaxial testing program on CW-SFS mixtures in this study

Mixture	Initial conditions		Specimen properties	
	σ'_3 (kPa)	v_0	G_s	MDUW (kN/m^3)
CW0-SFS100	30	1.596	3.34	22.7
	60	1.597		
	120	1.587		
	220	1.577		
CW25-SFS75	30	1.568	3.01	20.83
	60	1.565		
	120	1.560		
	220	1.546		
CW50-SFS50	30	1.517	2.73	19.52
	60	1.515		
	120	1.504		
	220	1.495		
CW75-SFS25	30	1.499	2.51	18.21
	60	1.493		
	120	1.481		
	220	1.470		
CW100-SFS0	30	1.451	2.27	16.9
	60	1.451		
	120	1.439		
	220	1.424		

σ'_3=effective confining pressure at the end of consolidation; v_0= specific volume after consolidation; MDUW=maximum dry unit weight

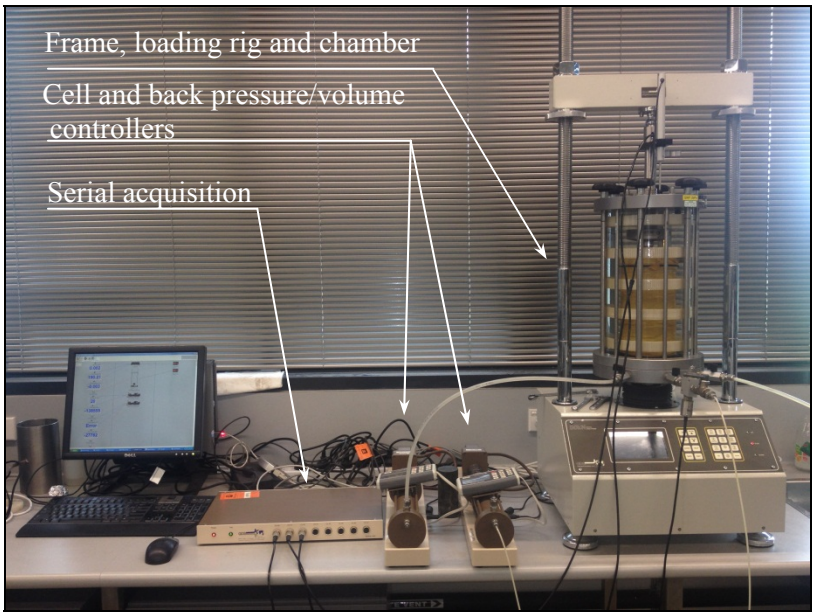

Figure 3.5 Isometric view of triaxial equipment used in this study (developed by GDS Instruments Ltd)

A GDS pressure/volume controller shown in Figure 3.6 was used for applying cell pressure, back pressure and measuring volume change of specimens. This controller could be controlled manually using the keypad or automatically using GDS software. To obtain accurate volume change, de-aired water was used. The maximum pressure rated is 3MPa and the chamber has a 200cc volume capacity. The accuracy of pressure and volume measurements is 1kPa and 1mm^3, respectively.

Figure 3.6 GDS Enterprise pressure/volume controller

In Figure 3.7, the 8-channel GDS serial acquisition digital box is shown. It can control and record data from different sources, i.e. for recording displacement, load cell, and pore water pressure transducer. Three options of data logging intervals are possible with this type of data logger and they are: linear, logarithmic, and exponential intervals. During saturation and consolidation stages, the logarithmic method was used, whereas during drained shearing, the linear method with 5 seconds intervals was adopted.

Figure 3.7 8-channel GDS serial acquisition

3.3.2 Swell test

As discussed earlier in Chapter 2, the existence of free lime (CaO) in the SFS can cause volume instability and swelling potential which may cause damage to infrastructures. The hydration of CaO is the primary reason that causes swelling. The rate of hydration depends significantly on the temperature of water. Therefore, to accelerate the swelling mechanism of CW-SFS mixtures, the specimens were placed within a temperature controlled water bath (73°C) as shown in Figure 3.8.

To study the swelling behaviour of CW-SFS mixtures, a series of tests were conducted in the laboratory. The first series was conducted to determine the swelling potential (i.e. no surcharge on specimen) and subsequently the swelling pressure of CW-SFS mixtures was evaluated. The effects of CW content and the initial density on the free swelling and the swelling pressure were investigated as summarized in Table 3.4. As shown, for free swelling, three different levels of relative compaction for each mixture (except CW100-SFS0); and for swelling pressure, one level of relative compaction were considered. Since there was no swelling potential observed for CW100-SFS0 mixture, only one test was conducted for comparison.

Figure 3.8 Test setup for one dimensional free swell test

The swelling tests were conducted on samples having 158mm in diameter and 112mm in height, in accordance with ASTM D4792. The PVC moulds were used instead of the conventional steel moulds as shown in Figure 3.9. This is because it

was observed that even nickel-coated moulds were corroded in hot water when submerged for extended periods of time as shown in Figure 3.10.

Table 3.4 Laboratory program for the swelling behaviour of CW-SFS mixtures

Mixture	Degree of compaction	
	Free swelling	Swelling pressure
CW0-SFS100	80	-
	90	90
	100	-
CW25-SFS75	80	-
	90	90
	100	-
CW50-SFS50	80	-
	90	90
	100	-
CW75-SFS25	80	-
	90	90
	100	-
CW100-SFS0	90	-

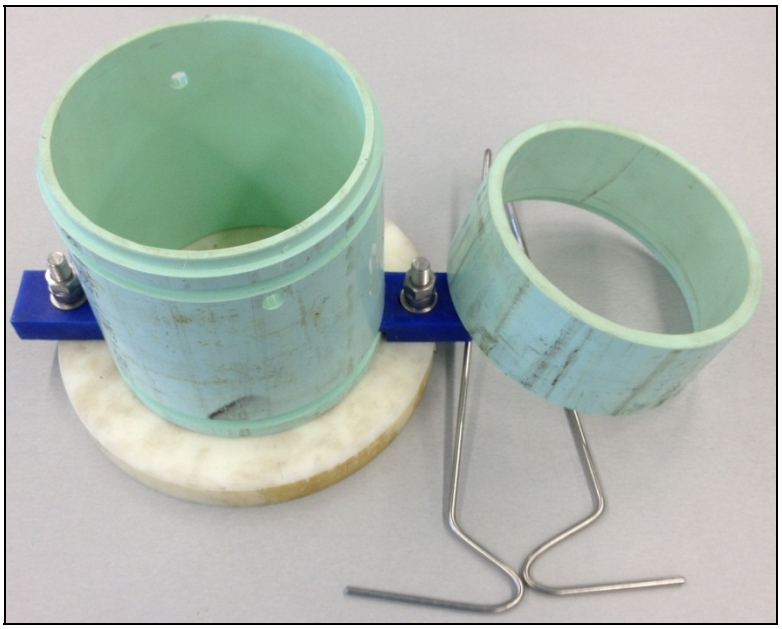

Figure 3.9 PVC mould for swell testing of CW-SFS mixtures

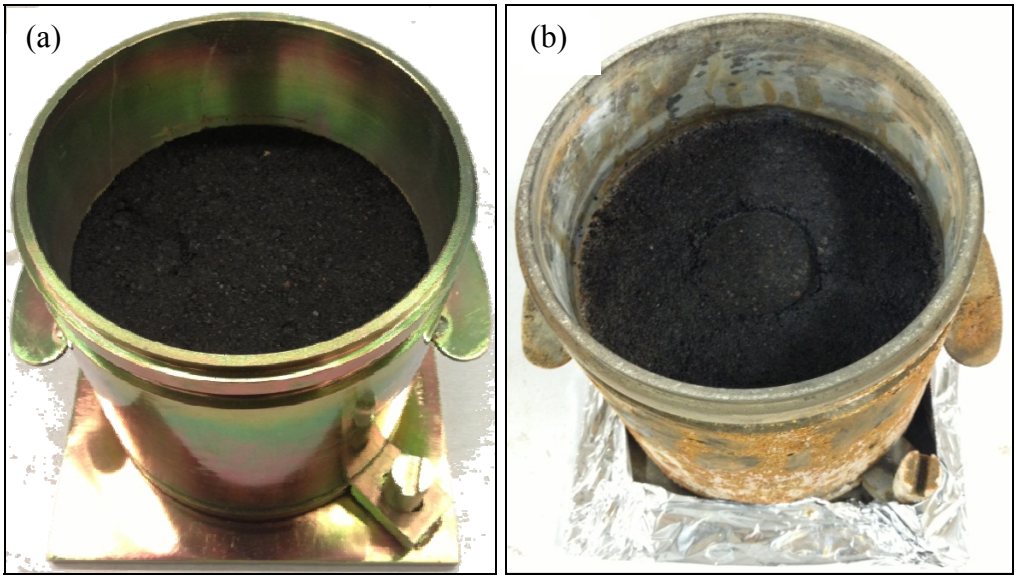

Figure 3.10 Corrosion of nickel-coated CBR mould due to exposure to the hot water for extended period of time (a) before, and (b) after

3.3.2.1 Free swelling behaviour

The swelling potential of the selected blends was evaluated through one-dimensional expansion tests using CBR moulds and a hot water bath at a temperature of 73^{o}C in accordance with ASTM D 4792-00 (Figure 3.8). In these tests it was found that the recommended 7 days curing period was insufficient for the mixtures to attain a nearly constant rate of swelling, and therefore larger testing periods of typically 30 to 60 days were considered. For the specimens having higher SFS content test, the duration often exceeded more than 100 days.

The apparatus used for the free swelling tests consisted of a stainless bath of 40 litres capacity (inside dimensions of 50×30×30cm^3), an internal element for increasing temperature, a submerged sensor for controlling temperature, a pump for circulating water, a digital panel for adjusting the temperature to the accuracy of 0.1°C, and a perplex lid for minimizing water evaporation. A dial gauge (accuracy of 0.1mm) was attached to a tripod and used to measure the vertical displacement with time.

The one-dimensional swell potential (i.e. free swelling, abbreviated as S_f hereafter) can be determined based on the difference in the vertical displacement monitored by a dial gauge with time as follows:

$$S_f = \frac{H - H_0}{H_0} \tag{3.1}$$

where H and H_0 represent the current and initial height of the specimen, respectively.

3.3.2.2 Swelling pressure

In the previous section, free swelling behaviour was examined through one-dimensional (vertical) expansion. Therefore, if the volume expansion is completely constrained in the vertical direction, the swell potential of the specimen can be readily converted into swelling pressure. This method is known as constant volume swell pressure (Nagaraj *et al.*, 2009, Sridharan *et al.*, 1986). As a result, a frame was

manufactured and the existing water bath was modified to accommodate two moulds simultaneously, as shown in Figure 3.11.

The additional components included in the experimental setup used for free swelling tests consisted of four threaded rods and beams for providing a fully constrained condition; two load cells which were attached to two separated top beams, and a data logger for recording load cell readings.

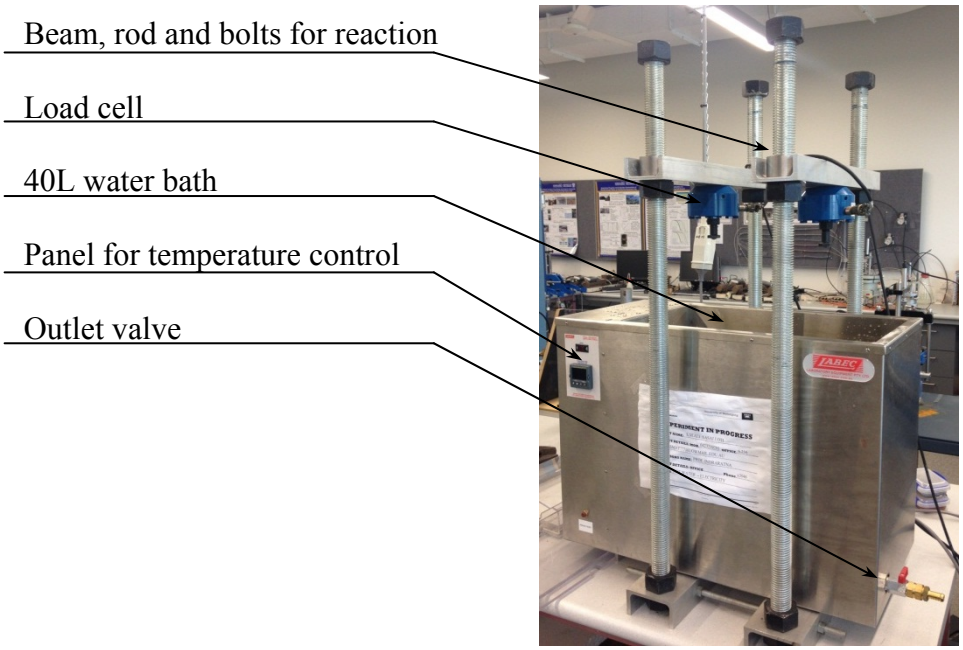

Figure 3.11 Testing equipment for swell pressure measurement

3.4 SPECIMEN PREPARATION

To attain the same initial gradation for all CW-SFS mixtures, the materials were initially sieved into different sizes (i.e., 13.2, 9.5, 6.7, 4.75, 2.36, and 1.18mm). For CW, since the fine particles (<1.18mm) were washed during the wet sieve method, coarser portions were crushed down to the fine sizes using a jaw crusher, a double roller crusher, and a disk pulveriser (Figure 3.12). For SFS, after oven-drying the material, it was sieved to the abovementioned sizes and stored in separated sealed plastic buckets (no wet sieve method was required).

For each CW-SFS mixture, the dry mass required of each particle size was back-calculated based on the PSD curve that was adopted for the mixtures (Figure 3.4), and then all the particle sizes were mixed thoroughly until a uniform appearance of the CW-SFS mixture was obtained.

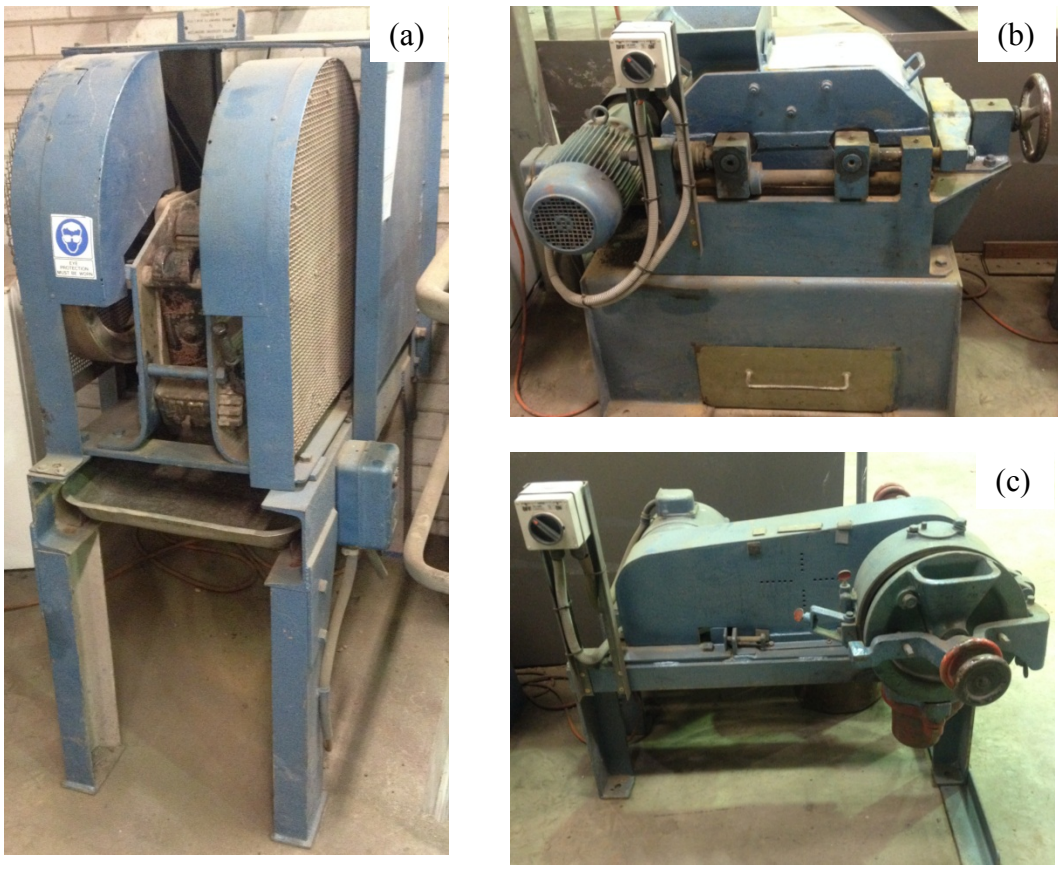

Figure 3.12 Crushing equipment for producing fine particles (a) jaw crusher, (b) double roller crusher, and (c) disk pulveriser

3.4.1 Triaxial test specimen

For triaxial testing, after the dried material had been mixed thoroughly, the required amount of water was added to the mixtures (i.e. 7%). This moisture content was adopted based on the water content obtained in the field trial. The triaxial specimens were prepared and compacted directly on the bottom triaxial pedestal using a split mould. To avoid friction between the mould and the specimen, a latex membrane (0.3mm thick) was placed inside the mould. After placing the membrane over the

pedestal, an O-ring was placed on the pedestal to provide an air-seal. The split mould was then mounted and tightened with four screws, and the top of the membrane was flipped over the mould as shown in Figure 3.13(a) and (b). A vacuum pressure of 15kPa was then applied between the membrane and the mould. Once the membrane was completely stretched and attached to the mould, a dried porous disk and a filter paper were placed inside the mould. Various stages of specimen preparation are shown in Figure 3.13.

The specimens were compacted using a drop hammer (500g weight subjected to a drop height of 320mm). For all tests, the specimens were prepared at an initial dry density equivalent to 90% relative compaction. Each specimen was compacted in seven layers (28.6mm/layer), with 30 drops of the hammer per layer (total applied energy is equal to 205 kJ/m^3). Before placing the subsequent layer, the previously compacted layer was roughened to avoid any layering during the shearing. Once the last layer was compacted, a filter paper and a porous disk were placed on the top.

After the compaction stage, the split mould was removed carefully. Since there was a strong possibility of puncturing the membrane during compaction, the membrane was cut and a new membrane was replaced over the compacted specimen as illustrated in Figure 3.13(f). Before placing the new membrane, the outer surfaces of bottom pedestal and top cap were lubricated with silicon grease to provide an airtight connection with the membrane. To ensure an isolated and sealed system (between specimen and water in the cell), two rubber O-rings and two latex bands were placed and tightened over the membrane on both ends of the specimen. A mild vacuum pressure (-10kPa) was applied inside the specimen to keep the specimen intact prior to rest of equipment setup. Furthermore, any leakage was checked by monitoring the pore water pressure transducer reading for 20 minutes. Afterwards, triaxial cell was mounted and placed on the base and the screws were tightened firmly.

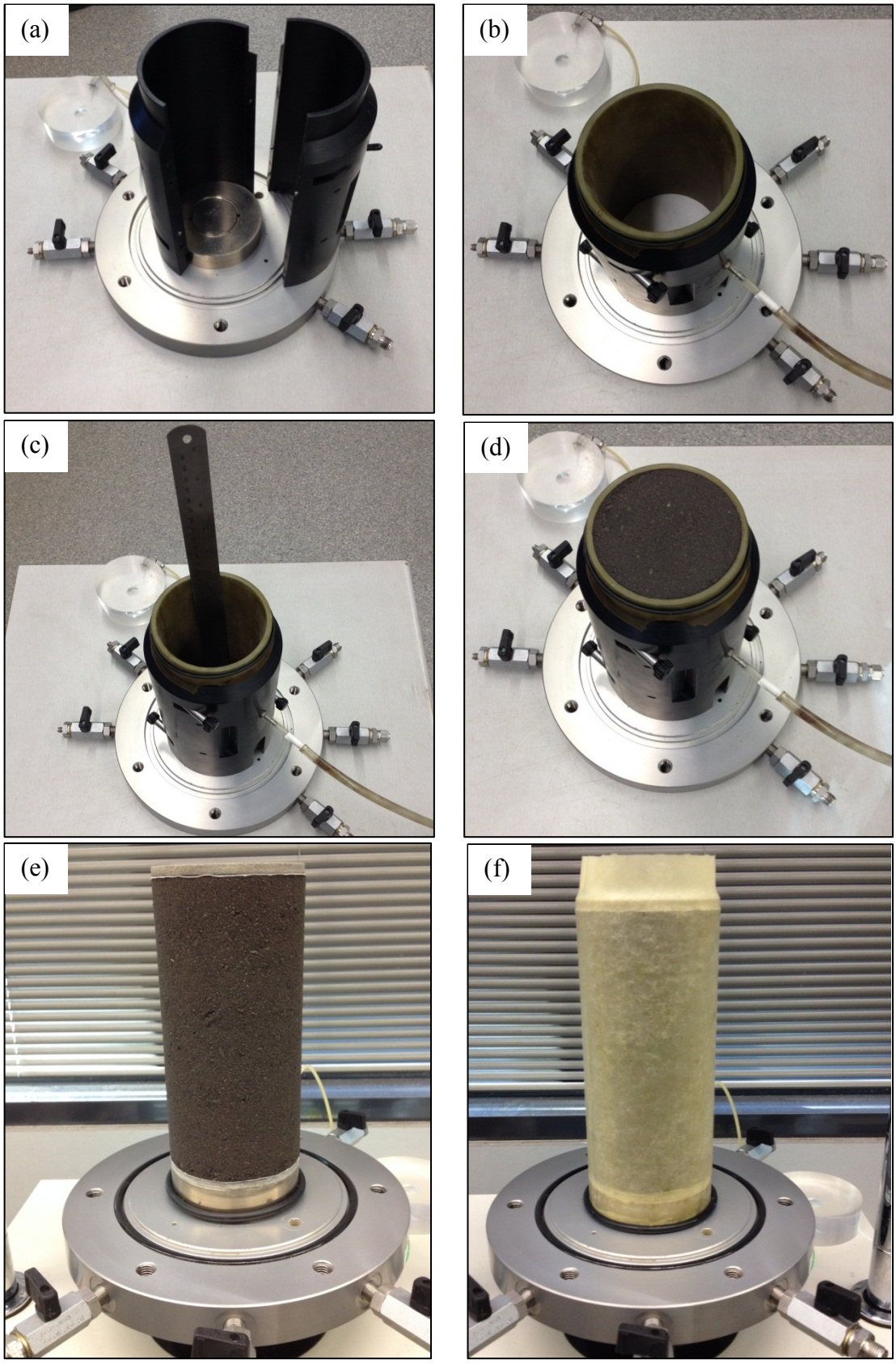
(a)
(b)
(c)
(d)
(e)
(f)

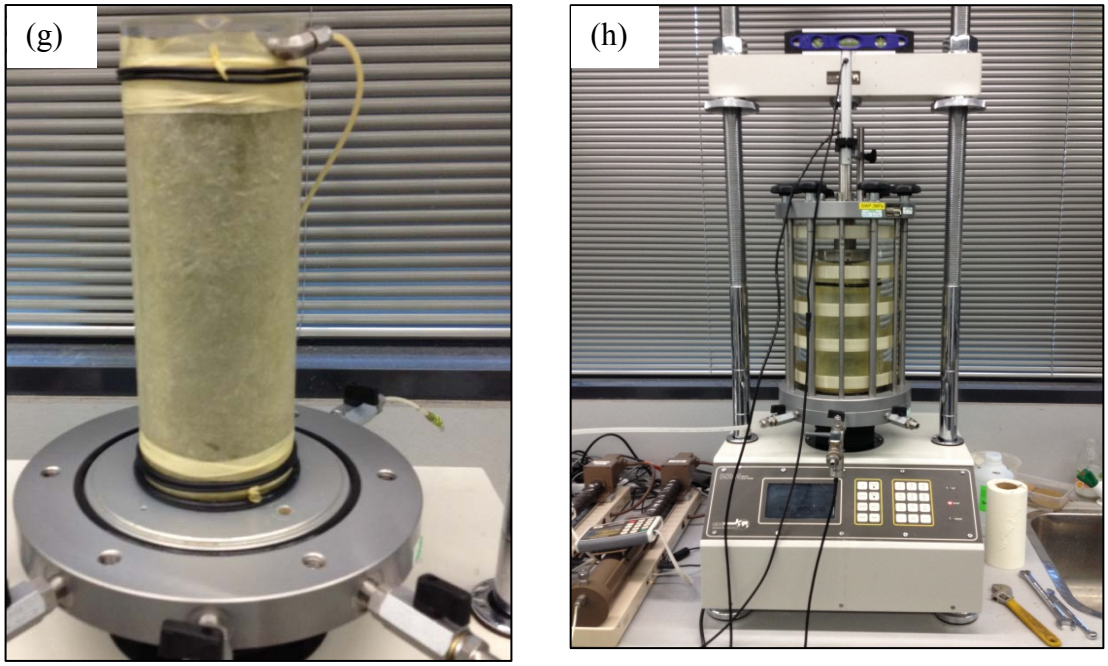

Figure 3.13 Stages for the specimen preparation for triaxial testing (a) triaxial pedestal and the split mould, (b) membrane placement inside the mould (c) height check for each compaction layer (d) photo of a finished specimen (e) view of the specimen after removing the membrane (f) placing a new membrane prior to testing (g) prepared specimen after placing top cap and o-rings (h) finished specimen inside the triaxial equipment and ready for testing

3.4.2 Swell test specimen

In Figure 3.14 the photographs of various stages of specimen preparation for swell testing are illustrated. After mixing the blended oven-dried CW and SFS with the same PSD as that of the triaxial specimens (see Figure 3.14a), the required amount of water was added depending on the target density. For specimens compacted to 80% and 90% relative compaction, 7% moisture was used. For 100% relative compaction, 9% moisture was mixed with the material. Then, the material was mixed thoroughly with water (Figure 3.14b).

To reduce the friction forces between the specimen and the mould, the internal surface of the mould was lubricated using petroleum jelly, and then the spacer disk (60mm thick) was placed inside the mould on the base as shown in Figure 3.14c. Then, the specimens were compacted in 5 layers using the same hammer as in triaxial tests. For each layer, the calculated wet mass of soil (based on the dry density) was placed inside the mould (Figure 3.14d) and then compacted to attain the required thickness (Figure 3.14e). The extension collar as shown in Figure 3.9 was used for the compaction of the last layer. Once the specimen was prepared (Figure 3.14f), a perforated base plate was placed on the specimen. The spacer disk was then removed and a filter paper placed on the top of the specimen (Figure 3.14g).

3.5 TRIAXIAL TEST PROCEDURES

After preparing the specimen, the cell was then assembled and filled with water at a rate such that there were no air bubbles entrapped inside the cell chamber. Afterwards, all the valves and pipes were de-aired and a cell pressure of 10kPa was applied to ensure the specimen would not deform during the first stage of saturation. After saturation, consolidation and shearing stages were carried out as explained in the following sections.

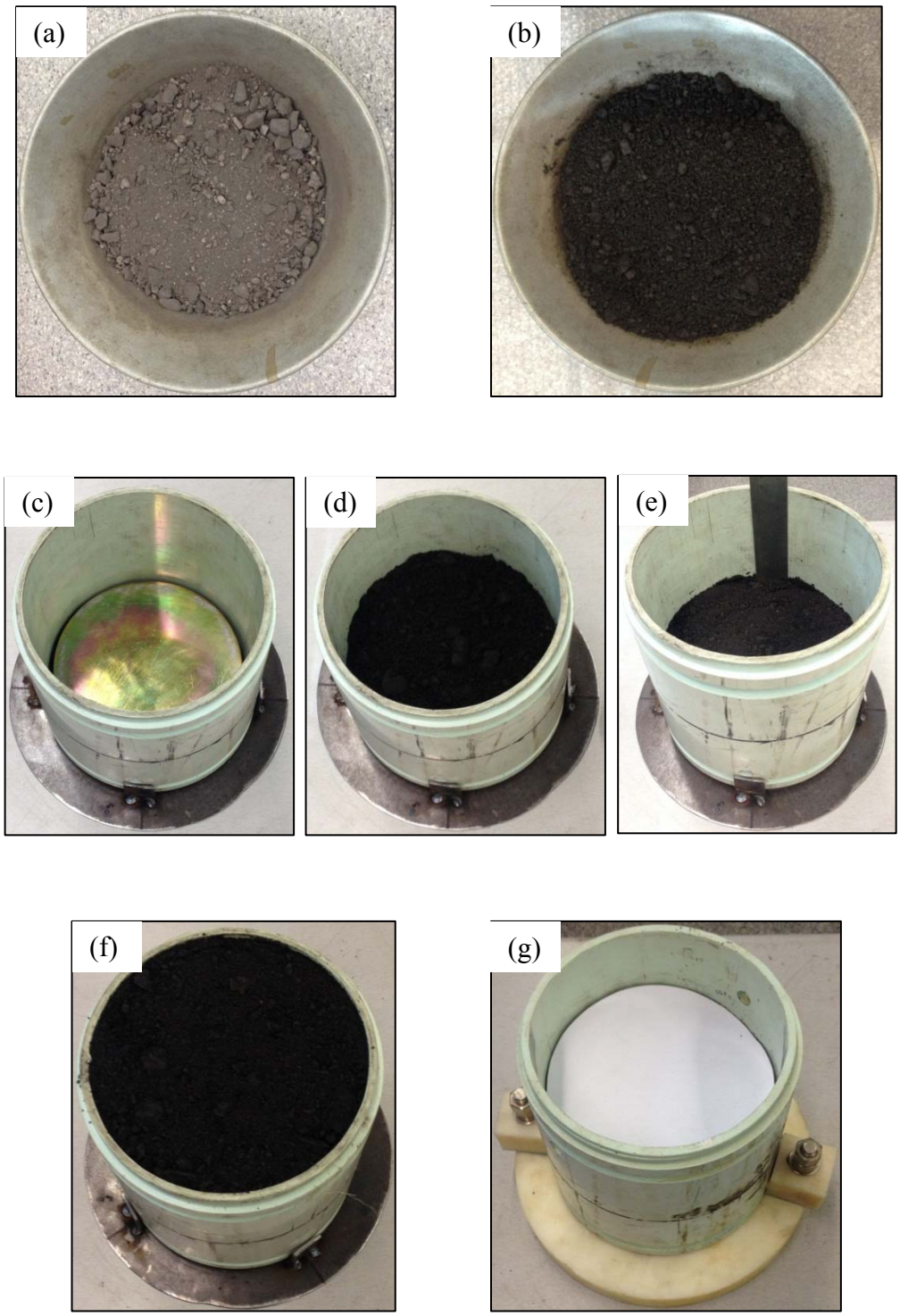

Figure 3.14 The sequential steps for the specimen preparation for swell testing

3.5.1 Saturation

One of the effective methods for specimen saturation specifically for granular material is replacing the air inside the specimen with carbon dioxide (CO_2; Selig *et al.*, 1979). However, SFS reacts with CO_2 as reported in literature (e.g. Johnson *et al.*, 2003, Huijgen and Comans, 2005, Nik Hisyamudin *et al.*, 2009). Therefore, this method was not used. The specimens were initially flooded with de-aired water from the base while the trapped air was expelled through the top cap drainage path. During this stage, a maximum back pressure of 8kPa was applied, while the applied cell pressure was 10kPa (i.e. the rate of water injected into the specimen was slow enough to prevent any fine particle migration).

Finally, the valve connecting to the top cap was closed and the test progressed to the subsequent stages. While maintaining an effective stress of 10kPa, a saturation ramp was applied until the back pressure reached 400kPa. The specimens were kept overnight under this pressure.

To examine the degree of saturation for the specimens, a B-value stage was carried out by incrementing the cell pressure by 20kPa. Typically a Skempton's B-value (Eq. (2.2), Skempton, 1954) higher than 0.97 was achieved. For those cases where B-value was smaller than 0.7, another saturation stage was applied. After this stage, the cell pressure was brought back to the original value before proceeding to the consolidation stage.

$$B_{Skempton} = \frac{\Delta u}{\Delta \sigma_3} \tag{3.2}$$

3.5.2 Isotropic consolidation

At this stage, the cell pressure was increased to the required mean effective pressure value, as reported in Table 3.3. The water inside the specimen was allowed to drain only from top of the specimen (i.e. one-way drainage). The end of the consolidation stage was detected by examining the rate of volume change of the specimen

measured by the back volume controller. Once this value was less than 1mm^3/min, it was assumed that the specimen was consolidated under the applied effective confining pressure.

The results of the consolidation stage were used to determine the cross-sectional area of the specimen after consolidation (by calculating volume change during consolidation), and the rate of displacement during the shearing stage was selected in accordance with ASTM D7181 (2011). For this, the t_{90} (the time for 90% consolidation) was calculated by the method proposed by Taylor (1948). An example of consolidation test results and the method for t_{90} calculation are shown in Figure 3.15. As described in ASTM standards, the maximum strain rate ($\dot{\varepsilon}$) can be calculated using Eq. (3.3).

$$\dot{\varepsilon} = \frac{4\%}{10t_{90}} \tag{3.3}$$

where t_{90} is the time for 90% consolidation.

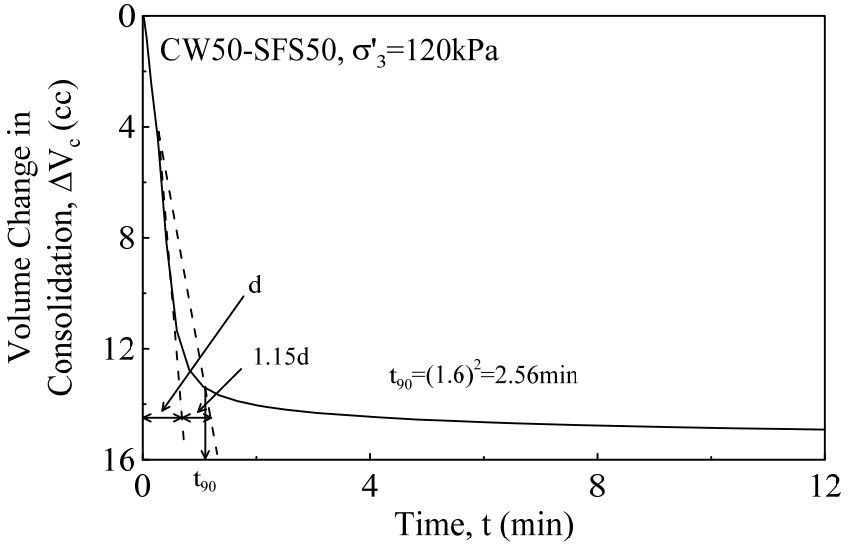

Figure 3.15 Consolidation graph of CW50-SFS50 under 120kPa confining pressure and the determination of t_{90}

3.5.3 Drained shearing

Once the consolidation stage was completed, the specimens were sheared at a constant rate of displacement of 0.2mm/min (6%/h). This rate of strain was calculated using Eq. (3.3) and selected in accordance with ASTM D7181 (2011). This rate of strain was slow enough to prevent generation of pore water pressure. During the shearing stage, the back and cell pressures were maintained constant, and the drainage valve connected to the back pressure/volume controller kept open to maintain a fully-drained condition. The shearing of the specimens was conducted in a strain control mode so that the post-peak behaviour could be captured. The test was carried out until no further changes in volume and deviatoric stress were measured (i.e. critical state). Typically axial strains of 20% or more were sufficient to achieve relative constant volume and deviatoric stress conditions.

Two methods were used to correct the cross-sectional area during shearing, depending on the volumetric shear behaviour of the specimen. The cross-sectional area of those specimens indicating contraction was corrected according to ASTM D7181 (2011) (i.e. Eq (3.8)). In the pre-peak range, this correction was also used for those specimens showing dilation. In contrast, in the post-peak range, a method proposed by La Rochelle *et al.*, (1988) was adopted instead.

In triaxial testing, all the calculations were based on the dimensions of specimen after consolidation. Therefore, it is important to determine the specimen height (H_c) and cross-sectional area (A_c) after consolidation. In this study, Eqs. (3.4) and (3.5), were employed as follows:

$$H_c = H_0 - \Delta H_0 \tag{3.4}$$

$$A_c = \frac{V_0 - \Delta V_{sat} - \Delta V_c}{H_c} \tag{3.5}$$

where, H_0 is initial height of specimen, ΔH_0 is change in height of specimen at the end of consolidation, V_0 is initial volume of specimen, ΔV_{sat} is change in volume of

specimen during saturation that could be calculated using Eq. (3.6), and ΔV_c is the change in volume of specimen during consolidation.

$$\Delta V_{sat} = 3V_0 \frac{\Delta H_s}{H_0} \tag{3.6}$$

where, ΔH_s is the change in height of specimen during saturation.

For the shearing stage, the axial strain (ε_1), cross-sectional area for a given applied axial load (A_L), deviator stress (q), volumetric strain (ε_v), lateral strain (ε_3), shear strain (ε_s), and mean effective stress (p') were calculated using Eqs. (3.7) to (3.13).

$$\varepsilon_1 = \frac{\Delta H}{H_c} \tag{3.7}$$

$$A_L = \frac{V_c - \Delta V_s}{H_c - \Delta H_s} \tag{3.8}$$

$$q = \sigma_1' - \sigma_3' = \frac{P}{A} \tag{3.9}$$

$$\varepsilon_v = \frac{\Delta V_s}{V_c} \tag{3.10}$$

$$\varepsilon_3 = \frac{\varepsilon_v - \varepsilon_1}{2} \tag{3.11}$$

$$\varepsilon_s = \frac{2(\varepsilon_1 - \varepsilon_3)}{3} \tag{3.12}$$

$$p' = \frac{\sigma_1' - 2\sigma_3'}{3} \tag{3.13}$$

where ΔH is the change in height of specimen during loading, H_c is the height of specimen after consolidation, V_c is the volume of specimen after consolidation, ΔV_ε is the change in volume of specimen from start of shearing to any strain, ΔH_ε is the change in height of specimen from start of shearing to any strain, σ_1' is the major effective stress, σ_3' is the effective confining pressure, P is the axial load on specimen, and p' is the effective mean stress.

3.5.4 Repeatability of test results

The repeatability of the triaxial test results was checked. Figure 3.16 shows an example of two drained triaxial results on two mixtures of CW100-SFS0. For these tests, specimens were prepared at the same density and water content as the first set of results. Although there were small variations between the two sets of results, overall there was a good agreement.

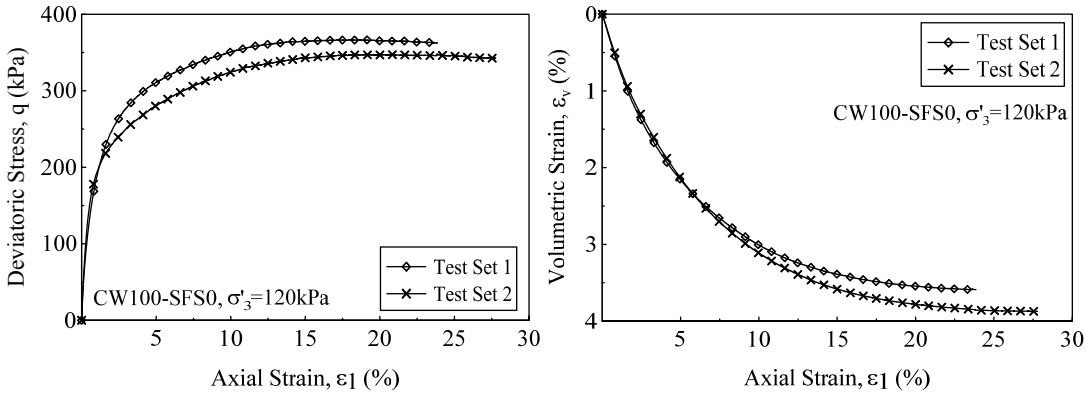

Figure 3.16 Repeatability of triaxial test result on CW100-SFS0 in drained shearing

3.6 SUMMARY

In this study, mixtures of coal wash and steel furnace slag were considered, in order to evaluate their suitability in terms of potential use as a structural fill. The laboratory programs describing the geotechnical properties of CW-SFS mixtures was discussed. The index properties of these two by-products, as well as the particle size distribution

considered for specimen preparation, were outlined. Due to the limitations of specimen size, only particles less than 16mm were used in the laboratory tests. In order to eliminate the effect of particle size distribution on the behaviour, specimens were prepared with the same initial PSD.

The laboratory procedures adopted for triaxial and swelling tests were described in detail. For triaxial testing, specimens of 100mm in diameter and 200mm in height were used, whereas for the swelling tests, a standard CBR size (i.e. 158mm in diameter and 112mm in height) was considered. The procedure adopted for specimen preparation, compaction, and triaxial testing were also described.

CHAPTER FOUR

4 PRELIMINARY GEOTECHNICAL PROPERTIES OF CW-SFS MIXTURES

4.1 INTRODUCTION

The first step to investigate the suitability of CW-SFS mixture as structural fill is to evaluate the basic geotechnical parameters for different mixtures. Therefore, a preliminary laboratory testing program was set out to explore these preliminary parameters which are mainly useful for practicing engineers. Furthermore, by comparing these parameters with conventional materials, one can determine which mixture is more applicable for the required condition.

In this chapter, the preliminary geotechnical properties of CW-SFS mixtures are presented and discussed. These properties include compaction characteristics (including maximum dry unit weight, optimum moisture content, and particle degradation), specific gravity, permeability, California Bearing Ratio (CBR) both for unsoaked and soaked conditions, one-dimensional compression test, and Unconfined Compression Strength (UCS). For some of these tests such as UCS, the behaviour of CW-SFS mixtures was investigated under different moisture contents. Furthermore, the swelling behaviour of the CW-SFS mixtures both in free swelling and constant volume conditions (i.e. swelling pressure) is described. The effect of CW content as well as density on the swelling response of the blends was also investigated.

4.2 COMPACTION CHARACTERISTICS

4.2.1 Specific gravity

Specific gravity (G_s) was determined according to AS 1289.3.5.1-2006. Due to the low value G_s for CW, kerosene ($G_{s,kerosene}$ = 0.82) was used in order to prevent any particle floatation on the wetting agent which was observed if distilled water being used. A vacuum pressure was applied to remove any entrapped air inside the particles. To consider any variation of chemical composition in different particle sizes on G_s, each CW-SFS mixture was initially prepared by mixing the exact proportion of each particle size to produce a mixture with the gradation as shown in previous chapter (see Figure 3.3). Afterwards, all the particles were crushed down to a size of smaller than 0.6mm and then the test was carried out to determine G_s of each mixture.

The average G_s for tested CW and SFS was 2.27 and 3.34, respectively. The relatively low G_s value for CW is due to the presence of coal residuals, carbon and ash (e.g. the specific gravity for coal is around 1.3). Due to the presence of metal compounds (e.g. Fe_2O_3, SiO_2) and free lime (CaO) in SFS, by mixing SFS with CW the average G_s values increased linearly. The variation of G_s with CW content (or SFS content) is shown in Figure 4.1 and it shows that SFS is heavier than conventional silty sand fills (with G_s around 2.5 to 2.7) whereas, CW is lighter.

4.2.2 Compaction curve

The variations in dry unit weight with moisture content for CW-SFS mixture were evaluated by imparting an energy level of 595 kJ/m^3 (i.e. standard Proctor compaction) as indicated in AS 1289.5.1.1-2003. Thus, for each specimen, three layers of equal volume were compacted by imparting 25 blows/layer using a 2.5kg hammer dropping a distance of 305mm. The tests were carried out over a broad range of moisture contents (i.e. 4-16%). Figure 4.2 shows the variation of dry unit weight against the moisture content for different mixtures as reported in Table 4.1.

For each mixture, as the moisture content increases, the dry unit weight increases up to the maximum value, where the moisture content corresponding to the maximum dry unit weight (MDUW or $\gamma_{d,\max}$) is known as optimum moisture content (OMC). Beyond this point, any further increase of moisture content results in the reduction of the dry unit weight. On the dry side of OMC, since the friction force between the particles is quite large and the amount of water is not sufficient to reduce the inter-particle friction, the dry unit weight is low. By increasing the moisture content, the water helps the particles to slip and rotate over each other (i.e. acting as a lubricant). Therefore, under the compaction energy particles can reach to a denser configuration resulting in the higher dry unit weight until reaching the $\gamma_{d,\max}$. After this point, additional moisture content replace soil particles and the dry unit weight starts to decrease (Holtz *et al.*, 2011).

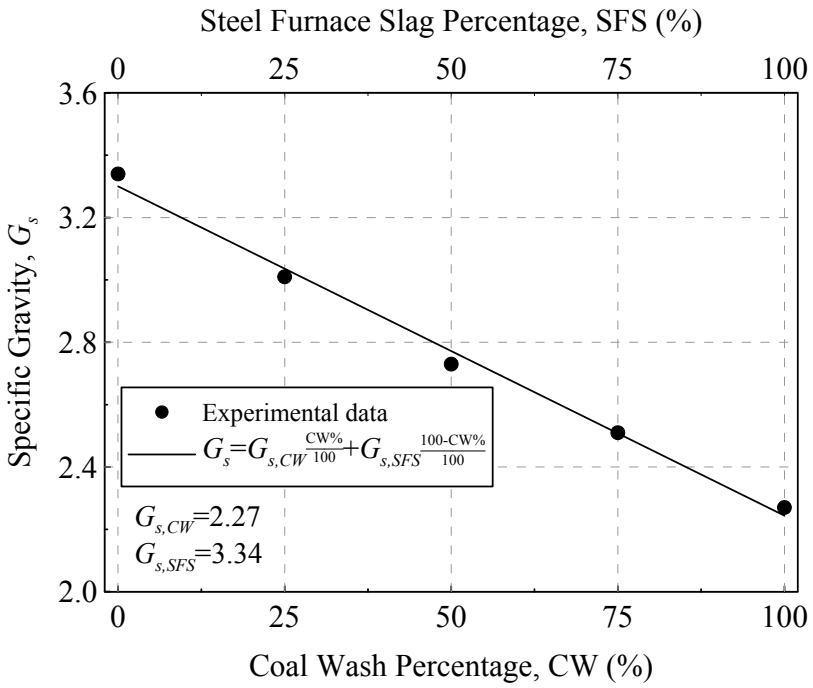

Figure 4.1 Specific gravity for CW-SFS mixtures

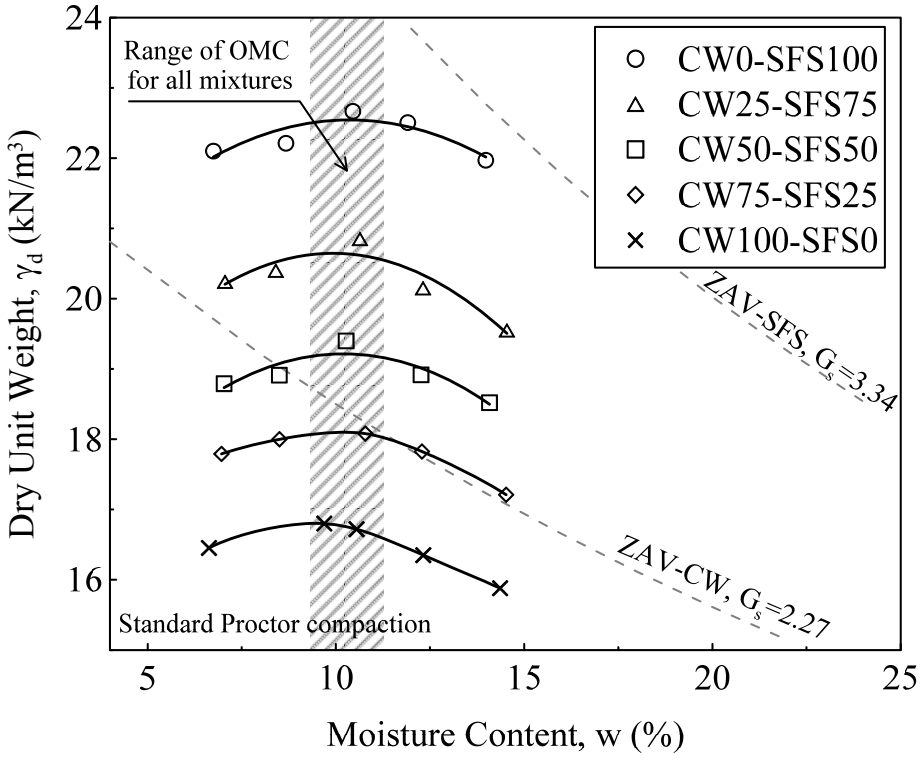

Figure 4.2 Typical compaction test results for CW-SFS mixtures

Test results show that as the SFS content increases from 0 to 100%, $\gamma_{d,\max}$ increases from about 16.9 kN/m^3 to about 22.7 kN/m^3, while the OMC slightly decreases from 10.5% to 9.7%. It is noted that $\gamma_{d,\max}$ of CW50-SFS50, having G_s=2.73, is comparable with those of most compacted natural fills, having G_s=2.65-2.7. In practical point of view, a lower dry density is advantageous when these wastes would be used as backfill behind retaining walls, since the pressure exerted on the retaining structure, as well as on the foundation structure, can be less. The marked increase in $\gamma_{d,\max}$ is essentially governed by a significant increase in G_s of the mixtures from 2.27 to 3.34 (see Table 4.1) caused by the high iron content of the SFS particles.

Table 4.1 Summary of compaction results on CW-SFS mixtures

Mixture	G_s	Water content, w (%)	Dry unit weight (kN/m^3)	Void ratio, e	BI (%)	$\gamma_{d,\max}$ (kN/m^3)	OMC (%)
		6.75	22.10	0.48	2.15		
		8.67	22.21	0.47	0.43		
CW0-SFS100	3.34	10.45	22.67	0.45	0.53	22.7	10.50
		11.91	22.51	0.46	1.74		
		13.98	21.97	0.49	2.87		
		7.06	20.24	0.46	4.22		
		8.40	20.40	0.45	2.15		
CW25-SFS75	3.01	10.64	20.85	0.42	1.15	20.83	10.54
		12.31	20.15	0.46	3.07		
		14.54	19.55	0.51	4.86		
		7.03	18.79	0.42	8.07		
		8.50	18.91	0.42	5.75		
CW50-SFS50	2.73	10.27	19.40	0.38	4.48	19.52	10.27
		12.26	18.92	0.42	6.80		
		14.08	18.52	0.45	8.95		
		6.96	17.79	0.38	11.29		
		8.50	18.00	0.37	7.96		
CW75-SFS25	2.51	10.78	18.08	0.36	10.13	18.21	10.70
		12.28	17.83	0.38	12.46		
		14.52	17.21	0.43	14.68		
		6.63	16.45	0.35	13.60		
		9.69	16.80	0.33	9.86		
CW100-SFS0	2.27	10.55	16.72	0.33	12.82	16.9	9.70
		12.32	16.35	0.36	14.95		
		14.36	15.88	0.40	17.25		

Although the maximum dry unit weight of the mixtures increased once the SFS content increased in the mixture, it is better to consider the effect of G_s on the density. The efficiency of compaction maybe better referred to the void ratio of each specimen as suggested in previous studies (e.g. Indraratna *et al.*, 1994b; Rujikiatkamjorn *et al.*, 2013). Therefore, the conventional presentation of compaction results ($\gamma_d - w$) can be misleading, and several zero air voids (ZAV) lines need to be plotted. In Figure 4.2, only those of pure CW and SFS materials are plotted for comparison. In Figure 4.3 the experimental data are plotted in terms of void ratio-moisture content relationships, and it can be seen that void ratio at $\gamma_{d,\max}$ increases with an increase in SFS content.

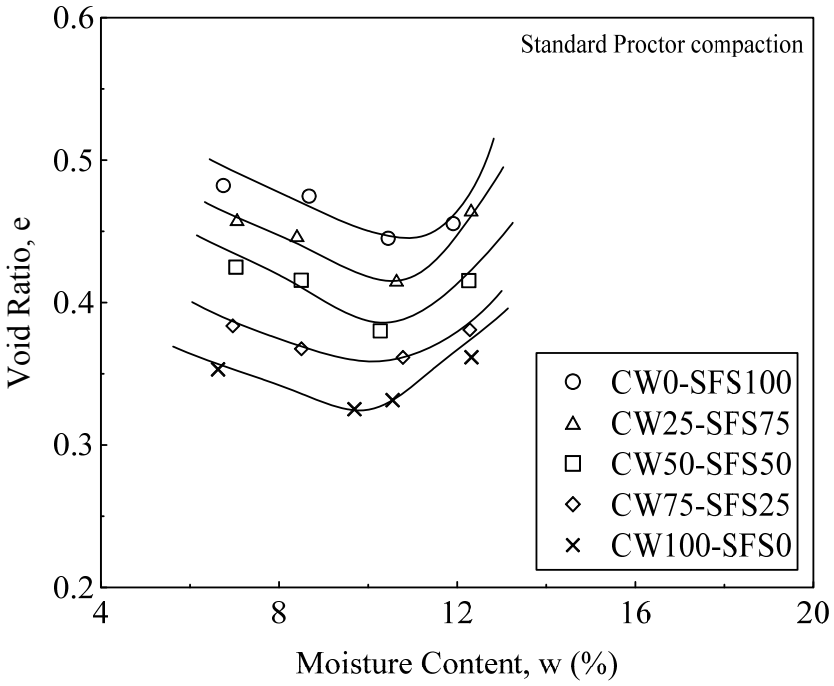

Figure 4.3 Void ratio-moisture content relationships for CW-SFS mixtures

An alternative way for presenting compaction results may be plotted in terms of void ratio (e) and water ratio (e_w) (Heitor, 2013). This alternative representation has significant advantages in relation to the conventional γ_d - w representation. Since G_s is incorporated in the determination of both e and e_w in Eqns. (4.1) and (4.2), the compaction characteristics of different blends can be adequately compared.

$$e = \frac{\gamma_w G_s}{\gamma_d} - 1 \tag{4.1}$$

$$e_w = wG_s \tag{4.2}$$

For instance, in the $\gamma_d - w$ plot, the mixture having the higher maximum dry unit weight is the CW0-SFS100 (Figure 4.2), however, in the e - e_w plot (Figure 4.4), it corresponds to one of highest void ratios. This indicates that the compaction process (i.e. equivalent energy level for given water content) was not as efficient compared with the ratios of other mixture. Thus, the associated porosity (n) is much larger. It is noteworthy that the CW100-SFS0, which has the lowest dry unit weight but shows the higher levels of densification, most likely due to the incidence particle breakage during compaction. The discrepancy between the γ_d - w and e - e_w is not surprising, as the values of the specific gravity of the two materials are quite different (i.e. SFS has G_s of 3.34 whereas CW has G_s of 2.27). Thus, a higher dry unit weight does not necessarily correspond to higher densification levels. Furthermore, the family of lines representing zero air void (ZAV) or fully saturated conditions in the $\gamma_d - w$ plane (Figure 4.2) is now a unique line in the e - e_w plane, which facilitates the interpretation of the compaction data of these blends.

Figure 4.4 shows that the void ratio at $\gamma_{d,\max}$ increases with an increase in SFS content. In the case of CW, the void ratio at $\gamma_{d,\max}$ is 0.33 (corresponding porosity of 25%), while for SFS the void ratio at $\gamma_{d,\max}$ is 0.45 (corresponding porosity of 31%). These results clearly show that using the same amount of energy (i.e. 600 kJ/m^3), CW can be compacted to a lower void ratio in comparison to SFS. The relatively low value of void ratio at $\gamma_{d,\max}$ for CW can be attributed to its relatively small specific gravity (G_s=2.27) compared to a conventional fill. In fact, for a clayey or sandy soil having a G_s=2.65, a $\gamma_{d,\max}$ of 17.2kN/m^3 would correspond to a void ratio of 0.51 (porosity of 34%). In the same way, compared to conventional fills, the relatively high void ratio at $\gamma_{d,\max}$ for SFS can be attributed to its higher specific gravity

(G_s=3.34). For a natural soil (G_s=2.65-2.70), $\gamma_{d,\max}$ of 22.9kN/m^3 would correspond to a void ratio of 0.14 (porosity of 12%).

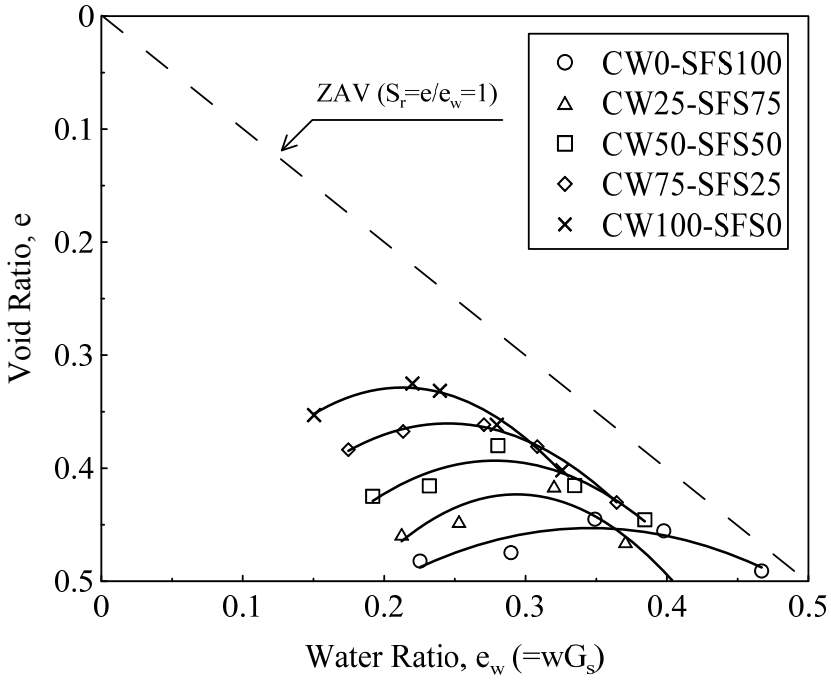

Figure 4.4 Representation of compaction results in e-e_w plane

As it was discussed in Chapter 2, since both CW and SFS are industrial wastes, their properties are not uniform, because the mineral components are likely to vary significantly. This variation is more dominant in CW and it depends on many parameters such as the source colliery, seam, and surrounding geology as well as the mining process and washing technique, as confirmed in this study. In fact, a series of compaction tests conducted on samples from different batches revealed that $\gamma_{d,\max}$ of CW and SFS might vary from 15.0kN/m^3 to 17.2kN/m^3 and 22.3kN/m^3 to 22.9kN/m^3, respectively. In Figure 4.5, the variation of $\gamma_{d,\max}$ for CW-SFS mixtures from different batches is shown. To eliminate the effect of dry unit weight for different batches, all of the tests in this study were carried out on a particular batch of CW and SFS with the compaction characteristics shown in Figure 4.2 and Table 4.1.

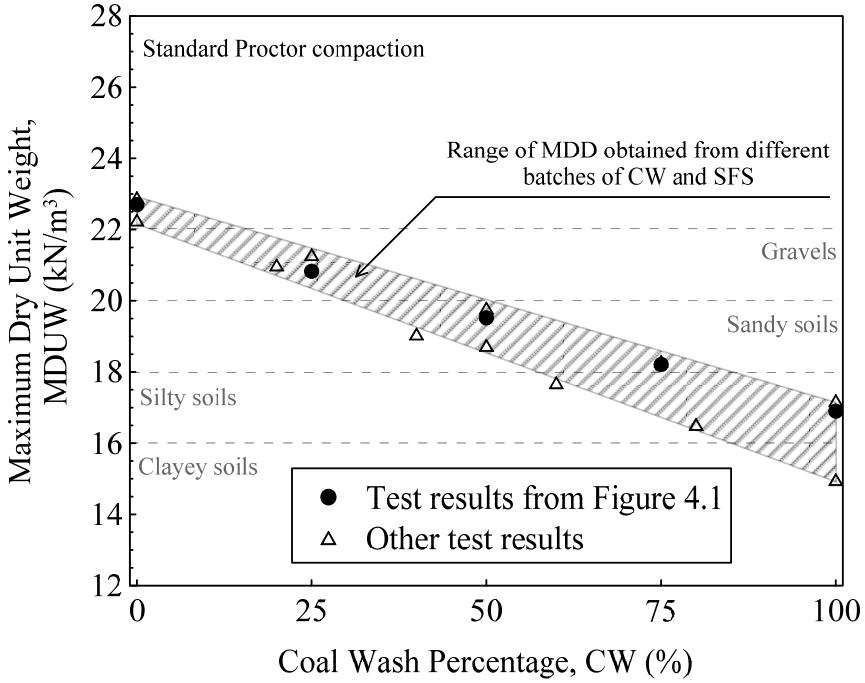

Figure 4.5 Variation of $\gamma_{d,\max}$ with CW content from different batches

4.2.3 Breakage in compaction

As discussed before, the rearrangement of particles during compaction is partly the results of particle movement and sliding relative to each other and is partly the degradation (i.e. breakage and crushing) of individual particles under the load applied by the compaction hammer. As a result of particle degradation, the PSD curve after compaction was shifted to the left (i.e. percentage of a particular size was increased). A typical degradation of CW-SFS mixture is shown in Figure 4.6. As can be seen, the maximum particle size still appeared after compaction and most particle breakage happened in particle sizes between 0.6mm to 9.5mm.

To determine the degradation of CW-SFS mixtures, a wet sieve analysis was conducted on the specimens after compaction. By quantifying the change in PSD before and after compaction, the breakage index (*BI*) could be determined. In this investigation, the particle degradation of CW-SFS mixtures was evaluated by adopting the method originally proposed by Indraratna *et al.* (2005) for railway ballast and then modifying it to suit these waste materials. This modification includes

adjusting the arbitrary boundary of maximum breakage which depends on the particle size distribution of the materials. The Breakage Index (*BI*) can be defined as:

$$BI = \frac{A}{A+B} \tag{4.3}$$

where *A* and *B* represent the area between an arbitrary line (the maximum breakage possible) and the PSD before and after shearing respectively. In Figure 4.7 the definition of "*A*" and "*B*" are presented.

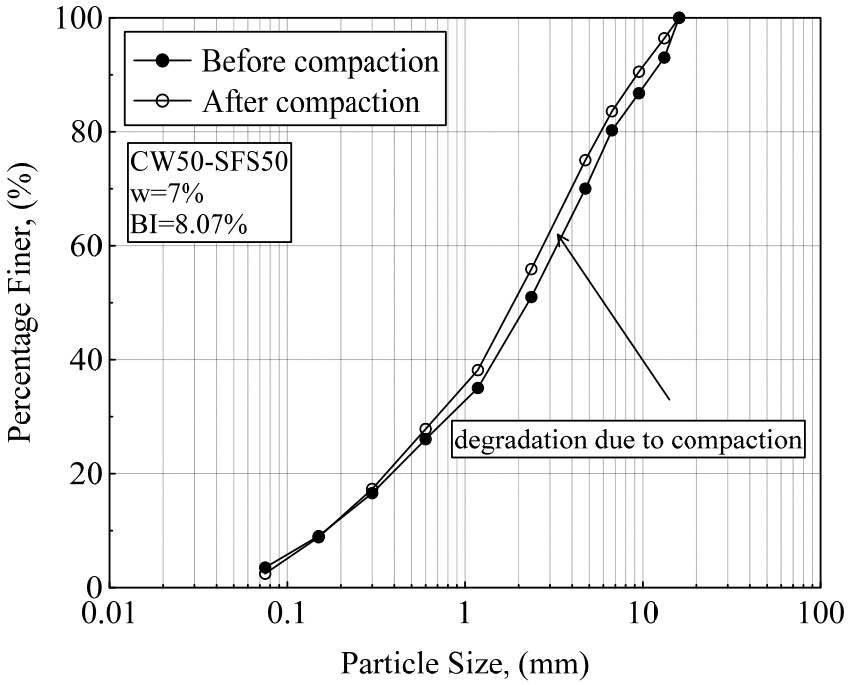

Figure 4.6 Typical particle breakage for CW-SFS mixture during compaction

The change in breakage index for CW-SFS mixture against moisture content is shown in Figure 4.2. Since SFS particles are stronger than CW, the breakage index at given moisture content increases as percentage of CW in mixture increases. For any CW-SFS mixtures, as the moisture content increases, the breakage index shows two trends relative to the OMC. On the dry side of OMC, increase in moisture content results in *BI* reduction. This tendency can be justified similarly to the compaction curve where the appearance of moisture reduces the frictional forces between the particles (Hausmann, 1990). Therefore, on such a dry specimen, the *BI* may be very high. Under this condition, the normal stress caused by the compaction forces at the

contact point of particles is quite large, therefore it exceeds the strength of the particles and results in breakage. Much of the particle breakage appeared to be split across the main body of the particle rather than just abrading the angular edges and corners. Although the particle degradation on the dry side is large, due to the influence of the suction, particles are inhibited from sliding. Therefore, the effectiveness of compaction on the density is compromised (Rujikiatkamjorn *et al.*, 2013).

By increasing the moisture content, the water reduces the suction between the particles and also the friction forces are much smaller, thus less particle breakage occurs and the majority of compaction energy is used by rearrangement and reorientation of particles, which results in the maximum dry density. Beyond the OMC (wet of OMC), increase in *BI* in a reducing rate was observed. The generation of pore water pressure between the particles, as well as inside the pores of individual particles, causes additional particle degradation. However, the rate of *BI* increase gradually diminished due to additional water content, and it expected to reach a steady value at higher levels of moisture.

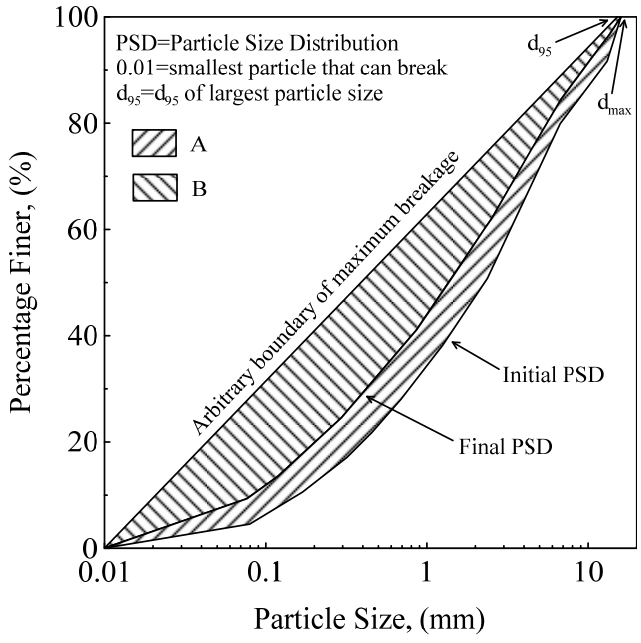

Figure 4.7 Definition of CW-SFS mixtures breakage index modified after Indraratna *et al.*, 2005

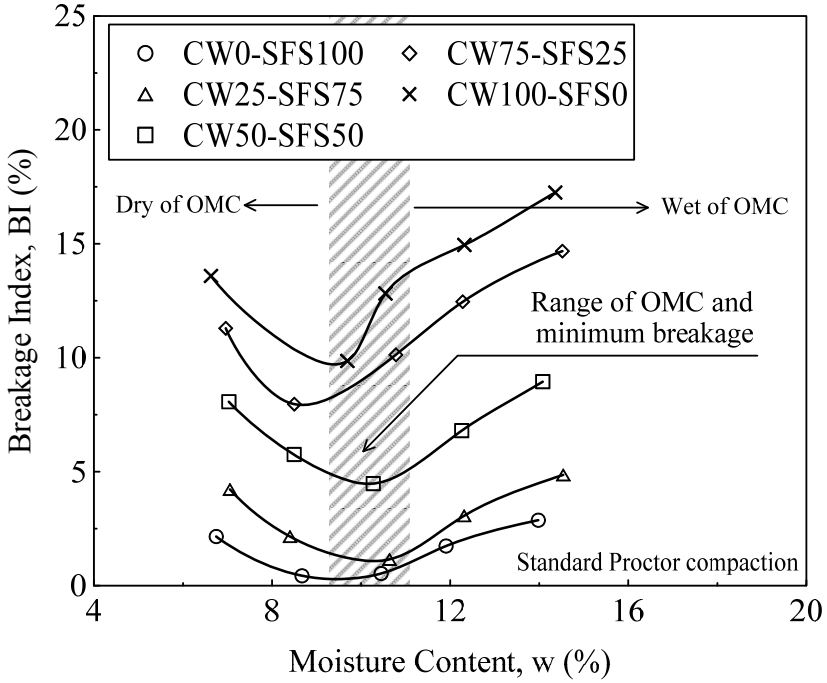

Figure 4.8 Variation of breakage index against moisture content for CW-SFS mixtures under Standard Proctor compaction

4.3 PERMEABILITY

One of the key parameters by which to evaluate the suitability of the blended waste material as a structural fill is permeability. The permeability should be within an acceptable range by considering two main criteria as follows: (i) permeability should be low enough for controlling erosion (migration of fine particle within a soil), and (ii) it should be high enough to prevent generation of excess pore water pressure during service time. The permeability coefficients for SFS and 75/25, 50/50, 25/75 CW-SFS blends were evaluated at approximately 20^{o}C room temperature by both falling-head (ASTM D5084) and constant-head (ASTM D2434) permeability tests. Falling-head permeability tests were conducted on CW specimens due to their relatively low permeability. Since the main objective of this study was to determine the permeability of the CW-SFS compacted at OMC, specimens were compacted using standard effort at their OMC (i.e. OMC reported in Table 4.1); then they were saturated prior testing.

The results of the permeability are presented in Table 4.2 and the variation for specimens compacted at their OMC is plotted in Figure 4.9. It is noted that both falling-head and constant-head tests provided similar results, confirming that the specimens were effectively fully saturated. Apparently, by increasing the SFS percentage from 0% to 100%, the permeability coefficient (k) decreases considerably from 5.1×10^{-5} cm/s (similar to sandy fills) to 5.0×10^{-7} cm/s (similar to clayey fills). Thus, it is evident that the decrease in k is a direct consequence of the decrease in void ratio with an increase in CW percentage. Furthermore, for the mixtures with more than 50% CW content, the reduction in permeability was observed to be significant.

In the case of port reclamation, a moderate permeability (1×10^{-6} cm/sec $\leq k \leq 1\times10^{-4}$ cm/sec) would be preferable in order to ensure rapid excess pore pressure dissipation and to minimise internal erosion. Otherwise, a lower permeability fill ($k < 1\times10^{-6}$ - 10^{-7} cm/sec) could be preferable to create water-front sealing zones.

Table 4.2 Permeability characteristics of CW-SFS mixtures

Material	$\gamma_{d,\max}$ (kN/m^3)	Void ratio at $\gamma_{d,\max}$	OMC (%)	k (cm/s) FH	k (cm/s) CH
CW0-SFS100	22.7	0.443	10.50	5.1×10^{-5}	4.5×10^{-5}
CW25-SFS75	20.83	0.417	10.54	3.6×10^{-5}	3.9×10^{-5}
CW50-SFS50	19.52	0.371	10.27	2.1×10^{-5}	2.0×10^{-5}
CW75-SFS25	18.21	0.351	10.70	6.2×10^{-6}	5.4×10^{-6}
CW100-SFS0	16.9	0.317	9.70	5.0×10^{-7}	N/A

$\gamma_{d,\max}$ and OMC = maximum dry unit weight and optimum moisture content from standard Proctor compaction tests; G_s = specific gravity of mixtures; and k = coefficient of permeability. FH = falling head permeability test; CH = constant head permeability test; and N/A= data not available

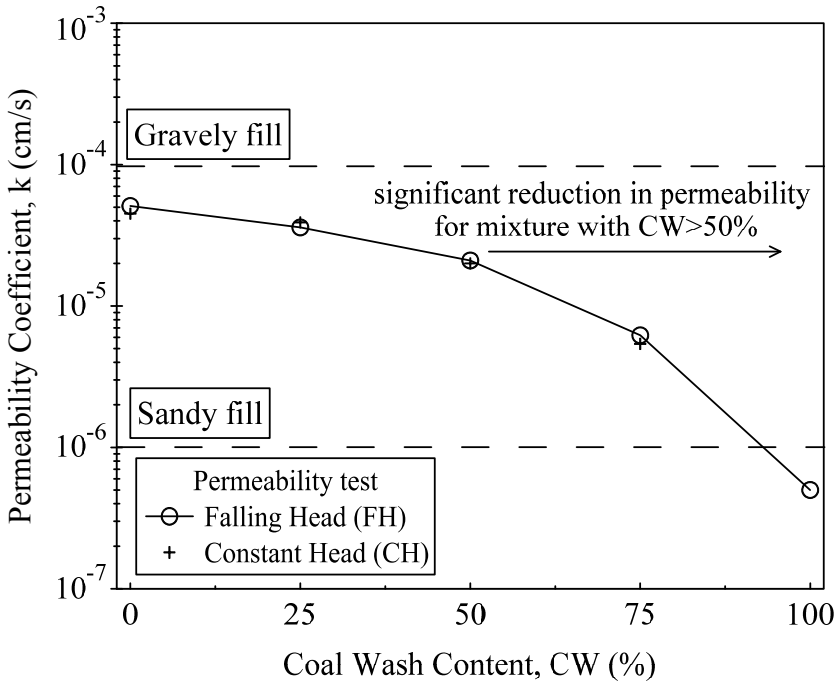

Figure 4.9 Permeability coefficients for CW-SFS blends (modified after Chiaro *et al.*, 2014b

4.4 1-D COMPRESSION

The preliminary settlement performance of the CW-SFS mixtures was investigated via one-dimensional compression test according to ASTM D4186. The main objective of this test was to define the settlement characteristics of the mixtures, including coefficients of compression and swelling (i.e. C_c and C_s) and the yield/past stress induced by compaction. For this series of tests, all CW-SFS mixtures were prepared to the same degree of compaction (90% of maximum dry unit weight for each mixture) in the compaction mould (i.e. 113mm in height and 105mm in diameter) and then a constant rate of strain (1%/hr) was applied on top of the specimen, and they were allowed to deform only in a vertical direction. One cycle of unloading and reloading was performed during the test to evaluate the elastic response of the mixtures. Due to the variation of G_s (see Table 4.1), the initial void ratio for CW-SFS mixtures was varied.

In Table 4.3, a summary of 1-D compression results is given and it indicates that the coefficients of compression (C_c) and swelling (C_s) generally increase with the increase in CW content. The yield/past stress atributed to the compaction energy decreased with the increase of CW content. This might be due to the bindings between the particles associated with SFS grains. In Figure 4.10 the relationships between void ratio and vertical stress for the CW-SFS mixture observed in 1-D compression tests are plotted. Unlike conventional materials like clays, which usually show a bilinear relationship in e-σ_v space, the CW-SFS mixtures were highly nonlinear. However, by increasing the CW content in the blends this trend approaches to being less nonlinear, as it can be seen for CW75-SFS25.

Table 4.3 Summary of 1-D compression results on CW-SFS mixtures

Material	Initial void ratio e_0	Final void ratio e_f	Coefficient of compression C_c	Coefficient of swelling C_s	Yield/past stress (kPa)
CW0-SFS100	0.603	0.516	0.121	0.0018	1500
CW25-SFS75	0.570	0.469	0.158	0.0011	1200
CW50-SFS50	0.520	0.407	0.166	0.0019	1000
CW75-SFS25	0.500	0.382	0.180	0.0024	900

For better comparison between the behaviour of CW-SFS blends, the results in Figure 4.10 can be normalized to the initial void ratio of individual blends and these are plotted in Figure 4.11. It was expected that the mixtures having higher initial void ratio would exhibit more deformation. However, the opposite results were observed and the mixtures with higher CW content (i.e. less initial void ratio) showed more deformation. This may be explained by the higher breakage of CW particles compared to the SFS.

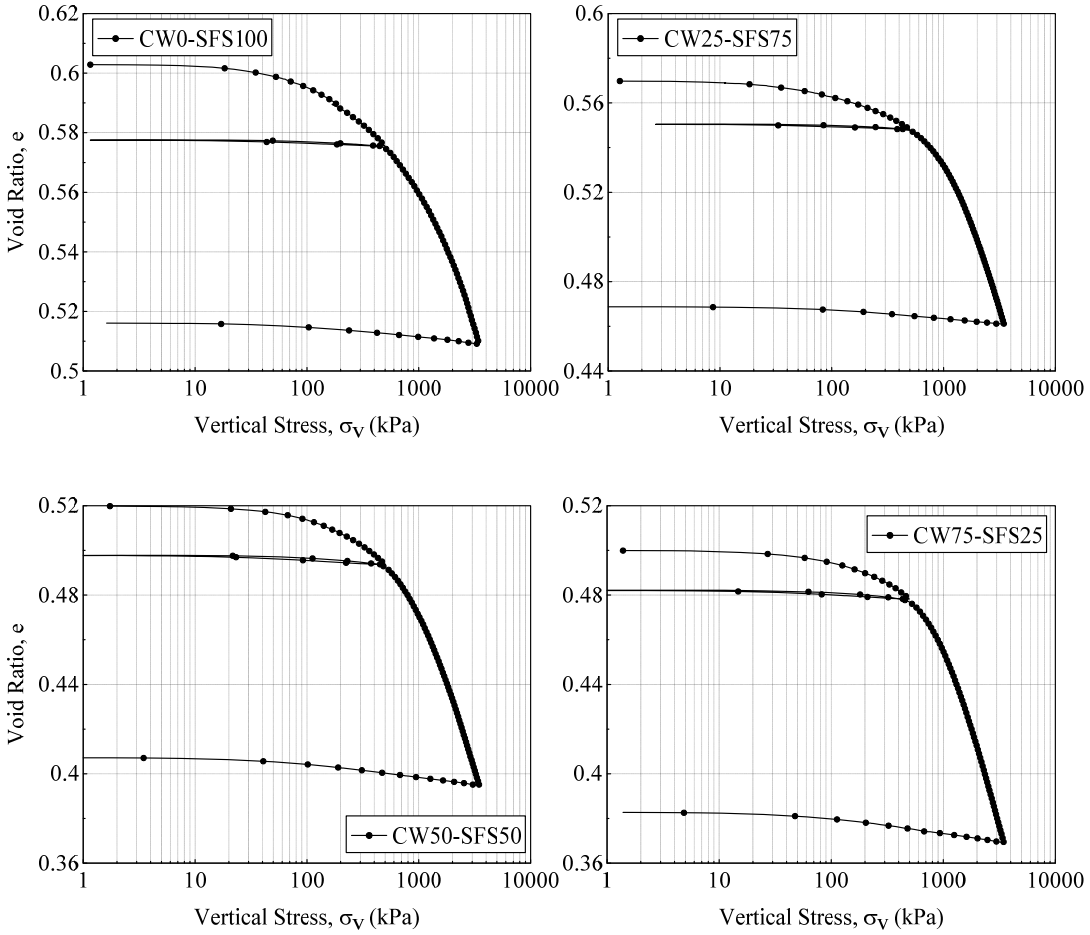

Figure 4.10 Settlement behaviour of CW-SFS mixtures in 1-D compression tests

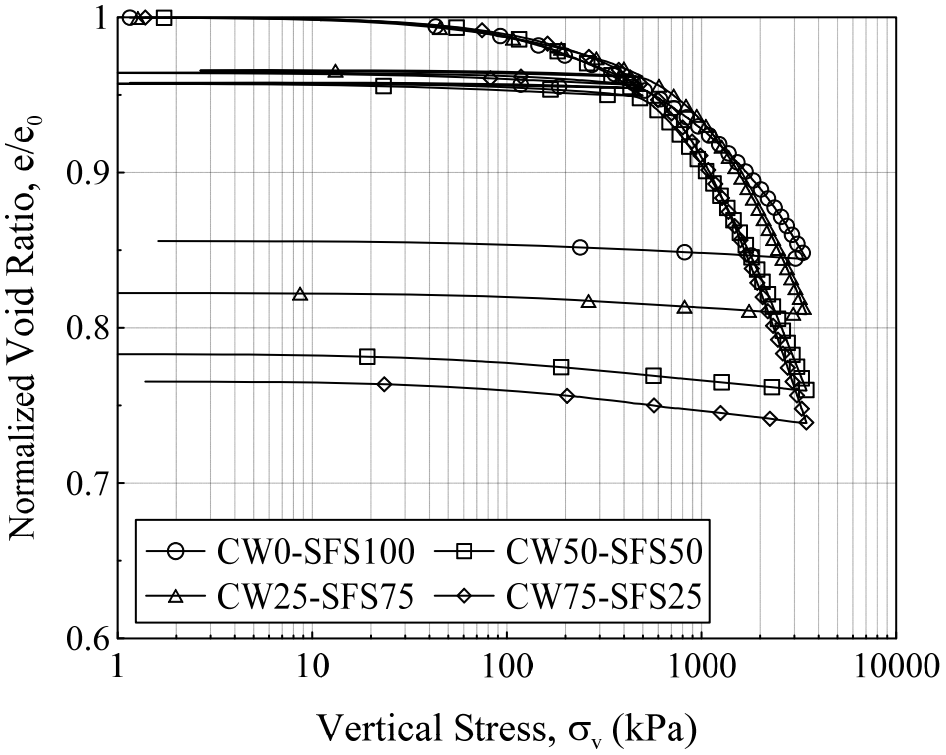

Figure 4.11 1-D compression lines for all CW-SFS mixtures (the vertical axis was normalized to the initial void ratio of each mixture for a better comparison)

4.5 CALIFORNIA BEARING RATIO

The preliminary strength of compacted CW-SFS mixtures were evaluated through California Bearing Ratio (CBR) tests according to ASTM D1883. The specimens were compacted at their OMC and for each CW-SFS blends, two tests were carried out (i.e. as compacted and in soaked condition). According to ASTM D1883, a plunger of 50mm in diameter was penetrated at a rate of 1mm/min into the compacted specimens. The variation of vertical stress with axial strain is shown in Figure 4.12 for as compacted (unsoaked) specimens, and for comparison, typical resilient modulus ($M_{R=}$ $d\sigma_v/d\varepsilon_v$) is illustrated as dashed lines. It is evident that by increasing SFS content in the blends, the resilient modulus increased significantly because SFS particles are stronger compared to CW particles. In addition, particle breakage associated with CW can cause the reduction in resilient modulus. For

instance, M_R for CW100-SFS0 and CW0-SFS100 was 20MPa and 80MPa, respectively.

The CBR values for as compacted (unsoaked) and soaked conditions are illustrated in Figure 4.13. The range of CBR value varies from 10% (CW) to 40% (SFS) for the unsoaked tests and from 7.8% (CW) to 31% (SFS) for the soaked tests. Figure 4.13 also shows that by mixing SFS with CW, CBR value increased significantly (e.g. CBR value for 100% CW and CW75-SFS25 was 10 and 24, respectively). This is mainly due to the higher crushability of CW particles compared to SFS grains. However, the effect of SFS on the CBR value was marginal for mixture with more than 50% SFS. Moreover, as expected, CBR values for soaked specimen are less than those of unsoaked specimens, as unsoaked compacted specimens sustain a greater suction (unsaturated). CBR values of 10% to 40% are recommended for structural fills (Hausmann, 1990). Therefore, except for the case of soaked CW specimens, the CBR values obtained in this study were generally similar to those typical values.

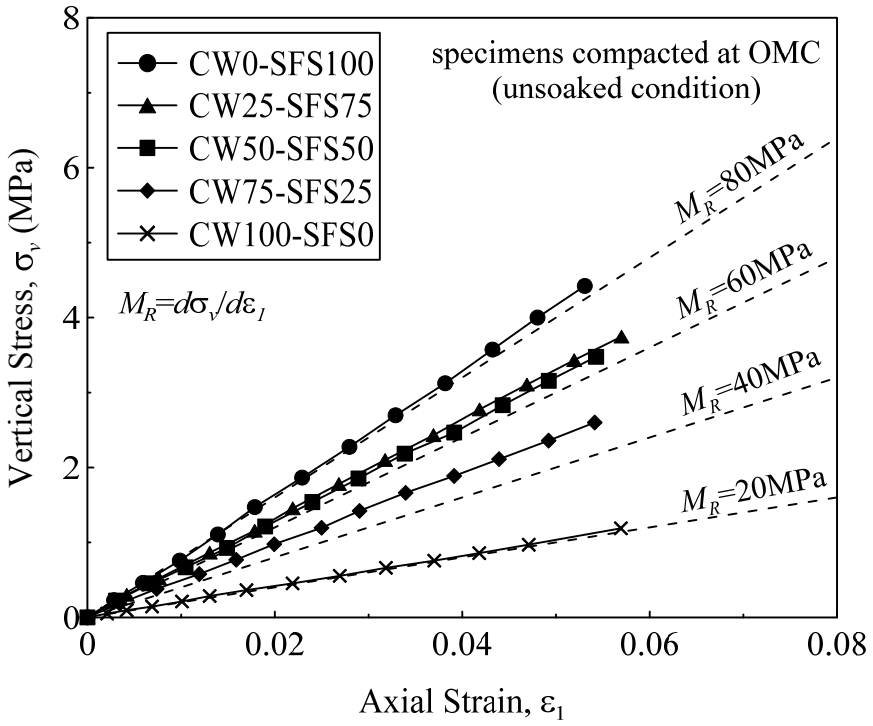

Figure 4.12 Settlement-pressure relationships from unsoaked CBR tests for CW-SFS mixtures (modified after Chiaro *et al.*, 2014b)

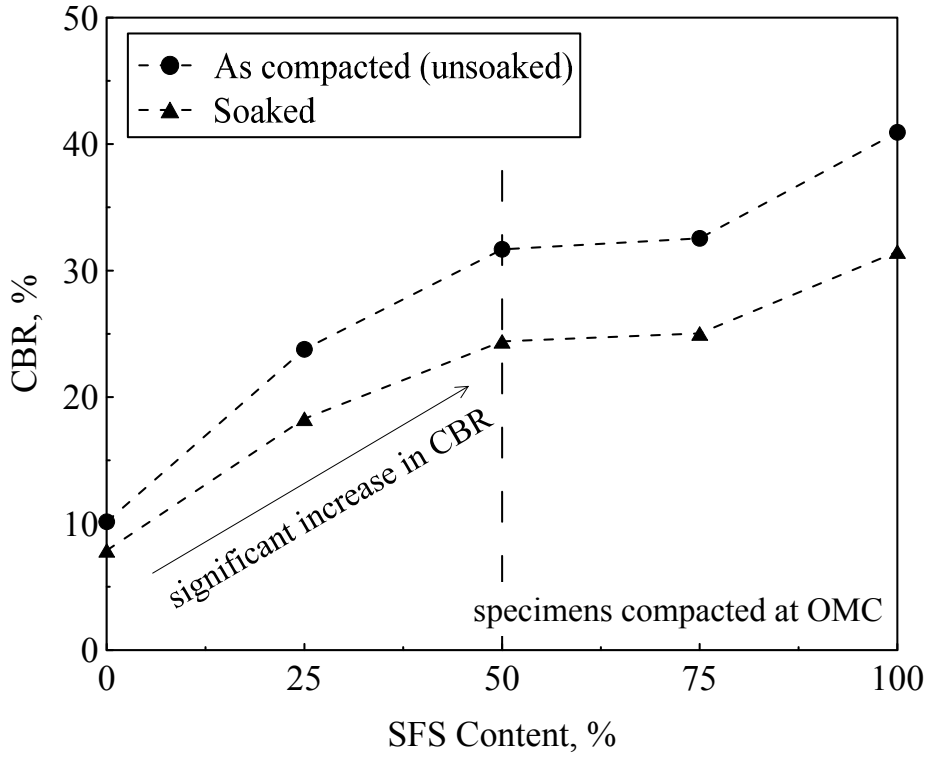

Figure 4.13 CBR characteristics for CW-SFS mixtures (Chiaro *et al.*, 2014b)

4.6 UNCONFINED COMPRESSION STRENGTH

The preliminary strength characteristics of CW-SFS mixtures can be analysed through unconfined compression strength (UCS). Therefore, a series of UCS tests was carried out on the mixtures compacted under standard Proctor energy and the specimens were 104.9mm in diameter and 115.5mm in height (i.e. compaction mould size). A range of moisture content was considered in order to investigate the effect of water content and density on the behaviour. The specimens were allowed to be cured under constant moisture and temperature for one day before the test. All CW-SFS mixtures were considered in this test except CW0-SFS100, because it was difficult for that particular blend to be extracted from the mould, due to lack of cohesion between particles. After the extraction, the specimens were subjected to shearing with the rate of 5mm/min. A total of 20 tests were conducted on 4 different CW-SFS mixtures and the summary of the results are provided in Table 4.4.

Table 4.4 Summary of UCS testing on CW-SFS mixtures

Name	Water content, w (%)	Unconfined compressive strength, $q_{u,max}$ (kPa)	Axial strain at peak strength (%)	Modulus of elasticity (MPa)
CW25-SFS75	5.63	52.70	2.63	2.438
	7.57	33.9	2.56	1.710
	9.81	23.45	2.64	0.989
	10.15	20.18	2.42	1.034
	12.50	25.12	3.08	0.963
CW50-SFS50	7.08	83.92	3.32	3.277
	8.26	77.12	3.37	2.909
	11.02	53.81	3.78	2.000
	12.13	24.75	3.14	1.000
	13.96	18.19	3.52	0.676
CW75-SFS25	4.63	113.91	3.74	4.100
	6.78	112.18	4.18	3.790
	8.77	93.05	5.71	2.090
	10.01	79.60	5.27	2.103
	11.70	37.76	5.71	0.952
CW100-SFS0	6.66	161.44	4.84	4.521
	10.14	97.46	5.28	2.546
	12.54	44.92	7.25	0.980
	14.15	25.54	9.67	0.395
	15.55	20.24	10.11	0.260

The stress-strain responses of CW-SFS mixtures for a range of moisture content values are shown in Figure 4.14 and it can be seen that for the mixture with higher CW content, the unconfined compressive strength was higher. The maximum axial stress for the mixtures varied between 20-160kPa depending on the mixture and the water content. These values correspond to an undrained shear strength of 10-80kPa (S_u=0.5$q_{u,max}$). As expected, by increasing the moisture content the axial stress

decreases, and the stress-strain response changes from brittle (i.e. for specimens with a low water content) to ductile (i.e. very high moisture content). In other words, for specimens on the dry side of OMC, a distinct peak stress followed by a significant post peak strain softening behaviour was observed. For these specimens the value of peak stress was considerably greater than the specimens with higher moisture content. In contrast, the behaviour for the specimens on the wet side of OMC was less brittle. This suggests that for the application of these mixtures in the field, the materials should be compacted close to the OMC but preferably, on the wet side of the OMC.

In Figure 4.15, variations of unconfined compressive strength ($q_{u,max}$) with moisture content for CW-SFS mixtures are presented. As expected, $q_{u,max}$ decreased as moisture content increased. The reduction of $q_{u,max}$ was more predominant for the specimens with higher CW content. For instance, the maximum and minimum value of $q_{u,max}$ observed for CW25-SFS75 were 53kPa and 20kPa, whereas for CW100-SFS0 they were 161kPa and 20kPa, respectively. Figure 4.15 also illustrates that the effect of CW percentage on the $q_{u,max}$ was more significant for the specimens compacted on the dry side of OMC. However, almost all of the specimens compacted with water content more than 12% exhibited similar $q_{u,max}$ equal to 20kPa, irrespective of CW content.

The variations of modulus of elasticity (E) with moisture content for four CW-SFS mixtures are presented in Figure 4.16. A reduction of E was detected as the moisture content increased for all CW-SFS mixtures. It was observed that under similar moisture content, the specimens with higher CW content exhibited higher E (e.g. modulus of elasticity corresponding to 8% moisture content were around 3.6MPa and 1.6MPa for CW100-SFS0 and CW25-SFS75, respectively). On the dry side of OMC, the influence of CW on elastic modulus was more dominant compared to the wet side of OMC. For higher moisture content, all of the mixtures approached the same value.

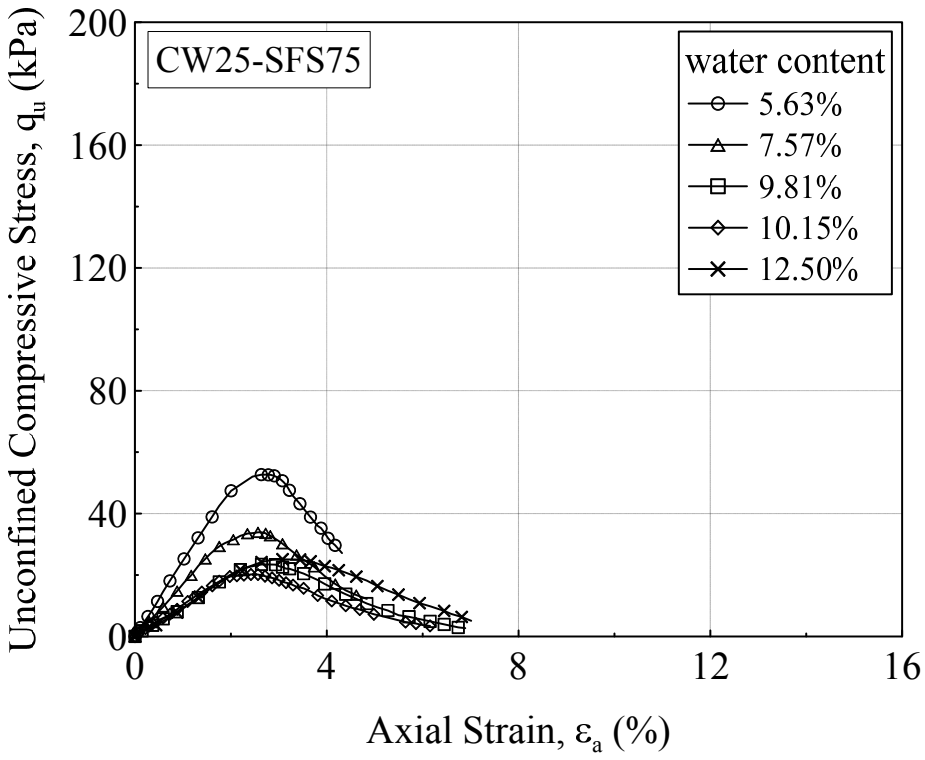

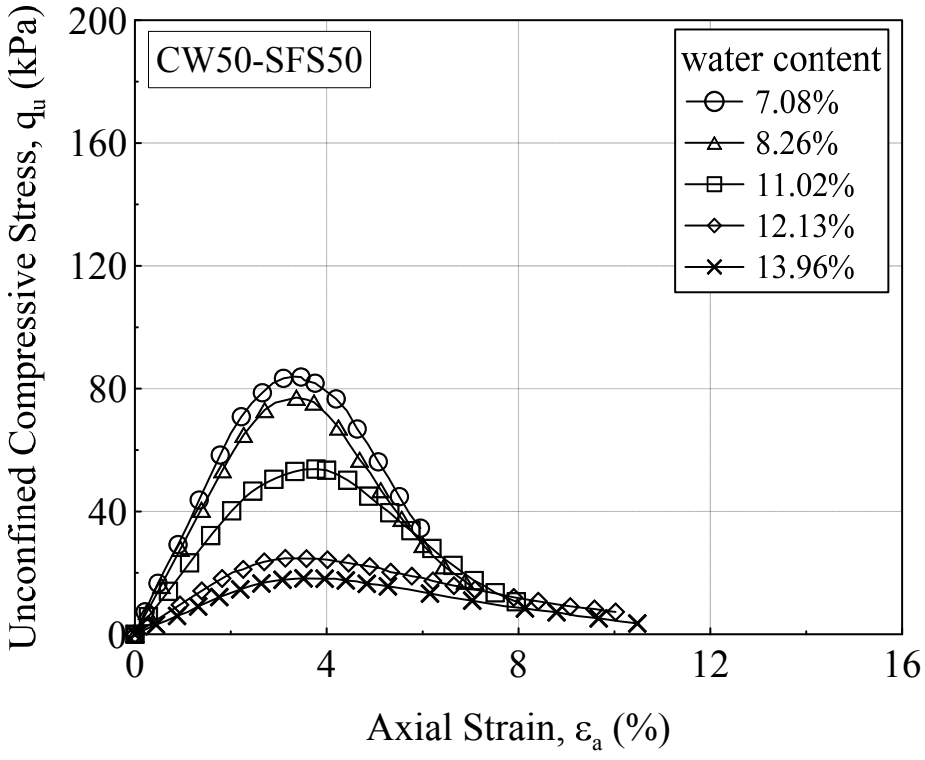

Figure 4.14 Results of UCS test on four CW-SFS mixtures compacted at different water content

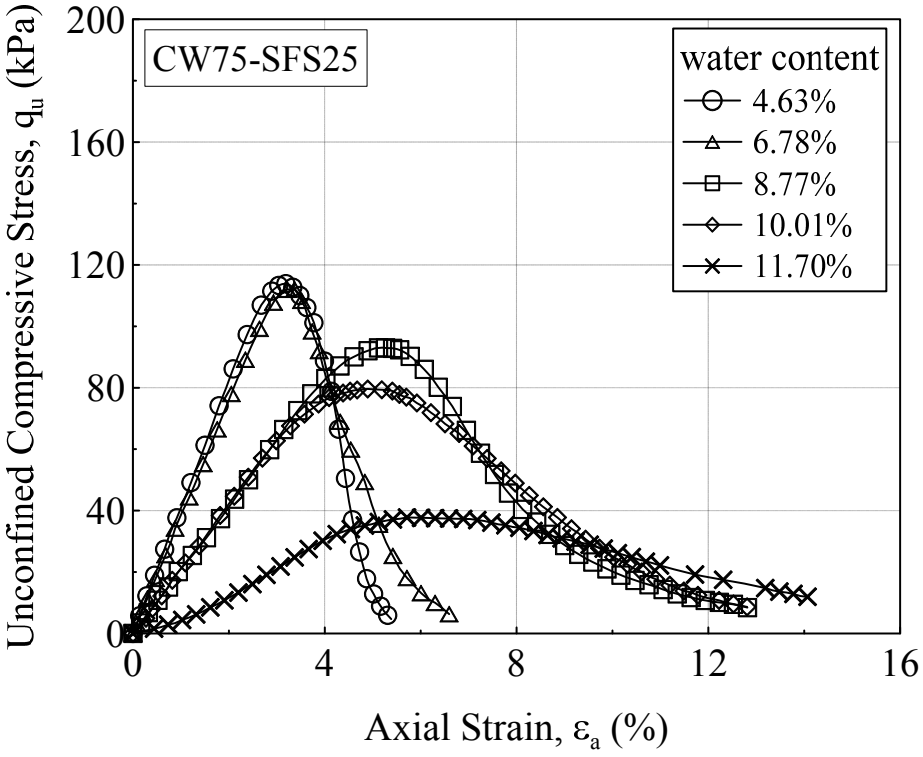

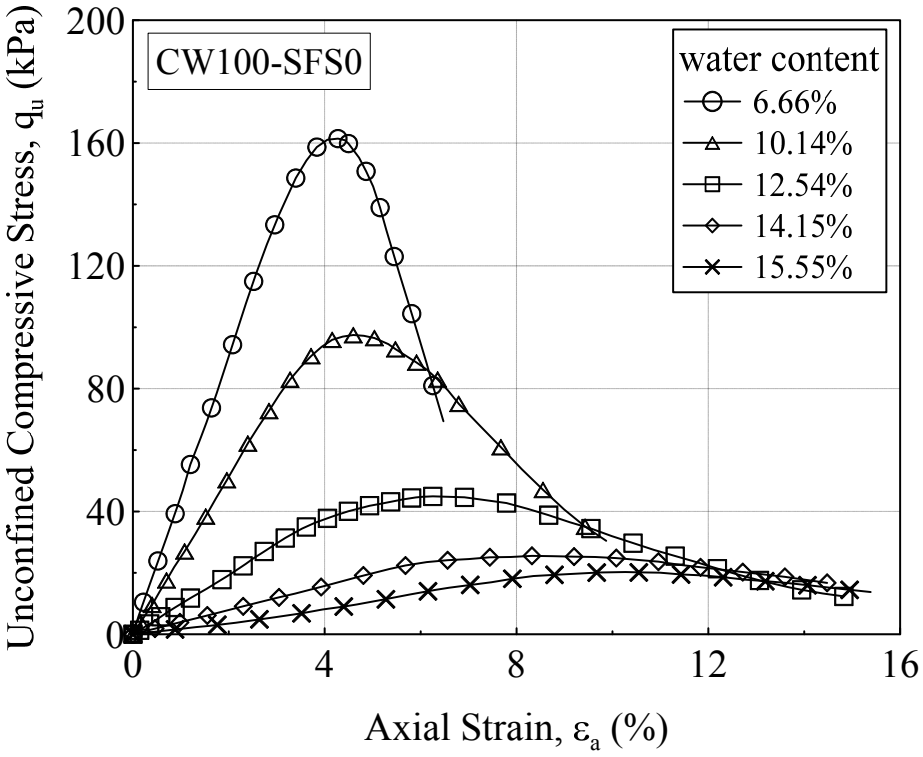

Figure 4.14 Results of UCS test on four CW-SFS mixtures compacted at different water content

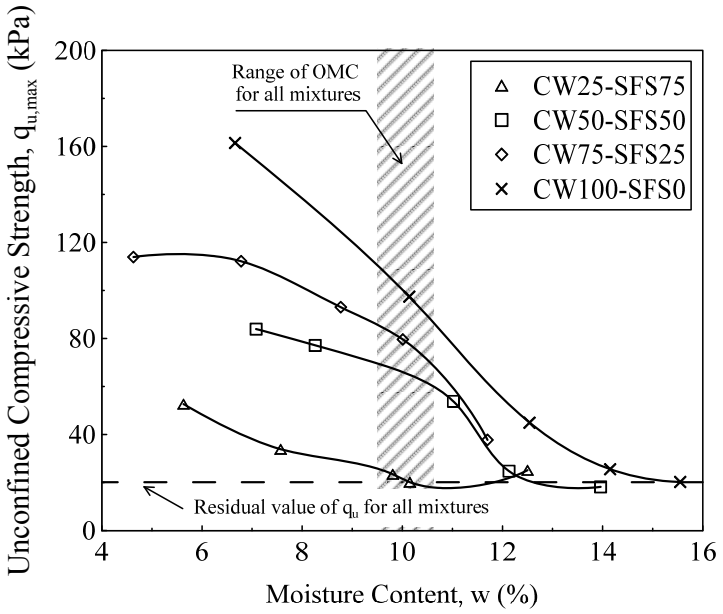

Figure 4.15 Variation of unconfined compressive strength with moisture content for CW-SFS mixture

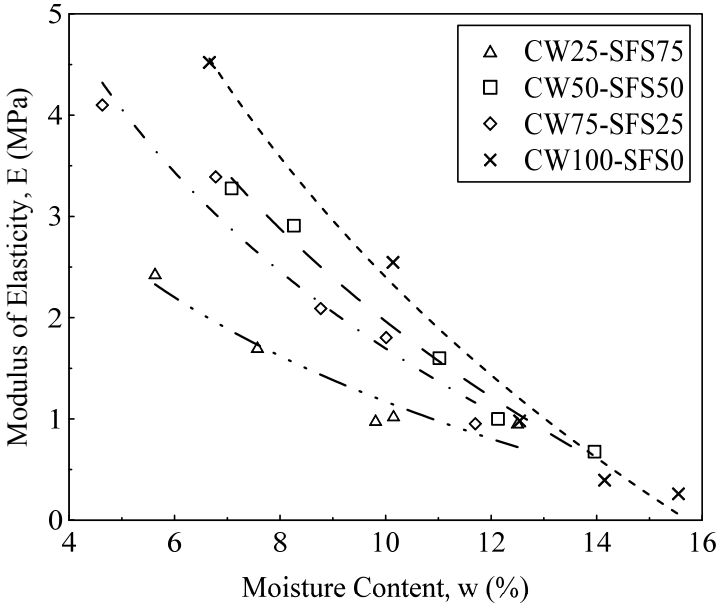

Figure 4.16 Modulus of elasticity with moisture content for CW-SFS mixtures calculated from UCS testing

The axial strain corresponding to the peak unconfined compressive strength ($q_{u,peak}$) against moisture content is plotted in Figure 4.17 and it shows that under a given moisture content, a greater axial strain was required for reaching $q_{u,peak}$ for the mixtures having a higher content of CW. The difference of the axial strain at peak strength between the specimens with higher moisture content and those with a lower one was insignificant for CW25-SFS75 and CW50-SFS50 (i.e. the blends with less than 50% coal wash). For these blends, axial strain of 2%-3% was required to mobilise the peak strength. By contrast, the blends with more than 50% coal wash required larger strain to reach the peak strength. These two types of behaviour may be attributed to the brittle and ductile behaviour as observed for these two sets of blends.

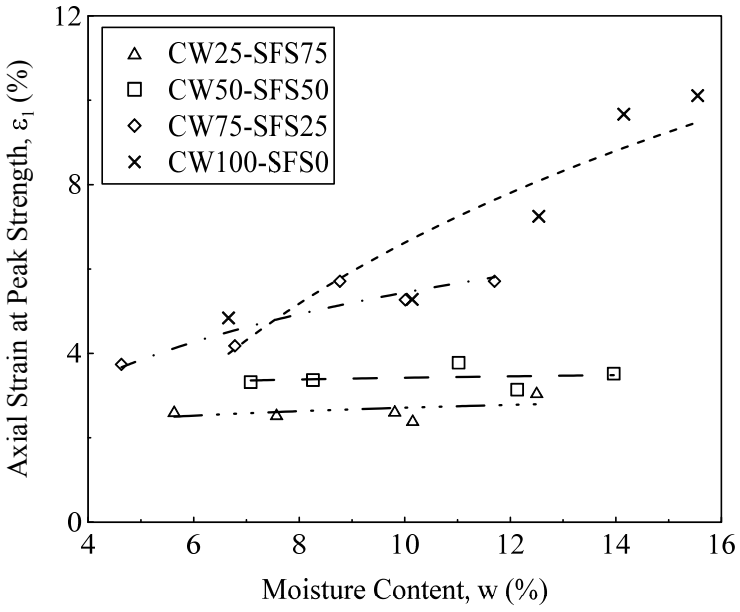

Figure 4.17 Variation of axial strain corresponding to peak strength with moisture content for CW-SFS mixtures

4.7 SWELLING BEHAVIOUR

As explained in Chapter 3, due to the presence of free lime (CaO) and free magnesium (MgO) in the chemical composition of steel furnace slag, this byproduct is unstable in volume (i.e. swelling potential). The hydration reaction of the free lime

and magnesium is the main cause for the volumetric expansion or heave associated with the SFS (Geiseler, 1996, Yildirim and Prezzi, 2011, Frías Rojas and Sánchez de Rojas, 2004). The amount of the total volume expansion depends on the free lime content in the unit volume of the specimen, as well as on the chemical composition of SFS and the particle size (Wang, 1992, Chen *et al.*, 2007). The expansion of the material being used as structural fill should be within an acceptable range to prevent damage to the upper structure and should be carefully considered. Therefore, it is essential to study the volume expansion of CW-SFS mixtures.

4.7.1 Free swelling (swelling potential)

As discussed in Chapter 3, free swell is the ratio of the change in height to the initial height of the specimen, expressed as percentage figures. Unlike the recommendation in the standard (i.e. ASTM D4792), it was found that the recommended 7 days testing period to determine the final swelling was insufficient for the material to attain nearly constant swelling potential. Therefore, larger testing periods of typically 30 days and in some cases more than 100 days were considered. A summary of the results for the swelling potential of CW-SFS blends prepared at different density is presented in Table 4.5.

The variations of swelling potential against time for the CW-SFS mixtures compacted at different levels of density are shown in Figure 4.18. This figure shows that the swelling potential was influenced significantly by the SFS content in the mixtures. It is evident from Figure 4.18 that the recommended 7 day in the ASTM D4792 was insufficient to capture the ultimate swelling potential, in particular for specimens with higher SFS content. As expected, the CW100-SFS0 exhibited shrinkage rather than swelling, because it does not contain any chemical component susceptible to swelling potential and once the specimen was inundated, the loss of suction between particles results in collapse behaviour and reduction in void ratio. On the other hand, the CW0-SFS100 exhibits maximum swelling potential. It was observed that volumetric swelling for the CW0-SFS100 compacted to the 100% MDD for standard Proctor was around 12%. However, it decreased to be less than

3% by adding 25% coal wash into the blend (i.e. more than 75% reduction in swelling) and for CW50-SFS50 was less than 1.5% (equivalent to 88% reduction compared to CW0-SFS100). This implies a significant influence of coal wash in the reduction of SFS swelling potential. Therefore, the swelling potential associated with the SFS can be effectively controlled by combining with the CW.

Table 4.5 Summary of swelling potential results on CW-SFS mixtures

Material	R.C (%)	γ_d (kN/m^3)	e_0	V_{SFS}/V_t (%)	S_f (%)
CW0-SFS100	83.1	18.87	0.736	58	2.70
	88.4	20.08	0.631	61	7.44
	97.6	22.16	0.478	68	12.19
CW25-SFS75	83.8	17.46	0.691	40	2.20
	88.4	18.41	0.603	42	2.98
	98.8	20.57	0.435	47	2.92
CW50-SFS50	80.1	15.64	0.711	24	1.08
	89.9	17.55	0.525	27	1.15
	99.8	19.48	0.374	30	1.16
CW75-SFS25	80.2	14.60	0.686	11	0.47
	89.4	17.52	0.405	12	0.64
	100.2	18.21	0.352	14	1.27
CW100-SFS0	100.3	16.95	0.313	0	-0.53

R.C = relative compaction; γ_d= dry unit weight; e_0 = initial void ratio; V_{SFS} = volume of SFS in the specimen; V_t = total volume of the specimen; and S_f = free swelling (swelling potential)

Figure 4.18 also illustrates the influence of relative compaction on the swelling potential and generally, by decreasing the density, the amount of swelling decreased. In the lower density specimen, the volume of voids is larger compared to the denser

specimen and therefore, part of the swelling potential is absorbed within the volume of the specimen. Furthermore, the amount of free lime and free magnesium per unit volume is less for the specimens with lower density and this results in less swelling potential. However, in some specimens such as CW75-SFS25, the opposite behaviour was observed. This might be due to the accuracy of the test results, especially for specimens with minor swelling potential (i.e. less than 1.5% which equals to 1.7mm change in height of the specimen). It is evident that for CW0-SFS100, by decreasing the relative compaction from 100% to 80%, the swelling potential decreased from around 12% to less than 3%. This means that the swelling potential of SFS can be minimised by compacting the material to a lower density in the field.

For better comparison of swelling potential behaviour between different CW-SFS mixtures, the results of all mixtures were grouped based on the relative compaction and plotted in Figure 4.19 for swelling potential and in Figure 4.20 for rate of swelling against time. These figures clearly illustrate the efficient influence of CW in swelling behaviour. The reduction both in free swelling and swelling rate is observed by increasing CW content in the mixture. The maximum swelling rate was 0.9mm/day for CW0-SFS100 and, as expected, the rate decreased as the density was decreased. For all mixtures except CW0-SFS100, the swelling rate after 10 days was within a small range 0.01 to 0.05mm/day.

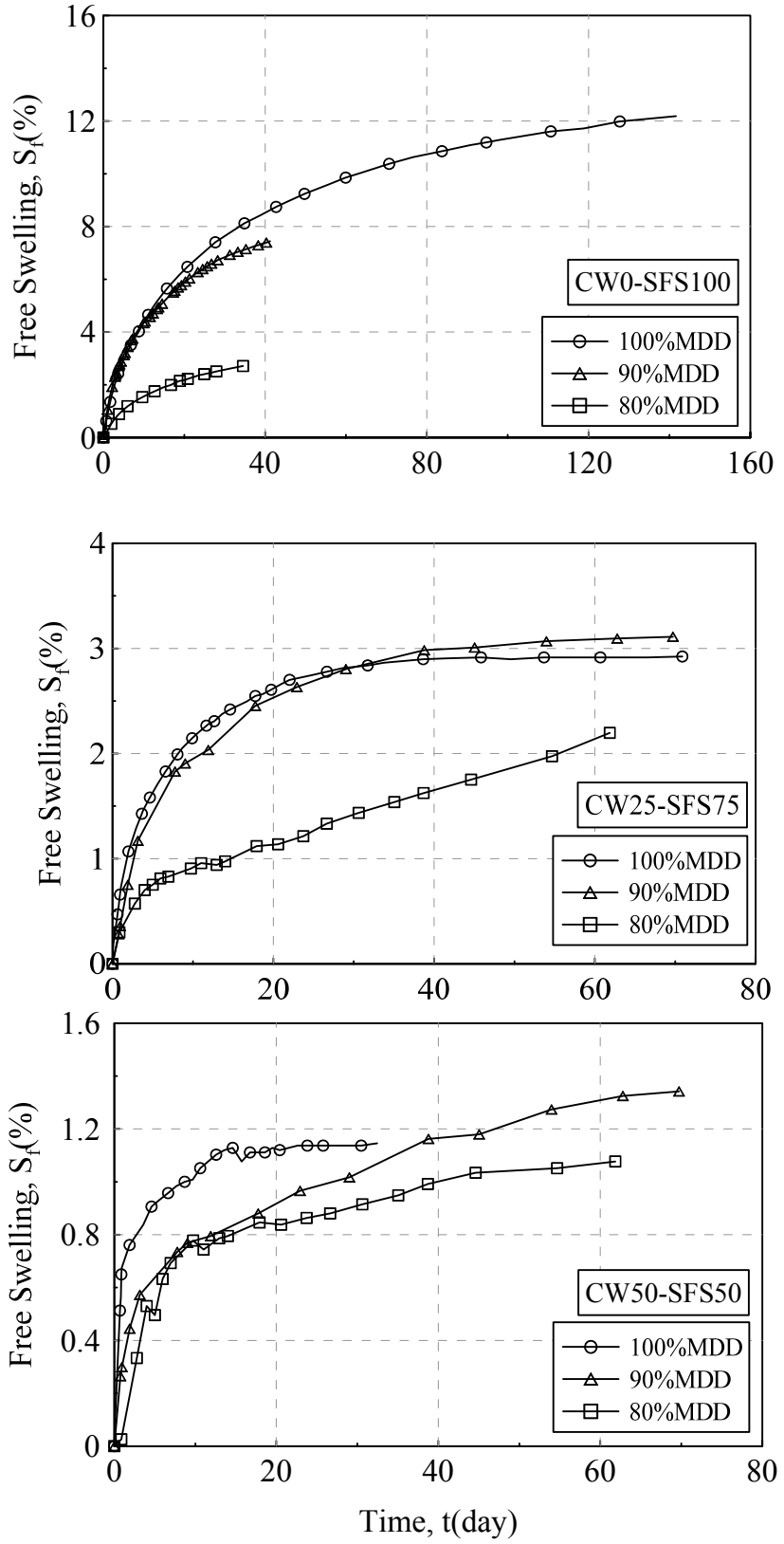

Figure 4.18 Swelling potential against time for CW-SFS mixtures

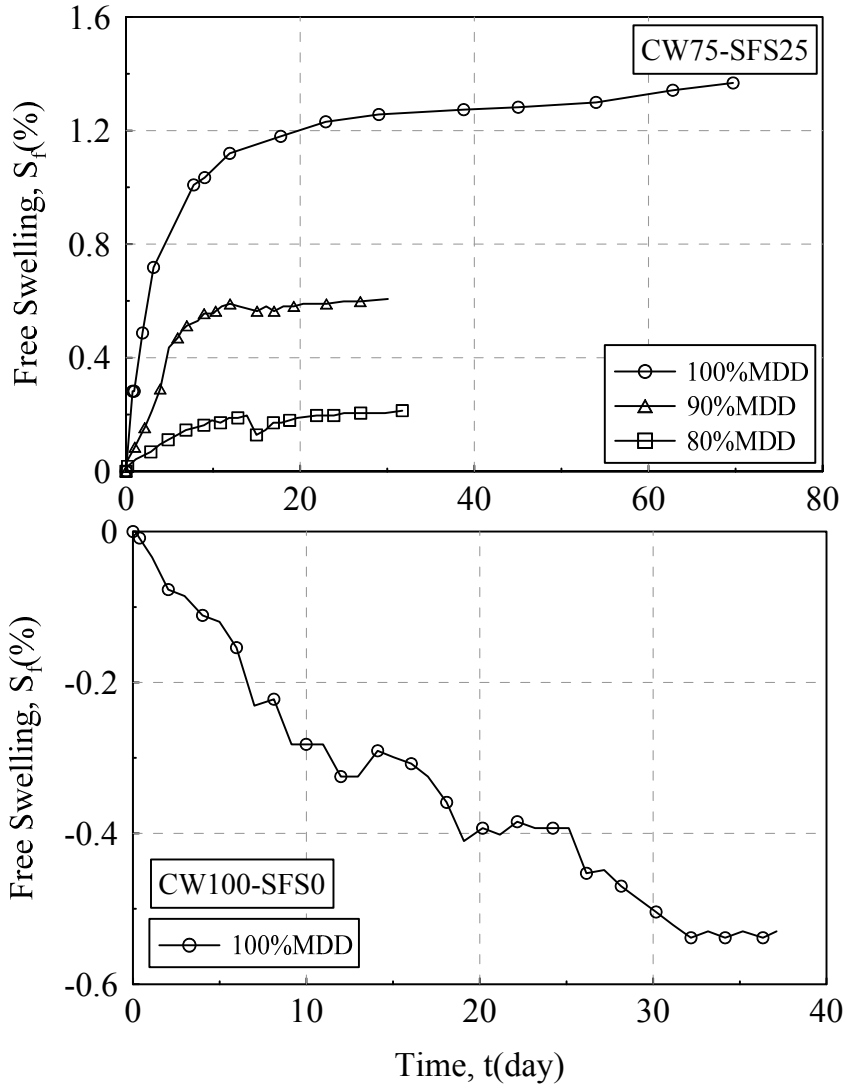

Figure 4.18 (continued) Swelling potential against time for CW-SFS mixtures

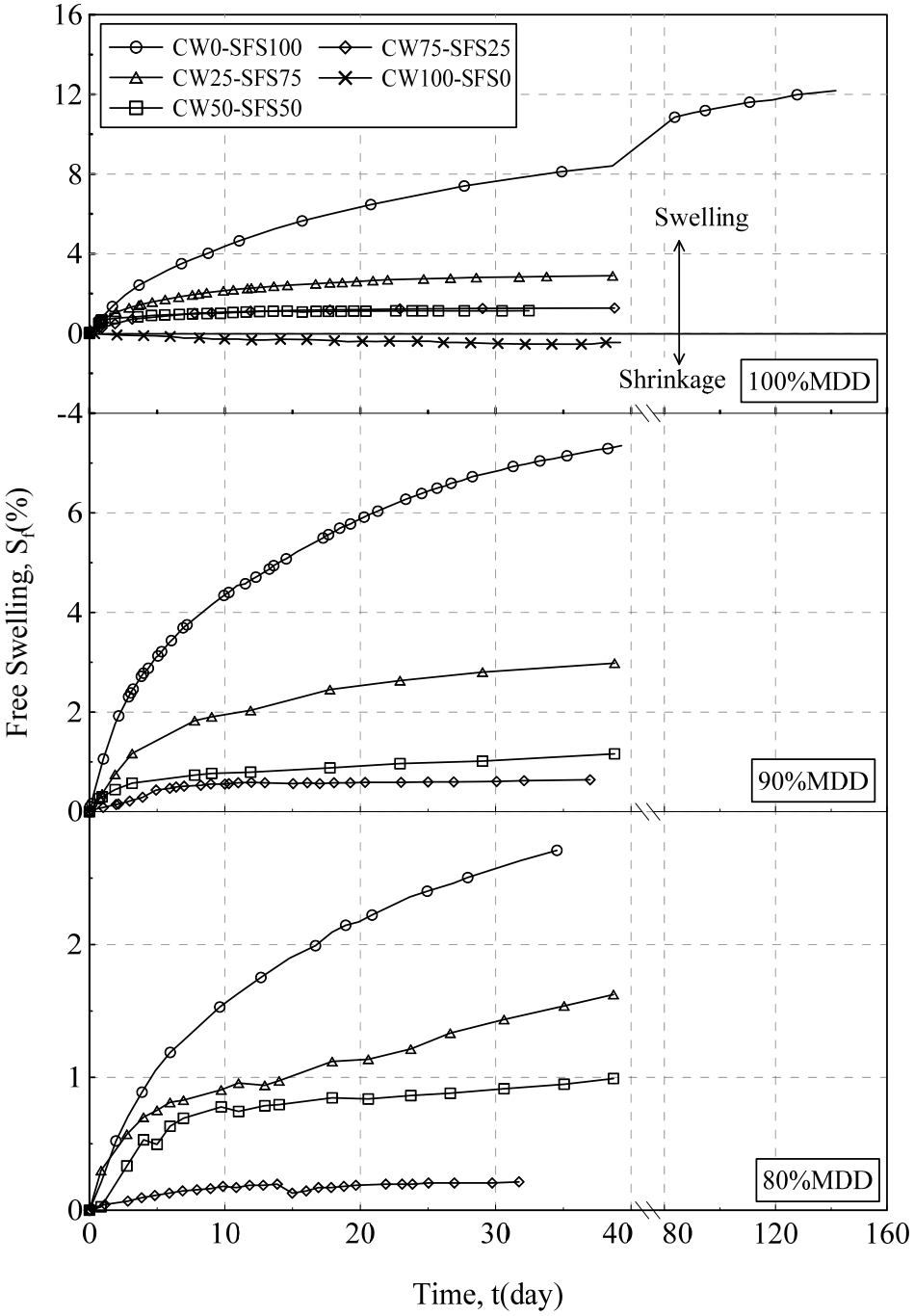

Figure 4.19 Effect of the CW on free swelling curves against time for CW-SFS mixtures

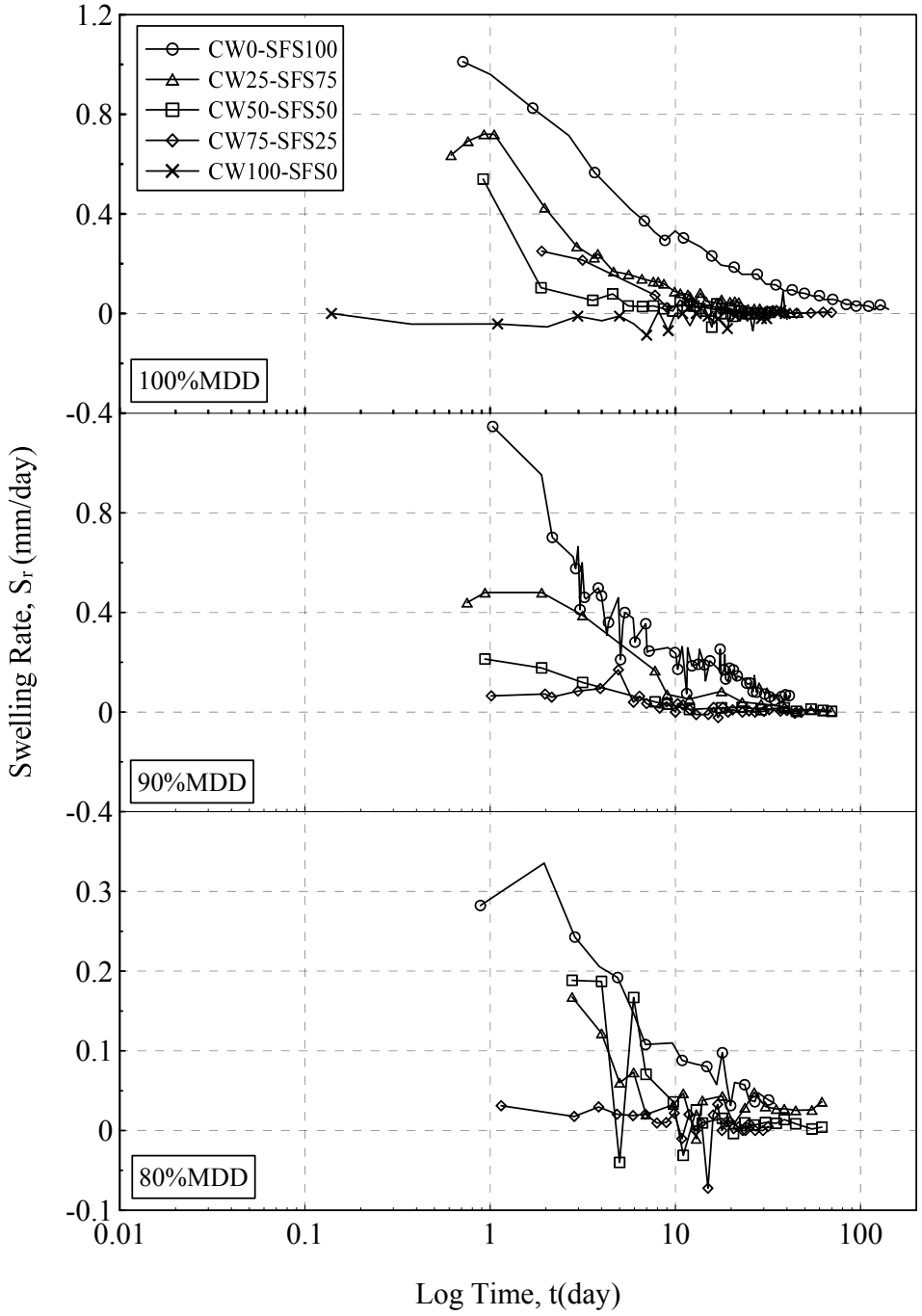

Figure 4.20 Rate of swelling with time for CW-SFS mixtures compacted at three levels of density

The variation of swelling potential with CW percentage for CW-SFS blends compacted at three levels of density is plotted in Figure 4.21. It is evident that there is a significant reduction in free swelling due to the inclusion of CW into the blends. However, the effect of CW is more dominant at higher density. This is attributed to the reduction of the SFS particles in the specimen volume. Therefore, the quantity of the chemical composition with swelling potential is considerably less, and thus results in lower swelling. Therefore, the amount of SFS in the specimen plays a significant role in swelling, as discussed later in this chapter.

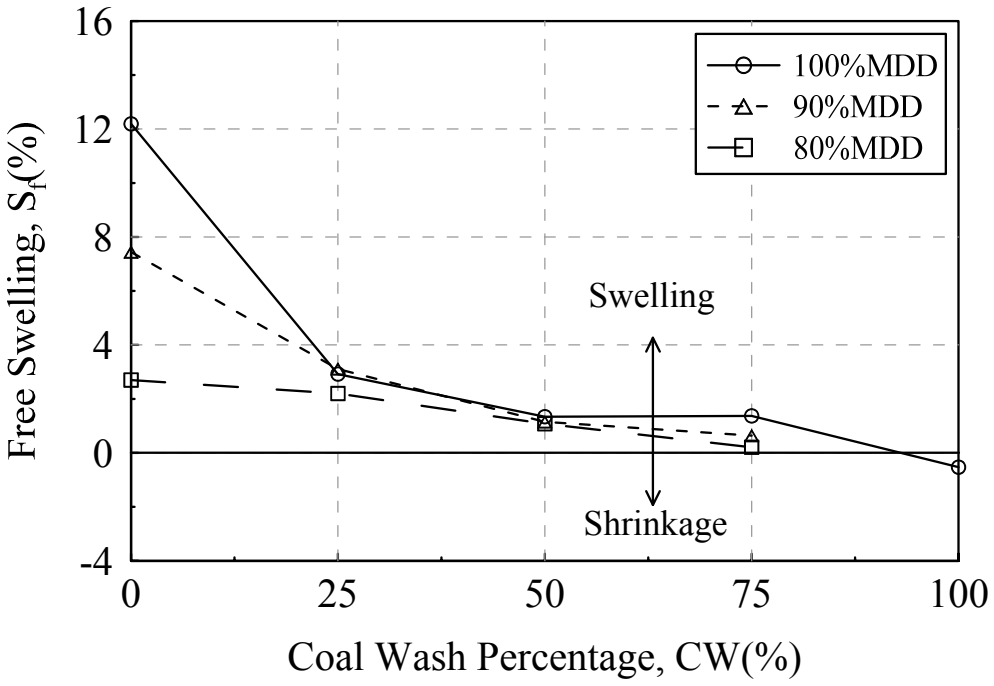

Figure 4.21 Variation of free swelling with coal wash content for CW-SFS mixtures compacted to different densities

In Figure 4.22, the effects of relative compaction on the free swelling of CW-SFS mixtures are illustrated and the results show that by increasing the density (i.e. relative compaction), the ultimate swelling is increased. However, it is evident that this increase is more dominant for CW0-SFS100 (i.e. only SFS) where there is no coal wash in the mixture and for the rest of the mixtures was negligible. This means that due to the inclusion of CW in the blend, the effect of density on the swelling potential could be reduced to being negligible. Figure 4.22 also shows that a linear relationship between the density and swelling potential for CW0-SFS100 can be

captured. This behaviour is directly related to the linear increase in the amount of the CaO and MgO in the SFS.

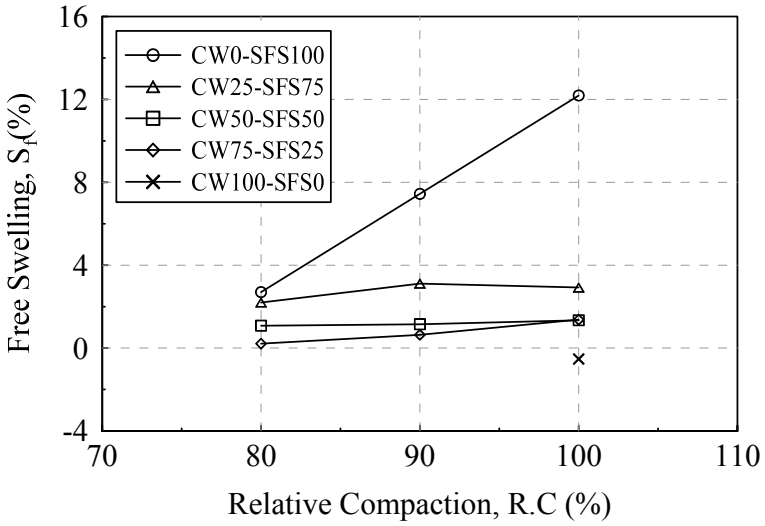

Figure 4.22 Effect of relative compaction on the free swelling of CW-SFS mixtures

It was identified that the volume ratio of SFS in the mixture (e.g. V_{SFS}/V_t) can be related to the swelling potential of the CW-SFS blends and this relationship is presented in Figure 4.23. The results show that while V_{SFS}/V_t was lower than 50%, free swelling was increased gradually, whereas for the mixtures with V_{SFS}/V_t higher than 50%, free swelling was increased rapidly.

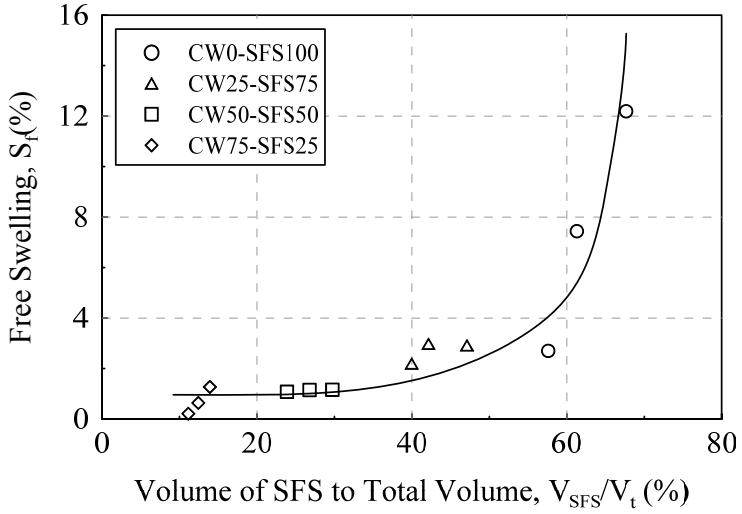

Figure 4.23 Variation of swelling potential with the percentage of SFS volume to the total volume for CW-SFS mixtures

4.7.2 Swelling pressure

There are several methods to measure swelling pressure of an expansive soil. These methods include the improved swell oedometer test (Nagaraj *et al.*, 2009, Thompson *et al.*, 2006, Sridharan *et al.*, 1986, Reyad, 1990) also known as swell-load method; the constant volume method (Basma *et al.*, 1995); and the swell overburden test (Gibbs, 1973). In the improved swell oedometer test (ISO), the specimen is allowed to swell freely in a vertical direction and then it is loaded until the initial void ratio is reached. Therefore, the swelling pressure is equal to the pressure that was required to bring the specimen to its initial void ratio after swelling. In the constant volume test (CV), swelling of the specimen is prevented by constraining the vertical swell and then the maximum pressure measured by a load cell is the swelling pressure. In the third method (i.e. swell overburden test), three or more specimens are loaded under different pressures and are allowed to swell or compress to reach equilibrium. By plotting the swell against pressure, the swelling pressure can be identified as that pressure corresponding to zero swelling.

In this investigation, the constant volume method was adopted, because the third method required several specimens and preparing identical specimens is invariably difficult and time-consuming. Similarly, due to the limitation on the maximum particle size that can be used in the oedometer equipment in comparison with the material investigated in the study (d_{max}=16mm), the first method could not be employed. Therefore, in the following, the results of the swelling pressure for CW-SFS mixtures are presented using the constant volume method. The detailed specimen preparation and testing procedures are described in Chapter 3.

The results of the swelling pressure with time using the constant volume method are summarised in Table 4.6 and shown in Figure 4.24, and these show similar patterns to those found in free swelling. By increasing the SFS content in the blend, a higher swelling pressure was observed. Furthermore, for mixtures having more SFS, the time required to reach the maximum swelling pressure was longer. It can be seen that for CW0-SFS100, the swelling pressure (S_p) was more than 100kPa, while for CW25-SFS75 it reduced significantly to a value lower than 60kPa, and for the other

two mixtures it was less than 25kPa. It is evident that the effect of CW content on the ultimate swelling pressure was insignificant for mixtures having more than 50% CW. The swelling pressure plays an important role in the selection of the optimum CW-SFS blends, because, if the swelling pressure is greater than the overburden pressure or the applied load on top of the fill material, it can cause serious damage to the upper structure. Therefore, based on the applied load (i.e. the surcharge on the CW-SFS layer such as pavement and the loading from structure) as compared with the swelling pressure (Table 4.6), the optimum CW-SFS blend can be chosen in terms of swelling pressure.

Table 4.6 Summary of swelling pressure results on CW-SFS mixtures

Material	R.C (%)	γ_d (kN/m^3)	e_0	V_{SFS}/V_t (%)	S_p (kPa)
CW0-SFS100	90	20.45	0.602	61	101.6
CW25-SFS75	90	18.77	0.572	42	58.6
CW50-SFS50	90	17.60	0.521	27	22.2
CW75-SFS25	90	16.41	0.500	13	14.1

R.C = relative compaction; γ_d= dry unit weight; e_0 = initial void ratio; V_{SFS} = volume of SFS in the specimen; V_t = total volume of the specimen; and S_p = swelling pressure

The effects of CW content on the ultimate swelling pressure of CW-SFS blends are presented in Figure 4.25, and it shows there is a significant reduction in swelling pressure once the CW content increases from zero to 50%. However, for mixtures having more than 50% CW, the influence of CW on the swelling pressure diminishes as similar behaviour was observed for the swelling potential (i.e. free swelling). This behaviour can be justified by considering the volume of the SFS in the blends, rather than the dry weight ratio of SFS to the total volume of the specimen (i.e. V_{SFS}/V_t). As it is reported in Table 4.6, for CW50-SFS50 only 27% of the volume is occupied by SFS, whereas this ratio for CW25-SFS75 is 42%. This means that the swelling

pressure behaviour for specimens having more than 50% CW (dry weight ratio) is mainly governed by the CW, as the volume of SFS in those specimens is minimal.

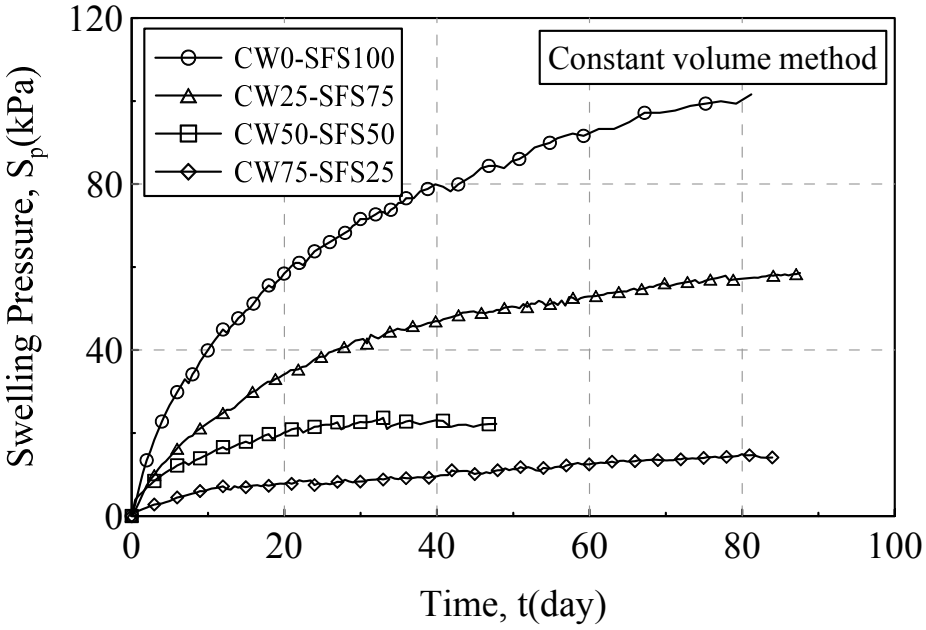

Figure 4.24 Variation of swelling pressure with time for CW-SFS mixtures

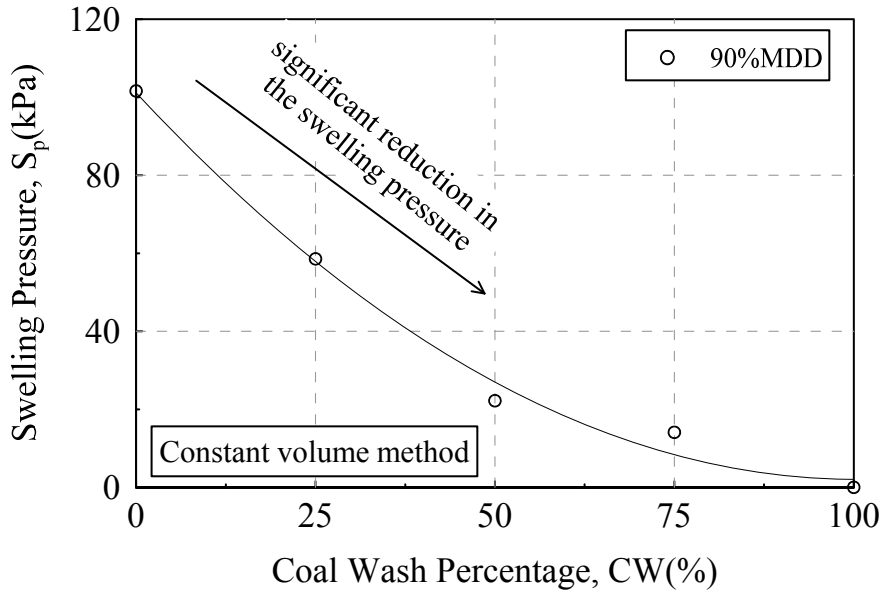

Figure 4.25 Effect of coal wash content on the swelling pressure of CW-SFS mixtures

4.7.3 Relationship between free swelling and swelling pressure

In previous sections, the results of the swelling behaviour of CW-SFS blends were presented. Those results were associated with two limits in terms of boundary conditions. The first type of boundary condition was free swelling and it means that the specimen was allowed to swell without any constraint, and resulting in maximum swelling potential. The second type of boundary condition was complete prevention of any swelling for the specimen, and this resulted in determining the swelling pressure. However, in real applications and projects, some swelling is allowed to take place without causing damage to the upper structures. This allowable free swelling is determined based on the type of structures and their sensitivity to the displacement. In this case, the boundary condition lies somewhere between the two types explained above. It is obvious that allowing a specimen to have any amount of swelling results in less swelling pressure. Therefore, the relationship between free swelling and swelling pressure should be established.

The easiest method to establish the correlation between free swelling and swelling pressure is by comparing the results of individual boundary condition together, and then determining the corresponding swelling pressure to free swelling for a given time after start of the test. Initially, the two points of correlation between free swelling and swelling pressure is known. The first point is the swelling pressure for no free swelling (i.e. the ultimate swelling pressure from the test) and the second one is the swelling corresponding to zero swelling pressure (i.e. the ultimate free swelling from the test). An example for this method is illustrated for CW0-SFS100 compacted to 90%MDD in Figure 4.26, and the horizontal arrows indicate points on the free swelling and swelling pressure curves. By finding the values on the two curves for different CW-SFS blends and plotting free swelling against swelling pressure, a linear relationship between these two parameters can be determined as shown in Figure 4.27.

An example to define swelling pressure corresponding to an allowable free swelling is shown in Figure 4.27. In a particular project, if 4% swelling is allowed on the compacted layer of CW0-SFS100, then the resultant swelling pressure on the upper

structure is around 56kPa. This pressure is around half of the swelling pressure (i.e. maximum swelling pressure). Therefore, the required overburden pressure or loading on the layer is much lower in the case where some percentage of swelling is allowed.

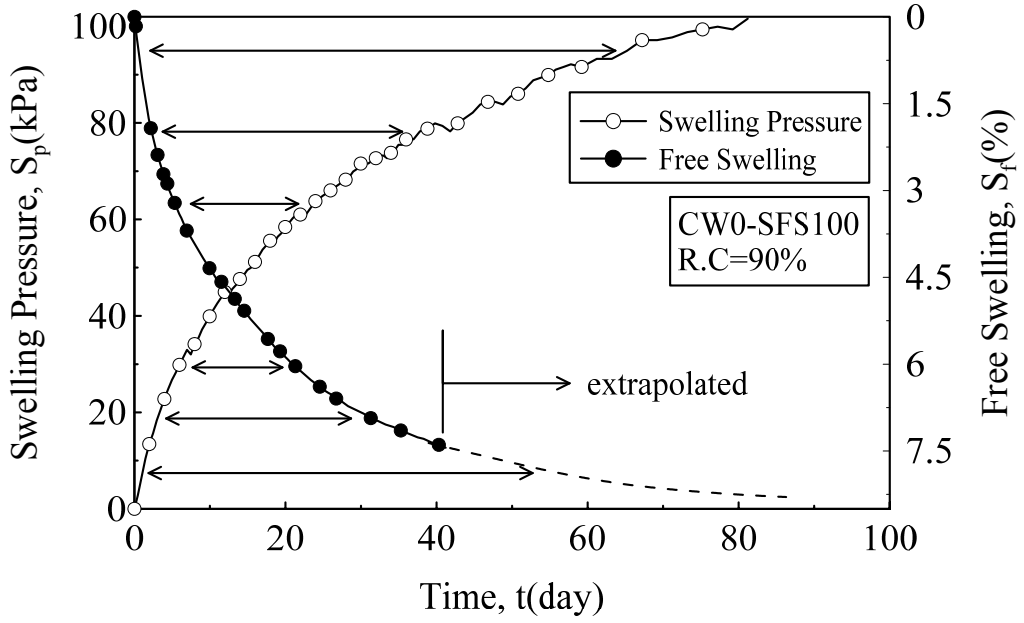

Figure 4.26 Method for determining correlation between swelling pressure and free swelling

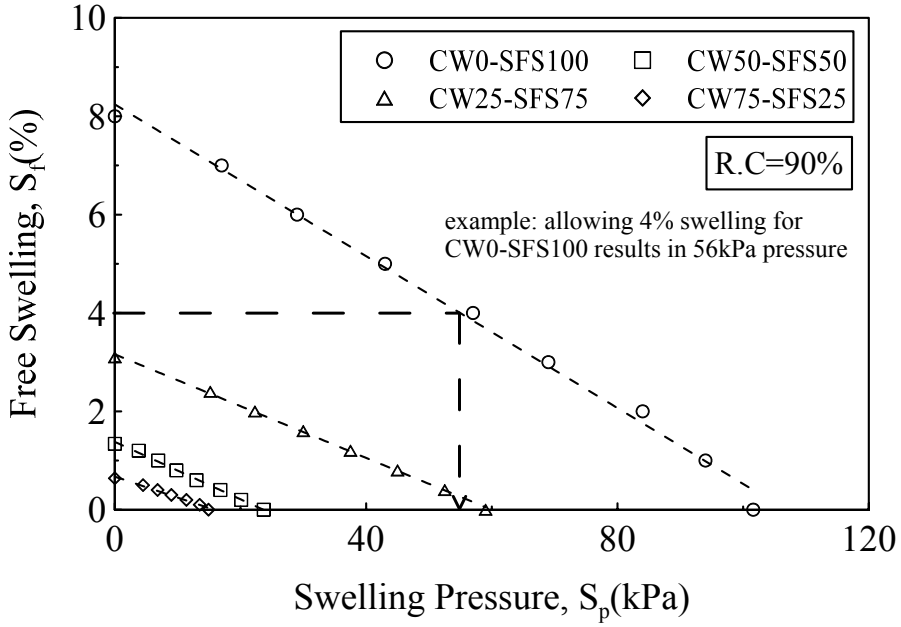

Figure 4.27 Relationship between free swelling and swelling pressure of CW-SFS mixtures compacted to 90%MDD

4.8 SUMMARY

This chapter presented a preliminary comprehensive investigation of the geotechnical properties of CW-SFS mixtures. Initially, the compaction characteristics of the blends, including the specific gravity, compaction curves and particle breakage during compaction were studied. It was observed that the maximum dry unit weight of mixtures increased with the increase in SFS content because of the higher G_s. Although post-compaction particle breakage of CW cannot be neglected (i.e. BI>10%), the addition of SFS to CW reduced the particle breakage significantly.

The permeability results revealed that with the exception of the CW specimen, CW-SFS blends usually have a moderate permeability (1×10^{-6} cm/sec $\leq k \leq$ 1×10^{-4} cm/sec) which is sufficient to ensure rapid excess pore pressure dissipation. The low permeability of the CW was a result of the overall small value of void ratio as well as existence of clayey fines in CW.

The strength characteristics of the mixtures were assessed by conducting 1-D compression tests, California Bearing Ratio (CBR), and unconfined compression tests (UCS). It was observed that more deformation was associated with the blends having more CW content in 1-D compression. Although all the specimens were prepared at the same level of compaction energy, the yield/past stress increased as the SFS content increased in the blend. In CBR testing, except for the soaked CW specimen, CBR values for CW-SFS blends were generally similar to typical sandy fills (i.e. CBR = 10% - 40%). And finally, the unconfined compressive strength increased with the increase of CW content in the mixture, and the behaviour of the mixtures in UCS test was observed to be more ductile for those specimens having more CW content.

The results of swelling behaviour indicated that due to the existence of free lime (CaO) in the chemical composition of SFS, the free swelling of this material is significant. It was observed that it swelled around 12% for 100%MDD but it reduced substantially to less than 3% by adding 25% CW. The effect of initial density was more dominant on CW0-SFS100. For instance, the free swelling for 100%MDD and

80%MMD was 12% and 3%, respectively. For other mixtures, the change on free swelling with respect to the initial density was negligible, because the controlling parameter on the ultimate free swelling was the volume of SFS particles compared to the volume of the specimen. It was identified that when the ratio of V_{SFS}/V_t was greater than 50%, the free swelling increased significantly.

Although free swelling can cause problems to the upper structures, it can be controlled by applying a surcharge on the layer and this includes the pavement layer, embankments, and dead loading from structures. The results of the swelling pressure by utilizing the constant volume method revealed that for specimens compacted to 90%MDD, the swelling pressure varied between 14.1kPa to 101.6kPa depending on the SFS content in the mixture. For the CW50-SFS50, the swelling pressure was around 22kPa. These values were the maximum swelling pressure if no free swelling was allowed. However, in practical applications, free swelling can occur to some extent and thus, the swelling pressure would reduce accordingly.

CHAPTER FIVE

5 STRESS-STRAIN BEHAVIOUR OF CW-SFS MIXTURES

5.1 INTRODUCTION

In Chapter 4, the preliminary geotechnical characteristics of CW-SFS mixtures were discussed and it was shown that particular mixtures were suitable to be used as structural fill in terms of permeability, load bearing capacity (i.e. CBR and UCS), and particle degradation. However, the detailed shear strength properties were not considered. To investigate in detail the stress-strain and volumetric behaviour of the mixtures, an extensive triaxial testing program was carried out on these materials.

In this chapter, the behaviour of mixtures of coal wash and steel furnace slag was studied, where the content of coal wash ranged from 0% (i.e., pure steel furnace slag) to 100% (i.e., pure coal wash). Different mixtures of 0/100, 75/25, 50/50, 25/75, 100/0 (percentage of CW/SFS based on their oven-dried weight) were tested under drained triaxial condition to evaluate their long term shear behaviour. The preliminary studies indicated that the permeability of these mixtures was high enough such that under port loading conditions a drained state could be maintained (Chiaro *et al.*, 2014b). The main purpose of the study on stress-strain behaviour of CW-SFS mixtures was to obtain parameters for analytical and numerical modelling. In addition, the effects of the confining pressure and percentage of coal wash on the mechanical behaviour of CW-SFS mixtures such as the stress-strain and volumetric strain behaviour, strength envelopes, critical state lines, isotropic compression lines, dilatancy behaviour, and particle breakage were evaluated. Finally, an analytical model based on the generalised plasticity was proposed in order to simulate the behaviour of CW-SFS mixture.

5.2 ISOTROPIC COMPRESSION BEHAVIOUR

The isotropic compression behaviour of CW-SFS was investigated through five tests on the mixtures to establish the isotropic compression line (ICL). For all cases except CW50-SFS50, the specimens were isotropically consolidated to a mean effective stress of 1.3MPa, which is considered to cover the confining pressure under port conditions and to reach the yield or past stress induced by compaction. To evaluate the elastic parameters of the CW-SFS mixtures, an unloading-reloading stage was carried out. For every increment of confining pressure, the specimen was allowed to consolidate until no further significant volume change or pore pressure change was observed. Specimens were prepared using the split mould method as discussed in Chapter 3. The list of tests discussed hereafter is given in Table 5.1.

Table 5.1 List of isotropic compression test on CW-SFS mixtures

Mixture	G_s	Dry unit weight, γ_d (kN/m^3)	Initial specific volume v_0	Degree of compaction (%)
CW0-SFS100	3.34	20.47	1.600	90.2
CW25-SFS75	3.01	18.81	1.569	90.3
CW50-SFS50	2.73	17.60	1.521	90.2
CW75-SFS25	2.51	16.44	1.498	90.3
CW100-SFS0	2.27	15.24	1.460	90.2

The results of the isotropic compression test on five mixtures are plotted in Figure 5.1. Although all the mixtures were prepared to the same degree of compaction (i.e. 90% $\gamma_{d,max}$ for each mixture), the initial specific volume (v_0) varied in different mixtures due to the variation of G_s (see Table 5.1). The ICLs for the mixtures were highly nonlinear in contrast to the conventional soils such as clays and the nonlinearity behaviour increased as SFS content increased in the mixtures. Figure 5.1 also shows that although the initial specific volume for the mixtures with higher CW content was smaller, the change in specific volume was more significant. This implies that the CW particles are more deformable and part of this deformation is associated with the particle degradation. The particle breakage analysis after isotropic compression test is shown in Figure 5.2. For comparison, the breakage after

specimen preparation (due to compaction) is also plotted. Figure 5.2 shows the effect of CW content on the breakage, and it is evident that the increase in CW content results in more breakage. For the specimen with more than 50% coal wash, the breakage index increased significantly and thus, the deformation under isotropic loading was larger for these blends (Figure 5.1).

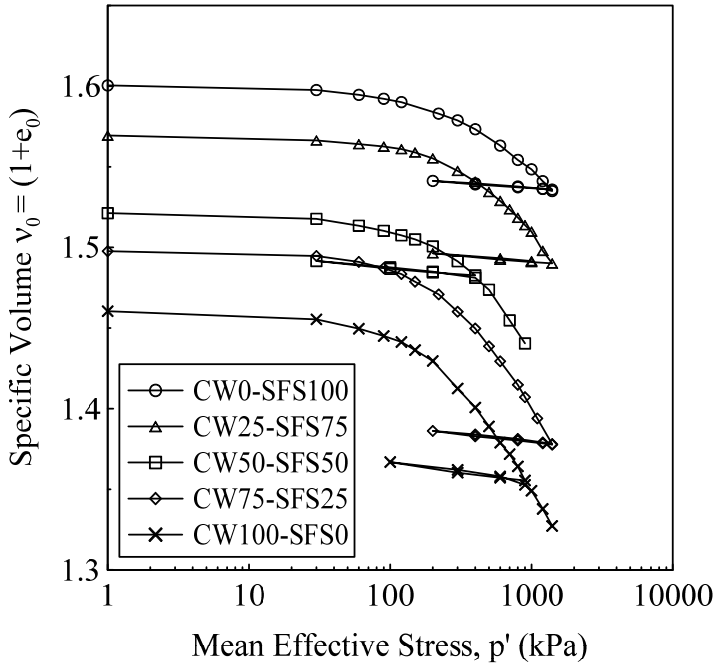

Figure 5.1 Isotropic compression test on CW-SFS mixtures

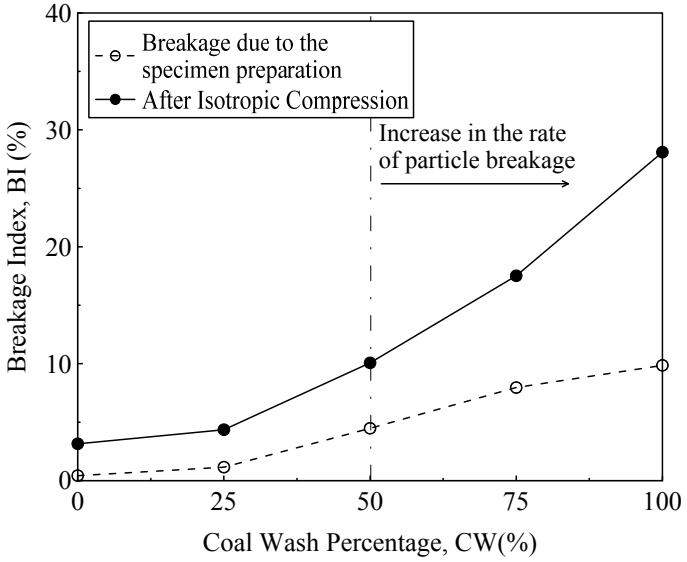

Figure 5.2 Effect of CW content on the breakage index in isotropic compression test

For a better comparison among the ICL of different mixtures, the results can be normalised to the initial specific volume of each mixture, as shown in Figure 5.3. Each mixture experienced three distinct stages of deformation: the initial elastic region (Region 1) where the change in specific volume over the pressure was very small, the second region where compression gradually increased with the applied stress (Region 2), and the 3rd stage in Region 3, which is beyond the yield point where there was a significant change in the specific volume under increasing mean effective stress. In region 2 the Equivalent Past Stress (p^*) can be determined using the Casagrande method (Casagrande, 1936), and the values of p^* are shown in Figure 5.4. Although all the mixtures were prepared under the same compaction energy, the equivalent past stress (p^*) decreased significantly with the increase in CW content (i.e. from 850kPa for CW0-SFS100 to 250kPa for CW100-SFS0). This can be attributed to relatively weak particles of CW and their inevitable breakage. In Region 3, the slope of the isotropic compression line (ICL) can be determined (i.e. λ_{ICL}) . The values of N (the specific volume corresponding to p'=1kPa), λ_{ICL} (slope of isotropic compression line), κ (unloading-reloading slope), and p^* (equivalent past stress) are listed in Table 5.2. The results of ICL on the CW-SFS mixtures indicated that the amount and rate of compression increased as the percentage of CW increased, even though the initial void ratio of this mixture with a higher CW content was actually smaller. This could be attributed to the breakage of CW particles at the same mean effective stress.

It was identified that by normalising the value of the mean effective stress to p^* for each mixture, the results of ICL for all the mixtures followed a unique trend; these results are illustrated in Figure 5.4. Therefore, the ICL of different mixtures can be predicted using the following empirical bilinear equations:

$$\frac{v}{v_0} = 1 - 0.026\frac{p'}{p^*} \qquad for\ \frac{p'}{p^*} < 1.5 \qquad \left(R^2 > 0.96\right) \tag{5.1}$$

$$\frac{v}{v_0} = 0.98 - 0.016\frac{p'}{p^*} \qquad for\ \frac{p'}{p^*} > 1.5 \qquad \left(R^2 > 0.96\right) \tag{5.2}$$

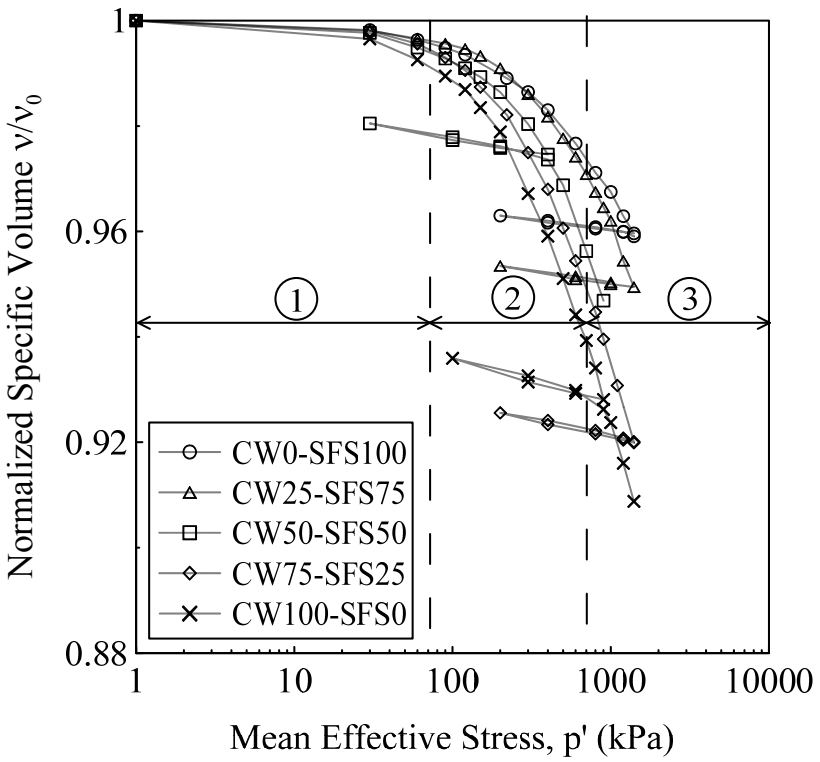

Figure 5.3 ICL for all CW-SFS mixtures (the vertical axis was normalised to the initial specific volume of each mixture for a better comparison)

Table 5.2 Summary of isotropic compression parameters for CW-SFS mixtures

Material	N	λ_{ICL}	κ	p^* (kPa)
CW0-SFS100	1.789	0.019	0.0027	850
CW25-SFS75	1.869	0.058	0.0031	630
CW50-SFS50	1.870	0.065	0.0034	400
CW75-SFS25	1.864	0.0067	0.0045	350
CW100-SFS0	1.737	0.056	0.0050	250

N = specific volume corresponding to p'=1kPa; λ_{ICL} = slope of isotropic compression line; κ = unloading-reloading slope; and p^* = equivalent past stress

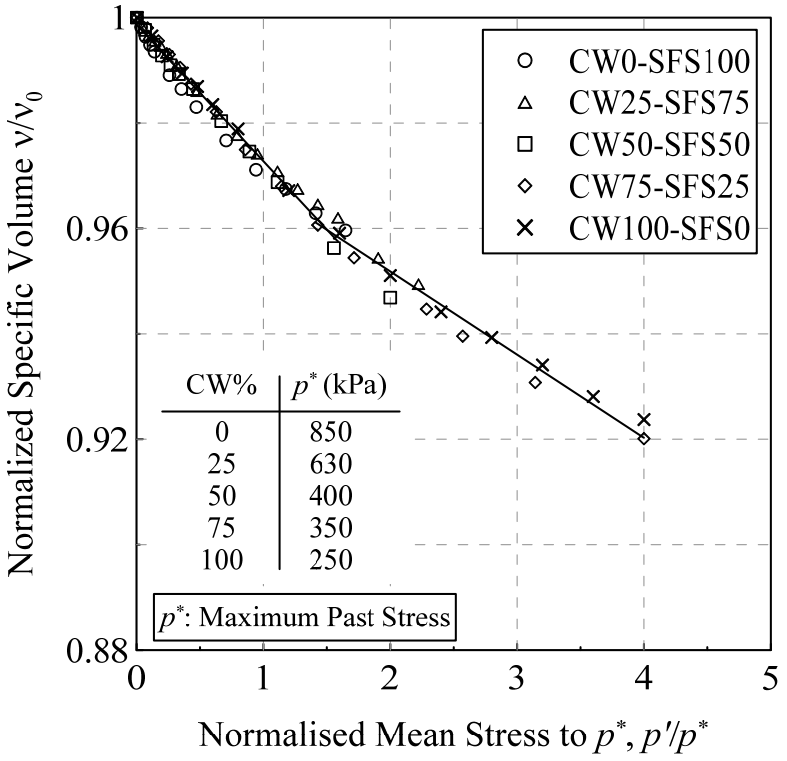

Figure 5.4 Results of isotropic compression test for all CW-SFS mixtures in double normalisation space (v/v_0-p'/p^*)

5.3 TRIAXIAL COMPRESSION

5.3.1 Stress-strain behaviour

To assess the stress-strain and volumetric strain behaviour of CW-SFS mixtures, a series of consolidated isotropically drained (CID) triaxial tests were conducted on five blends. The specimen preparation, saturation, consolidation, and shearing were outlined in detail in Chapter 3. The specimens were consolidated to four different effective confining pressures (30, 60, 120, and 220kPa) to mimic port loading conditions and then sheared under drained conditions. As a result of these tests, the effect of coal wash content and confining pressure were evaluated. Table 5.3 presents a summary of the CID triaxial test, including the peak deviatoric stress (q_{peak}), the peak effective mean stress (p'_{peak}), and the peak friction angle (ϕ'_p). The results of the drained triaxial tests in terms of deviatoric stress-strain, volumetric strain, stress path,

and critical state line (CSL) for CW0-SFS100, CW25-SFS75, CW50-SFS50, CW75-SFS25, and CW100-SFS0 blends are plotted in Figure 5.5 to Figure 5.9.

As expected, by increasing the effective confining pressure from 30kPa to 220kPa, the peak deviatoric stress (q_{peak}), the axial strain at q_{peak}, the amount of volumetric contraction, and the initial deformation modulus increased correspondingly. Under low confining pressures (i.e. 30kPa and 60kPa), the volumetric responses of the mixture initially indicated a small contraction followed by volumetric dilation, and the peak deviatoric stress occurred at maximum dilation. In contrast, at higher effective confining pressures there was only contractive behaviour, which means that the dilative and contractive behaviour of any mixture depends on the initial void ratio and confining pressure (i.e. the location of initial conditions compared to the CSL) (Roscoe *et al.*, 1963, Rowe, 1962, Been and Jefferies, 1985). For those specimens on the dry side of CSL, a dilative behaviour and strain-softening was observed, and for the specimens on the wet side of CSL, there was volumetric contraction and corresponding strain hardening. This behaviour was similar to that reported by a number of previous studies on the behaviour of granular material, for instance, reported by Indraratna *et al.*, (1998) and Modoni and Gazzellone (2011).

The only mixture which showed dilative behaviour, even under high confining pressure (i.e. 220kPa), was CW0-SFS100. This can be explained by referring to Table 5.2 and the value of equivalent past stress (p^*) which is 850kPa. This implies that for the specimen consolidated to 220kPa confining pressure, it is still far below p^*. Furthermore, it is evident in Figure 5.5d that the initial state (i.e. specific volume and confining pressure) for this specimen is on the dry side of CSL, and therefore, the dilative behaviour and post-peak strain softening are to be expected.

Table 5.3 Summary of the peak state for drained triaxial tests

Mixture	Initial conditions		Peak state			
	σ'_3 (kPa)	v_0	p'_{peak} (kPa)	q_{peak} (kPa)	ϕ'_p (˚)	$(q/p')_{peak}$ (-)
CW0-SFS100	30	1.596	98	191	47.9	1.95
	60	1.597	167	314	46	1.88
	120	1.587	293	510	42.7	1.74
	220	1.577	453	741	41.1	1.63
CW25-SFS75	30	1.568	89	170	46.8	1.91
	60	1.565	158	291	44.8	1.84
	120	1.560	250	393	38.6	1.57
	220	1.546	447	681	37.5	1.52
CW50-SFS50	30	1.517	78	141	44.1	1.81
	60	1.515	147	261	43.2	1.77
	120	1.504	242	367	37.4	1.52
	220	1.495	440	660	37	1.50
CW75-SFS25	30	1.499	72	130	43.9	1.81
	60	1.493	142	246	42.4	1.73
	120	1.481	242	367	37.4	1.52
	220	1.470	436	650	36.8	1.49
CW100-SFS0	30	1.451	73	124	43.5	1.70
	60	1.451	124	192	38.2	1.55
	120	1.439	242	348	35.6	1.44
	220	1.424	433	622	35.6	1.44

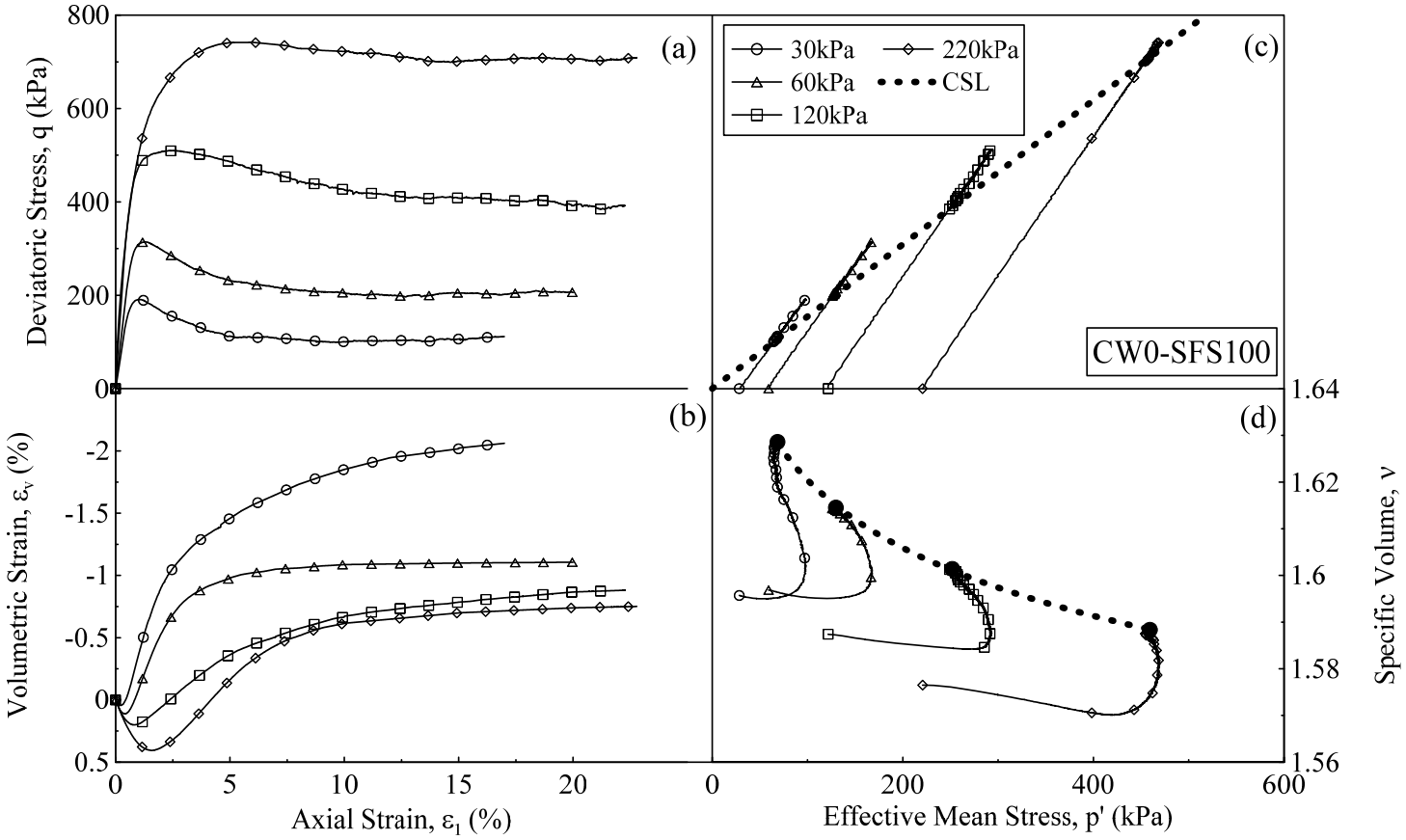

Figure 5.5 Triaxial test on CW0-SFS100 under four confining pressures in terms of (a) stress-strain (b) volumetric behaviour (c) stress path in *q-p′* space, and (d) stress path in *v-p′* space

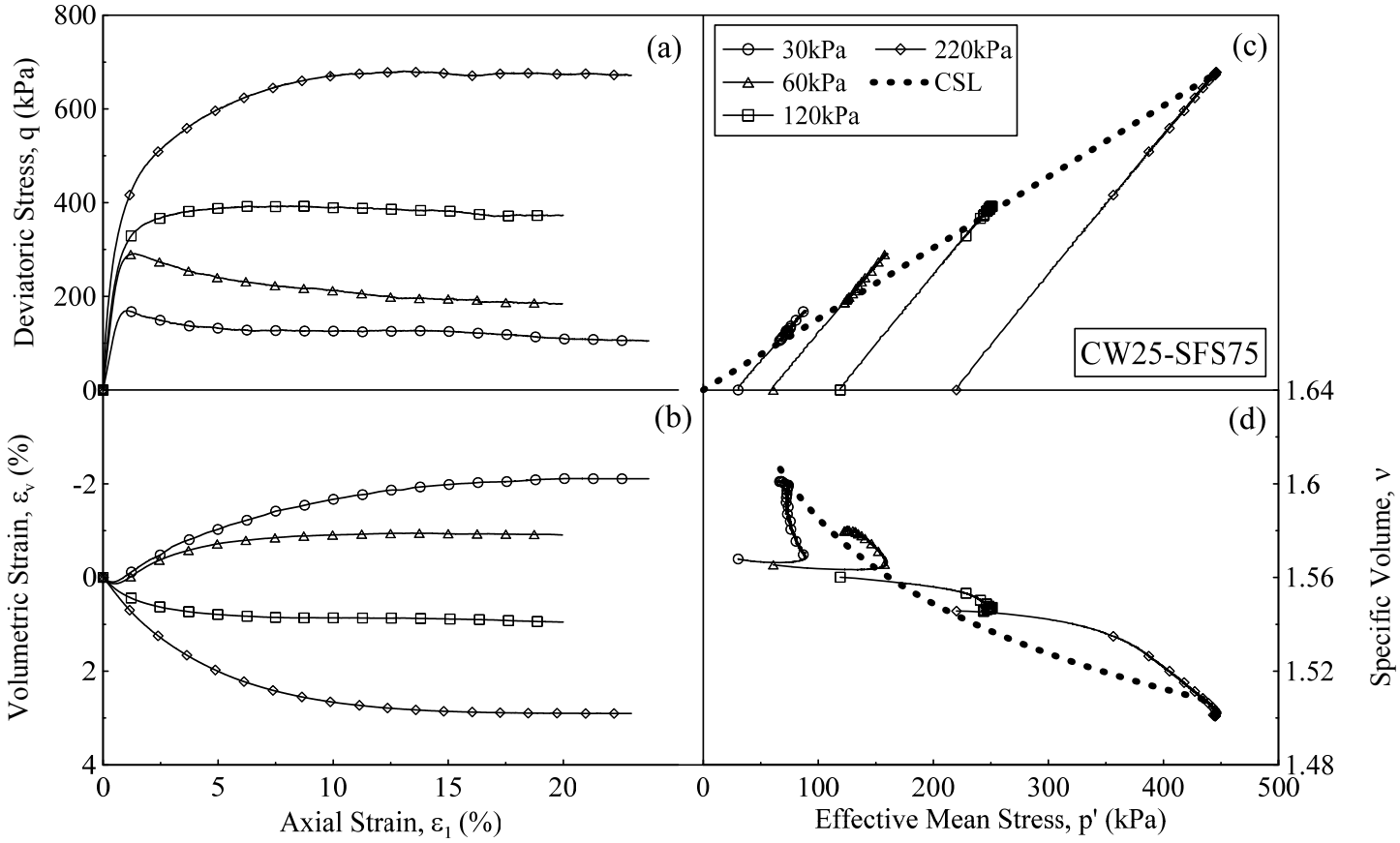

Figure 5.6 Triaxial test on CW25-SFS75 under four confining pressures in terms of (a) stress-strain (b) volumetric behaviour (c) stress path in *q-p′* space, and (d) stress path in *v-p′* space

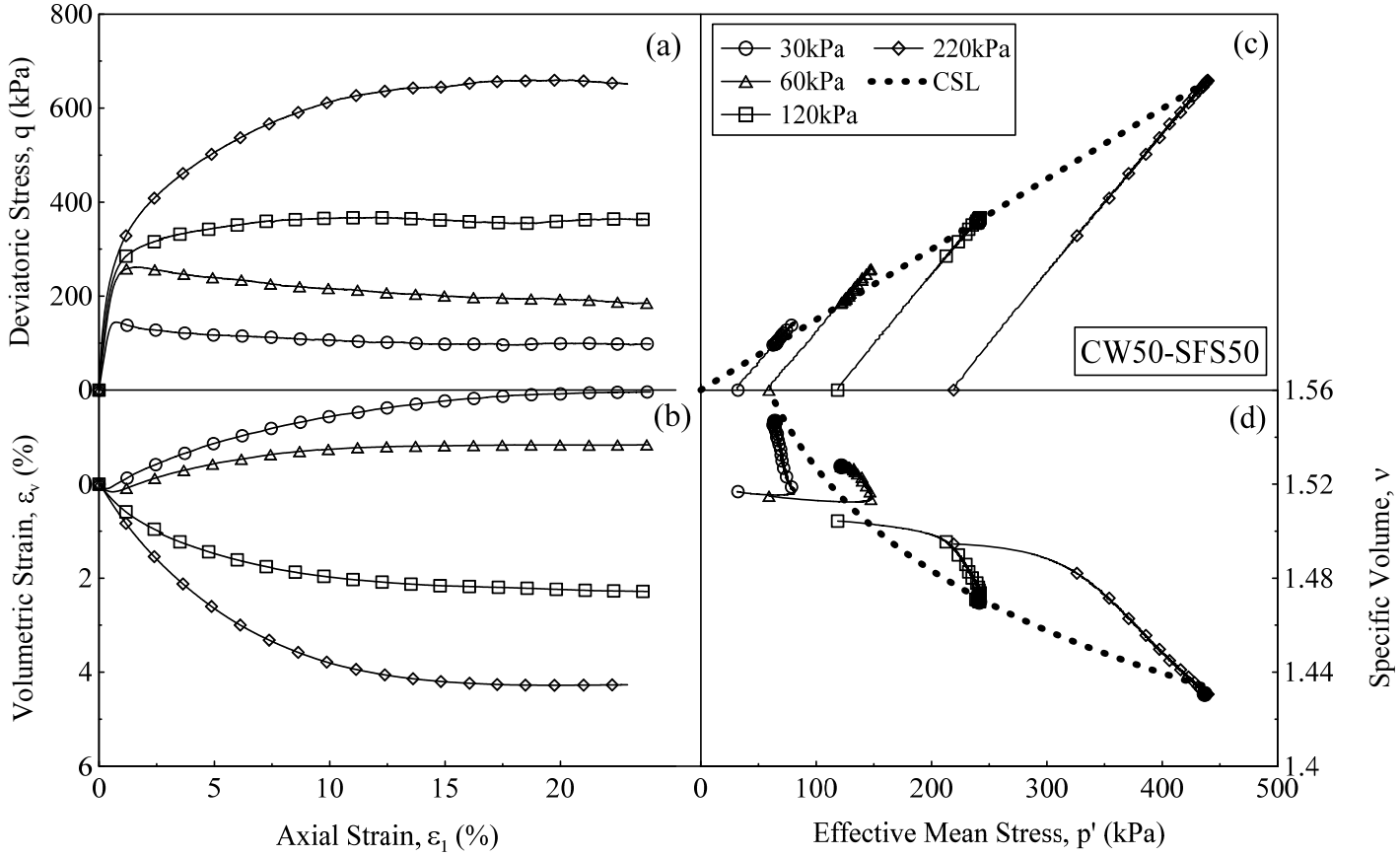

Figure 5.7 Triaxial test on CW50-SFS50 under four confining pressures in terms of (a) stress-strain (b) volumetric behaviour (c) stress path in *q-p′* space, and (d) stress path in *v-p′* space

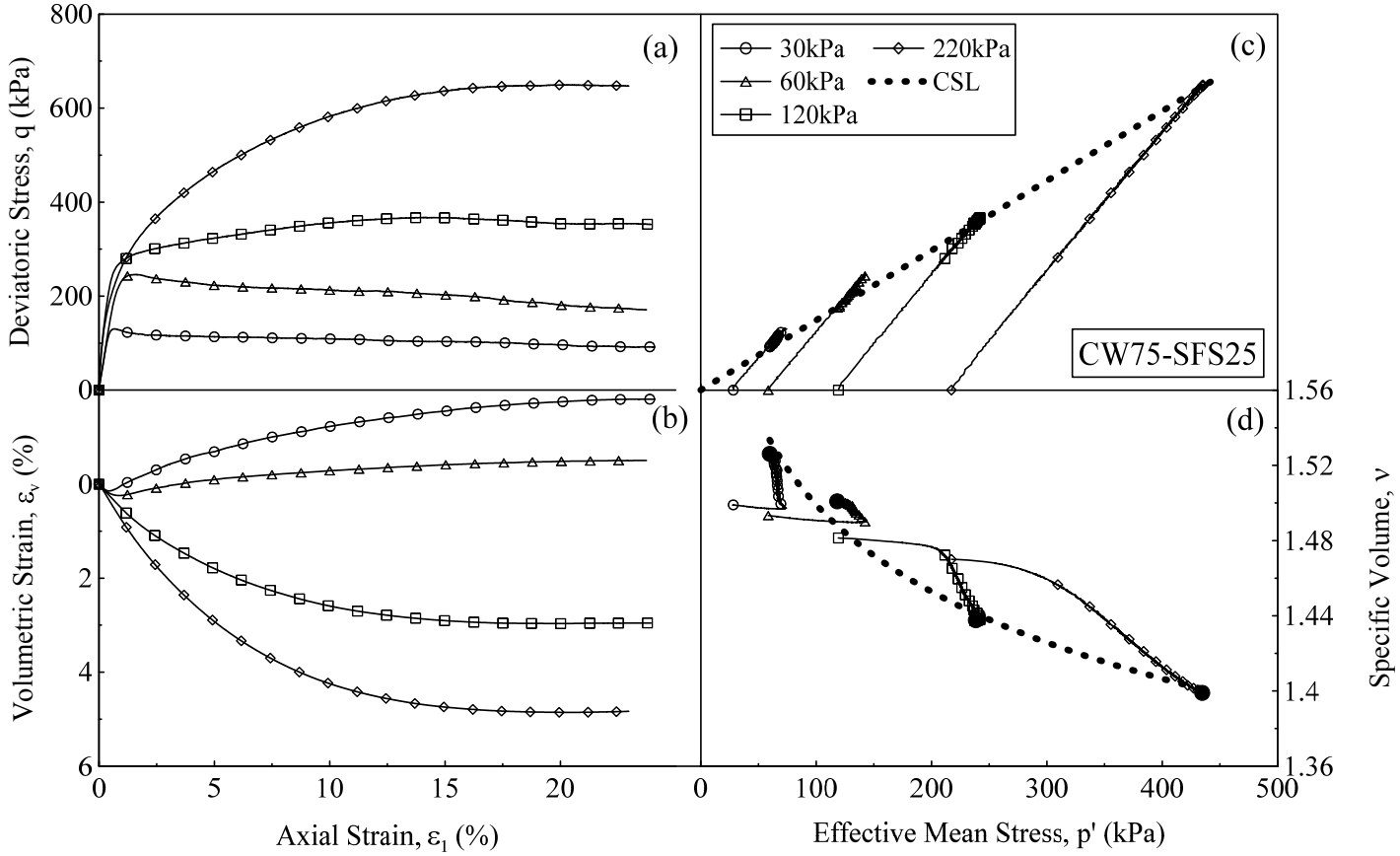

Figure 5.8 Triaxial test on CW75-SFS25 under four confining pressures in terms of (a) stress-strain (b) volumetric behaviour (c) stress path in *q-p′* space, and (d) stress path in *v-p′* space

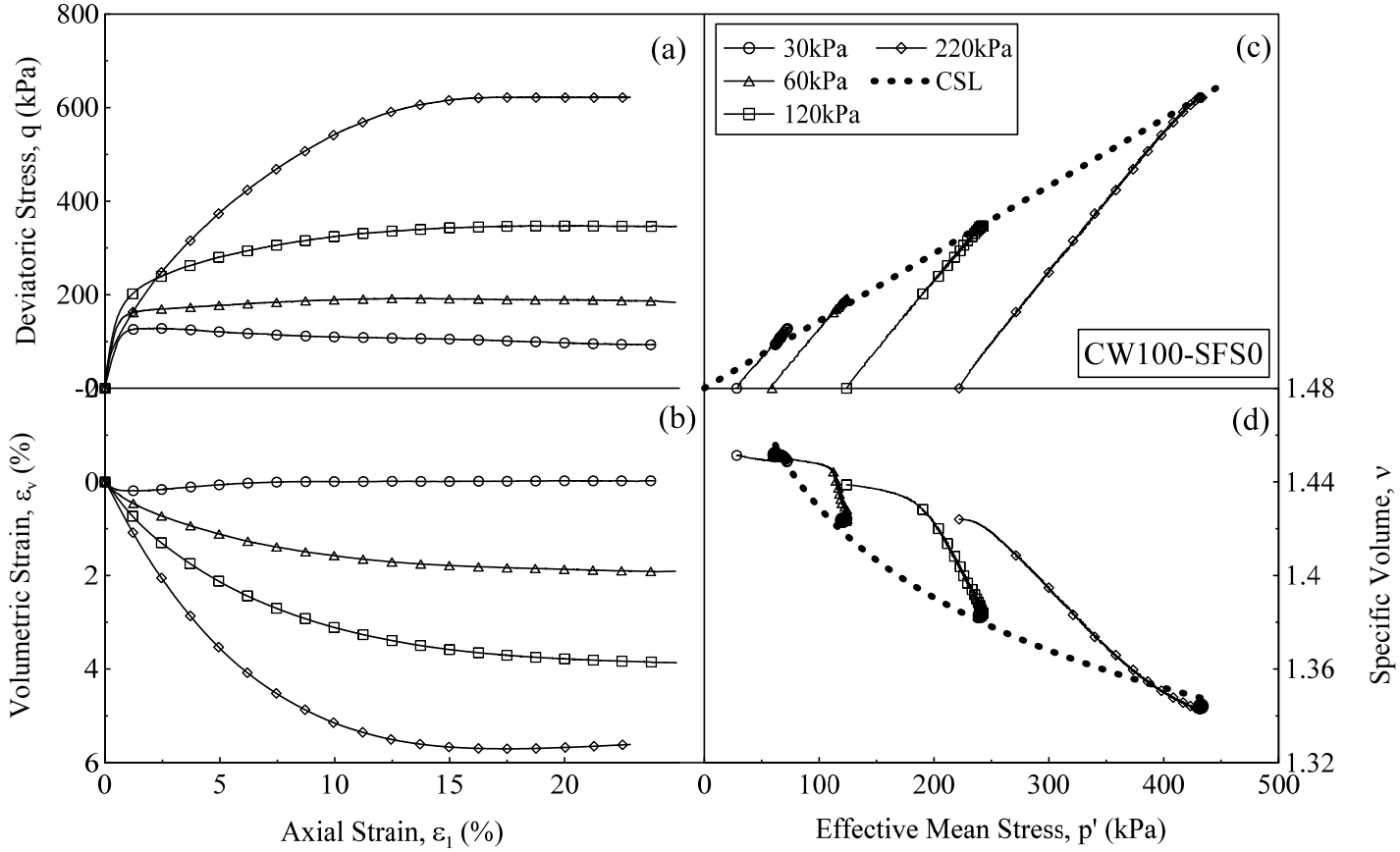

Figure 5.9 Triaxial test on CW100-SFS0 under four confining pressures in terms of (a) stress-strain (b) volumetric behaviour (c) stress path in *q-p′* space, and (d) stress path in *v-p′* space

The effect of CW content on the stress-strain response can be analysed by comparing the results of all mixtures sheared under the same confining pressure, and these results are shown in Figure 5.10. It was evident that the CW content had a significant influence on the shear behaviour. Once the percentage of CW increased, the peak deviatoric stress decreased, and the specimen generally showed a higher volumetric strain. Furthermore, the initial deformation modulus also decreased in mixtures having a higher percentage of CW, such that the increased amount of CW changed the stress-strain response of CW-SFS mixtures from brittle to ductile. CW0-SFS100 always showed a higher deviatoric stress than the other mixtures, but at a larger axial strain (>15%) this difference was marginal. Under 30kPa of effective confining pressure, all the mixtures exhibited a distinct peak and post-peak strain-softening, whereas under 120kPa, only the CW0-SFS100 showed a similar trend, while there was a strain-hardening response in all the remaining mixtures. The ε_v-ε_1 curves plotted in Figure 5.10 also show that an increasing the percentage of CW also increases the volumetric contraction for a given effective confining pressure. However, the effect of CW on the volumetric strain diminished at higher effective confining pressure, where all the mixtures except CW0-SFS100 exhibited contractive behaviour. The significant contraction of CW100-SFS0 can be attributed to the increased breakage in CW particles compared to the SFS particles. The degradation of CW-SFS mixtures with a breakage analysis will be discussed later.

It is evident from Figure 5.10 that the concept of a critical state can be applied to CW-SFS mixtures, because the deviatoric stress and the change in volume for all the mixtures of CW-SFS approached an almost constant value at the end of each test (for an axial strain larger than 20%). In Figure 5.11, the stress paths in v-lnp' space are plotted such that the solid points represent the values of v and p' at the end of tests. It is evident that a higher percentage of CW increased the slope of the critical state line (λ_{CSL}), but there was insignificant change in λ_{CSL} for those mixtures containing more than 50% coal wash. The critical state parameters for CW-SFS mixtures are summarised in Table 5.4. Figure 5.11 clearly shows a dilative behaviour of the specimens which were initially below the CSL and volumetric contraction for those above the CSL.

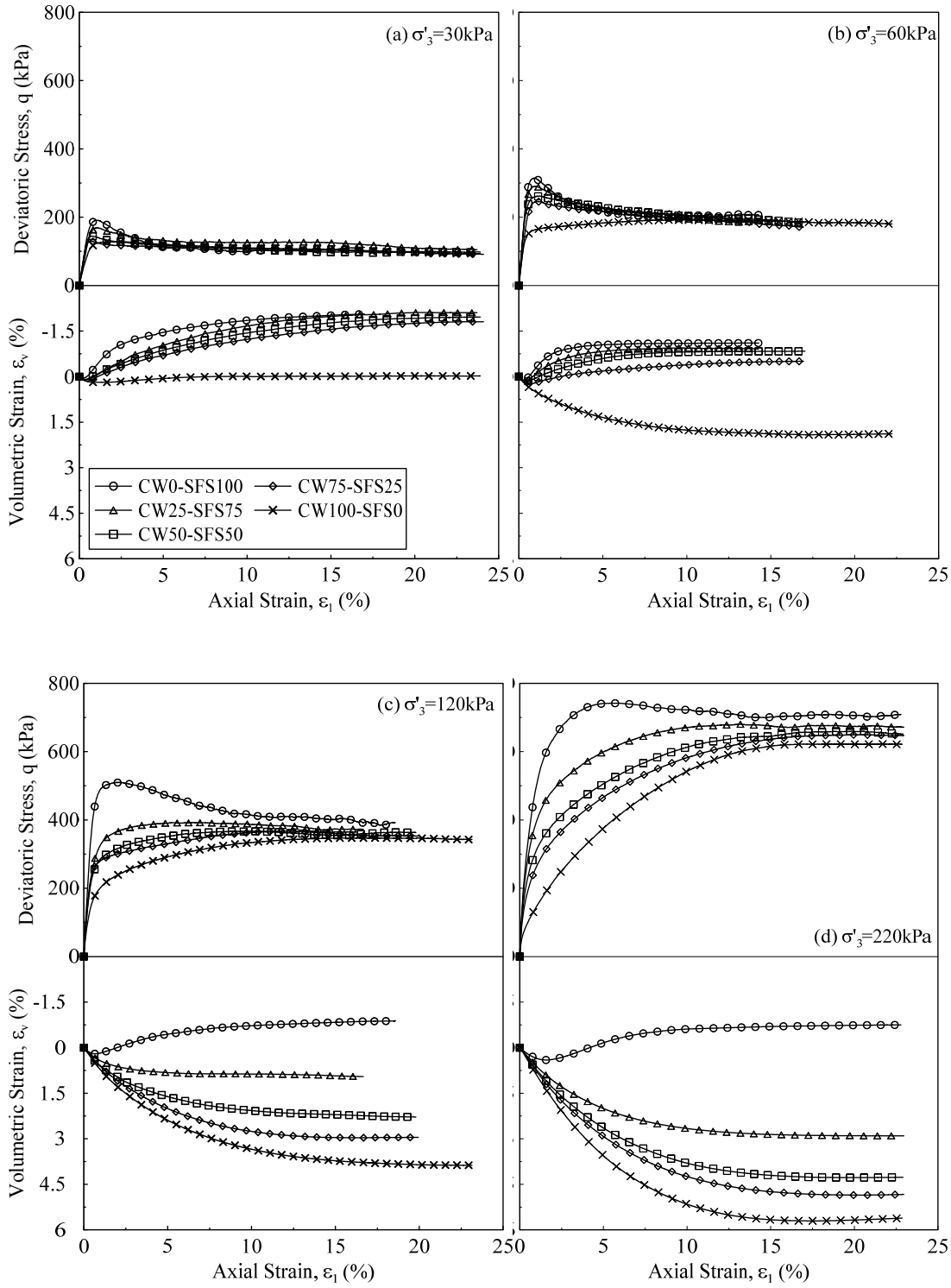

Figure 5.10 Stress-strain behaviour of CW-SFS mixtures during drained triaxial shearing at confining pressures of (a) 30kPa, (b) 60kPa, (c) 120kPa, and (d) 220kPa

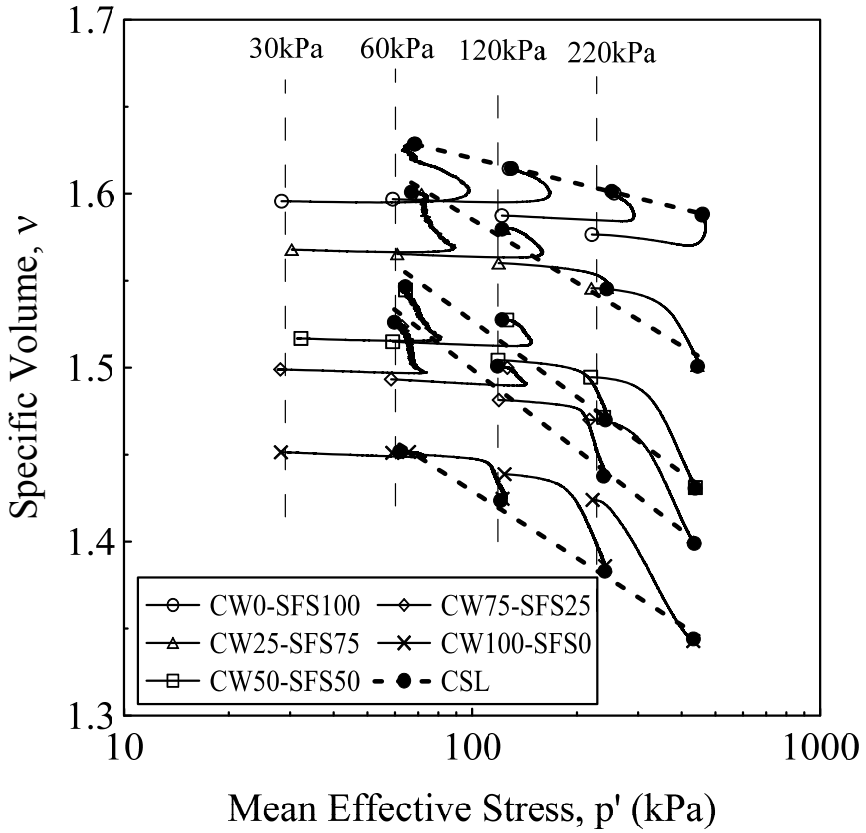

Figure 5.11 Stress path and the location of CSL in *v-lnp′* space

Table 5.4 Summary of the critical state line parameters of CW-SFS mixtures

Material	Γ	λ_{CSL}	M
CW0-SFS100	1.709	0.019	1.545
CW25-SFS75	1.827	0.052	1.517
CW50-SFS50	1.817	0.063	1.496
CW75-SFS25	1.808	0.067	1.485
CW100-SFS0	1.685	0.056	1.439

Γ = specific volume corresponding to p'=1kPa on CSL; λ_{CSL} = slope of CSL in *v-lnp′* space; and M = slope of CSL in *q-p′* space

Figure 5.12 illustrates the volumetric strain at the critical state against the effective confining pressure for all the CW-SFS mixtures. As expected, under low effective

confining pressure, volumetric dilation occurred during shearing and once the effective confining pressure increased, the mixtures showed volumetric contraction at a decreasing rate. Under a given effective confining pressure those mixtures with a higher percentage of CW exhibited more contraction partly due to particle breakage during shearing. In the range of 50-100kPa effective confining pressure, the mixtures CW75-SFS25, CW50-SFS50, and CW25-SFS75 showed no change in volume at the end of the test; in fact, the only mixture that showed dilation, even at a high effective confining pressure (220kPa), was CW0-SFS100.

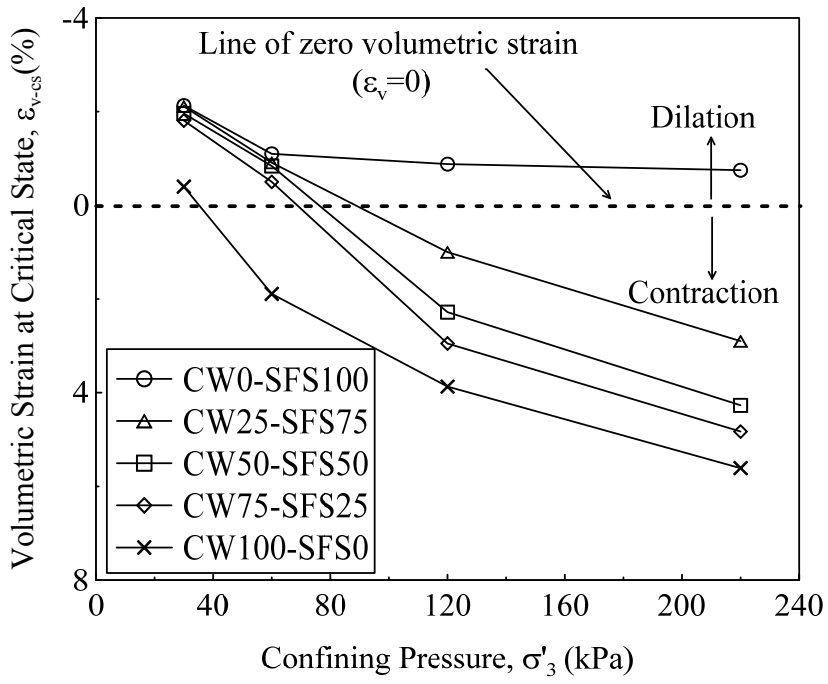

Figure 5.12 Variation of volumetric strain at critical state over confining pressure for all CW-SFS mixtures under four confining pressures

5.3.2 Shear strength characteristics

Since both CW and SFS are granular materials, their shear behaviour was mainly influenced by the peak friction angle (ϕ_p) and the effective confining pressure. Figure 5.13 illustrates Mohr-Coulomb circles for all CW-SFS mixtures sheared at four confining pressures and shows nonlinear envelopes. The peak friction angle can be determined by the gradient of the envelope and as expected, larger friction angles

were observed for the specimens sheared at lower confining pressures due to the dilation. The variations of peak friction angle (ϕ_p) against the effective confining pressure for CW-SFS mixtures are shown in Figure 5.14. All the CW-SFS mixtures showed a nonlinear relationship between ϕ_p and σ'_3. This is in agreement with past studies on granular materials, as reported by Indraratna *et al.*, 2013b. The peak friction angle increased with the SFS content but diminished as σ'_3 increased. Under low σ'_3 the volumetric behaviour of the CW-SFS mixtures was dilative, so ϕ_p was greater than the critical state friction angle (ϕ_{cs}). It was expected that ϕ_p would approach ϕ_{cs} at a higher confining pressure where dilation was absent. Figure 5.14 also shows that the difference of ϕ_p between the mixtures with a higher percentage of SFS and those with less SFS was large under smaller values of σ'_3 (<120kPa), and this difference decreased significantly once σ'_3 increased. This means that the influence of SFS percentage on ϕ_p was greater at low confining pressures, and this influence was less pronounced when σ'_3 increased.

Figure 5.15 shows the peak deviatoric stress and peak mean effective stress with confining pressure. As expected, the q_{peak} and p'_{peak} increased with the effective confining pressure and the content of SFS; both q_{peak} and p'_{peak} showed a nonlinear relationship with the effective confining pressure, and the slope of these curves decreased when the effective confining pressure increased. This implies that the influence of SFS on the shear behaviour was suppressed at higher effective confining pressures.

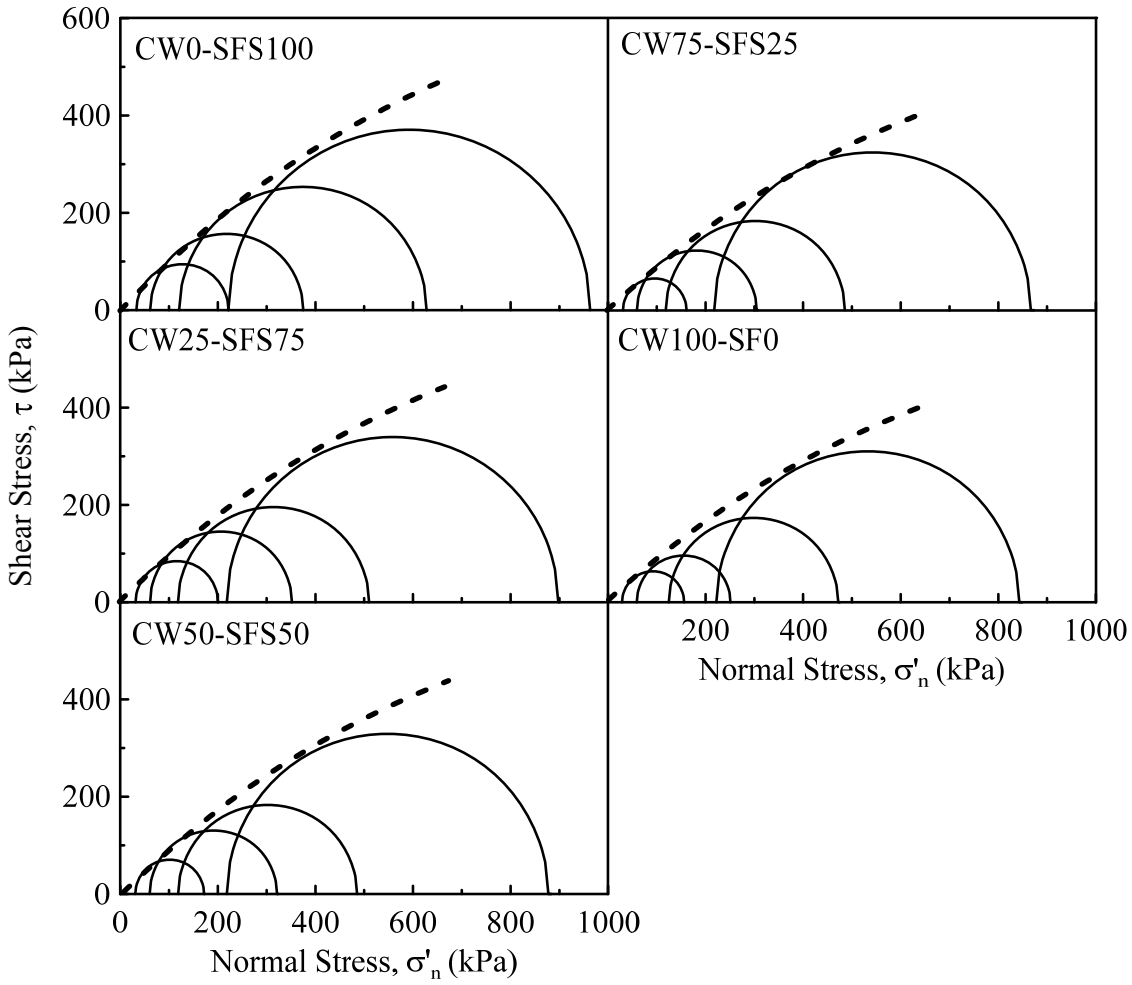

Figure 5.13 Nonlinear Mohr-Coulomb strength envelopes for CW-SFS mixtures

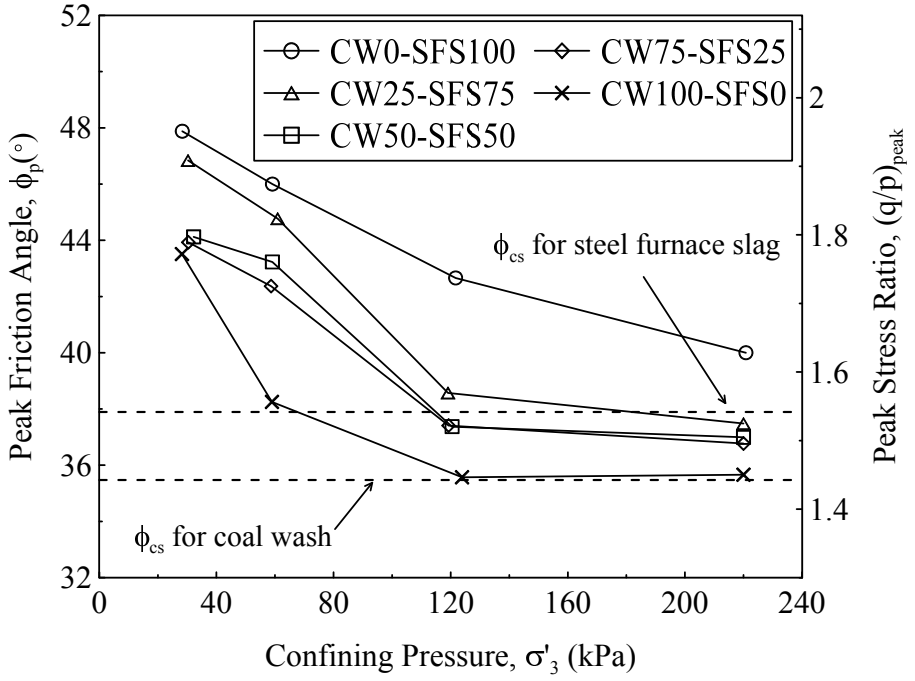

Figure 5.14 Variation of peak friction angle and peak stress ratio against confining pressure for CW-SFS mixtures under drained triaxial condition

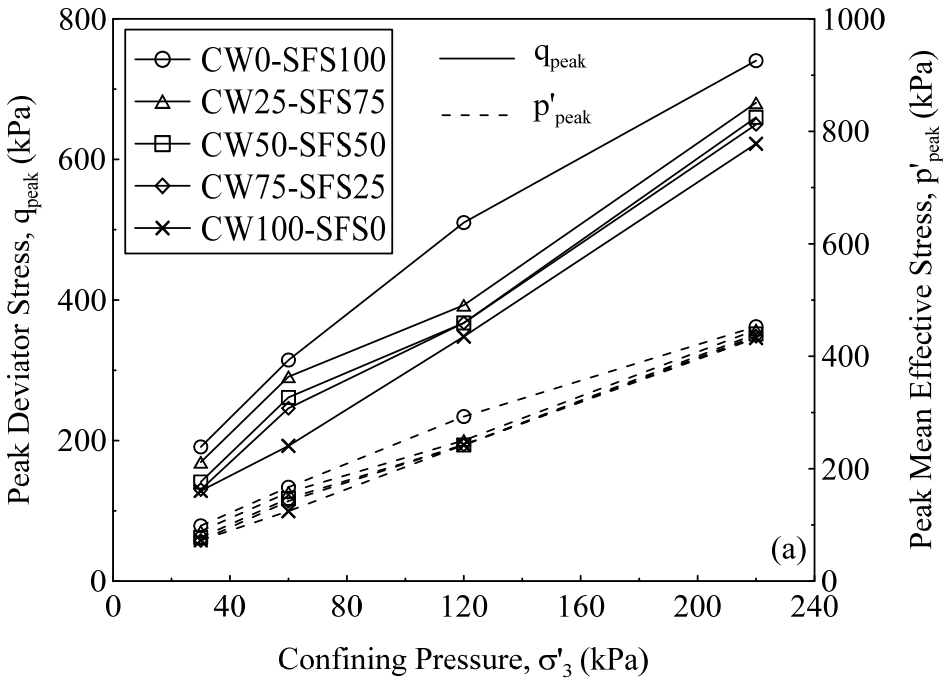

Figure 5.15 Effect of confining pressure on the peak deviatoric and peak effective mean stress with nonlinear shear envelopes

An empirical equation based on the above observations to predict the q_{peak} and p'_{peak} for the CW-SFS mixtures compacted at 90% $\gamma_{d,max}$ can be expressed by:

$$q_{peak} = a(\sigma'_3)^b \tag{5.3}$$

$$p'_{peak} = m(\sigma'_3)^n \tag{5.4}$$

where a, b, m and n are empirical coefficients that depend on the percentage of CW, and they were defined by the curve fitting for the experimental results on the materials tested in this study. It is important to mention that due to some variation of the properties of CW and SFS, these coefficients might be altered depending on the source materials. These coefficients can be determined by the following expressions:

$$a = 18.8e^{-0.009\alpha} \qquad \left(R^2 > 0.94\right) \tag{5.5}$$

$$b = 10\alpha + 0.67 \qquad \left(R^2 > 0.98\right) \tag{5.6}$$

$$m = 7e^{-0.008\alpha} \qquad \left(R^2 > 0.96\right) \tag{5.7}$$

$$n = 0.0014\alpha + 0.77 \qquad \left(R^2 > 0.96\right) \tag{5.8}$$

where α is the value of CW content expressed in percentage.

The shear strength envelopes of CW-SFS mixtures can be characterised quite well in terms of the peak stress ratio $(q/p)_{peak}$ to the corresponding confining pressure (Figure 5.14). The following non-linear relationship can be derived using Eqs 5.3 and 5.4 for the shear strength envelopes of CW-SFS mixtures.

$$\left(\frac{q}{p'}\right)_{peak} = \frac{a}{m}(\sigma'_3)^{b-n} \quad but \quad n << b \;\Rightarrow\; \left(\frac{q}{p'}\right)_{peak} = \frac{a}{m}(\sigma'_3)^b \tag{5.9}$$

The results of this study indicated that the peak stress ratio increased as the CW percentage in the mixture decreased. The observed increase in $(q/p)_{peak}$ could be attributed to the greater inter-particle friction angle and interlocking SFS particles.

5.3.3 Deformation characteristics

The deformation properties of a material consist of elastic and plastic. The elastic part is recoverable upon the removal of the load and the plastic is the permanent deformation. The elastic deformation properties are described by Young's modulus (E), shear modulus (G), and Poisson's ratio (v). Two of these parameters are sufficient, as the third one can be calculated using Equation (5.10). Both E and G can be identified in two methods, one known as 'tangent modulus', which is the slope of stress-strain curve at a point, and the other one is 'secant modulus', which is defined as the ratio of deviatoric stress to the corresponding strain. These elastic parameters are state-dependent (i.e. initial density and confining pressure).

$$G = \frac{E}{2(1+\nu)} \tag{5.10}$$

The variations of initial deformation modulus (E_i) and initial Poisson's ratio (v_i) over confining pressures for all CW-SFS mixtures are presented in Figure 5.16. An axial strain smaller than 1% was used to determine E_i and v_i. For a given confining pressure, increasing CW% in the mixture reduces both E_i and v_i. This might be attributed to greater ductility of CW. On the other hand, E_i increases with the confining pressure in a decreasing rate. For higher confining pressures, the change in E_i and v_i is insignificant.

Variations of secant deformation modulus (E_{sec}) and secant shear modulus (G_{sec}) with shear strain for CW-SFS mixtures under four confining pressures are presented in Figure 5.17 and Figure 5.18, respectively. The contours of shear strains corresponding to three levels of peak stress (e.g. $0.25q_{peak}$, $0.5q_{peak}$, and $0.75q_{peak}$) are also plotted as dashed lines. It was observed that the addition of a small amount of SFS in the mixture influenced significantly the G_{sec} (e.g., secant shear modulus results corresponding to 0.5% axial strain under 120kPa confining pressure were around 11MPa and 18MPa for CW100-SFS0 and CW75-S25, respectively). Under low confining pressures (less than 60kPa), a region where secant shear modulus was constant could be defined (range of 0.1% to 0.4% strain). In this region the behaviour

of CW-SFS mixtures was observed to be almost linear elastic. However, beyond this region the nonlinear behaviour of CW-SFS was clearly visible. The shear strain corresponding to $0.25q_{peak}$ under four confining pressures was constant for all mixtures except CW100-SFS0. This implies that the deformation to mobilize 25% of peak strength is relatively independent of the confining pressure. Figure 5.18 also shows that the shear strain corresponding to any levels of shear stress (under any given confining pressure) increased once the CW percentage increased in the mixture. This specifies that more deformation is expected for mixtures with higher CW percentage under any given loading.

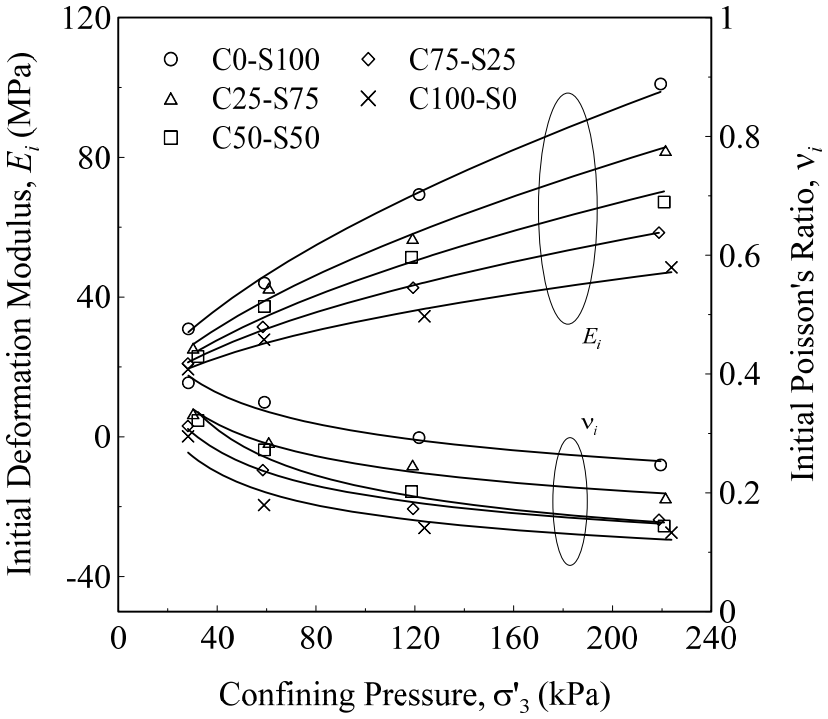

Figure 5.16 Influence of confining pressure on the initial deformation modulus (E_i) and initial Poisson's ratio (ν_i)

Table 5.5 Summary of elastic parameters of CW-SFS mixtures in isotropically drained triaxial shearing

Material	σ'_3 (kPa)	e_0	E_i (MPa)	G_i (MPa)	v_i
CW0-SFS100	28.3	0.596	30.9	11.1	0.38
	59.1	0.597	44.0	16.2	0.35
	121.7	0.587	69.4	26.8	0.29
	219.5	0.557	101.0	40.5	0.24
CW25-SFS75	30.3	0.568	25.4	9.5	0.33
	60.9	0.565	42.6	16.5	0.28
	119.1	0.560	56.8	22.8	0.24
	221.5	0.546	82.0	34.4	0.19
CW50-SFS50	32.2	0.517	23.0	8.7	0.32
	59.1	0.515	37.3	14. 7	0.27
	118.6	0.504	51.4	21.4	0.20
	220.9	0.495	67.2	29.4	0.14
CW75-SFS25	28.1	0.499	21.0	8.0	0.31
	58.5	0.493	31.4	12.7	0.23
	119.3	0.481	42.7	18.2	0.17
	217.2	0.470	58.5	25.3	0.15
CW100-SFS0	28.2	0.451	19.3	7.5	0.29
	59.0	0.451	27.8	11.8	0.17
	123.9	0.439	34.5	15.12	0.14
	221.8	0.424	48.5	21.4	0.13

σ'_3 = effective confining pressure; e_0 = initial void ratio (after consolidation); E_i = initial deformation modulus; G_i = initial shear modulus and v_i = initial Poisson's ratio

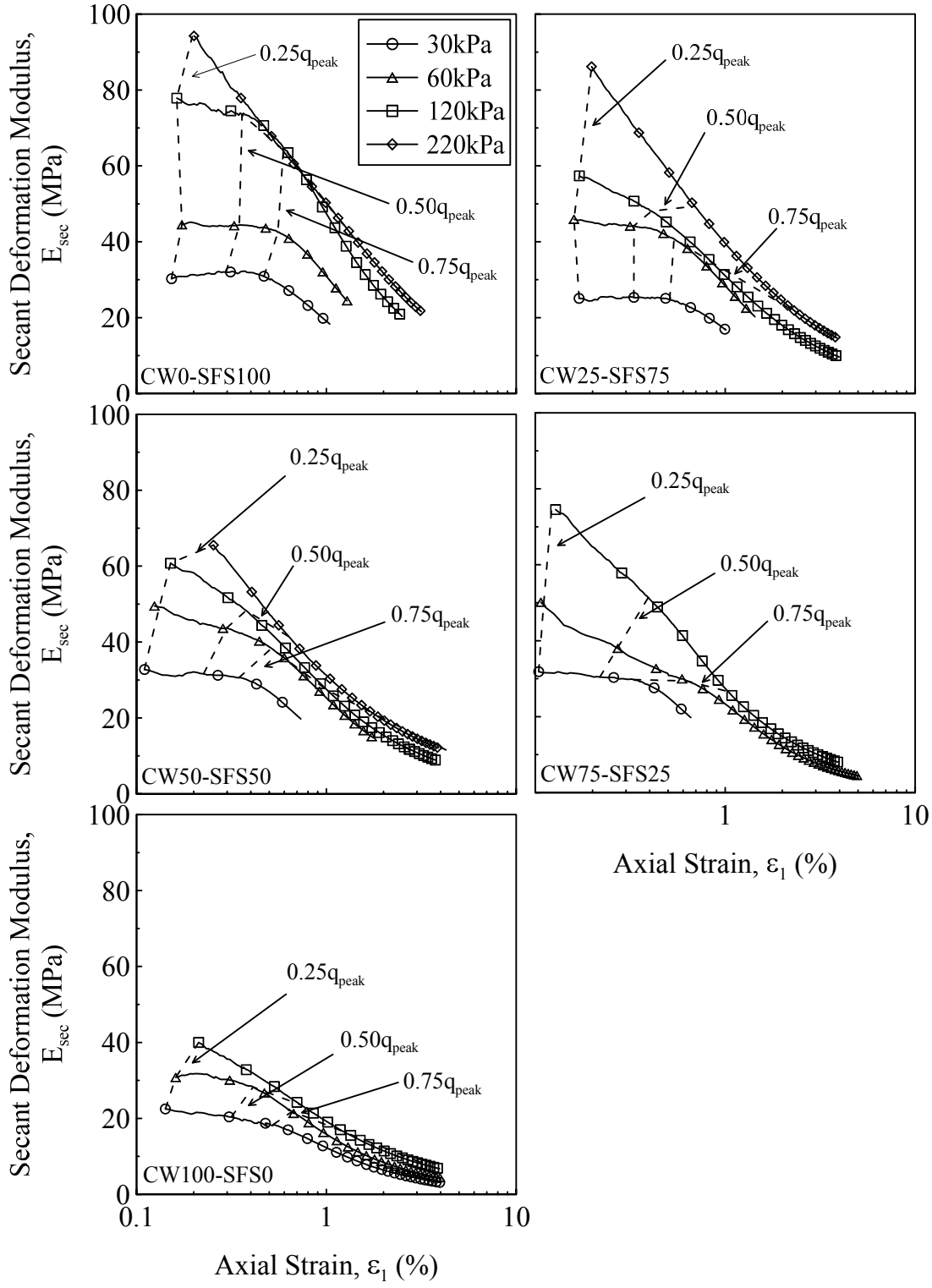

Figure 5.17 Variation of secant deformation modulus (E_{sec}) with axial strain under different confining pressures for CW-SFS mixtures

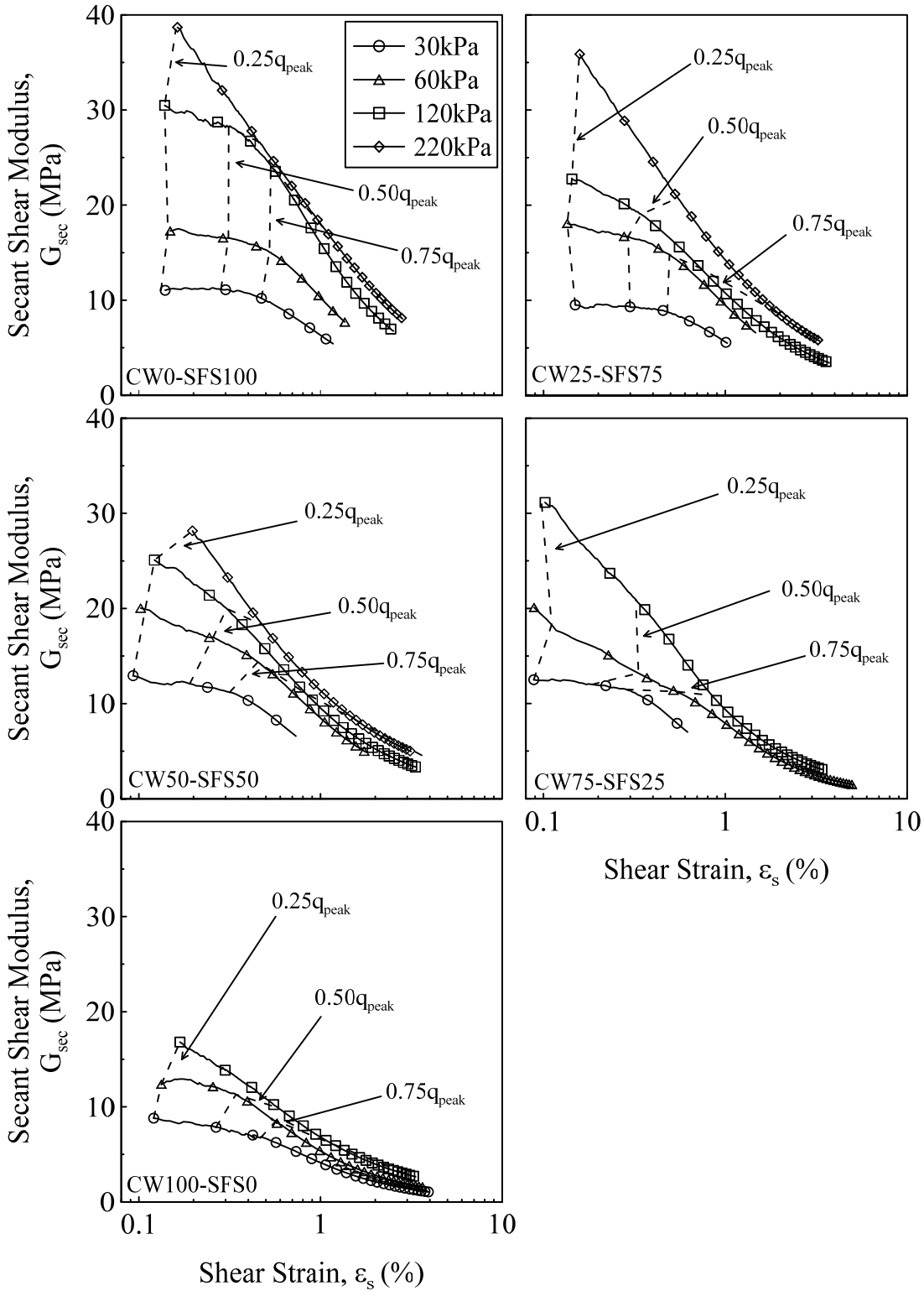

Figure 5.18 Variation of secant shear modulus (G_{sec}) with shear strain under different confining pressures for CW-SFS mixtures

The axial strains vs. confining pressure corresponding to peak stress and 50% peak stress are plotted in Figure 5.19, and it shows that under a given effective stress, a greater axial strain was needed to mobilise ϕ_p for mixtures with higher content of CW. Under smaller effective confining pressures (e.g., σ'_3<60kPa), the corresponding axial strain at peak stress was less than 2% for most CW-SFS mixtures (except CW100-SFS0), whereas for σ'_3>120kPa the ε_1 was greater than 10% (Figure 5.19*(a)*). In performance based design, engineers are interested in determining the level of strain that corresponds to the mobilised shear stress. Figure 5.19*(b)* presents the axial strain corresponding to 50% peak stress (i.e. factor of safety =2 which is usually considered in practice), and shows that for most of CW-SFS mixtures, the strain required to mobilise $0.5q_{peak}$ is less than 1%. This implies that in a practical application such as typical port conditions, the expected strain under the loading levels would be smaller than 1% by limiting the applied load to within 50% of its peak strength. Based on Figure 5.19*(b)*, one may conclude that most mixtures apart from CW100-SFS0 can be used as structural fill in terms of strain levels.

5.3.4 Degradation during shearing

Particle breakage influences the strength and deformation characteristics of CW-SFS mixtures because it imposes increased volumetric contraction during shearing. To determine the degradation of CW-SFS mixtures, a wet sieve analysis was conducted on the specimens after triaxial shearing. By quantifying the change in PSD before and after shearing, the breakage index (*BI*) can be determined and the method was described in detail in section 4.2.3.

Figure 5.20 presents the *BI* analysis for CW-SFS mixtures subjected drained triaxial tests. The Hardin's method (Hardin, 1985) for breakage quantification is also plotted for comparison. These results include particle breakage while the specimens were being prepared. The breakage index against the content of CW due to compaction and shearing is plotted in Figure 5.20*(a)*. The results indicate that for a given confining pressure, *BI* increases when the CW fraction increases. This was clearly

due to the lower strength CW particles compared to the SFS particles. A bilinear relationship could be determined where the slope for blended specimens with CW>50% was higher than the remaining mixtures with a CW<50%, and as expected, this slope increased with the increase in confining pressure. This implies that from a practical perspective, the greater volumetric strain (or settlement) attributed to particle breakage may occur with mixtures with a high percentage of CW. In Figure 5.20*(b)*, *BI* is plotted against the confining pressure for all CW-SFS mixtures, and for all the mixtures it increased with the increase in confining pressure, but at a decreasing rate. In other words, it was expected that the *BI* for each CW-SFS mixture would reach a threshold value where any further increase in the confining pressure would not significantly influence the extent of particle degradation.

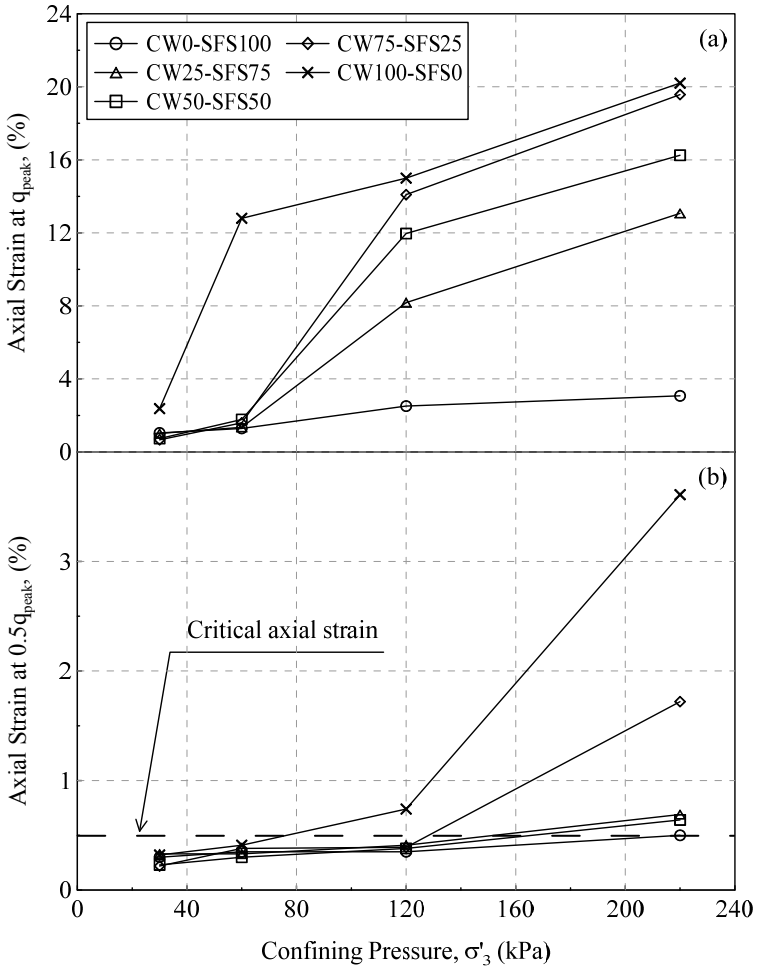

Figure 5.19 Effect of confining pressure and percentage of coal wash on the (a) the axial strain corresponding to peak deviatoric stress and (b) the axial strain at $0.5q_{peak}$

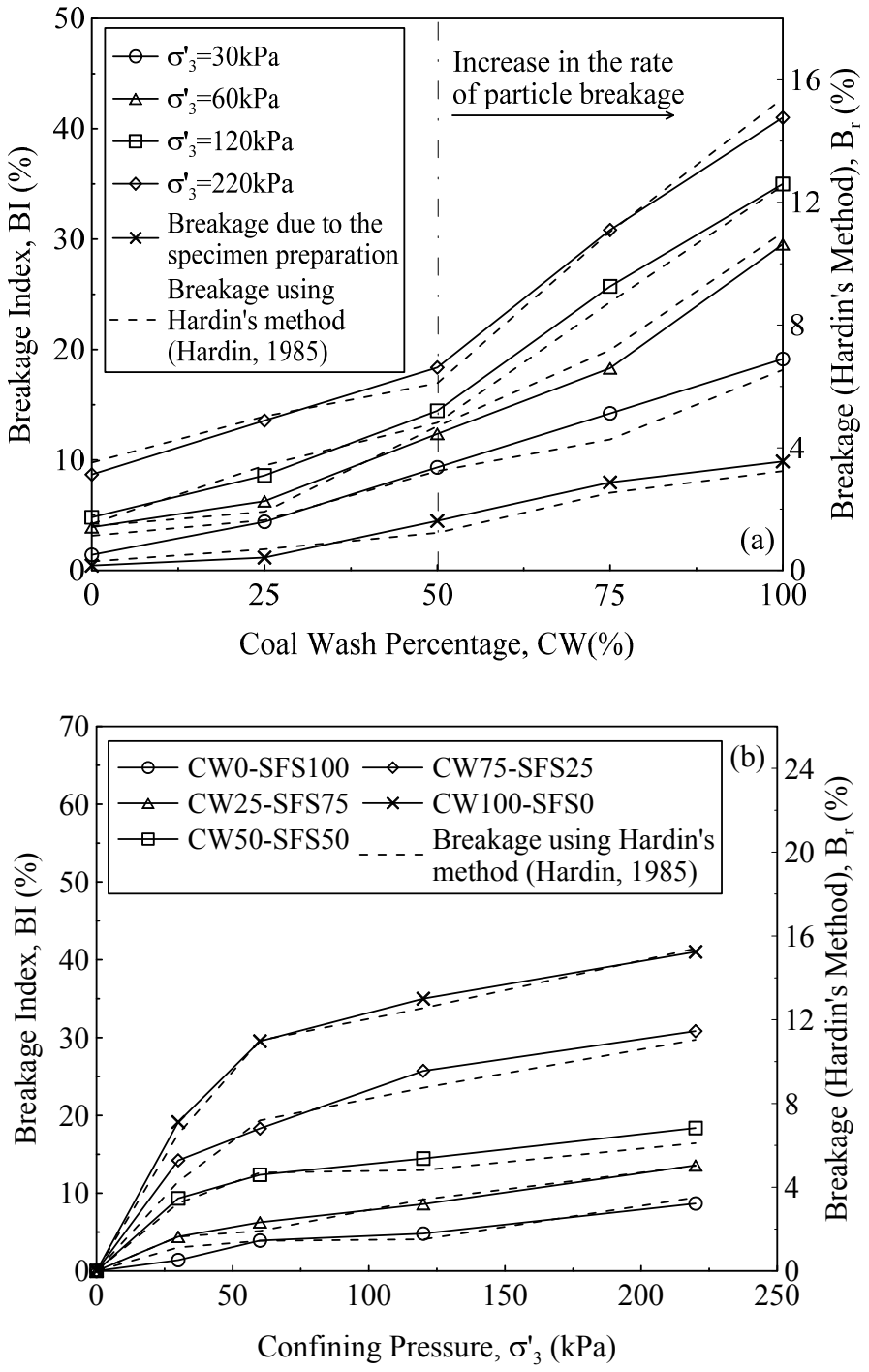

Figure 5.20 Breakage analysis on CW-SFS mixtures (a) the effect of the percentage of coal wash on *BI* under four confining pressures and (b) the effect of confining pressure on the *BI* for each CW-SFS mixtures

5.3.5 Stress-dilatancy response

In a dense granular material, the expansion of volume after initial compression during shearing is known as dilation. It is used to measure the amount of volume change under a given confining pressure as well as the peak deviatoric stress. The dilatancy ratio (i.e. $d_g=\delta\varepsilon_v/\delta\varepsilon_s$) is suggested by various researchers as being incorporated in order to explain dilatancy response (Rowe, 1962, Nova and Wood, 1979, Been and Jefferies, 1985, Bolton, 1986, Li and Dafalias, 2000, Russell and Khalili, 2004). Dilation plays a key role in justifying the reduction in peak friction angle as the confining pressure increases, and the zero rate of dilatancy corresponds to the critical state. Furthermore, the dilation concept in drained triaxial shearing can be used for the predicted behaviour of a granular material. In this study, the effects of confining pressure and coal wash content on the dilatancy response of CW-SFS blends were investigated. The relationships between the dilatancy, confining pressure and coal wash content were evaluated and described.

In Figure 5.21, the stress-dilatancy relationships of CW-SFS mixtures under four confining pressures are plotted. The results show that the behaviour of CW0-S100 (Figure 5.21a) is dilative after initial contraction, even under a relatively high confining pressure (i.e. 220kPa). Also under any given confining pressure, the amount of dilation decreased to reach zero at the critical state. As expected, the maximum dilatancy ratio was decreased with the increase in the confining pressure (e.g. the maximum dilatancy ratio was -0.8 and -0.2 for the confining pressures of 30kPa and 220kPa, respectively as shown in Figure 5.21a). By comparing the response of stress-dilatancy for different CW-SFS mixtures (Figure 5.22), it is evident that under a given σ'_3, the plotted trend generally shifted to the right as the CW content increased in the blend. This means that under low σ'_3 in which the behaviour was dilative, the amount of dilation decreases with the increase in the CW percentage. Also, under a high σ'_3, the degree of contraction increased as the CW content increased in the mixture.

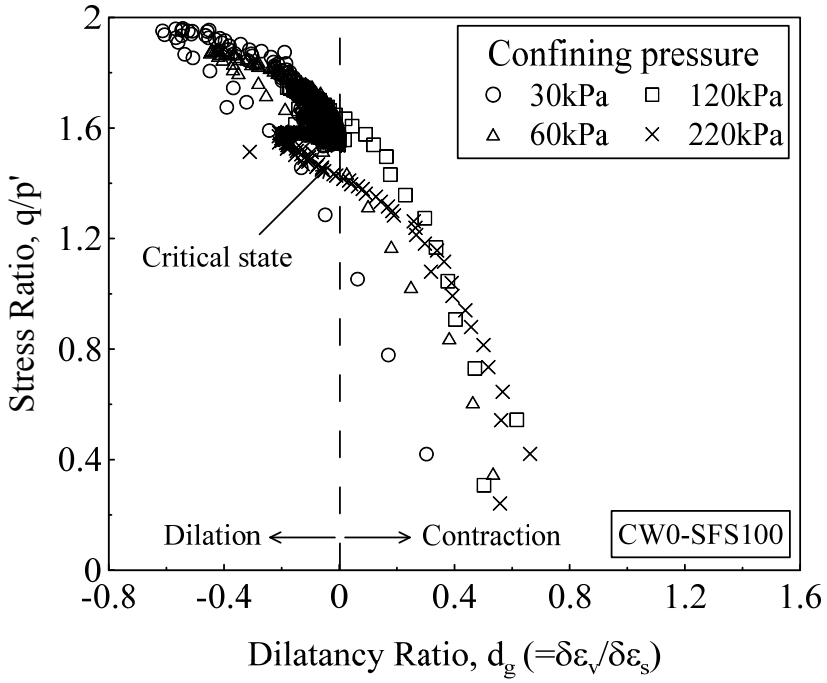

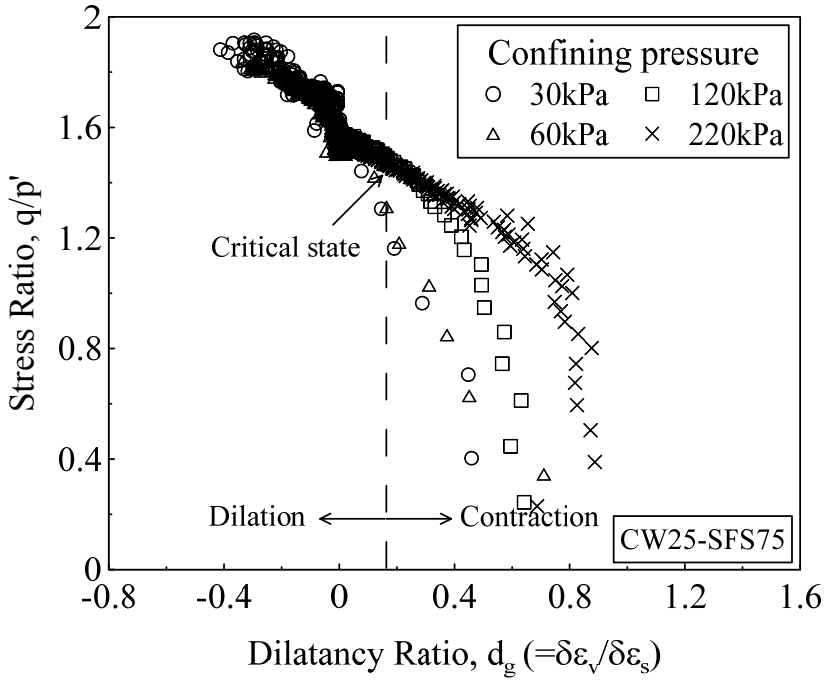

Figure 5.21 Stress-dilatancy response of CW-SFS mixtures in drained triaxial shearing

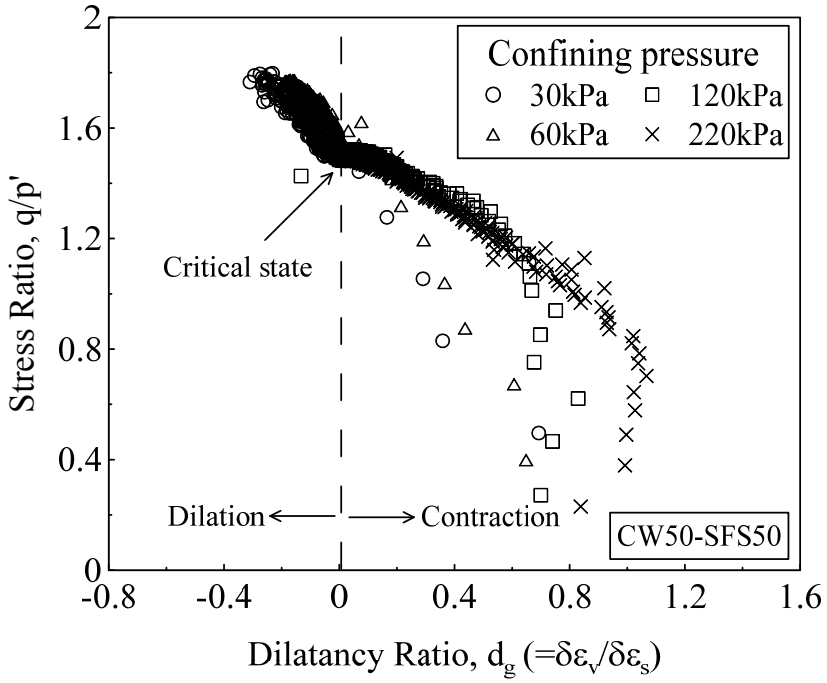

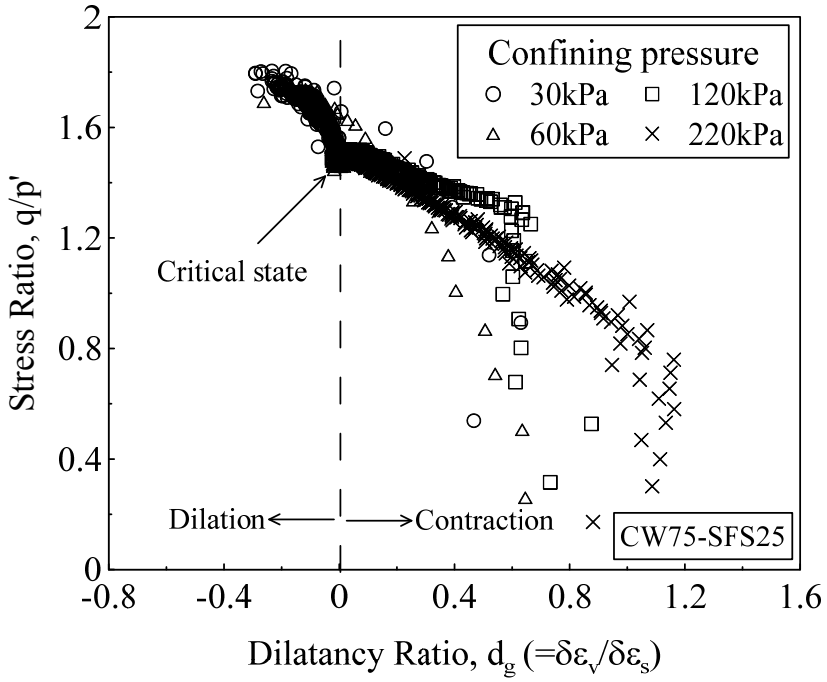

Figure 5.21 (continued) Stress-dilatancy response of CW-SFS mixtures in drained triaxial shearing

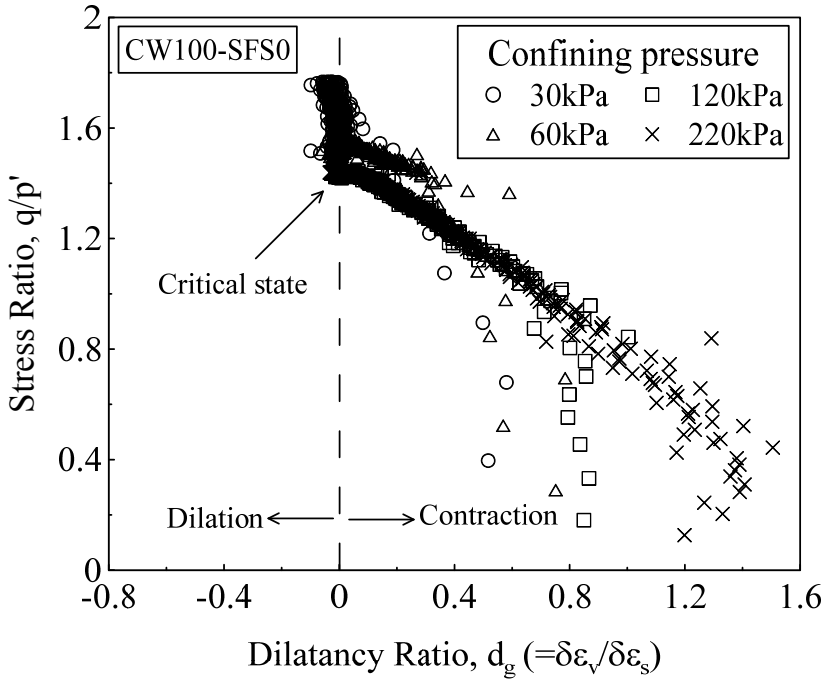

Figure 5.21 (continued) Stress-dilatancy response of CW-SFS mixtures in drained triaxial shearing

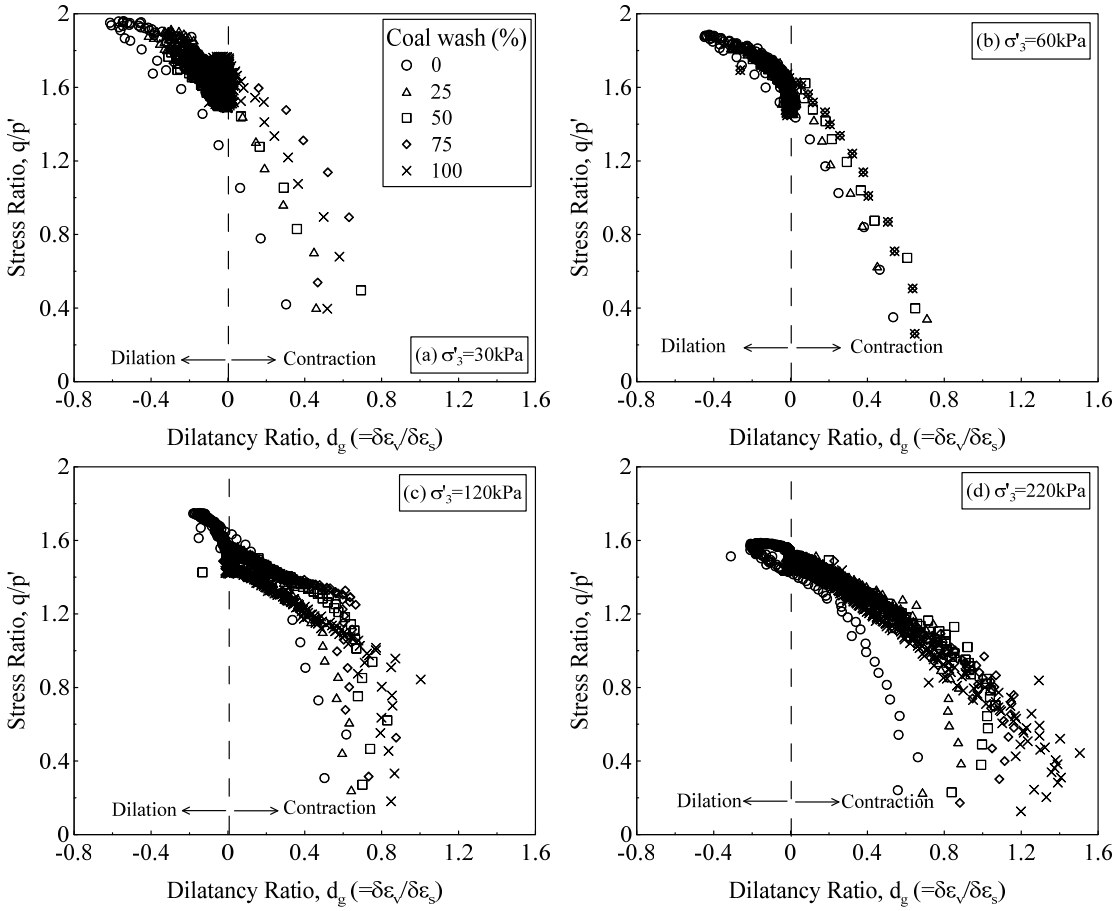

Figure 5.22 Influence of coal wash content on the stress-dilatancy response of CW-SFS mixture

5.4 MODELLING THE BEHAVIOUR OF CW-SFS MIXTURES

Although the behaviour of CW-SFS under drained triaxial condition was discussed in the previous section, the adoption of these mixtures as structural fill must be supported by analytical relations that are capable of describing the stress-strain behaviour under field loading conditions. In this section, an analytical model for the behaviour of CW-SFS blends under drained triaxial conditions is developed for all CW-SFS mixtures (except CW0-SFS100 as the similarity in behaviour was observed). The critical state (CS) condition for these mixtures was observed and thus the concept of the CS was captured in the analytical model. Consequently, a set of empirical expressions was defined to capture the overall triaxial drained behaviour of four different waste materials under the CS framework. It is noteworthy to mention

that the current model is a significant extension of the constitutive model proposed by Chiaro *et al.* (2014a) based on generalised plasticity and the critical state concept. In Table 5.6 the comparison of model features between current model and Chiaro *et al.* (2014a)'s model is listed. The current model is applicable to a wider range of mixtures i.e. CW content is more than 25% by weight. The CSL was observed to be nonlinear and thus, the model parameters were recalibrated. Finally, the current model was implemented in ABAQUS for general loading and boundary conditions and validated using field trial test results (the numerical implementation is discussed in Chapter 7).

Table 5.6 Comparison of model features of current study with those of Chiaro *et al.* (2014a)

Feature	Current model	Chiaro *et al.* (2014a)'s model
Theoretical formulation and governing equations	Both models use established approach by Pastor *et al.*(1990), Li and Dafalias (2000), and Ling and Yang (2006) in terms of loading direction, plastic flow direction, and hardening modulus	
Material	Applicable for mixtures containing more than 25% CW	Applicable for mixtures containing more than 50% CW
Model parameters	Nonlinear CSL and associated properties such as the critical void ratio at reference pressure of 1kPa (Γ^*); and the slope of critical state (λ^*). Recalibration of model parameters to cover more mixtures and confining pressures	Parallelism of CSL (linear)
Numerical implementation	Programmed both in MATLAB (for triaxial condition) and UMAT subroutine (in ABAQUS for general loading and boundary conditions)	Programmed only in MATLAB
Field application	Validated using field loading and boundary conditions (results of plate load test)	No validation to field condition

The framework of the model is inspired by previous studies of Ling and Yang (2006) and Manzanal *et al.* (2011). In this model, the current state of the specimen (in terms of pressure and void ratio) is considered through the state parameter (ψ). In addition, the state parameter is included in the formulation of flow rule, plastic flow, and plastic modulus. The main feature of the model is that an explicit set of 11 soil parameters can describe the stress-strain of different CW-SFS mixtures that consolidated under various confining pressures.

In some past studies, it was shown that the behaviour of various types of soils could be easily predicted without the formulation of the yield surface and plastic potential (Pastor *et al.*, 1990; Ling and Liu, 2003). Similarly, the concept of critical state indicates that once the specimen is sheared to large strain, it reaches a state whereby the shear stress and volumetric strain remain relatively constant with progressive distortion of the specimen (Roscoe *et al.*, 1958; Schofield and Wroth, 1968; Vesic and Clough, 1968). Therefore, this type of framework is able to predict soil behaviour under different initial condition (i.e. confining pressure and void ratio) using a set of soil parameters for critical state line, dilatancy, and elasticity condition (e.g. Jefferies, 1993; Imam *et al.*, 2005; Modoni *et al.*, 2011)

5.4.1 Critical state for CW-SFS mixtures

As discussed in previous sections, the behaviour of CW-SFS mixtures is dependent on the stress level (p') and void ratio (e) similar to granular materials such as sand and gravel. The stress-strain behaviour of four CW-SFS mixtures is depicted in detail in Figures 5.6 to 5.9. These figures clearly show a dilative volumetric strain, and at the same time, the peak deviatoric stress is followed by strain softening of those specimens that sheared under a relatively low confining pressure of p'_0=30kPa. In contrast, under relatively high confining pressure such as 120 and 220kPa, volumetric contraction and strain hardening were observed. Nevertheless, the constant shear stress and volumetric strain were detected for all specimens irrespective to the initial condition at a shear strain (ε_s) of approximately 20% which is referred to as the critical state locus (CSL; Roscoe *et al.*, 1958; Schofield and

Wroth, 1968; Vesic and Clough, 1968). Its projection in the *p'-q* and *p'-e* plots is shown in Figures 5.6 to 5.9 (c) and (d), respectively. The boundary that is set by CSL clearly shows the dilative/contractive and strain softening/hardening behaviour. Been and Jefferies (1985) proposed a parameter known as state parameter (ψ^*) which can be used to describe the void ratio and stress dependency of a material. The state parameter is the vertical distance between the current void ratio (*e*) and the void ratio on the critical state line and it is expressed as follows:

$$\psi^* = e - e^*_{cs} = \nu - \Gamma^* \tag{5.11}$$

For the condition of $\psi^* > 0$, the behaviour of the soil is compressive in volumetric strain and shows associated strain hardening. For the condition of $\psi^* < 0$ (i.e. the initial state of the specimen is below the CSL), the specimen is expected to dilate and the peak deviatoric stress followed by strain softening would occur. Finally, at the critical state condition as well as the phase transformation state, the state parameter is zero ($\psi^* = 0$).

The results of the CSL for the CW-SFS mixtures are shown in Figure 5.11. It is evident that not only the location of the CSL was shifted vertically due to the variation in the initial specific volume, but also the slope of CSL (ν^*_{cs}) was altered depending to the CW content (f_{CW}). In the *p'-q* plot, the slope of the CSL (i.e. M^*_{cs}) decreased as the CW content increased in the blend. Therefore, based on the CSL characteristics which are tabulated in Table 5.4, the following equations can be used to describe the CSL for any given mixture (modified after Chiaro *et al.*, 2014a):

$$\nu^*_{cs} = \Gamma^* - \lambda^* \ln p' \tag{5.12}$$

where:

$$\Gamma^* = 1.751 + 0.40 f_{CW} - 0.45 f^2_{CW} \tag{5.13}$$

$$\lambda^* = 0.028 + 0.11 f_{CW} - 0.09 f_{CW}^2 \tag{5.14}$$

$$M_{cs}^* = 1.545 - 0.098 f_{CW} \tag{5.15}$$

In the above, ν_{cs}^*, Γ^*, and λ^* are the critical specific volume; critical specific volume at reference pressure of 1kPa and slope of CSL in *p′-e* plot, respectively; and M_{cs}^* is the slope of CSL in *p′-q* plot.

5.4.2 Generalised plasticity framework

Due to the symmetry for the triaxial specimen, the axisymmetric condition (i.e. $\sigma_2' = \sigma_3'$ and $\varepsilon_2 = \varepsilon_3$) is adopted for the formulation of stress and strain and they are expressed by following equations:

$$\sigma = \begin{Bmatrix} p' \\ q \end{Bmatrix} = \begin{Bmatrix} \sigma_1' + 2\sigma_3'/3 \\ \sigma_1' - \sigma_3' \end{Bmatrix} \tag{5.16}$$

$$\varepsilon = \begin{Bmatrix} \varepsilon_v \\ \varepsilon_s \end{Bmatrix} = \begin{Bmatrix} \varepsilon_1 + 2\varepsilon_3 \\ 2(\varepsilon_1 - \varepsilon_3)/3 \end{Bmatrix} \tag{5.17}$$

where, p' is the effective mean stress; q is the deviator stress; ε_v is the volumetric strain; ε_s is the shear strain; σ_1' and σ_3' are the effective major and minor principal stresses, respectively; and ε_1 and ε_3 are the major and minor principal strains, respectively.

In the generalized plasticity framework, the incremental stress ($d\sigma$) and strain ($d\varepsilon$) relationship is expressed as (Pastor *et al.*, 1990, Manzanal *et al.*, 2011):

$$\{d\sigma\} = D^{ep}\{d\varepsilon\} \Rightarrow \begin{Bmatrix} dp' \\ dq \end{Bmatrix} = \left\{ D^e - \frac{D^e m n^T D^e}{H + n^T D^e m} \right\} \begin{Bmatrix} d\varepsilon_v \\ d\varepsilon_s \end{Bmatrix} \tag{5.18}$$

where, D^e is the elastic stiffness tensor; D^{ep} is the elasto-plastic stiffness tensor (Mroz and Zienkiewicz, 1984); m is the plastic flow direction vector; n is the loading direction vector and H is the plastic modulus.

5.4.2.1 Increment of elastic and plastic strains

In the model, it is assumed that the plastic strain occurs for any given shear stress. It means that the purely elastic region does not exist and the specimen is assumed to yield from the very small strains. In the classical theory of plasticity, the increment of total strain ($d\varepsilon$) is decomposed into elastic ($d\varepsilon_e$) and plastic ($d\varepsilon_p$) components (Poulus and Davis, 1974):

$$d\varepsilon_v = d\varepsilon_v^e + d\varepsilon_v^p = dp'/K + d\varepsilon_v^p \tag{5.19}$$

$$d\varepsilon_s = d\varepsilon_s^e + d\varepsilon_s^p = dq/3G + d\varepsilon_s^p \tag{5.20}$$

where,

$$G = \frac{3(1-2\nu)}{2(1+\nu)}K \tag{5.21}$$

$$K = \frac{(1+e)p'}{\kappa} \tag{5.22}$$

in the above ν is the Poisson's ratio; p' is the current effective mean stress; κ is the unloading-reloading slope; and e is the current void ratio.

5.4.2.2 Dilatancy relationship

The dilatancy relationship proposed by Li and Dafalias (2000) which relates the ratio of plastic strain increments ($d_g = d\varepsilon_v^p / d\varepsilon_s^p$) to the stress ratio ($\eta = q/p'$) is employed as follows and this equation is an extension of the linear stress-dilatancy proposed by Manzari and Dafalias (1997):

$$d_g = \xi_g \left[M_{cs} \exp\left(\mu_g \psi\right) - \eta \right] \tag{5.23}$$

where, ξ_g and μ_g are dilatancy material constants.

Equation (5.23) shows that the dilatancy relationship is state-dependent through (ψ). It shows that for two conditions, the dilatancy is zero: (i) for the critical state condition (i.e. ψ=0 and $\eta = M_{cs}$), (ii) for the state known as phase transformation (PT) where the soil behaviour transforms from contractive to dilative (i.e. d_g=0 and $\eta \neq M_{cs}$). For contractive soil, $M_{cs} \exp\left(\mu_g \psi\right) > M_{cs}$ and thus PT state is never reached during the shearing process. Alternatively, for a dilative soil, the PT state is achieved when $\eta = M_{cs} \exp\left(\mu_g \psi_{pt}\right)$, where ψ_{pt} is the value of state parameter at PT state.

5.4.2.3 Loading and plastic flow directions

A non-associated flow rule was considered, thus the vectors of plastic flow and loading directions do not coincide with each other. Pastor *et al.* (1990) and Ling and Liu (2003) indicated that in generalised plasticity, there is no need to define equations for yield and plastic potential surfaces. However, by defining loading and plastic flow vectors, the model can describe the behaviour of a soil. In the triaxial space, plastic flow direction vector (m) and loading direction vector (n) are given as:

$$m = \left\{ \begin{array}{l} m_v = d_g / \sqrt{1 + d_g^2} \\ m_q = 1 / \sqrt{1 + d_g^2} \end{array} \right\} \tag{5.24}$$

$$n = \left\{ \begin{array}{l} n_v = d_f / \sqrt{1 + d_f^2} \\ n_q = 1 / \sqrt{1 + d_f^2} \end{array} \right\} \tag{5.25}$$

where, d_f is the loading direction component:

$$d_f = \xi_f \left[\eta_f \exp\left(\mu_f \psi\right) - \eta \right] \tag{5.26}$$

in which ξ_f, η_f and μ_f are material parameters describing the plastic potential.

5.4.2.4 Plastic modulus

The dependency of plastic modulus (H) to the state parameter (ψ) is considered in this model. The plastic modulus proposed by Li and Dafalias (2000) and modified by Ling and Yang (2006) was used in the proposed model as follows:

$$H = h_0\left(\frac{\eta_{pk}}{\eta} - 1\right)\left(1 - \frac{\left(\xi_f - 1\right)}{\xi_f}\frac{\eta}{\eta_f}\right)^4\sqrt{\frac{p}{p_{atm}}} \tag{5.27}$$

where according to Li and Dafalias (2000):

$$\eta_{pk} = M_{cs}\exp\left(-\mu_{pk}\psi\right) \tag{5.28}$$

in the above h_0 and μ_{pk} are hardening material constants. It is noteworthy, H depends on the difference between the current stress ratio η and the virtual peak stress ratio η_{pk}. H may be positive (hardening) for $\eta_{pk} > \eta$, negative (softening) for $\eta_{pk} < \eta$ or zero (peak failure) for $\eta_{pk} = \eta$.

5.4.3 Evaluation of model parameters

In the model, 11 model parameters were calibrated using experimental triaxial results for the CW-SFS blends (for mixtures having more than 25% coal wash content). These parameters are listed in Table 5.7. The elastic properties of the mixtures were evaluated using the isotropic consolidation results (Table 5.2) and the Poisson's ratio was assumed to be constant (ν = 0.25). In addition, empirical equations were incorporated to relate the CSL parameters (Γ^*, λ^*, and M_{cs}^*) to the CW content (f_{CW}).

Table 5.7 Comparison of model parameters of current study with those of Chiaro *et al.* (2014a)

Soil parameters	Symbol	Current model	Chiaro *et al.* (2014a)'s model
Elastic	κ	$0.0023+0.0027f_{CW}$	$0.002+0.003f_{CW}$
	ν	0.25	0.25
Critical state	Γ^*	$1.751+0.40f_{CW}-0.45f_{CW}^2$	$0.695+0.229f_{CW}$
	λ^*	$0.028+0.11f_{CW}-0.09f_{CW}^2$	0.061
	M_{cs}^*	$1.545-0.098f_{CW}$	$1.44-0.12f_{CW}$
Loading direction	ξ_f	1.45	1.45
	μ_f	5	5
Dilatancy	ξ_g	1.45	1.45
	μ_g	3	3
Plastic modulus	h_0(kPa)	100000	100000
	μ_{pk}	14	14

κ= unloading-reloading slope; ν=Poisson's ratio; Γ^*= the critical void ratio at reference pressure of 1kPa; λ^*= the slope of critical state line in p'-e plot; M_{cs}^*= the slope of CSL in p'-q plot; ξ_f, μ_f= material parameters describing plastic potential; ξ_g, μ_g= dilatancy material constants; and h_0, μ_{pk} hardening material constants

Figure 5.23 illustrates an example of a typical calibration of dilatancy parameter, in which $\xi_g = 1.45$. Alternatively, $\mu_g = 3$ was determined by evaluating Equation 5.23 at the PT state, thus (Chiaro *et al.*, 2014a):

$$d_g = 0 \quad \Rightarrow \quad M_{cs}\exp(\mu_g\psi) - \eta = 0 \quad \Rightarrow \quad \mu_g = \frac{1}{\psi_{pt}}\ln\left(\frac{\eta_{pt}}{M_{cs}}\right) \tag{5.29}$$

where, η_{pt} and ψ_{pt} are the values of η_f and ψ at phase transformation state, respectively.

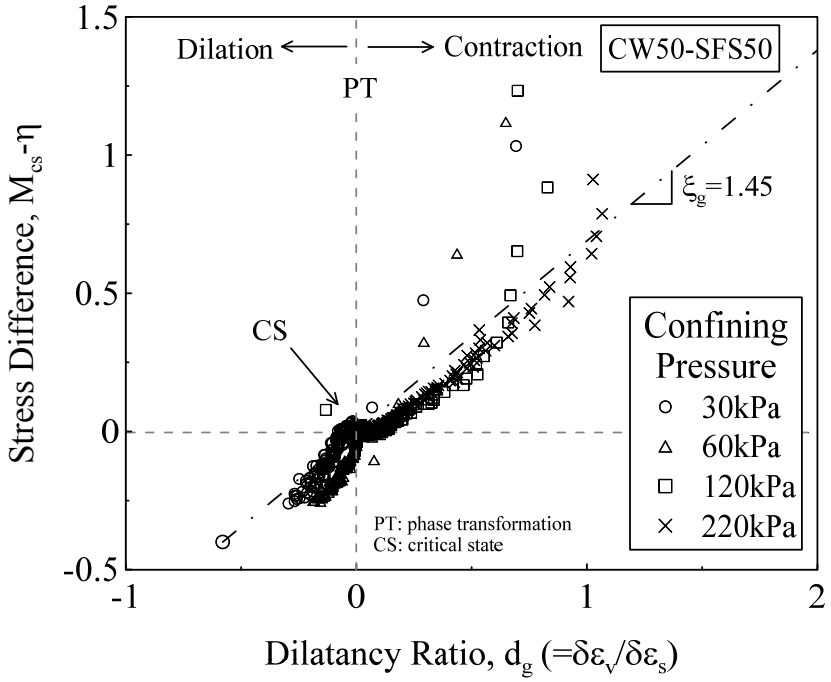

Figure 5.23 Typical determination of dilatancy parameter ξ_g

In the basic generalised plasticity models, η_f is independent from confining pressure and constant for a given material. In addition, the ratio between η_f and M_{cs} is similar to the relative density of the soil. Here, for compacted CW-SFS blend, the following relationship was used, which allows calculating η_f once M_{cs} is known:

$$\eta_f = \frac{D_c}{100} M_{cs} \tag{5.30}$$

where, D_c (%) is the degree of compaction.

In addition μ_f was evaluated using the shape of volumetric behaviour and $\xi_f = \xi_g$ was adopted (as suggested by Manzanal *et al.*, 2011). Consequently, hardening

parameter (h_0) was calibrated by matching the shear stress curves, and μ_{pk} was determined by evaluating Equation (5.28) at the deviator peak stress state where:

$$H = 0 \quad \Rightarrow \quad M_{cs} \exp(m_{pk}\psi) - \eta = 0 \quad \Rightarrow \quad m_{pk} = \frac{1}{\psi_{pk}} \ln\left(\frac{M_{cs}}{\eta_{pk}}\right) \tag{5.31}$$

in the above, η_{pk} and ψ_{pk} are the values of η and ψ at deviator peak stress state, respectively.

5.4.4 Comparison between experimental results and model simulation

The constitutive equations described in previous section were programmed in a MATLAB code as provided in Appendix A. The comparison between current model prediction (dashed lines), Chiaro *et al.* (2014a)'s model, and the triaxial test results (symbols) for four CW-SFS blends under four confining pressures is plotted in Figure 5.2. It is evident that the current model prediction is in a good agreement with the experimental results compared to the Chiaro *et al.* (2014a)'s model, particularly in volumetric strain. The volumetric dilation behaviour followed by strain softening for specimens sheared under relatively low confining pressure (e.g. p'_0=30kPa) as well as the volumetric contraction with strain hardening for specimens sheared under relatively high confining pressure (e.g. p'_0=220kPa) were captured successfully. Furthermore, despite the various initial conditions (in terms of void ratio and confining pressure), the critical state condition which was considered in the proposed model was reached for axial strain greater than 20%.

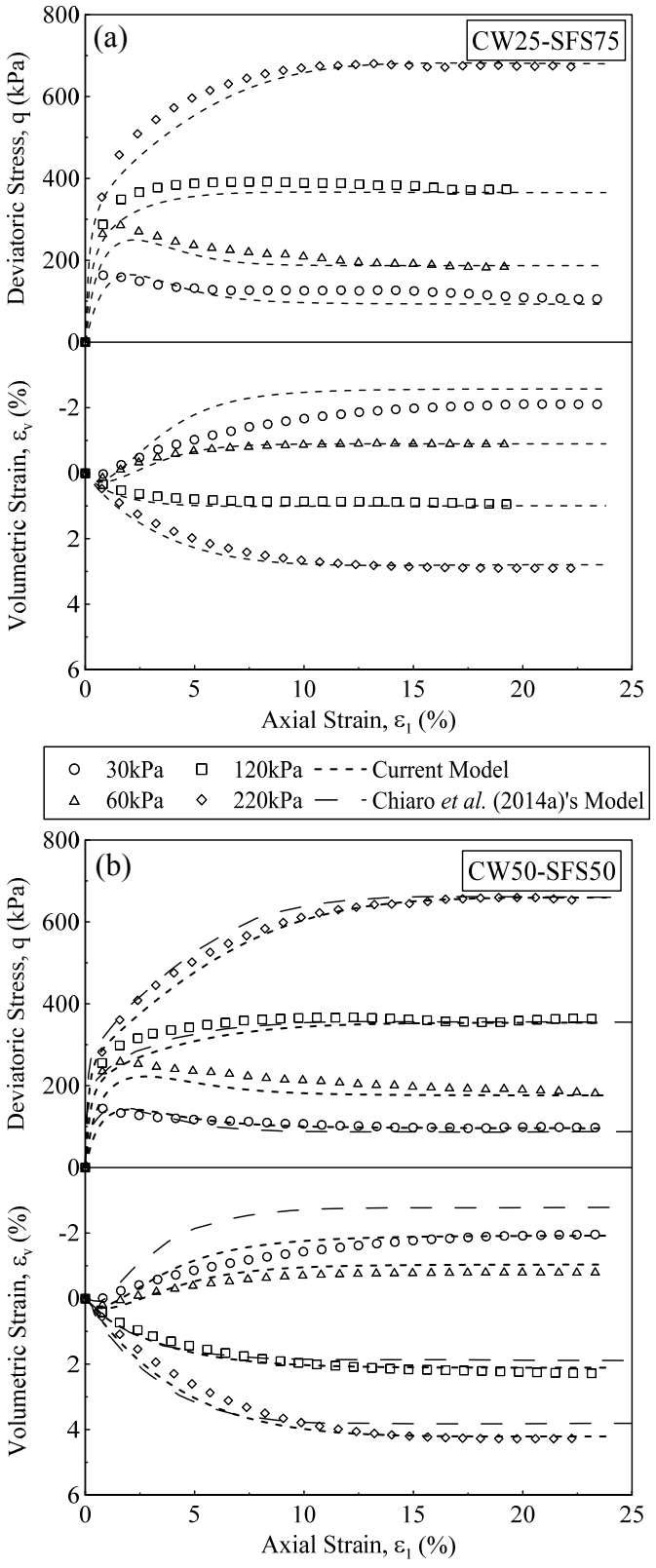

Figure 5.24 (a) and (b) Comparison between experimental data and model simulation for CW25-SFS75 and CW50-SFS50 mixtures under triaxial condition

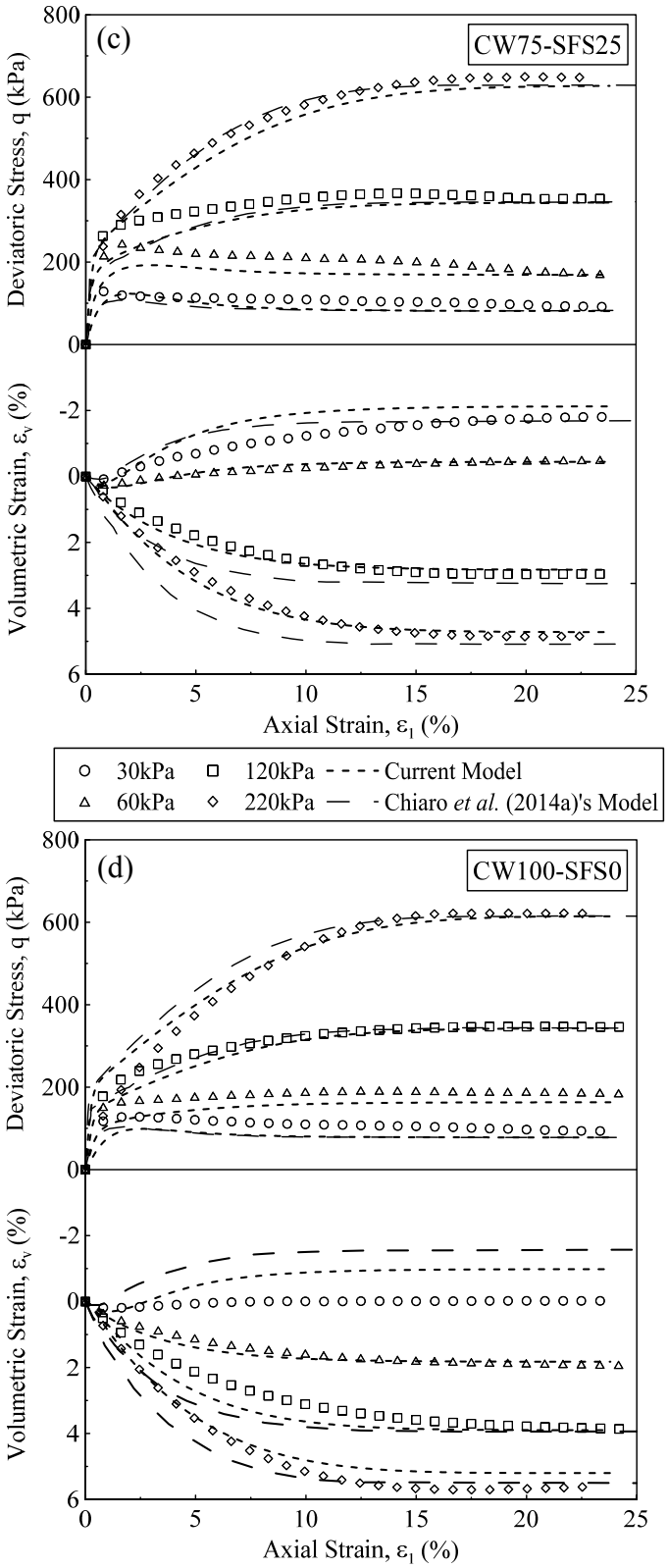

Figure 5.24 (c) and (d) Comparison between experimental data and model simulation for CW75-SFS25 and CW100-SFS0 mixtures under triaxial condition

5.5 SUMMARY

(1) It was observed through a series of isotropic compression tests that the specimens with a higher percentage of CW showed greater compressibility. This is because the CW particles were softer and more crushable, compared to SFS particles which also confirmed through the breakage analysis. In addition, the maximum past yield stress (p^*) increased as the content of SFS was increased. A bilinear empirical equation of v/v_0 and p'/p^* was proposed in order to predict the isotropic compression of all the CW-SFS mixtures compacted under the same level of compaction energy.

(2) The stress-strain behaviour of CW-SFS mixtures was influenced by the percentage of CW. As the proportion of SFS in mixtures increased, the peak deviatoric stress increased and the axial strain corresponding to the q_{peak} decreased. The effect that the content of SFS had on the shear behaviour diminished at higher confining pressures exceeding 120kPa.

(3) The volumetric strain at the end of the test was influenced significantly by the amount of CW in the mixture, such that there was more contraction in those specimens with a higher percentage of CW. Part of this volumetric contraction could be attributed to the degradation of coal wash particles (e.g. the *BI* values under 120kPa confining pressure for CW100-SFS0 and CW0-SFS100 were 4.8% and 35%, respectively).

(4) The shear strength envelopes of CW-SFS mixtures were found to be non-linear and exhibited negligible cohesion, while the curvature of shear strength plots decreased as the percentage of CW increased. The mixtures with high SFS percentage showed a higher shear strength than those with a higher CW percentage.

(5) It was observed that the addition of a small amount of SFS (approximately 25%) increased the secant shear modulus of the mixture significantly. The axial and shear strains corresponding to any levels of mobilized shear stress increased once the percentage of CW increased. This implies that under the same loading conditions, a larger deformation is associated with mixtures having more CW content; however, based on the critical strain criterion

proposed, only mixtures having 100% coal wash exhibit axial deformation over the prescribed allowance of 0.5%.

(6) The study on the breakage characteristics of CW-SFS mixtures during shearing revealed that under a given confining pressure, those specimens with less CW showed less particle breakage due to the influence of SFS. The rate of particle breakage for specimens with more than 50% CW increased significantly. This change was markedly greater at confining pressures exceeding 60kPa.

(7) A constitutive model based on generalised plasticity and critical state framework was proposed to describe the stress-strain behaviour of four CW-SFS mixtures sheared at various confining pressures under drained triaxial condition. The comparison between model prediction and the triaxial results indicated an acceptable agreement. More importantly, the model was able to capture (i) dilative behaviour followed by strain softening as well as (ii) contractive behaviour with strain hardening depending on the initial conditions of the specimens. Furthermore, the developed model captures the critical state condition for an axial strain greater than 20%, irrespective of the initial conditions.

CHAPTER SIX

6 FIELD ASSESSMENT OF CW-SFS MIXTURES

6.1 INTRODUCTION

In this chapter, initially an acceptance criterion for granular waste material was proposed to identify a suitable waste material as structural fill. Based on this criterion and the laboratory results discussed in Chapters 4 and 5, an optimisation method for the CW-SFS mixtures was suggested and two blends were identified as suitable fill to be tested in a field trial. The results of the field trial performance of these two selected mixtures of CW and SFS are presented and discussed. The *in-situ* density was determined for different roller passes using both sand cone replacement and nuclear densometer methods. In addition, the post compaction strength of the compacted layers and deformation behaviour were evaluated using the dynamic cone penetration (DCPT) and plate load tests (PLT), respectively. The time-dependent behaviour of the mixtures was observed as the strength of the materials increased with time due to the hydration reaction associated with the free lime content of SFS. Furthermore, the post-compaction swelling potential was also monitored. The results of this investigation indicated that the optimum mixtures of CW and SFS used in the field trial were suitable as structural fill.

6.2 ACCEPTANCE CRITERIA FOR GRANULAR WASTE FILLS

Generally, two main parameters are considered for the use of conventional material (e.g. sand and gravel) in practical applications: (i) shear strength or bearing capacity in order to control post-compaction settlement during service time, and (ii) permeability depending on the project specifications. Davies *et al.* (2011) suggested that a structural fill material should possess a friction angle greater than 30° or CBR

values of at least 10%. In relation to permeability, the recommended value is in the range of 1×10^{-6} to 1×10^{-4} cm/sec (Look, 2007). This range is adequate to ensure sufficient drainage to prevent the generation of excess pore water pressure and internal erosion. However, it was observed that waste materials such as CW and SFS can pose serious problems because of the swelling potential and significant particle breakage. Therefore, the acceptance criteria for waste materials should be modified accordingly to account for these adverse effects.

Four stages of acceptance are proposed herein (Figure 6.1). Stage 1 considers the shear strength and bearing capacity of the waste material, while Stage 2 represents the swelling characteristics. Stages 3 and 4 consider post-compaction particle breakage and permeability of the waste material, respectively. In Stage 1, if the friction angle of a waste material and/or CBR value is greater than 30° and 10%, respectively, it can then be considered suitable as a structural fill. Otherwise, it could only be recommended for general fills.

In terms of volume instability (i.e. Stage 2 of the acceptance criteria), depending on the overburden pressure on the compacted layer, acceptable level of free swelling can be adjusted. In the case of insignificant surcharge (i.e. less than 10kPa), the maximum allowable swelling is 3%. Once the criterion for volume expansion is satisfied, particle breakage should be considered to ensure that the deformation due to particle breakage is within an acceptable range. Under future representative port loading condition (i.e. 120kPa), breakage index of the waste material should be less than 12% in order to be used as structural fill. Otherwise, this waste material can be adopted as a general fill.

Finally, depending on the project scheme, the permeability of the potential waste material is considered (Stage 4). For structural fills, as suggested by Look (2007), to prevent the generation of excess pore water pressure, as well as internal erosion, the permeability should be similar to that of sandy fills (i.e. 1×10^{-6} cm/sec $\leq k \leq 1 \times 10^{-4}$ cm/sec). For the case of water-front fill, the permeability of the waste material

should be less than 1×10^{-6} cm/sec. Otherwise, the potential waste material can be considered as general fill.

6.2.1 Optimisation of CW-SFS mixtures

Since the results on the shear strength characteristics of CW-SFS mixtures indicated that all of the mixtures satisfied the bearing capacity criteria (ϕ' >30^o and CBR >10%), three main parameters were considered in optimising CW-SFS mixtures as illustrated in Figure 6.2: (i) permeability, (ii) swelling potential, and (iii) particle breakage. The permeability of the optimum mixture should be at a moderate level to ensure proper drainage (to prevent generation of excess pore water pressure under loading) and at the same time avoid internal erosion. Therefore, mixtures with more than 85% CW should be ignored.

In relation to the swelling potential, it was observed that mixtures with a relatively high amount of SFS (e.g. more than 65%) exhibits more than 3% volume expansion that can damage the upper structure, and should be avoided. In addition, particle breakage can cause excessive deformation and differential settlement. Under future typical port loading conditions (vertical stress @120kPa), mixtures having more than 62.5% CW can exhibit excessive particle degradation (*BI*>12%), thus should not be considered for practical applications. Overall, optimum CW-SFS blends are those in the range of CW-SFS 35/75 and CW-SFS 60/40 (Figure 6.2).

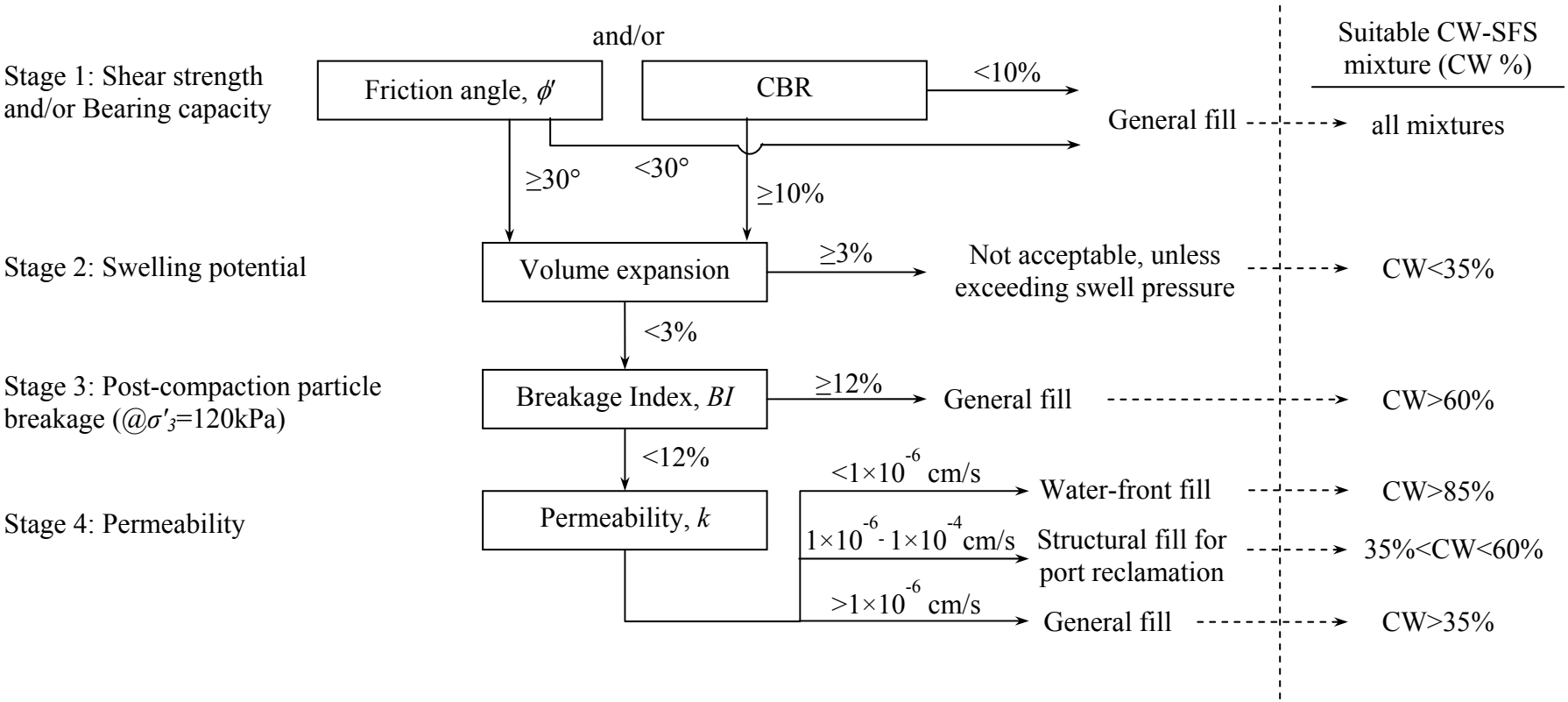

Figure 6.1 Proposed acceptance criteria for CW-SFS blends as structural fills (modified after Chiaro *et al.*, 2014b)

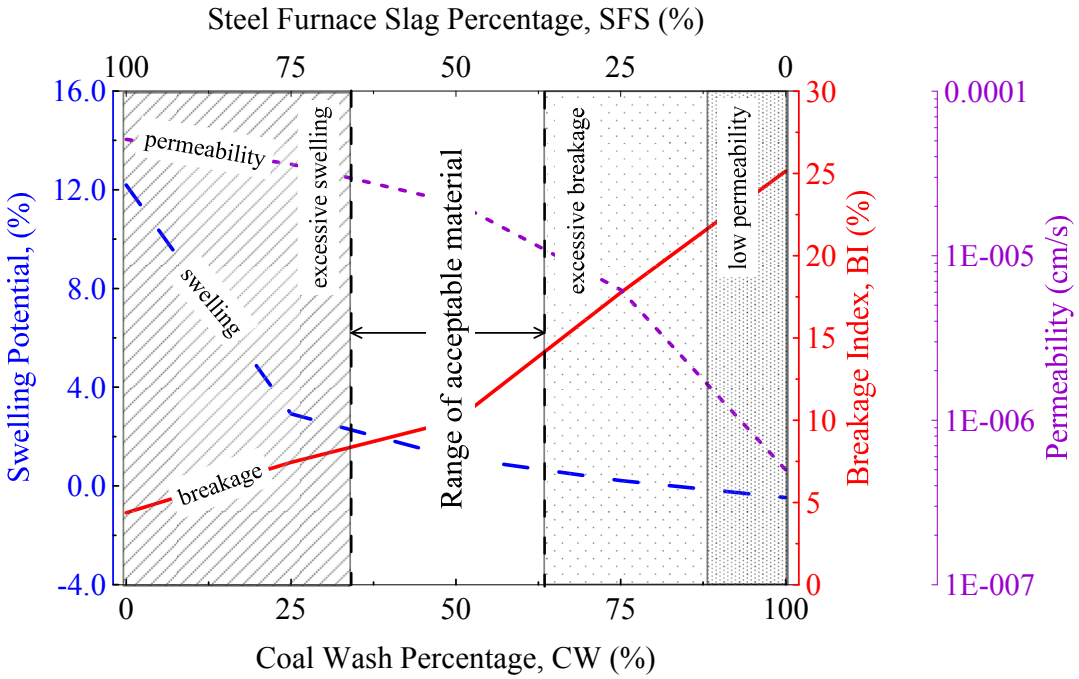

Figure 6.2 Optimisation of CW-SFS blends as structural fill for port reclamation (modified after Chiaro *et al.*, 2014b)

6.3 PORT KEMBLA OUTER HARBOUR RECLAMATION

Located on the east coast of Australia, Port Kembla is one of three major ports in the state of New South Wales (NSW), besides Sydney and Newcastle. The Port Kembla Harbour was established in the late 1890's to facilitate the export of coal from the mines of the Wollongong region. Since that time, it has rapidly grown to accommodate both the expansion of traditional industries along with the development of new ones. Port Kembla Port Corporation (PKPC) is currently expanding its Outer Harbour (Figure 6.3) to provide additional land and berthing facilities to cater for future trade growth. While the recent Inner Harbour development provides facilities to cater for the growth of existing trades, the Outer Harbour development has the potential to address the needs of new industry. It includes the reclamation of approximately 42 hectares of land and the construction of 7 new berths (Lai *et al.*, 2011).

Most of the land reclamation to date within the Inner Harbour has been carried out using blast furnace slag. However, as blast furnace slag is in short supply, CW-SFS

mixture has now been considered to be used above the tidal level. Generally, the dredged material from the surrounding area is considered suitable as fill material, but since the dredged fills in Port Kembla area are contaminated by pyrites that produce sulphuric acid upon excavation (oxidation) and can threaten marine species and the surrounding coastal environment, and also since blast furnace slag is in short supply, PKPC decided to use a mixture of CW-SFS for reclamation, at least for the above high tide level.

Laboratory investigation on the geotechnical properties of different mixtures of CW and SFS (as elaborated in Chapters 4 and 5), enabled the selection of two mixtures to be used in the field trial following the optimisation method explained earlier. It is important to mention that, at the request of PKPC, the two blends were initially selected based only on the strength and permeability properties, as at that time the roles of swelling and particle breakage were not completely established. Nevertheless, the field trial was an essential part of this investigation in order to properly measure *in-situ* swelling and to understand the advantages and limitations of using CW-SFS blends as compacted fill material (Chiaro *et al.*, 2014b).

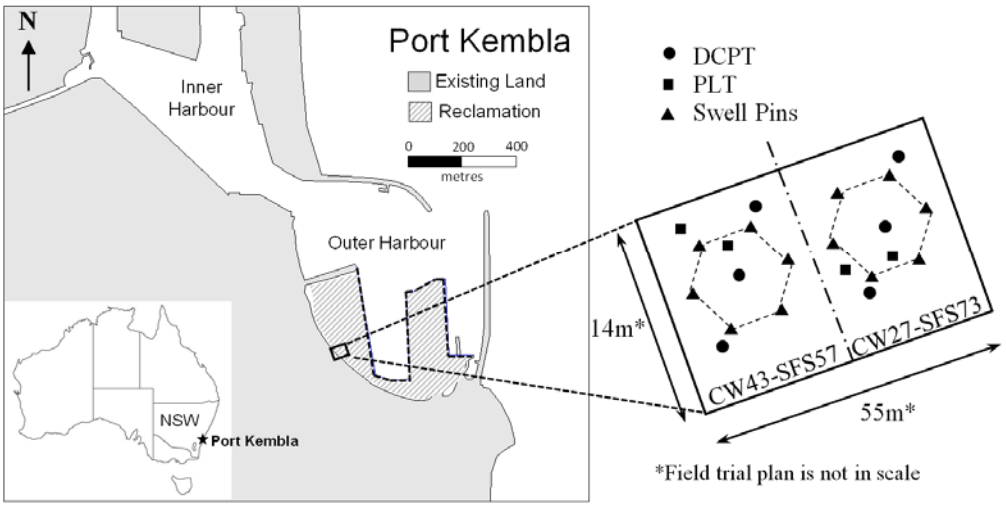

Figure 6.3 Layout of Port Kembla reclamation project and the field trial

The field trial was conducted at the Port Kembla Outer Harbor reclamation site shown in Figure 6.3. An area of 55m by 14m was provided by PKPC for the field trial, and the depth of layer was 1.4m (i.e. total volume of 1078m^3). The area was

divided into two equal parts to assess the performance of two selected mixtures CW43-SFS57 and CW27-SFS73 prepared by weight percentage, which is equivalent to CW50-SFS50 and CW20-SFS80 by volume percentage, respectively. In the laboratory, typically the mixes are prepared by weight, but given the difficulty associated with preparing those mixes by weight in the field, a volume ratio was adopted instead. The mixing and placing of the materials was performed by an excavator and the materials were spread and levelled by a motor grader in the designated area. The compaction was carried out by a 13-tonnes smooth steel drum roller and a layer thickness of 300mm was adopted. At the end of each layer, the *in-situ* density was determined by performing sand cone replacement (SCR) and nuclear densometer (ND) tests. A total of 37 SCR and 34 ND measurements were conducted on the two mixtures (Figure 6.4 and Figure 6.5). In Figure 6.4, the stage sequence of the field trial assessment is shown and in Figure 6.5 the field trial area prior to and after compaction is illustrated.

6.4 FIELD INVESTIGATION

6.4.1 Compaction

At the end of each compacted layer, the *in-situ* density was routinely monitored. A total of 37 sand cone replacement (SCR) and 34 nuclear densometer (ND) tests were conducted. Figure 6.6 shows the results obtained during compaction in terms of dry unit weight and moisture content from the SCR and ND tests. Since the moisture contents of the specimens from ND were unreliable, the average moisture content from SCR specimens was taken for the calculation of dry unit weight for ND specimens. The maximum dry unit weights (MDUW) from laboratory tests for CW43-SFS57 and CW27-SFS73 were 20.21 and 21.13kN/m^3, respectively. The lines corresponding to 90%, 95%, and 100% of relative MDUW were also plotted for comparison. Figure 6.6 shows that for both mixtures, four roller passes were sufficient to reach a relative compaction of 90% and further passes had insignificant influence on the dry unit weight. The *in-situ* dry unit weight of CW43-SFS57 was in

the range of 16.5-20kN/m^3 while for the CW27-SFS73 it was 18.9-20.9kN/m^3. The higher value for the latter mixture is due to the higher content of SFS, which has higher specific gravity compared to CW.

Figure 6.4 Field trial testing: (a) construction site (55m×14m×1.4m), (b) mixing stage using an excavator, (c) levelling off the layer by a motor grader, (d) compaction stage by vibratory smooth steel drum, (e) density control using sand cone replacement (SCR), and (f) *in-situ* density measurement using a nuclear densometer (ND)

Figure 6.5 Field trial in Port Kembla: (a) prior to fill placement; (b) during compaction; and (c) after compaction

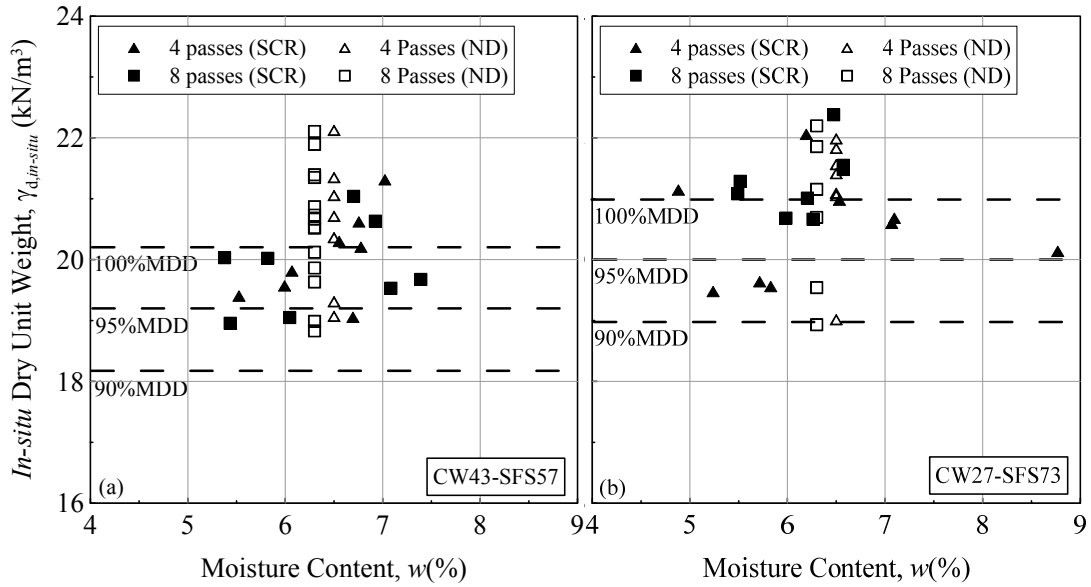

Figure 6.6 Field dry unit weight and moisture content determined by SCR and ND for (a) CW-43-SFS57 and (b) CW27-SFS73

The results of the particle size distribution on the collected specimens for the sand cone replacement are plotted in Figure 6.7. It is evident that although the material prior to compaction consisted of large particles, a significant amount of particle degradation occurred during compaction, particularly for CW particles, due to the energy applied by the vibratory steel drum. Therefore, most of the large particles (>20mm) were broken down to smaller particles and the gradation of the specimens prepared in the laboratory was close to the one for the field after compaction.

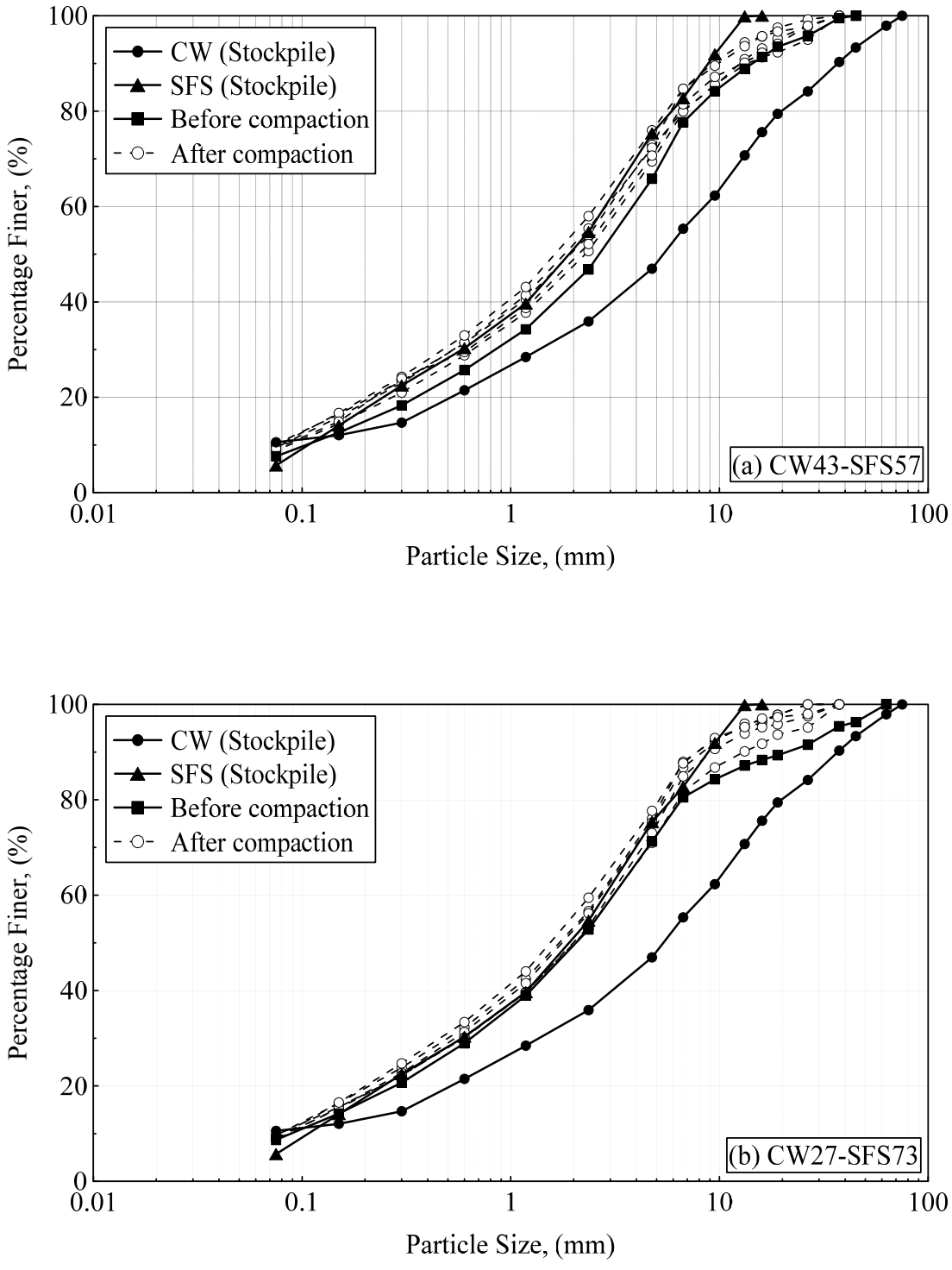

Figure 6.7 Particle size distribution before and after compaction for (a) CW43-SFS57 and (b) CW27-SFS73

6.4.2 Dynamic Cone Penetration Test (DCPT)

To assess the strength of the mixtures along the depth of compaction layers, 6 Dynamic Cone Penetration Tests (DCPTs) were performed in accordance to ASTM D6951 (three tests for each mixture), and the locations of these tests are shown in Figure 6.3. In this test the number of blows required to drive the cone penetrometer 100mm into the compacted layers was measured throughout the test. Finally, the equivalent *in-situ* CBR was calculated from the measured penetration as follows (ASTM D6951),

$$CBR = 292 / DCP^{1.12} \tag{6.1}$$

where DCP is the penetration per blow (mm/blow).

The results of the DCPTs are presented in Figure 6.8. As it was expected, at shallow depth (<300mm), the equivalent *in-situ* CBR values were small due to the low confinement. However, for greater depths, the CBR value increased significantly up to layer 2. In layer 1, there was a decrease in CBR, and that might be attributed to poor compaction within that layer. Although the results of the DCPT for the two mixtures were similar (i.e. increased with depth), the CBR values of CW43-SFS57 were slightly higher and more scattered than those of CW27-SFS77. This could be due to the existence of larger particles of CW, which implies that the cone penetration could have been impeded by the larger particles. By comparing the equivalent *in-situ* CBR values with the other conventional fill such as dense to very dense sand which is in a range of 25-50 (Look, 2007), these mixtures may be considered suitable to be used as structural fill in terms of shear strength.

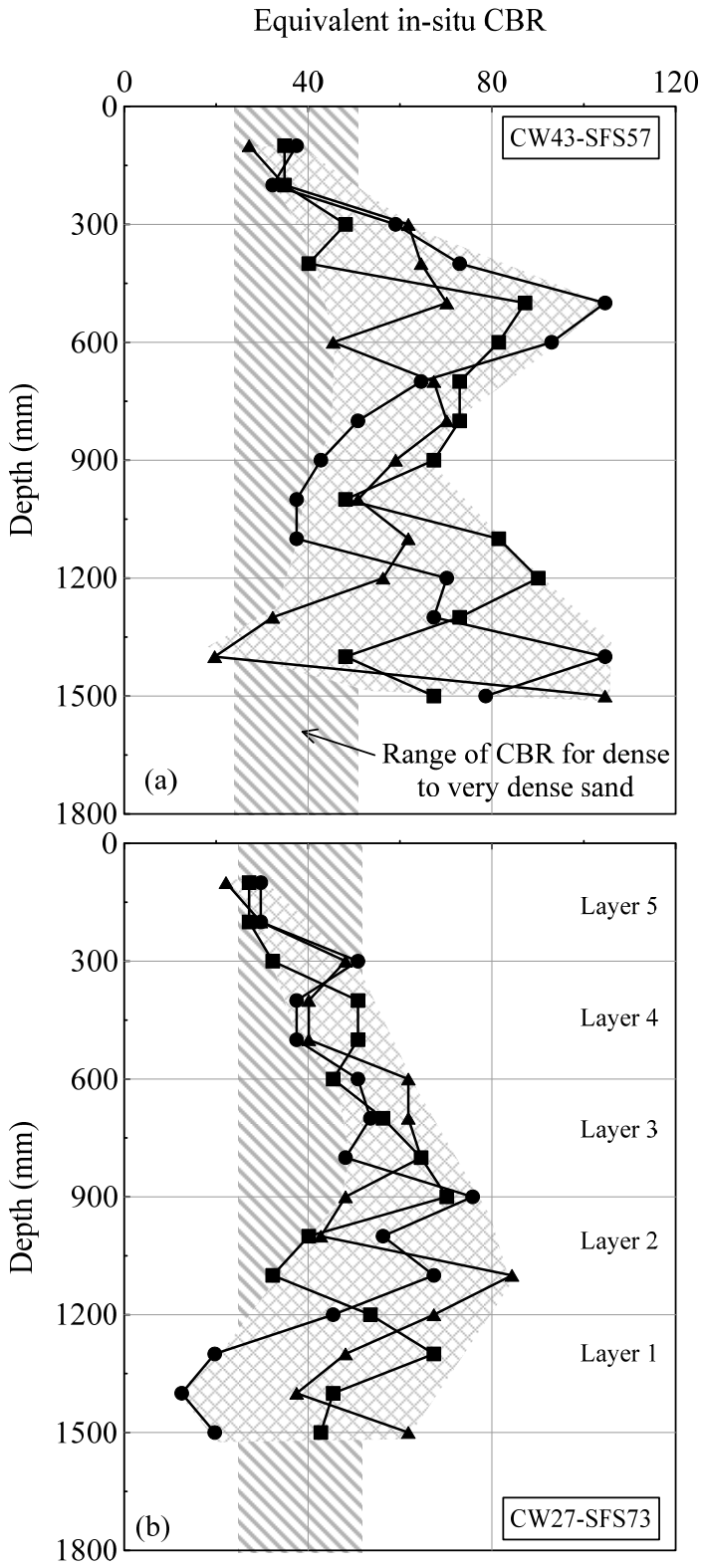

Figure 6.8 Variation of the equivalent *in-situ* CBR with depth for (a) CW-SFS57 and (b) CW27-SFS73

6.4.3 Plate Load Test (PLT)

In total, four Plate Load Tests (PLTs) were conducted for assessing the deformation behaviour of the mixtures in two stages. The first and second stages were 30 and 170 days after compaction, respectively. The reason for the two stages of PLT was to investigate the effects of chemical reaction on the strength of the CW-SFS mixtures due to the presence of free lime (CaO) and free magnesium (MgO) in the SFS. The tests were conducted using a 300mm diameter rigid circular plate in accordance with ASTM D1194. The reaction was provided by a heavy truck and the load was applied through a hydraulic jack. Three dial gauges were used in a triangle pattern to measure displacement (to accuracy of 0.01mm) and they were fixed to a reference beam (Figure 6.9a). For each loading increment, the settlements were measured at fixed time intervals and the load was maintained until the change in settlement was less than 0.01mm/min.

Figure 6.9 (a) Plate load test setup in the field trial (b) settlement on the surface after plate load test

The settlement curves against time for the tests conducted 30 and 170 days after compaction are plotted in Figure 6.10 and Figure 6.11, respectively. It is shown that once the change in vertical displacement of dial gauges was negligible, the next step of loading or unloading was allowed to proceed. The variation of applied pressure with settlement, for the two stages (i.e. 30 and 170 days after compaction) is plotted in Figure 6.12.

It was evident that yielding did not occur for the maximum pressure applied (i.e. 1000kPa). Therefore, the maximum load-bearing capacity could not be defined from these tests. Furthermore, these mixtures underwent swelling with time; this caused a crust-type layer to be formed on the surface, and thus a sitting pressure equal to 400kPa was identified in the results of the second stage. Under relatively low pressure, this layer prevented the propagation of stress in the underlying layer. As it can be observed, beyond this pressure level (400kPa) the pressure-settlement curve is governed by a quasi-elastic response (i.e. unloading-reloading stages follow the same line). From the results of the unloading-reloading stages, the moduli of reaction in the elastic region (K_s) for CW43-SFS57 and CW27-SFS73 were 5.60 and 10.80 MPa/mm, respectively.

The results showed that under typical port loading conditions which include 50kPa live load (Lai *et al.*, 2011) to 120kPa (to be increased in the future), the settlement of the two mixtures would be less than 1mm (Figure 6.12). Therefore, these mixtures demonstrated suitability to be used as structural fill in terms of settlement. The strength gain with time was more significant for the mixture with higher SFS content (CW27-SFS73). For instance, the settlements under 500kPa applied pressure for the mixture CW27-SFS73 at the 30 and 170 days were 6.0mm and 2.4mm, whereas for CW43-SFS57 the corresponding settlements were approximately 7.2mm and 7.5mm, respectively (the settlement under the plate after removal was hardly visible, as shown in Figure 6.9b).

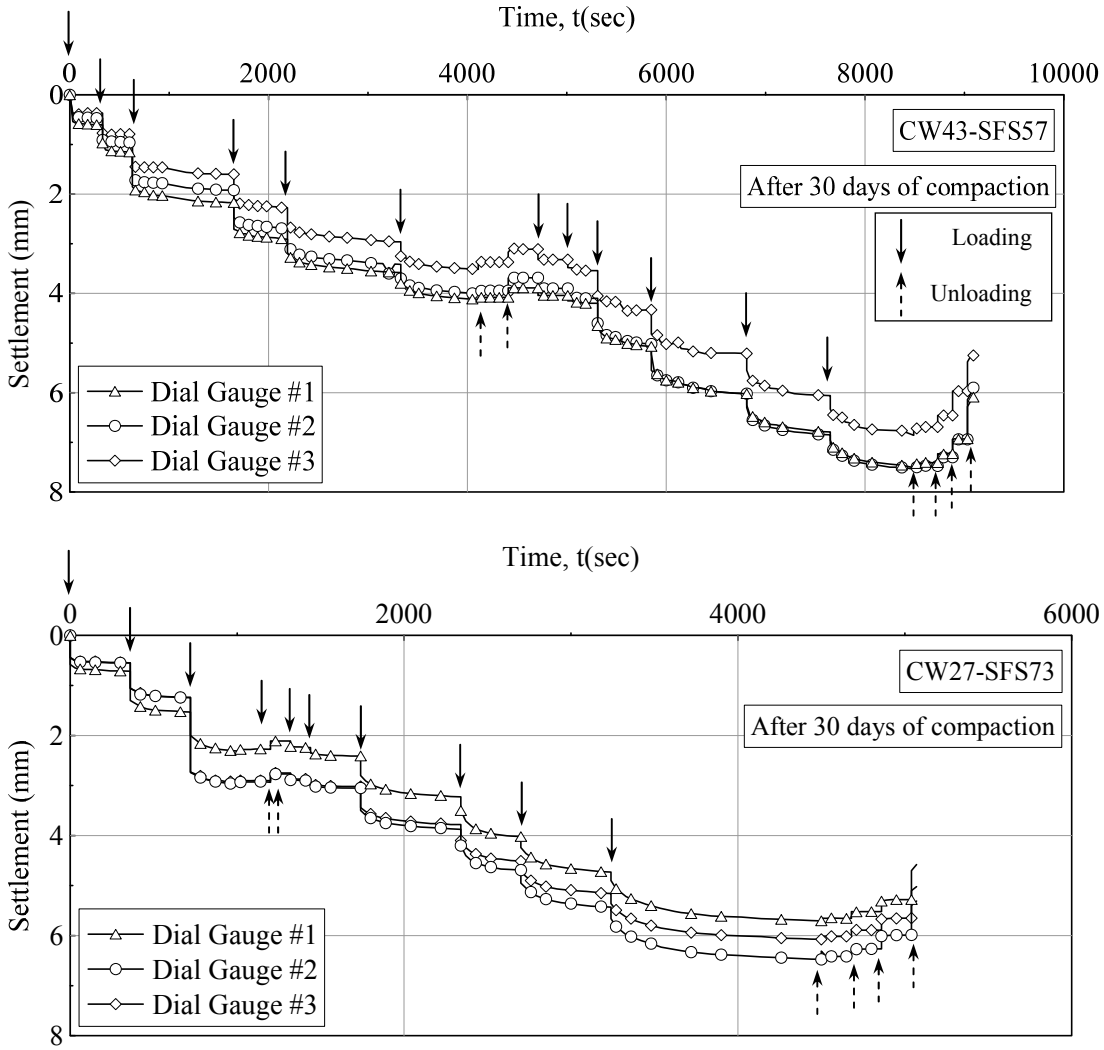

Figure 6.10 Results of settlement with time in the plate load test on two selected CW-SFS mixtures after 30 days of compaction

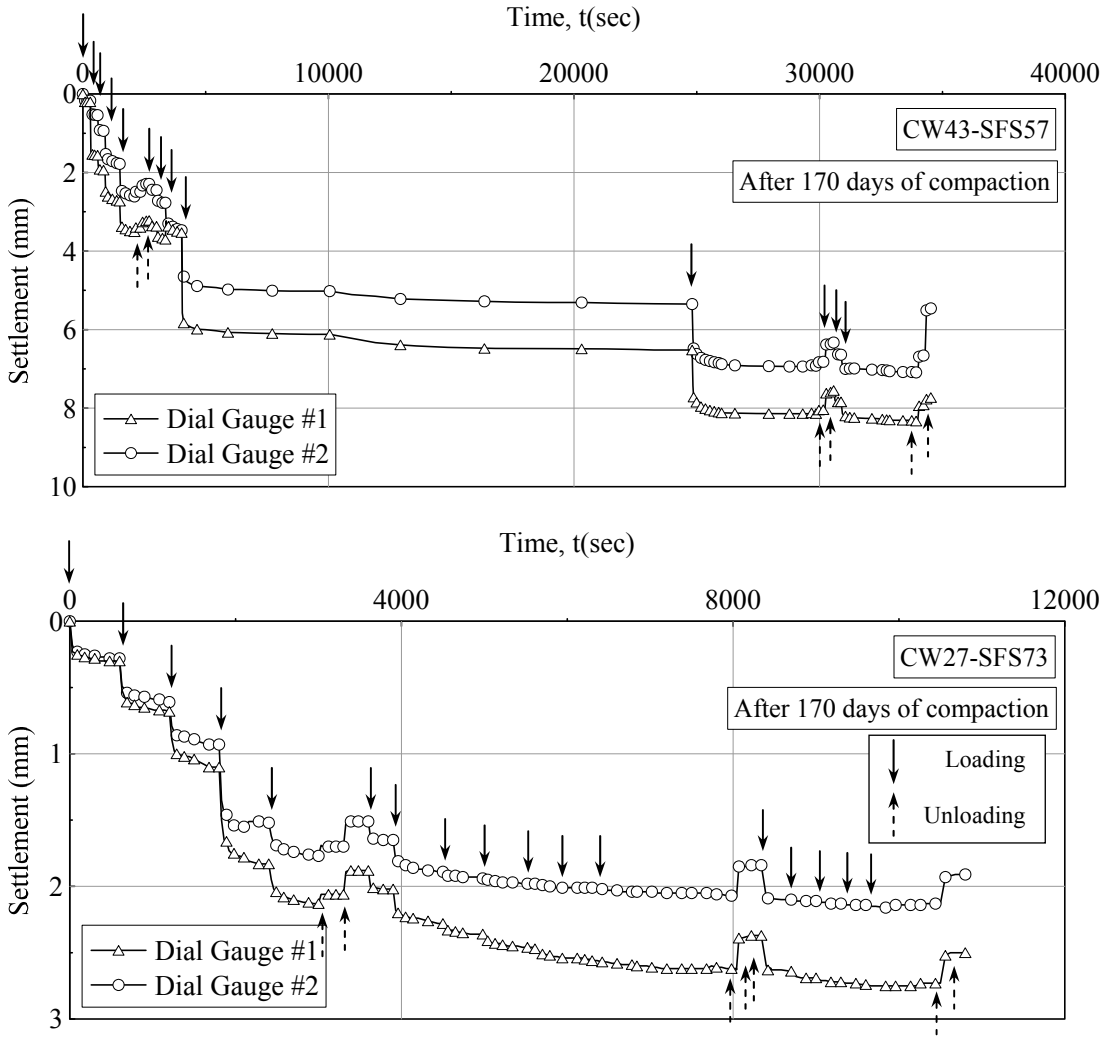

Figure 6.11 Results of settlement with time in the plate load test on two selected CW-SFS mixtures after 170 days of compaction

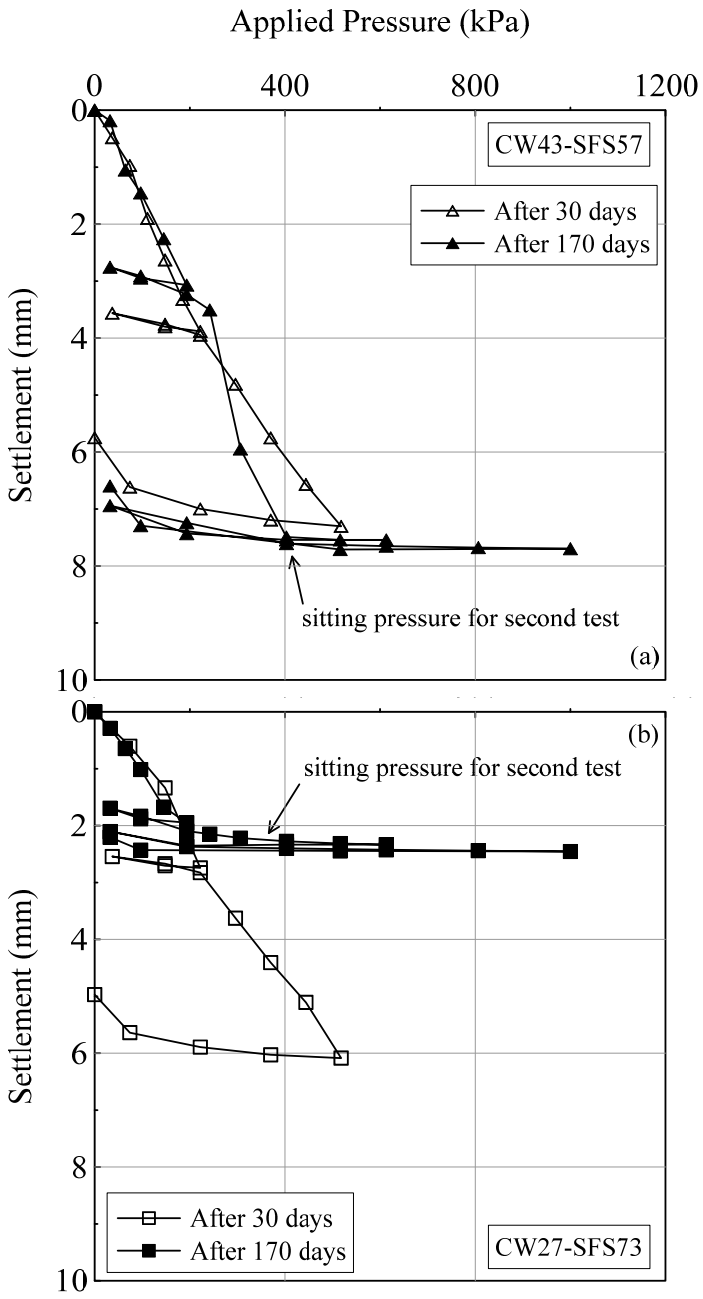

Figure 6.12 Variation of pressure against settlement in plate load test for (a) CW43-SFS57 and (b) CW27-SFS73

6.4.4 Swelling potential

After compaction, 12 steel rods (300mm long) were installed into the compacted layer in a hexagonal pattern and acted as surveying pins for monitoring the vertical expansion with time (Figure 6.13). Each rod was embedded 200mm into the layer and protruded 100mm above the top surface. The variation of the level of the steel rods was measured in relation to a surface benchmark for 6 months. Initially, the readings were taken weekly and then the time intervals were increased to a monthly basis.

The swell potential, which is the ratio of vertical expansion to the layer thickness in percentage, was determined by surveying, and the results are plotted in Figure 6.13. As expected, the mixture with higher SFS content showed more swelling, due to the higher content of CaO and MgO. After 154 days, the swelling potential for CW43-SFS57 and CW27-SFS73 were 6.3% and 5%, respectively. Since the vertical expansion of SFS requires moisture for hydration, the rate of swelling potential increased significantly between 15 and 35 days due to continuous rainfall for several days.

Although the swelling potential of the mixture is an unfavourable factor for these materials, any surcharge applied (e.g. pavement, live loads) would reduce the vertical expansion substantially, as it was reported by Wang *et al.*, 2010. In fact, provided that the applied load exceeds the swell pressure (usually determined in the laboratory), no vertical expansion would occur.

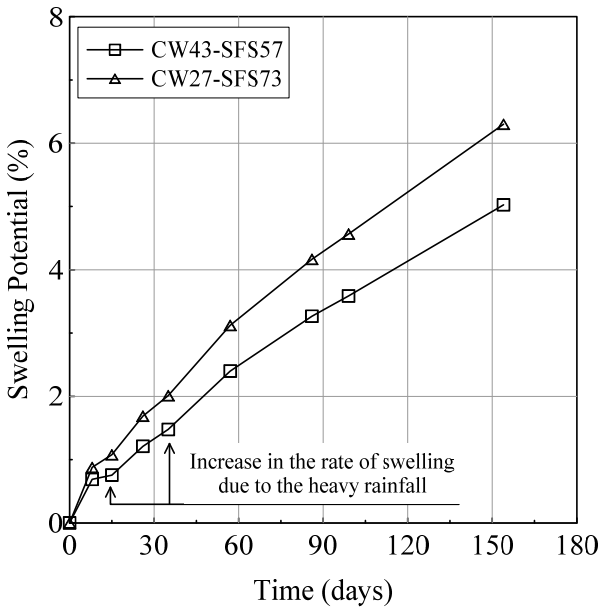

Figure 6.13 Variation of swelling potential for the CW-SFS mixtures in the field

6.5 SUMMARY

While CW-SFS fills have shear resistance, bearing capacity and permeability properties similar or superior to conventional sandy fills, their use may still be restricted by excessive swelling and/or particle breakage. Consequently, the acceptance criteria merely based on shear strength and permeability may not be sufficient to fully judge whether or not such a granular waste blend meets all the requirements for an acceptable reclamation fill. Therefore, an optimisation method was proposed to adopt the most suitable blended waste for the project specifications and requirements, and two CW-SFS blends were chosen to be assessed in large scale in field trial.

Field performance of two CW and SFS mixtures were evaluated and discussed by conducting DCPTs, PLTs, and swell monitoring. The two selected mixtures were identified through laboratory studies as suitable reclamation fill. The following conclusions were extracted from this study:

1- It was observed that a minimum 4 passes of a 13-tonne vibratory smooth roller was adequate to compact the mixtures to the dry unit weight exceeding 90% relative

compaction. Further passes had insignificant effect on the final dry unit weight of the mixtures.

2- The results of DCPT on the mixtures showed that the average equivalent *in-situ* CBR was between 46 and 60 and this value was greater than the minimum required of 25. This implies that the shear and compression strength of the compacted CW-SFS mixtures was adequate to be qualified as an acceptable structural fill.

3- The results of the PLT indicated that the settlement-deformation of the compacted CW-SFS mixtures increased with time due to hydration of the SFS component. The increase in the compression strength was more significant in the mixture with a higher SFS content. For this mixture, the vertical settlement under 500kPa applied pressure decreased from 6.0mm to 2.3mm.

4- Although the two mixtures exhibited promising results in terms of strength and settlement behaviour, the vertical expansion of the two blends was 6.3% and 5% respectively, due to the existence of CaO and MgO in the SFS fraction.

The field investigation confirmed that the compacted mixtures of CW-SFS had similar properties to conventional sandy fills used for land reclamation, in terms of dry unit weight and shear strength. However, the SFS content in the mixture should be limited due to its swelling potential, and further laboratory investigation is essential to establish the swell pressure for different mixtures, so that long term stability can be ensured.

It is important to note that, the results presented in this paper are only indicative and not necessarily applicable to all types of CW-SFS blends, since the geotechnical properties of such wastes can vary significantly, depending on the chemical contents of the materials, the original source and manufacturing processes.

CHAPTER SEVEN

7 NUMERICAL ANALYSIS OF THE BEHAVIOUR OF CW-SFS MIXTURES

7.1 INTRODUCTION

In Chapter 5, the behaviour of the CW-SFS mixtures was predicted by developing a mathematical model, and then the experimental results under triaxial conditions were compared to the model predictions. The model simulation was programmed in the MATLAB code. However, for more complex loading and boundary conditions, it was necessary to establish a subroutine for that model and then implement it into a finite element software.

The main objective of this chapter is to describe the method for the implementation of the CW-SFS prediction model into UMAT subroutine for the finite element code, ABAQUS (Hibbitt *et al.*, 2012). It also covers model verification using the drained triaxial results on the different CW-SFS mixtures, and then compares the numerical model with the field study.

7.1 BACKGROUND ON CONTINUUM PLASTICITY

In this section, a brief review on the continuum plasticity required for the implementation of the developed constitutive model for CW-SFS mixtures is discussed for completeness. It contains definitions for stress and strain tensors, mean and deviatoric stress in general space, and generalized elasto-plastic matrix. Most of the fundamental equations are provided in Anandarajah (2011), Davis and Selvadurai (2002), and Zienkiewicz and Taylor (2000). In addition, the derivation of the yield surface and plastic potential to the stress components in the general stress space is also described.

7.1.1 Stress and strain tensors

The stress and strain can be defined both in tensor or vector notations. The tensor definition of the stress and strain in the three-dimensional space can be defined as:

$$\sigma = \begin{bmatrix} \sigma_{11} & \sigma_{12} & \sigma_{13} \\ \sigma_{12} & \sigma_{22} & \sigma_{23} \\ \sigma_{13} & \sigma_{23} & \sigma_{33} \end{bmatrix} \tag{7.1}$$

$$\varepsilon = \begin{bmatrix} \varepsilon_{11} & \varepsilon_{12} & \varepsilon_{13} \\ \varepsilon_{12} & \varepsilon_{22} & \varepsilon_{23} \\ \varepsilon_{13} & \varepsilon_{23} & \varepsilon_{33} \end{bmatrix} \tag{7.2}$$

In the case of axisymmetric condition, the stress and strain are reduced to the following equations:

$$\sigma = \begin{bmatrix} \sigma_{11} & \sigma_{12} & 0 \\ \sigma_{12} & \sigma_{22} & 0 \\ 0 & 0 & \sigma_{33} \end{bmatrix} \tag{7.3}$$

$$\varepsilon = \begin{bmatrix} \varepsilon_{11} & \varepsilon_{12} & 0 \\ \varepsilon_{12} & \varepsilon_{22} & 0 \\ 0 & 0 & \varepsilon_{33} \end{bmatrix} \tag{7.4}$$

It should be noted that in commercial finite element (FE) software such as ABAQUS, the vector (Voigt) notation of stress and strain is used. Voigt notation is the way to reduce the order of a tensor due to symmetry and it is advantageous over the tensorial notation for describing plasticity equations. Considering the vector notation, the stress and strain in ABAQUS for the axisymmetric conditions are stored as:

$$\sigma = \begin{bmatrix} \sigma_{11} & \sigma_{22} & \sigma_{33} & \sigma_{12} \end{bmatrix}^T \tag{7.5}$$

$$\varepsilon = \begin{bmatrix} \varepsilon_{11} & \varepsilon_{22} & \varepsilon_{33} & \gamma_{12} \end{bmatrix}^T \tag{7.6}$$

where γ_{12} is the engineering shear strain ($\gamma_{12} = 2\varepsilon_{12}$).

The mean (p) and deviatoric stress (q) for axisymmetric condition is defined as:

$$p = \frac{1}{3}\left(\sigma_{11} + \sigma_{22} + \sigma_{33}\right) \tag{7.7}$$

$$q = \sqrt{3J_2}$$
$$J_2 = \frac{1}{6}\left[\left(\sigma_{11} - \sigma_{22}\right)^2 + \left(\sigma_{22} - \sigma_{33}\right)^2 + \left(\sigma_{33} - \sigma_{11}\right)^2\right] + {\sigma_{12}}^2 \tag{7.8}$$

where J_2 is the second deviatoric stress invariant.

7.2 ALGORITHM FOR STRESS INTEGRATION

To calculate the stress increment under a given strain increment, a numerical algorithm to integrate the constitutive equations is required. The accuracy of the numerical analysis is dependent on the integration method. There are many methods for the numerical integration such as: radial return map, one step forward Euler, one step backward Euler, and sub-stepping methods (Auricchio and Taylor, 1995; Schreyer *et al.*, 1979; Nguyen, 1977; Sloan, 1987). Due to the accuracy and the simplicity of the sub-stepping method, this method was adopted for the implementation of CW-SFS constitutive model into ABAQUS.

The algorithm for the UMAT subroutine consists of two main stages. The first stage is known as the elastic predictor. In this stage, the increment of strains that enters into the UMAT as input parameters is initially considered as elastic-only strains and thus, the elastic increment of stress is calculated. The second stage is called 'plastic corrector' and in this stage, based on the elastic predictor stress and by following the formulation of yield and plastic flow surfaces, the initial elastic predictor is refined until convergence is reached. In the next section, the detailed description of the stress integration algorithm to calculate the stress increment corresponding to the strain increment that is computed within the ABAQUS and transferred to UMAT is provided.

7.2.1 Determination of the continuum elasto-plastic tangent modulus

The incremental relations between stresses and strains are determined through the derivation of continuum elasto-plastic tangent modulus. In order to implement the CW-SFS model into the UMAT subroutine, all the derivations, stresses and strains should be given in matrix form. In the theory of plasticity, the increment of strains decomposed into elastic and plastic components according to the following equation:

$$\partial\varepsilon = \partial\varepsilon_e + \partial\varepsilon_p \tag{7.9}$$

The increment of elastic strain is calculated by Hooke's law and the increment of plastic strain is assumed to be governed by flow rule using Equations (7.10) and (7.11):

$$\partial\varepsilon_e = D^{e^{-1}}\partial\sigma \tag{7.10}$$

$$\partial\varepsilon_p = \partial\lambda\frac{\partial g}{\partial\sigma} \tag{7.11}$$

where D^e is the elastic stiffness matrix, $\partial\lambda$ is a scalar multiplier (or plastic multiplier) and g is the plastic potential. The following equation is used for calculating the plastic multiplier as follow:

$$\partial\lambda = \frac{n^T D^e \partial\varepsilon_e}{H + n^T D^e m} \tag{7.12}$$

In chapter 5, it was shown that the increment of stress tensor can be determined using the following equation (i.e. generalized elasto-plastic matrix):

$$\begin{gathered}\partial\sigma = \left[D^{ep}\right]\partial\varepsilon \\ \partial\sigma = \left(D^e - \frac{D^e m n^T D^e}{H + n^T D^e m}\right)\partial\varepsilon\end{gathered} \tag{7.13}$$

where, D^{ep} is the continuum elasto-plastic tangent stiffness (continuum Jacobian) matrix (Mroz and Zienkiewicz, 1984); m is the plastic flow direction vector ($\frac{\partial g}{\partial\sigma}$);

n is the loading direction vector ($\frac{\partial f}{\partial \sigma}$) and H is the plastic modulus. In axisymmetric conditions, the elastic stiffness matrix (D^e), the increment of stress and strain tensors are given by:

$$D^e = \begin{bmatrix} 2G+\lambda & \lambda & \lambda & 0 \\ \lambda & 2G+\lambda & \lambda & 0 \\ \lambda & \lambda & 2G+\lambda & 0 \\ 0 & 0 & 0 & G \end{bmatrix} \tag{7.14}$$

$$\partial\sigma = \{\partial\sigma_{11} \quad \partial\sigma_{22} \quad \partial\sigma_{33} \quad \partial\sigma_{12}\}^T \tag{7.15}$$

$$\partial\varepsilon = \{\partial\varepsilon_{11} \quad \partial\varepsilon_{22} \quad \partial\varepsilon_{33} \quad \partial\gamma_{12}\}^T \tag{7.16}$$

where G is the shear modulus and λ is the Lame parameter. For the CW-SFS model, it was shown that the elastic properties are state dependent (i.e. pressure dependent) and they are given by:

$$G = \frac{3(1-2\nu)}{2(1+\nu)}K \tag{7.17}$$

$$\lambda = K - \frac{2G}{3} \tag{7.18}$$

in the above ν is the Poisson's ratio; K is the bulk modulus and is defined by $K = \frac{(1+e)p}{\kappa}$ (p' is the current effective mean stress; κ is the swelling-recompression index; and e is the current void ratio).

For determining the loading direction vector (n) and plastic flow direction vector (m), it is essential to establish the derivation of yield function and plastic potential in general space conditions. This can be done by using the chain rule of differentiation as follows:

$$\left\{\frac{\partial f}{\partial \sigma}\right\}=\begin{Bmatrix}\frac{\partial f}{\partial \sigma_{11}}\\ \frac{\partial f}{\partial \sigma_{22}}\\ \frac{\partial f}{\partial \sigma_{33}}\\ \frac{\partial f}{\partial \sigma_{12}}\end{Bmatrix}=\begin{Bmatrix}\frac{\partial f}{\partial p'}\frac{\partial p'}{\partial \sigma_{11}}+\frac{\partial f}{\partial q}\frac{\partial q}{\partial \sigma_{11}}\\ \frac{\partial f}{\partial p'}\frac{\partial p'}{\partial \sigma_{22}}+\frac{\partial f}{\partial q}\frac{\partial q}{\partial \sigma_{22}}\\ \frac{\partial f}{\partial p'}\frac{\partial p'}{\partial \sigma_{33}}+\frac{\partial f}{\partial q}\frac{\partial q}{\partial \sigma_{33}}\\ \frac{\partial f}{\partial p'}\frac{\partial p'}{\partial \sigma_{12}}+\frac{\partial f}{\partial q}\frac{\partial q}{\partial \sigma_{12}}\end{Bmatrix}=\begin{Bmatrix}n_p\frac{\partial p'}{\partial \sigma_{11}}+n_q\frac{\partial q}{\partial \sigma_{11}}\\ n_p\frac{\partial p'}{\partial \sigma_{22}}+n_q\frac{\partial q}{\partial \sigma_{22}}\\ n_p\frac{\partial p'}{\partial \sigma_{33}}+n_q\frac{\partial q}{\partial \sigma_{33}}\\ n_p\frac{\partial p'}{\partial \sigma_{12}}+n_q\frac{\partial q}{\partial \sigma_{12}}\end{Bmatrix} \tag{7.19}$$

$$\left\{\frac{\partial g}{\partial \sigma}\right\}=\begin{Bmatrix}\frac{\partial g}{\partial \sigma_{11}}\\ \frac{\partial g}{\partial \sigma_{22}}\\ \frac{\partial g}{\partial \sigma_{33}}\\ \frac{\partial g}{\partial \sigma_{12}}\end{Bmatrix}=\begin{Bmatrix}\frac{\partial g}{\partial p'}\frac{\partial p'}{\partial \sigma_{11}}+\frac{\partial g}{\partial q}\frac{\partial q}{\partial \sigma_{11}}\\ \frac{\partial g}{\partial p'}\frac{\partial p'}{\partial \sigma_{22}}+\frac{\partial g}{\partial q}\frac{\partial q}{\partial \sigma_{22}}\\ \frac{\partial g}{\partial p'}\frac{\partial p'}{\partial \sigma_{33}}+\frac{\partial g}{\partial q}\frac{\partial q}{\partial \sigma_{33}}\\ \frac{\partial g}{\partial p'}\frac{\partial p'}{\partial \sigma_{12}}+\frac{\partial g}{\partial q}\frac{\partial q}{\partial \sigma_{12}}\end{Bmatrix}=\begin{Bmatrix}m_p\frac{\partial p'}{\partial \sigma_{11}}+m_q\frac{\partial q}{\partial \sigma_{11}}\\ m_p\frac{\partial p'}{\partial \sigma_{22}}+m_q\frac{\partial q}{\partial \sigma_{22}}\\ m_p\frac{\partial p'}{\partial \sigma_{33}}+m_q\frac{\partial q}{\partial \sigma_{33}}\\ m_p\frac{\partial p'}{\partial \sigma_{12}}+m_q\frac{\partial q}{\partial \sigma_{12}}\end{Bmatrix} \tag{7.20}$$

where $n_p=\xi_f\left\lfloor\eta_f\exp\left(\mu_f\psi\right)-\eta\right\rfloor$, $m_p=\xi_g\left\lfloor M_{cs}\exp\left(\mu_g\psi\right)-\eta\right\rfloor$, and $n_q=m_q=1$. It can be seen that for defining the gradients of yield surface, there is no need to have an explicit formulation for the yield surface.

The gradient of the mean and deviatoric stresses in axisymmetric conditions are given by the derivation of Equations (7.7) and (7.8):

$$\frac{\partial p}{\partial \sigma_{11}}=\frac{\partial p}{\partial \sigma_{22}}=\frac{\partial p}{\partial \sigma_{33}}=\frac{1}{3}\quad,\quad\frac{\partial p}{\partial \sigma_{12}}=0 \tag{7.21}$$

$$\frac{\partial q}{\partial \sigma_{11}} = \frac{1}{2}\frac{\frac{1}{2}\left[(2)(\sigma_{11}-\sigma_{22})+(2)(-1)(\sigma_{33}-\sigma_{11})\right]}{\sqrt{3J_2}} = \frac{1}{2\sqrt{3J_2}}\left[\sigma_{11}-\sigma_{22}-\sigma_{33}+\sigma_{11}\right]$$

$$= \frac{1}{2\sqrt{3J_2}}\left[3\sigma_{11}-(\sigma_{11}+\sigma_{22}+\sigma_{33})\right] = \frac{1}{2\sqrt{3J_2}}(3\sigma_{11}-3p')$$

$$\Rightarrow \frac{\partial q}{\partial \sigma_{11}} = \frac{\sqrt{3}}{2\sqrt{J_2}}(\sigma_{11}-p') \tag{7.22}$$

$$Similarly: \frac{\partial q}{\partial \sigma_{22}} = \frac{\sqrt{3}}{2\sqrt{J_2}}(\sigma_{22}-p)$$

$$\frac{\partial q}{\partial \sigma_{33}} = \frac{\sqrt{3}}{2\sqrt{J_2}}(\sigma_{33}-p)$$

$$and: \frac{\partial q}{\partial \sigma_{12}} = \frac{\sqrt{3}}{\sqrt{J_2}}\sigma_{12}$$

Finally, the gradients of yield surface and plastic potential can be determined by combining Equations (7.19) to (7.22):

$$\left\{\frac{\partial f}{\partial \sigma}\right\} = \begin{Bmatrix} \frac{n_p}{3}+\frac{\sqrt{3}}{2\sqrt{J_2}}(\sigma_{11}-p) \\ \frac{n_p}{3}+\frac{\sqrt{3}}{2\sqrt{J_2}}(\sigma_{22}-p) \\ \frac{n_p}{3}+\frac{\sqrt{3}}{2\sqrt{J_2}}(\sigma_{33}-p) \\ \frac{\sqrt{3}}{\sqrt{J_2}}\sigma_{12} \end{Bmatrix} \tag{7.23}$$

$$\left\{\frac{\partial g}{\partial \sigma}\right\} = \begin{Bmatrix} \frac{m_p}{3}+\frac{\sqrt{3}}{2\sqrt{J_2}}(\sigma_{11}-p) \\ \frac{m_p}{3}+\frac{\sqrt{3}}{2\sqrt{J_2}}(\sigma_{22}-p) \\ \frac{m_p}{3}+\frac{\sqrt{3}}{2\sqrt{J_2}}(\sigma_{33}-p) \\ \frac{\sqrt{3}}{\sqrt{J_2}}\sigma_{12} \end{Bmatrix} \tag{7.24}$$

7.2.2 Sub-stepping algorithm method

The sub-stepping algorithm method of iteration was proposed by Sloan (1987) and it is based on the Euler integration scheme. In this method, each step is divided into a number of sub-steps based on the error calculation at individual sub-steps (or iteration) and then the time increment is automatically adjusted (i.e. decreases or increases) corresponding to the calculated error in the previous time increment. In the Euler integration scheme, initially (i.e. at the time t_i the total strain increment $\{\partial\varepsilon_i\}$ is assumed to be fully elastic and the elastic stress predictor is calculated using the following equation:

$$\Delta\sigma_e = \{\partial\sigma_i^{trial}\} = \{\sigma_{i-1}\} + [D^e]\{\partial\varepsilon_i\} \tag{7.25}$$

As explained in Chapter 5, the proposed model for CW-SFS mixtures assumes that for any given shear stress increment, both elastic and plastic deformations always occur, so that a purely elastic region does not exist (i.e. soil continuously yields from the very small strains). Therefore, the trial stress (which is purely elastic) should be corrected based on the plastic strain increment, which can be calculated by following the flow rule. The sub-stepping scheme comes into effect at this point of the subroutine, which may be summarized as follows (Sloan, 1987):

1. Calculate the trial stress (elastic predictor) using Equation (7.25) and assume an error tolerance (*ETOL*) for the iteration
2. Set the sub-step dimensionless parameter (i.e. T) equal to zero and the first increment of sub-step (ΔT) equal to 1 ($\Delta T = 1$)
3. Conduction step 4 to 8 while $T < 1$
4. For the $k = 1,2$, compute $\Delta\sigma_k$ according to the following equations:

$$\{\Delta\sigma_k\} = \Delta T\Delta\sigma_e - \Delta\lambda_k[D^e]\left\{\frac{\partial g}{\partial\sigma}\right\}_k \tag{7.26}$$

$$\partial\lambda_k = \frac{\left\{\frac{\partial f}{\partial \sigma}\right\}_k^T \Delta\sigma_e}{H_k + \left\{\frac{\partial f}{\partial \sigma}\right\}_k^T [D^e] \left\{\frac{\partial g}{\partial \sigma}\right\}_k} \tag{7.27}$$

$$\begin{aligned} \{\sigma_1\} &= \{\Delta\sigma_e\} \\ \{\sigma_2\} &= \{\sigma_1\} + \{\Delta\sigma_1\} \end{aligned} \tag{7.28}$$

5. Determine the first sub-step error and the new stress as given by:

$$Error = \frac{1}{2}\left(-\Delta\sigma_1 + \Delta\sigma_2\right) \tag{7.29}$$

$$\{\sigma_i\} = \{\sigma_{i-1}\} + \frac{1}{2}\left(\{\Delta\sigma_1\} + \{\Delta\sigma_2\}\right) \tag{7.30}$$

6. Calculate the relative error for the sub-step according to:

$$R = \max\left\{\frac{\|Error\|}{\|\sigma_i\|}, 10^{-14}\right\} \tag{7.31}$$

7. If $R < ETOL = 10^{-2}\ to 10^{-5}$ then the current sub-step is acceptable and the stresses and dimensionless parameter (i.e. T) can be updated according to:

$$\begin{aligned} \{\sigma\} &= \{\sigma_i\} \\ T &= T + \Delta T \end{aligned} \tag{7.32}$$

Now, the size of the next sub-step can be changes based on the calculated error as given by:

$$\begin{aligned} \Delta T &= I\Delta T \\ I &= \min\left\{0.8\sqrt{\frac{TOL}{R}}\ , 2\right\} \end{aligned} \tag{7.33}$$

The total time increment should be checked to be less than 1 for each increment by controlling the following equation:

$$\Delta T = \min\{\Delta T\ , 1 - T\} \tag{7.34}$$

8. If $R > ETOL$, this means that the result of the sub-step was not accurate enough; thus the size of the sub-step should be decreased and then rechecked by going back to the step 3 according to:

$$\Delta T = I\Delta T$$
$$I = \max\left\{0.8\sqrt{\frac{TOL}{R}}\ ,\ 0.1\right\} \tag{7.35}$$

9. Finally, the new increment of stress at time t_i is calculated and updated.

7.3 DEVELOPMENT OF UMAT SUBROUTINE IN ABAQUS

The numerical method for the integration described in the previous section was used to find the updated stresses as well as the material tangential modulus (Jacobian matrix) in the UMAT subroutine for the ABAQUS. This method was adopted for the implementation of the model developed for CW-SFS mixtures. In the UMAT subroutine, the following steps were carried out for the calculation (the summary of the flow chart is presented in Figure 7.1):

1- The total strain increment ($\partial\varepsilon^{total}$) is calculated by the main software (ABAQUS) based on the global stiffness matrix, loading and boundary conditions specified for the meshed model.
2- Based on the current state parameters including void ratio, state parameter, and effective mean stress (e, ψ, p'), the elastic parameters (G, K, λ) for defining the elastic stiffness matrix (D^e) are calculated.
3- Initially, $\partial\varepsilon^{total}$ is assumed to be the only elastic strain increment and therefore the increment of the elastic stress predictor ($\Delta\sigma_e$ or $\partial\sigma_i^{trial}$) is calculated using the D^e in step 2.
4- Now, the increment of stress should be corrected based on the amount of plastic strain occurring following the method described in section 7.2.2.
5- Once the corrected increment of stress is calculated, the updated tangent stiffness modulus is calculated and given back to the main software to update

the global stiffness matrix using the Newton-Raphson iteration method. It is important to ensure that the tangent stiffness modulus in the UMAT be accurate enough, as it is being used by ABAQUS to update the global stiffness matrix and the calculation of the new strain increment. In addition, parameters that are not calculated in ABAQUS as output variables are stored as solution-dependent state variable (known as STATEV) such as volumetric strain, state parameter, and void ratio.

6- The new increment of strain is then defined by the main software using the updated global stiffness matrix, and then the steps 1 to 6 are repeated until the end of loading (or displacement) applied on the geometry.

The performance of the UMAT subroutine for the CW-SFS model was verified and calibrated by comparing with the drained triaxial results, and then the application of the model was investigated by establishing a plate load test and comparing the numerical results with the field trial tests. These phases of the study are described in the following sections.

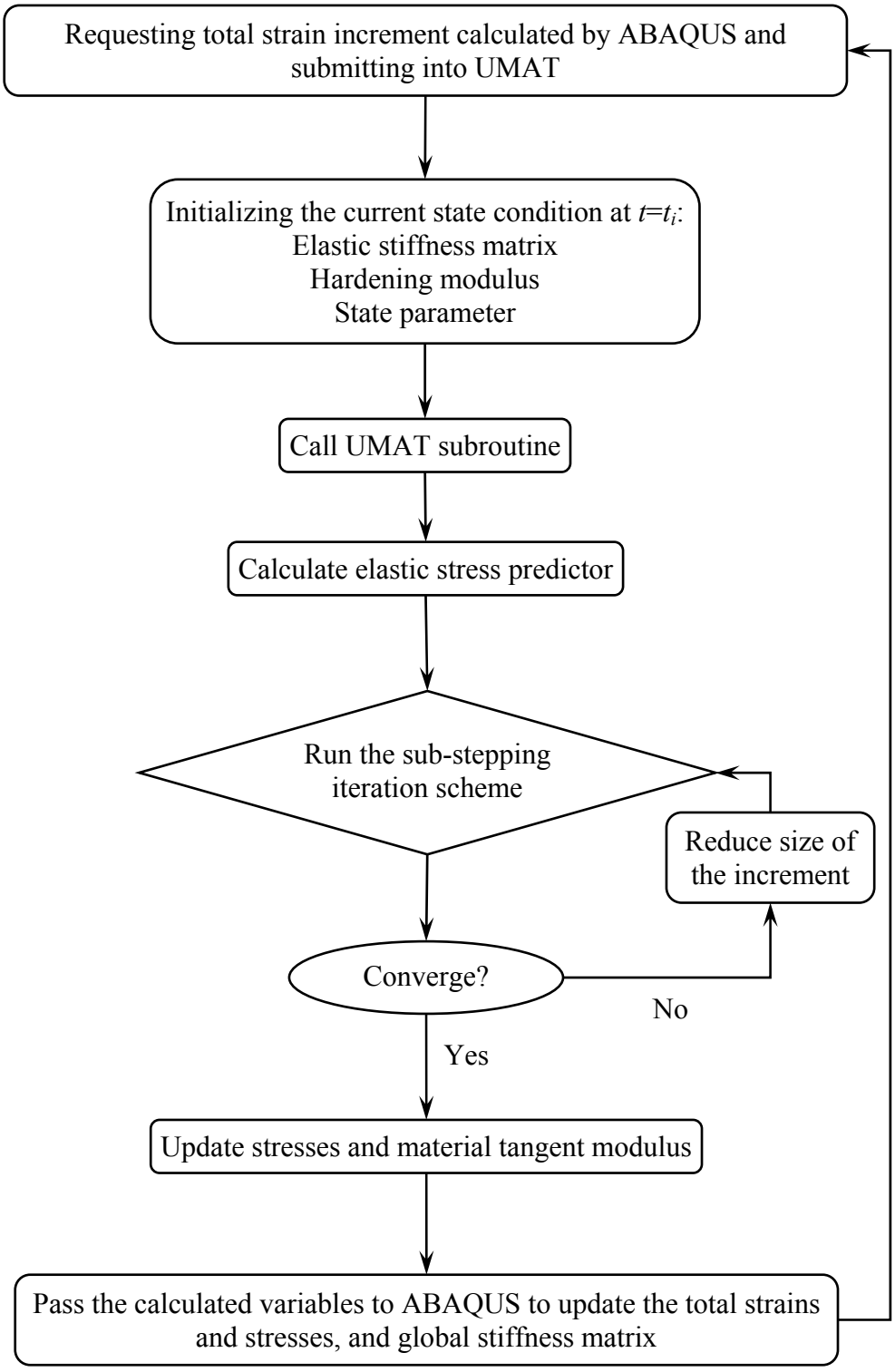

Figure 7.1 Flow chart for the UMAT subroutine in ABAQUS

7.3.1 Verification of numerical model

In the previous sections, the stress update algorithm (i.e. sub-stepping method) for the mathematical model developed for CW-SFS mixtures was described. This method was implemented in the ABAQUS software using the UMAT subroutine (more details in Appendix B). In this section, the verification of this subroutine is described, and it includes the comparison between the laboratory triaxial test results, the MATLAB code developed in Chapter 5 (i.e. the explicit programming using the forward Euler approach with very small strain increment such as 10^{-5}) and the FE model in the ABAQUS. Due to the symmetry in triaxial specimen, instead of three dimensional geometry, the axisymmetric model can be used as shown in Figure 7.2.

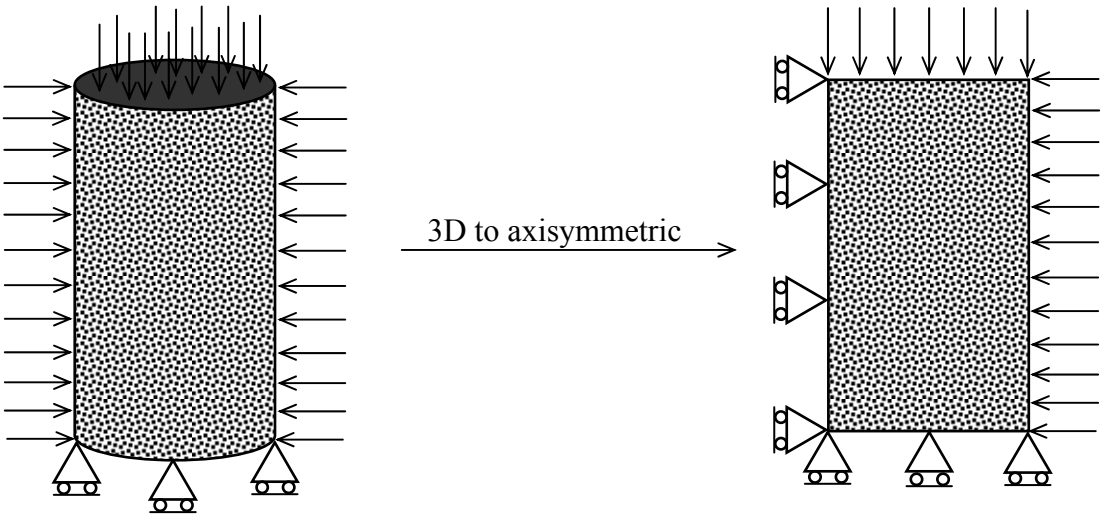

Figure 7.2 Conversion of three dimensions triaxial specimen to axisymmetric

The first step of verification is checking the response of the single element in the FE code under the triaxial loading. The single element consists of four nodes and it is referred as CAX4 in ABAQUS. The boundary conditions for the model were defined in a way that the left and the bottom faces are allowed to move vertically and horizontally, respectively. Then, two steps of loading were applied on the element. Firstly, the required isotropic pressure (i.e. confining pressure) was applied on the top and right faces of the axisymmetric model. Then shearing was applied by subjecting a downward displacement on the top face of the element, and it was

equivalent to 25% axial strain while maintaining the confining pressure from the previous step (Figure 7.3).

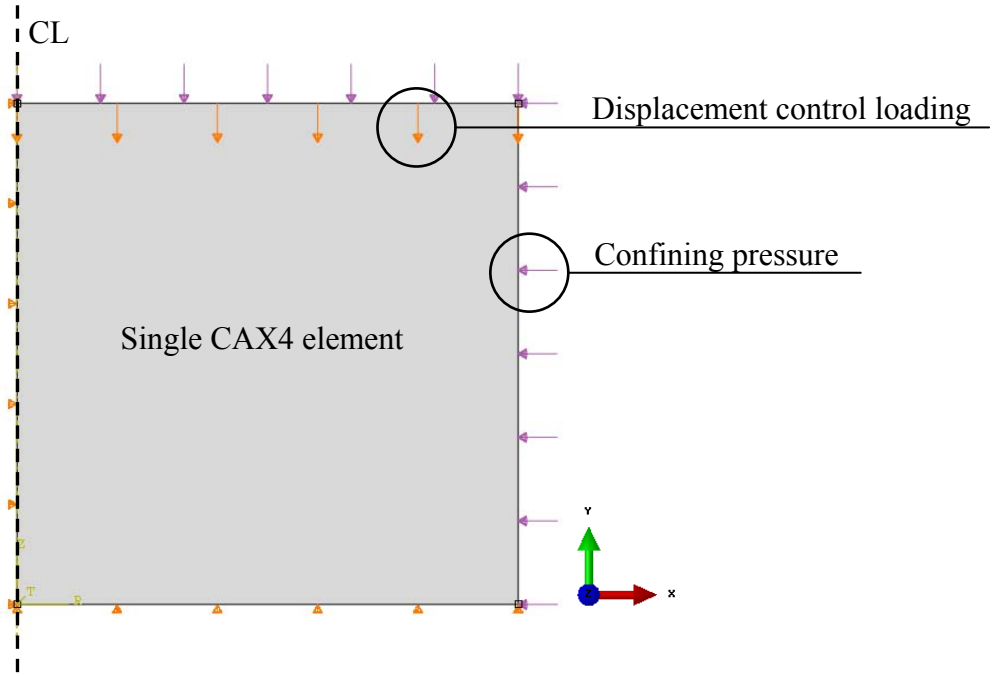

Figure 7.3 Boundary and loading condition for the axisymmetric single CAX4 element in ABAQUS for model verification under triaxial condition

The model parameters used in the FE simulations were the same as those reported in Chapter 5 (Table 5.6). The verification of the numerical model for the single element illustrated in Figure 7.3 with the laboratory results and the MATLAB code for CW50-SFS50 under two confining pressures (i.e. 60kPa and 120kPa) are presented in Figure 7.4. It is evident that the UMAT subroutine based on the CW-SFS constitutive model can successfully predict the behaviour. The stress-strain behaviour (i.e. volumetric compression with the strain-hardening and the dilative behaviour with the strain-softening after the peak) was observed to depend on the initial conditions in terms of the void ratio and the mean stress. As a result, the triaxial specimens for all CW-SFS were simulated using the developed UMAT subroutine. The discretised mesh for the triaxial specimen is shown in Figure 7.5. The boundary and loading conditions for the triaxial specimen are similar to the single element (i.e. Figure 7.3).

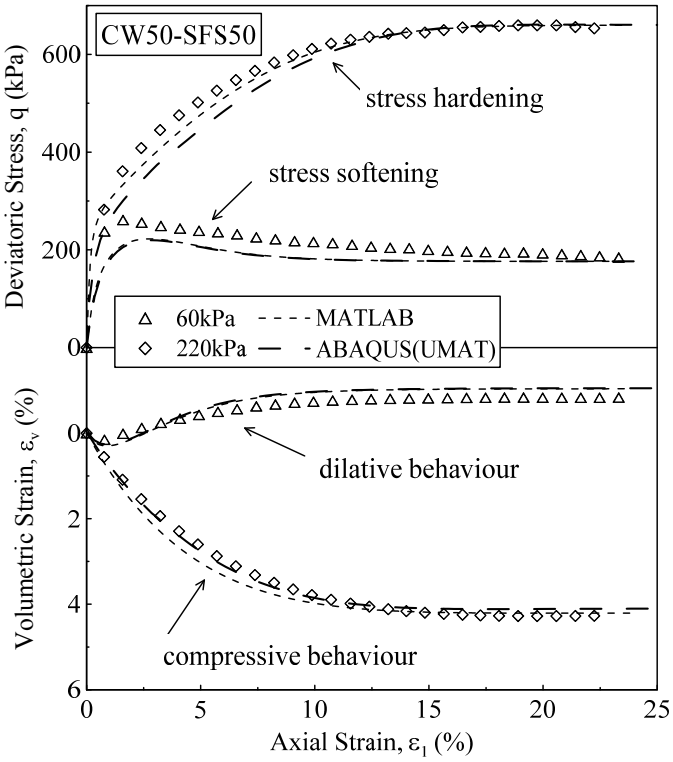

Figure 7.4 Verification of the UMAT subroutine using single element for CW50-S50 under two confining pressures

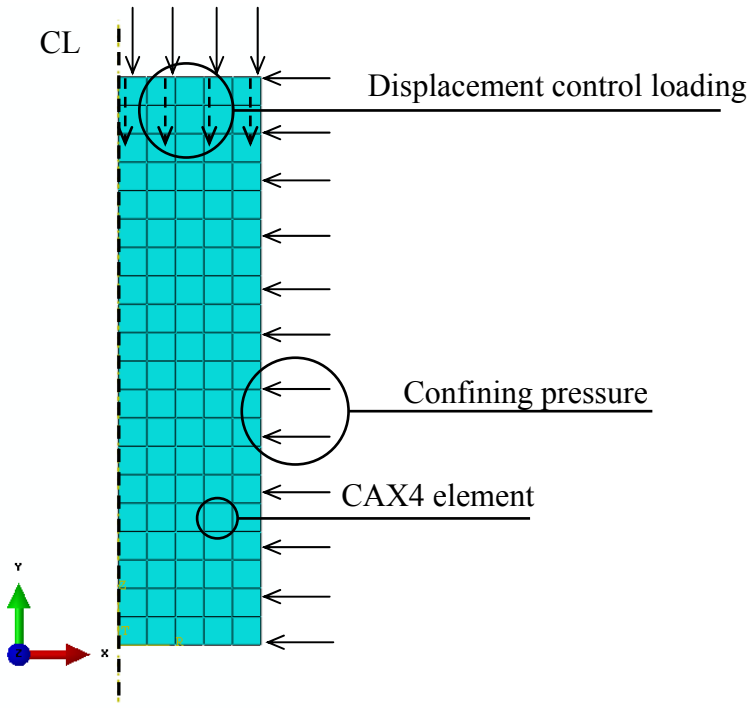

Figure 7.5 Discretised mesh for the simulation of the triaxial specimen

The prediction of the numerical model with the laboratory results and the MATLAB code for all mixtures under four confining pressures is presented in Figure 7.6 and includes the variation of deviatoric stress and volumetric strain with axial strains. It is evident that there is a good agreement between numerical model and the experimental results as well as with the MATLAB code. The numerical model was capable to capture both contractive response with strain hardening for the specimen under high confining pressure (e.g. 220kPa) and the dilative behaviour followed by strain softening for the specimen under lower confining pressure (e.g. 30kPa). Similar to the experimental observation, the numerical model captured the critical state condition after around 20% axial strain.

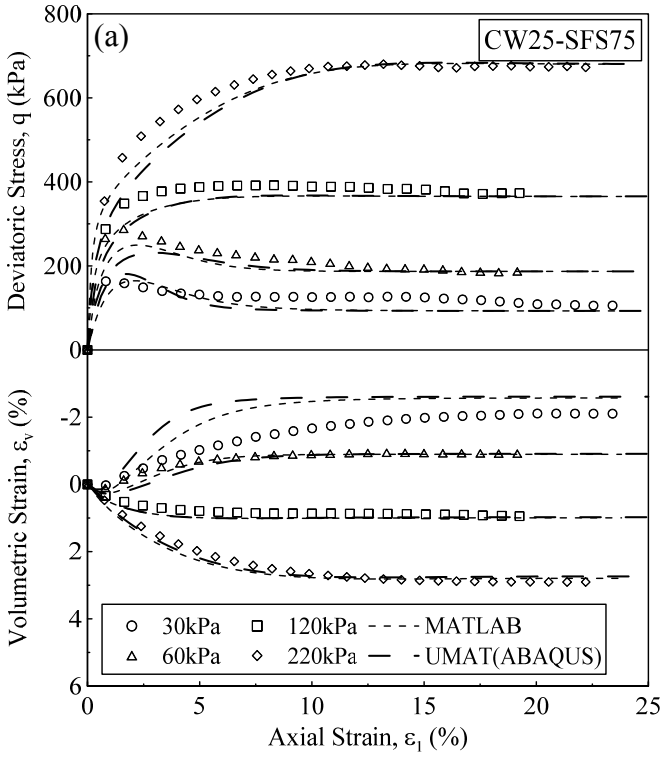

Figure 7.6 (a) Verification of numerical model with experimental results and MATLAB simulation under triaxial conditions for CW25-SFS75

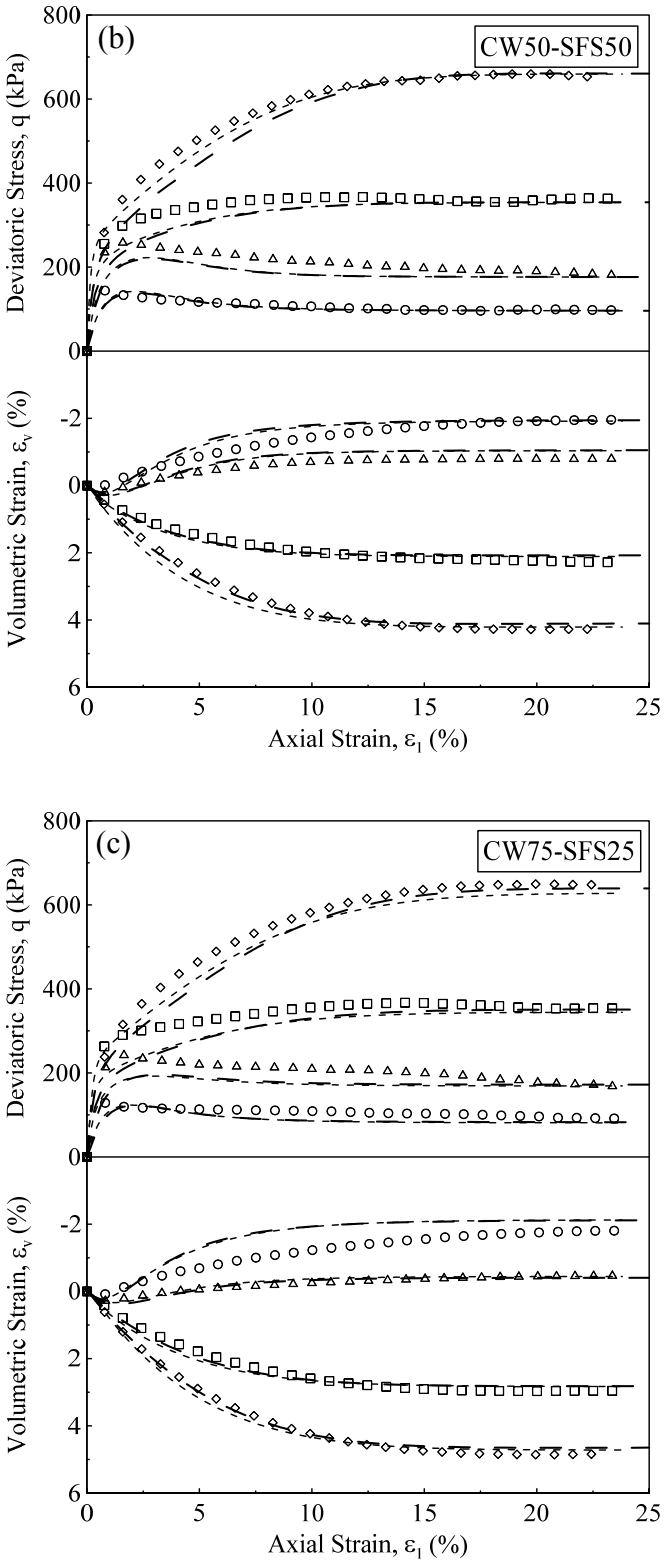

Figure 7.6 (b) and (c) Verification of numerical model with experimental results and MATLAB simulation under triaxial conditions for CW50-SFS50 and CW75-SFS25

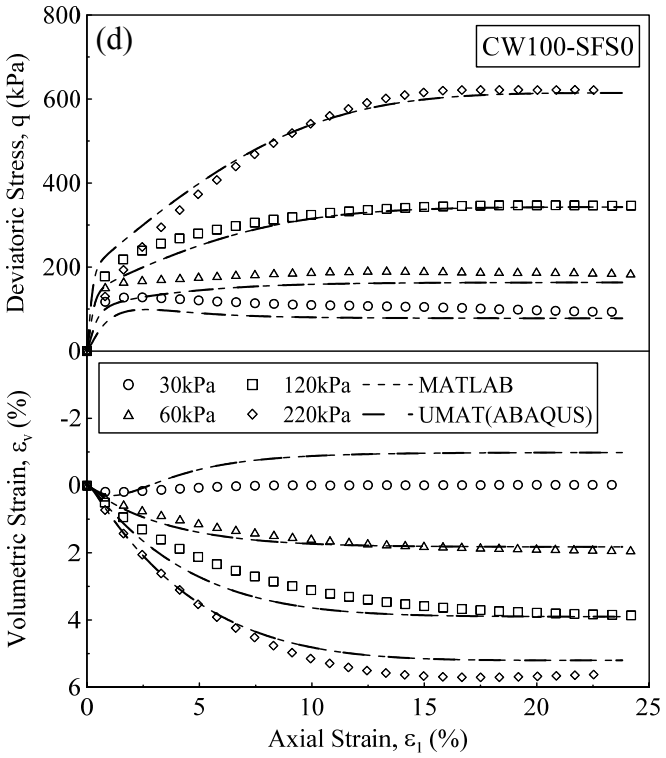

Figure 7.6 (d) Verification of numerical model with experimental results and MATLAB simulation under triaxial conditions for CW100-SFS0

7.3.2 Practical application of the numerical model

The main objective of the implementation of the constitutive model into the ABAQUS was to evaluate the numerical model in general loading and boundary conditions similar to the field application, and to allow more detailed investigation into the behaviour of CW-SFS mixtures. For this point, a numerical model for the plate load test (PLT) was established to simulate the results of the field trial tests. Due to the symmetry in the PLT, all FE analysis were performed using an axisymmetric mesh having 4-noded stress-strain elements (CAX4) and thus, only half of the domain was considered. To eliminate the effect of boundary conditions on the results, the size of the numerical domain was considered large enough as shown in Figure 7.7. The bottom boundary of the mesh was fully constrained (i.e. both horizontal and vertical directions) and the two side boundaries were allowed to move in the vertical direction only. Under the loading area (i.e. PLT), the size of the mesh

was finer as shown in Figure 7.7 compared to other areas as stress concentration is expected to occur.

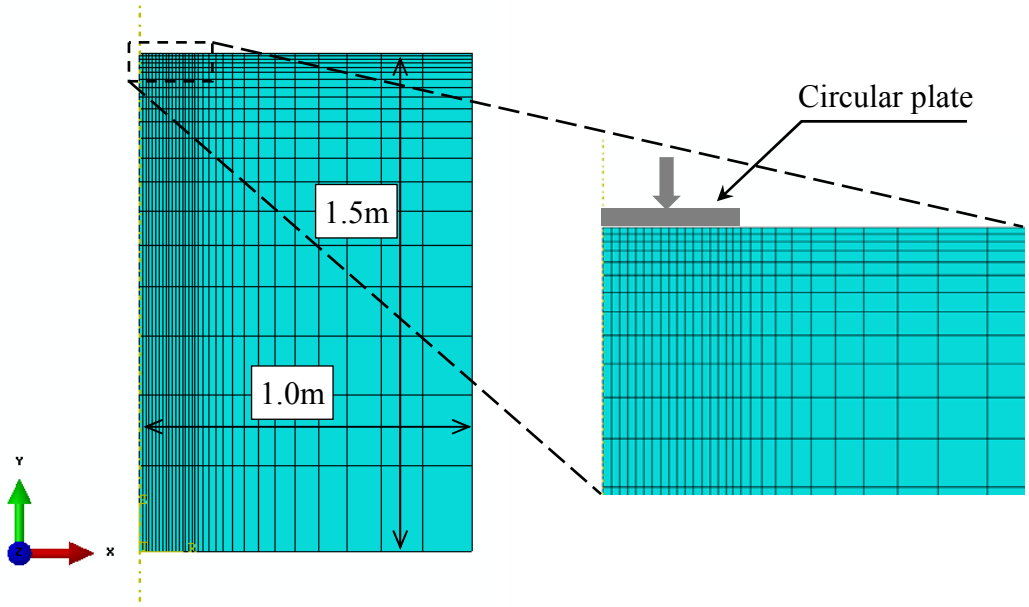

Figure 7.7 Geometry and mesh of CW-SFS layer in the field trial under plate load test

The materials used in the field trial investigation were slightly varied compared to those that were tested under controlled conditions in the laboratory. In addition, the ratio of the CW and SFS in the field was less stringently controlled in comparison to the laboratory specimens. Therefore, the parameters for the constitutive model differed to those used for the model verification (i.e. section 7.3.1). The calibrated material parameters for two blends that were tested in the field are summarized in Table 7.1.

Two steps of loading were applied on the model. Initially, the geostatic stresses (i.e. *in-situ* stresses) were propagated by defining the unit weight of the soil and applying gravity force. An example of *in-situ* vertical stresses for CW43-SFS57 is plotted in Figure 7.8 along with the vertical displacement that is zero (it should be noted that only the top 1.15m of the geometry is shown). In the second step, the displacement was applied on the loaded area as the analysis was performed under displacement-controlled conditions. The magnitudes of the displacements were set to the values

monitored in the field trial tests under load intervals and the vertical displacements and stresses were monitored. In Figure 7.9, the contours for the propagation of vertical displacement and stress are plotted at three different levels of vertical displacement applied to the specimen CW43-SFS57.

Table 7.1 Parameters used in numerical simulation of the plate load test

Soil parameters	Symbol	Values	
		CW43-SFS57	CW27-SFS73
In-situ condition	γ_d (kN/m^3)	19.0	21.3
	G_s	2.88	3.05
	e_0	0.486	0.404
Elastic	κ	0.0035	0.0030
	ν	0.20	0.2
Critical state	Γ^*	1.840	1.826
	λ^*	0.062	0.051
	M_{cs}^*	1.502	1.518
Loading direction	ξ_f	1.25	1.25
	μ_f	2	2
Dilatancy	ξ_g	1.45	1.45
	μ_g	3	3
Plastic modulus	h_0 (kPa)	100000	200000
	μ_{pk}	14	14
	μ_f	1.412	1.53

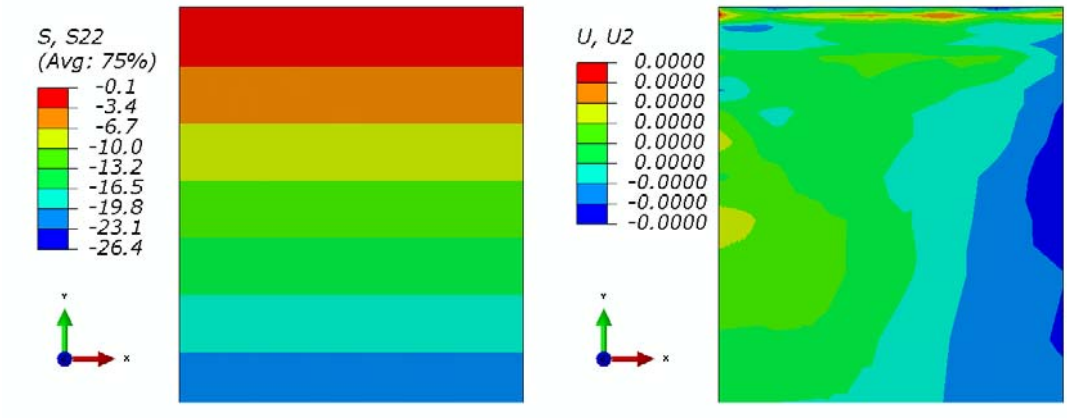

Figure 7.8 *In-situ* vertical stress and displacement for CW43-SFS57

Two plate load tests (PLT) on CW43-SFS57 and CW27-SFS73 were simulated using similar loading conditions and geometry in the field trial. Throughout the simulation, the vertical displacement and stress were compared with the field results. The results of the numerical prediction in comparison with the field trial for plate load tests are presented in Figure 7.10. It is evident that the overall behaviour in the numerical model is in good agreement with the field trial. However, several factors caused disagreement to some extent between the test results and the FE prediction. Firstly, the constitutive model and material properties were developed based on the saturated triaxial conditions, whereas in the field, the PLT was conducted under partially saturated conditions. In the field it was impossible to maintain saturation of the PLT area due to rapid drainage of the materials. Secondly, in the developed model, the time dependency on the strength as occurred in SFS (due to cementitious properties) was not considered, though in the field, the material gained strength over the time (this was illustrated in Chapter 6). Therefore, the settlement occurred under a given applied pressure was more in the numerical model as compared to the test result.

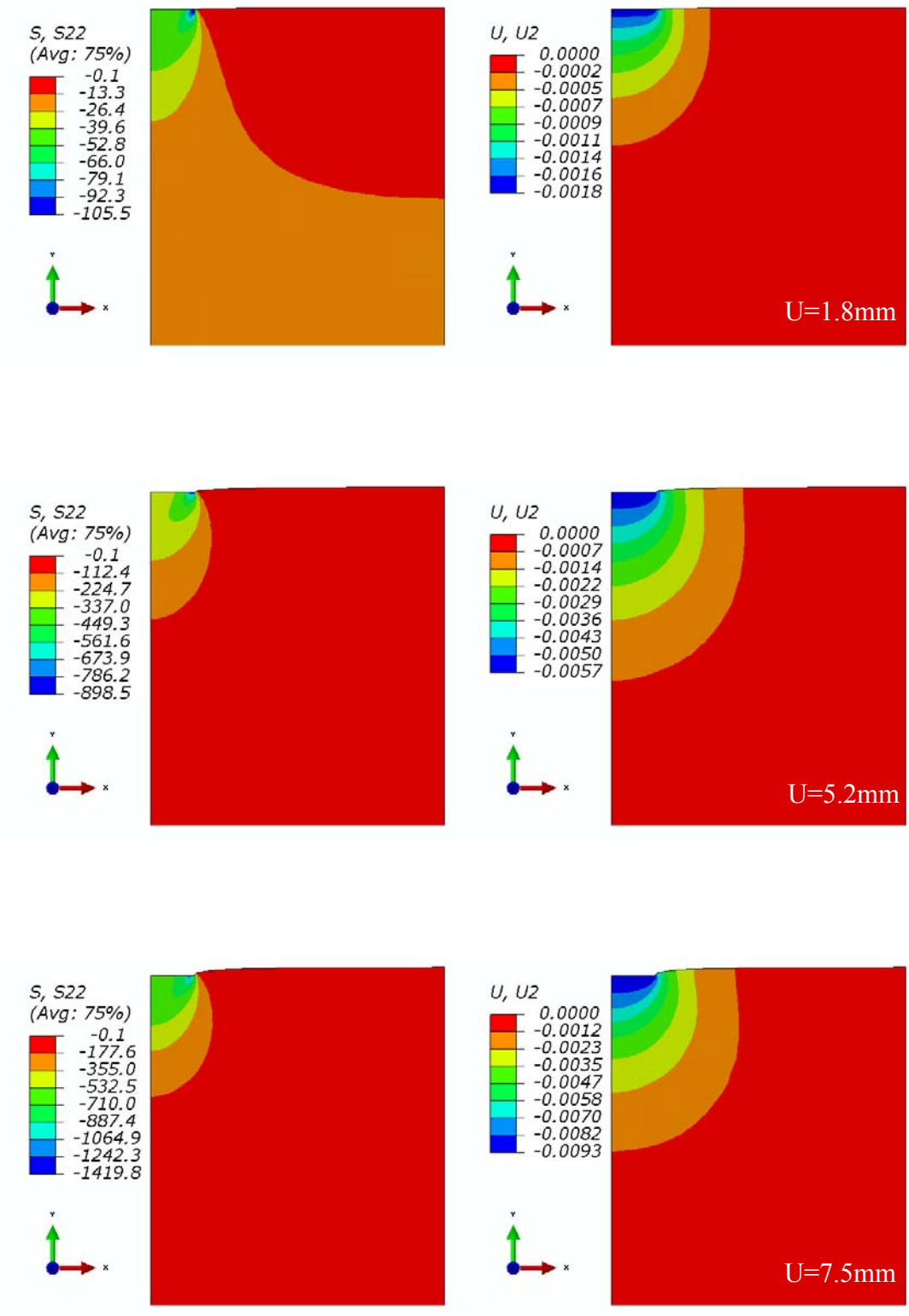

Figure 7.9 Propagation of the vertical load and deformation under displacement controlled condition for CW43-SFS57

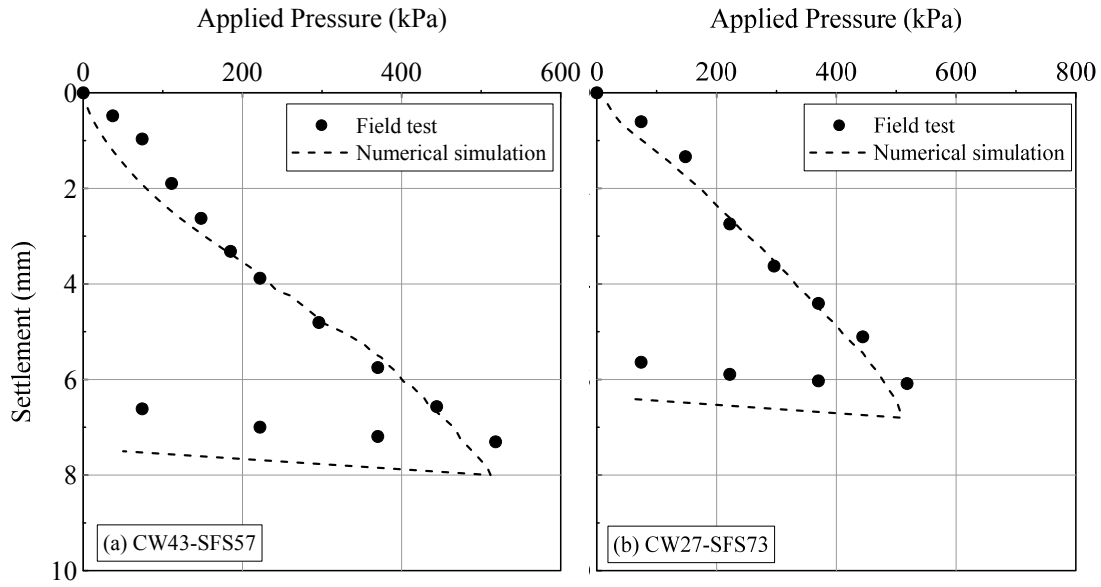

Figure 7.10 Numerical and field trial result comparison for the plate load test for (a) CW43-SFS57, and (b) CW27-SFS73

7.4 SUMMARY

In order to investigate the behaviour of the CW-SFS blends in more general loading and boundary conditions similar to the field, the proposed constitutive model described in Chapter 5 was implemented in the finite element code, ABAQUS. The implementation of the constitutive model was presented in this chapter by developing a user-defined UMAT subroutine. Initially, the governing stress and strain tensors and their definitions in the ABAQUS were presented, and then the algorithm used for the stress integration, and the continuum elasto-plastic tangent modulus in the UMAT subroutine, were elaborated. It was found that the sub-stepping algorithm method based on the Euler integration scheme (Sloan, 1987) could easily and successfully be used for the proposed model. The salient feature of this method is the adjustment of the sub-step increment (i.e. decreasing or increasing the increments) by calculating the corresponding error in each increment.

After developing the UMAT subroutine, it was validated by comparing the results of the numerical analysis with the laboratory triaxial and MATLAB code. An axisymmetric geometry with boundary conditions similar to the triaxial specimen

was modelled in ABAQUS and the loading was applied using displacement controlled conditions. It was shown that the numerically predicted stress-strain behaviour of CW-SFS blends was in good agreement with the laboratory data. Finally, the practical application of the developed numerical model was demonstrated by preparing a model to simulate the plate load test and comparing the results with the field trial investigation. The overall pressure-settlement curves for the two selected CW-SFS blends were in good agreement with the field results. However, the settlement under any given pressure was greater in the numerical simulation as compared to the field results. This is likely due to the variables of strength increment associated with the SFS in real conditions as well as the partially drained conditions in the field compared to the saturated laboratory specimens.

CHAPTER EIGHT

8 CONCLUSIONS AND RECOMMENDATIONS

8.1 INTRODUCTION

Recently, due to the increase in population density and urbanisation in Australia, the need for more land to accommodate new facilities and infrastructure including development and expansion of existing ports has increased significantly. Obviously, fresh aggregates from quarries such as sand are commonly-used fill material, and usually dredged material is considered for land reclamation, as adopted all around the world. However, in some cases the use of these materials is uneconomical and environmentally restricted, thus other materials such as industrial wastes are considered for use as structural fill.

This research study was part of an industrial project for the expansion of Port Kembla Outer Harbour in the Wollongong region, Australia. Port Kembla Port Corporation (PKPC) is developing the outer harbour to provide additional berth facilities and land to cater for future trade growth. Since the dredged material in surrounding areas is contaminated by pyrites that are likely to produce sulphate acid during excavation and threaten the environment, PKPC envisaged the use of industrial wastes, mainly coal wash and steel furnace slag, as fill material. However, the behaviour of coal wash (CW) and steel furnace slag (SFS) and their mixtures is not clearly understood. As the basis of this thesis, extensive laboratory tests were conducted on different CW-SFS mixtures in order to determine the geotechnical parameters of, and evaluate the suitability of these materials as structural fill; this research is also intended as a basis for recommending the optimum mixture to the industry and providing a mathematical and numerical model to capture stress-strain behaviour.

Chapter 3 outlined the basic characteristics of the material, experimental program and the specimen preparation for different tests along with a brief explanation of the equipment. In Chapter 4, the results of the preliminary geotechnical investigation on the CW-SFS blends were presented, whereas Chapter 5 described the stress-strain behaviour of CW-SFS mixtures under monotonic triaxial tests and provided a constitutive model by which the mechanical behaviour of these materials can be captured. In Chapter 6, the optimisation method for the CW-SFS mixtures was introduced, following the assessment of the selected blends on a large scale through field trial investigation; and finally, the numerical validation and field application of the blended waste materials were presented in Chapter 7 by implementing the constitutive model into ABAQUS software. The outcomes of this study with regard to the geotechnical properties, the mechanical behaviour and practical application of the CW-SFS blends are provided in the following sections.

8.2 PRELIMINARY GEOTECHNICAL BEHAVIOUR OF CW-SFS MIXTURES

The first step to investigate the suitability of CW-SFS blends as structural fill was to conduct preliminary geotechnical tests and establish the empirical relationships between these parameters to the CW or SFS percentage in the mix. The results of the preliminary investigations on the CW-SFS mixtures shown in Chapter 4 indicated that the maximum dry unit weight of the blends could be increased with the increase in the SFS content, as the specific gravity of the SFS was greater than CW (due to the presence of heavy iron composition in the SFS). The post-compaction particle breakage associated with the blends with more CW content was observed to be substantial, hence the excessive particle degradation likely to cause additional settlement damage under loading. The permeability of the blends decreased as the CW content increased in the mixture because of the lower void ratio, as well as the existence of clayey fines in the CW. According to the results, the permeability of all CW-SFS blends except CW100-SFS0 was in the moderate range (1×10^{-6} cm/sec $\leq k \leq 1\times10^{-4}$ cm/sec) and was sufficient to dissipate generation of pore water pressure and prevent internal erosion. Under the 1-D compression test, more deformation was

observed for the blends having more CW content, which can be attributed to the higher breakage index (i.e. the coefficient of compression was greater for CW compared to SFS which was 0.180 and 0.121, respectively), whereas the yield/pass stress was greater for the mixtures with more SFS content, i.e. in the range of 900-1500 kPa.

In relation to the shear strength properties, the results of CBR and UCS tests showed that a higher SFS content in the mixtures results in higher CBR value. However, all of the mixtures except CW100-SFS0 in soaked conditions showed CBR of more than 10%, which is comparable to the typical sandy fills. The UCS increased with the increase in CW content, and the behaviour of the specimens having more CW in the mixtures was observed to be ductile compare to the relatively more brittle behaviour for the specimens with a higher percentage of SFS. For a given mixture, by increasing the moisture content, the UCS decreased significantly from the dry side of OMC to OMC, whereas the reduction in UCS was minor on the wet side of OMC.

It was identified that the swelling behaviour of CW-SFS mixtures plays an important role for the application of these materials in the field, and the laboratory investigation revealed that due to the presence of free lime (CaO) in the chemical composition of SFS, the free swelling was greater for the specimens with more SFS content. It was observed that the maximum free swelling was for the CW0-SFS100 compacted to 100% $\gamma_{d,max}$, which was around 12%. However, by blending SFS with 25% CW, it was reduced drastically to less than 3%, and the effect of CW content on the free swelling was negligible for the specimens with more than 50% CW in the mix. Although swelling is an aspect detrimental for the application of these materials in the field, it can be controlled by applying a surface surcharge close to the swell pressure, i.e. overburden of the top layers. In the laboratory, the maximum swelling pressure was determined by conducting a constant volume method test and identified that CW0-SFS100 (100% SFS) compacted to 90% $\gamma_{d,max}$ showed more than 110kPa swelling pressure, whereas for CW25-SFS75 and CW50-SFS50 swelling pressure was significantly less, and it was around 60kPa and 22kPa, respectively. This means

that if the overburden pressure loading on the compacted layer is greater than the swelling pressure, no swelling would be observed.

8.3 STRESS-STRAIN BEHAVIOUR OF CW-SFS MIXTURES

To enable an in-depth investigation on the stress-strain behaviour of compacted CW-SFS mixtures, a series of isotropically-consolidated drained triaxial tests were carried out at different confining pressures. The results of the isotropic compression showed that although all of the mixtures were prepared under same degree of compaction (i.e. 90% $\gamma_{d,max}$), the compressibility of the blends having more CW content was greater, because the CW particles were more crushable and weaker compared to the SFS particles. By normalizing the specific volume to initial value for each blend and the mean effective stress to the equivalent past stress, a unique bilinear relationship between v/v_0 and p'/p^* was proposed to capture the compression behaviour of all mixtures under isotropic loading.

The stress-strain behaviour was influenced by the CW content in the mixtures, especially on the volumetric strain. It was identified that the peak deviatoric stress (or peak friction angle) decreased by increasing CW percentage in the blend, whereas the axial strain required to mobilise the peak deviator stress increased. The effect of SFS on the q_{peak} diminished at confining pressure greater than 120kPa. In terms of volumetric strain, more contraction was observed for the specimens with a higher CW content, because, the amount of particle degradation was noticeable for the specimens with more CW content. The increase on the secant shear modulus was significant via blending a small amount of SFS with CW. This means that more deformation is expected to occur for mixtures composed of high CW content under the same loading conditions. By following the critical strain criterion that was proposed, only 100% coal wash exhibited axial deformation over the prescribed allowance of 0.5%. The results of the particle degradation analysis indicated that significant particle breakage occurred for the specimens having more CW content in the mix and the rate of particle breakage with the CW content increased considerably

for the mixtures having more than 50% CW; moreover, it was more noticeable at confining pressures exceeding 60kPa.

Based on the triaxial results, a constitutive model was developed to capture the stress-strain behaviour of different CW-SFS under monotonic loading. The model was proposed based on generalized plasticity and critical state framework as observed in the laboratory investigation. The model parameters were defined based on the CW content in the mix and the model prediction demonstrated an adequate simulation in comparison with the experimental results. The contractive behaviour with strain-hardening under higher confining pressure as well as the dilative response with strain-softening at lower confining pressure were captured, according to the location of the initial condition (i.e. state parameter) relative to the critical state line.

8.4 PRACTICAL IMPLICATIONS

Based on the laboratory investigation presented in Chapters 4 and 5, initially an acceptance criterion for granular waste material was proposed to identify a suitable waste as structural fill, subsequently, an optimisation method for the CW-SFS blends was proposed in order to identify the most appropriate mixture of CW-SFS to meet the common end-product specifications for land reclamation, and in particular for the Port Kembla Outer Harbour reclamation scheme. Due to the heterogeneity of the CW and SFS, the behaviour of two selected CW-SFS mixtures (i.e. CW43-SFS57 and CW27-SFS73 by weight) was assessed in a large scale field trial. The results of the investigation revealed that these waste materials could be compacted to reach the maximum standard Proctor density. The results of the dynamic cone penetration tests showed that the average equivalent in-situ CBR values were between 46 and 60, which means that the shear strength of these mixtures were greater than medium to dense sandy fills. By conducting plate load tests at two time intervals after compaction, it was observed that the compressive strength of the mixtures increased, and it was more significant for the mixture with higher SFS due to the presence of free lime in the SFS and its cementitious properties. On the other hand, the hydration of the free lime caused swelling of around 6%.

Finally, in order to evaluate the general behaviour of the CW-SFS blends under different loading conditions, the proposed constitutive model was successfully implemented into the finite element software (i.e. ABAQUS) by developing a subroutine known as UMAT. Initially the response of the numerical model was verified with the laboratory triaxial results, and then the practical value of the model was examined by comparing the results of the plate load test from the field trial investigation. The model demonstrated a good agreement with the field data. Therefore, the developed numerical model can assist practicing engineers in their design to predict of the behaviour of CW-SFS blends under different loading and boundary conditions, for comparable land reclamation scheme.

8.5 RECOMMENDATIONS FOR FUTURE STUDY

Considering that this research study proved the suitability of industrial wastes to be used as structural fill which can benefit the economy and the environment, the following recommendations for the future research can be identified.

- The results of this study were limited to particular coal wash and steel furnace slag. Since the properties of the industrial waste materials vary significantly, it is beneficial to investigate the variation of the source material on geotechnical behaviour to cover a wider range of the materials, in particular the effect of free lime content and the quality of fines of coal wash. This will provide more information to practicing engineers and will increase the level of confidence in utilising these materials.
- Since the mechanical behaviour of the granular material is highly influenced by the particle size distribution, it is beneficial to conduct a series of triaxial tests with variation of initial PSD and propose the appropriate shear strength envelopes with relation to the PSD parameters such as C_u and C_c.
- The scope of this research was limited to one level of degree of compaction and drained monotonic loading. In the actual field conditions, the material could be compacted to other levels of compaction and also subjected to cyclic loading. By considering that the extent of particle degradation is significant in

particular for coal wash under cyclic loading, it is recommended that further studies be conducted on the behaviour of the optimum mixture under undrained conditions and cyclic loading, as well as the effects of initial degree of compaction on the stress-strain response.

- Although the suction values for compacted granular materials like CW-SFS mixtures are not typically high, the presence of clayey fines in the CW could result in larger values of suction. In addition, in the field, the compacted layers of CW-SFS mixtures are generally placed and remain in partially saturated condition. Therefore, it is recommended that the mechanical behaviour of unsaturated CW-SFS mixtures be further investigated in the laboratory.
- The proposed constitutive model was based on the drained monotonic triaxial results. By conducting cyclic loading as described, the model can be extended to capture the cyclic behaviour and implemented into a finite element code. This will enable practitioners to capture the behaviour of these mixtures in a broader range of loading and boundary conditions.
- As it was observed, considering the gain in strength in the SFS due to the hydration of free lime and its cementitious properties, it is recommended that further studies be conducted on the long-term behaviour of CW-SFS mixtures by conducting triaxial tests on the specimens cured under water (both fresh and sea water) for different time periods (such as 7, 14, 28 days). It will be possible to describe long-term behaviour by comparing the shear strength envelopes between these conditions.
- Further experimental studies on the swell behaviour of CW-SFS mixtures subjected to different surcharges should be conducted. The results of such studies will capture the required loading corresponding to a level of swelling of the compacted CW-SFS mixtures.
- It is recommended that detailed CT-Scan testing be carried out to understand more, the structure (fabric) of these compacted wastes. Time-dependent changes of the CW-SFS mixtures in terms of structural alterations will provide better insight to the long-term behaviour and longevity.

- The optimum mixture in this study was recommended for the above tidal level in reclamation project. To investigate the suitability of the CW-SFS mixtures to be used under water, an extensive environmental investigation should be carried out.

REFERENCES

ASTM D1140 (2006). Standard test methods for amount of material in soils finer than No. 200 (75-μm), *Annual Book of ASTM Standards*, ASTM International, West Conshohocken, PA.

ASTM D1194 (1994). Standard test methods for bearing capacity of soil for static load and spread footings, *Annual Book of ASTM Standards*, ASTM International, West Conshohocken, PA.

ASTM D1883 (2007). Standard test methods for CBR (Calirfornia Bearing Ratio) of laboratory-compacted soils, *Annual Book of ASTM Standards*, ASTM International, West Conshohocken, PA.

ASTM D2434 (2000). Standard test methods for permeability of granular soils (constant head), *Annual Book of ASTM Standards*, ASTM International, West Conshohocken, PA.

ASTM D4186 (2012). Standard test methods for one-dimensional consolidation properties of saturated cohesive soils using controlled-strain loading, *Annual Book of ASTM Standards*, ASTM International, West Conshohocken, PA.

ASTM D4792 (2006). Standard test methods for potential expansion aggregates from hydration reactions, *Annual Book of ASTM Standards*, ASTM International, West Conshohocken, PA.

ASTM D5084 (2010). Standard test methods for measurement of hydraulic conductivity of saturated porous materials using a flexible wall permeameter, *Annual Book of ASTM Standards*, ASTM International, West Conshohocken, PA.

ASTM D5333 (2003). Standard test methods for measurement of collapse potential of soils, *Annual Book of ASTM Standards*, ASTM International, West Conshohocken, PA.

ASTM D6951 (2009). Standard test methods for use of the dynamic cone penetrometer in shallow pavement applications, *Annual Book of ASTM Standards*, ASTM International, West Conshohocken, PA.

ASTM D7181 (2011). Standard test method for consolidated drained triaxial compression test for soils, *Annual Book of ASTM Standards*, ASTM International, West Conshohocken, PA.

Australian Standard (AS) 1289.3.5.1-2006. Methods of testing soils for engineering purposes - Soil classification tests - Determination of the soil particle density of a soil - Standard method.

Australian Standard (AS) 1289.5.1.1-2003. Methods of testing soils for engineering purposes - Soil compaction and density tests - Determination of the dry density/moisture content relation of a soil using standard compactive effort.

Aiban, S. A. (2006). Utilization of steel slag aggregate for road bases. *Journal of testing and evaluation,* 34(1)**,** 65-75.

Albrecht, M. C. (1980). Coal Preparation Process. Unit and bulk materials handling, *ASME Annual Meeting***,** 279-289.

Anandarajah, A. (2011). *Computational Methods in Elasticity and Plasticity: Solids and Porous Media*, Springer.

Andreas, L., Hermann, I., Lidstrom-Larsson, M. and Lagerkvist, A. (2005). Physical properties of steel slag to be reused in a landfill cover. *Proceedings of Sardinia, Tenth International Waste Management and Landfill Symposium*, Environmental Sanitary Engineering Centre, Cagliari, Italy, Oct. 3-7.

Auricchio, F. and Taylor, R. L. (1995). Two material models for cyclic plasticity: Nonlinear kinematic hardening and generalized plasticity. *International Journal of Plasticity,* 11(1)**,** 65-98.

Auriol, J.-C., Cui, Y.-J., Ferber, V. and Magnan, J.-P. (2008). Wetting-induced volume changes in compacted silty clays and high-plasticity clays. *Canadian Geotechnical Journal,* 45(2)**,** 252-265.

Environmenr Protection Authority. (2010). *Standard for the production and use of waste derived fill*.

Basma, A. A., Al-Homoud, A. S. and Husein, A. (1995). Laboratory assessment of swelling pressure of expansive soils. *Applied Clay Science,* 9(5)**,** 355-368.

Been, K. and Jefferies, M. G. (1985). A state parameter for sands. *Géotechnique,* 35(2)**,** 99-112.

Bolton, M. D. (1986). The strength and dilatancy of sands. *Geotechnique,* 36(1)**,** 65-78.

Casagrande, A. (1936). The determination of the pre-consolidation load and its practical signifcance. *Proceeding of the first international conference on soil mechanics and foundation engineering*, Cambridge. 60-64.

Cement Concrete & Aggregates Australia (2008). Use of recycled aggregates in construction.

Cerato, A. and Lutenegger, A. (2006). Specimen Size and Scale Effects of Direct Shear Box Tests of Sands. *ASTM Geotechnical Testing Journal,* 29(6)**,** 1-10.

Charles, J. A. and Watts, K. S. (1996). The assessment of the collapse potential of fills and its significance for building on fill. *Proceedings of the Institution of Civil Engineers. Geotechnical engineering,* 119(1)**,** 15-28.

Chen, C. Y., Elnaggar, H. A. and Bullen, A. G. R. (1976). Degradation and the relationship between shear strength and various index properties of coal refuse. *New Horizones in Construction Materials*, Envo Publishing, Bethlehem, Penn, 41-52.

Chen, Q., Johnson, D. C., Zhu, L., Yuan, M. and Hills, C. D. (2007). Accelerated carbonation and leaching behavior of the slag from iron and steel making industry. *Journal of University of Science and Technology Beijing, Mineral, Metallurgy, Material,* 14(4)**,** 297-301.

Chiaro, G., Indraratna, B. and Tasalloti, S. M. A. (2014a). Predicting the Behaviour of Coal Wash and Steel Slag Mixtures under Triaxial Conditions. *Canadian Geotechnical Journal*. *DOI: 10.1139/cgj-2013-0476 (in press, available online)*

Chiaro, G., Indraratna, B., Tasalloti, S. M. A. and Rujikiatkamjorn, C. (2014b). Optimisation of coal wash-slag blend as a structural fill. *Ground Improvement, DOI: 10.1680/grim.13.00050 (in press, available online)*.

Cho, G., Dodds, J. and Santamarina, J. (2006). Particle Shape Effects on Packing Density, Stiffness, and Strength: Natural and Crushed Sands. *Journal of Geotechnical and Geoenvironmental Engineering,* 132(5)**,** 591-602.

Crawford, C. B. and Burn, K. N. (1969). Building damage from expansive steel slag backfill. *Soil mechanics and Foundations Division,* 95**,** 1325-1334.

Davies, P., Philip, R. E. D. and James, D. M. (2011). Geotechnical design for the Port Botany expansion project, Sydney. *Proceedings of the Institution of Civil Engineers. Geotechnical engineering,* 164(3)**,** 149-167.

Davis, R. O. and Selvadurai, A. P. S. (2002). *Plasticity and Geomechanics*, Cambridge University Press.

Department of Environment, Climate Change and Water NSW (2009). *Waste classification guidelines, Part 1: Classifying waste*.

Dippenaar, R. (2005). Industrial uses of slag (the use and re-use of iron and steelmaking slags). *Ironmaking & Steelmaking,* 32(1)**,** 35-46.

El-Ehwany, M. and Houston, S. L. (1990). Settlement and Moisture Movement in Collapsible Soils. *Journal of Geotechnical Engineering,* 116(10)**,** 1521-1535.

Emery, J. J. (1982). Slag utilization in pavement construction. *Extending Appregate Resources, ASTM STP 774***,** 95-118.

Emery, J. J., Dresdale, R. G. and Nicholson, P. S. (1973). Steel slag asphalt mixes. *18th Annual Conference of Canadian Technical Asphalt Association,* 59-79.

Faraone, N., Tonello, G., Furlani, E. and Maschio, S. (2009). Steelmaking slag as aggregate for mortars: Effects of particle dimension on compression strength. *Chemosphere,* 77(8)**,** 1152-1156.

Frías Rojas, M. and Sánchez De Rojas, M. I. (2004). Chemical assessment of the electric arc furnace slag as construction material: Expansive compounds. *Cement and Concrete Research,* 34(10)**,** 1881-1888.

Geiseler, J. (1996). Use of steelworks slag in Europe. *Waste Management,* 16(1-3)**,** 59-63.

Ghionna, V., Pedroni, S., Tenani, P. and Veggi, S. (1996). Geotechnical investigation on steel slags mixtures for landfills embankments construction. *Proceeding of the Second International Conference on Environmental Geotechnics*, Osaka, Japa, November 5-8, Balkema, Rotterdam. 709-714.

Gibbs, H. J. (1973). Use of a consolidometer for measuring expansion potential of soils. *Proceedings of Workshop on Expansive Clays and Shales in Highway Design and Construction*, University of Wyoming, Laramie. 206–213.

Haibin, L. and Zhenling, L. (2010). Recycling utilization patterns of coal mining waste in China. *Resources, Conservation and Recycling,* 54(12)**,** 1331-1340.

Hardin, B. O. (1985). Crushing of soil particles. *Journal of Geotechnical Engineering, ASCE,* 111(10)**,** 1177-1192.

Hausmann, M. R. (1990). *Engineering principles of ground modification*, McGraw-Hill Ryerson, Limited.

Heitor, A. (2013). *Assessment of Post-compaction Characteristics of an Unsaturated Silty Sand.* PhD thesis. University of Wollongong.

Hibbitt, Karlsson and Sorensen (2012). ABAQUS user's manual, version 6.12, Hibbitt, Karlsson, Sorensen Inc., Pawtucket, RI.

Hogland, W. and Stenis, J. (2000). Assessment and system analysis of industrial waste management. *Waste Management,* 20(7)**,** 537-543.

Holtz, R. D., Kovacs, W. D. and Sheahan, T. C. (2011). *An introduction to geotechnical engineering,* NJ, Pearson.

Holubec, I. (1976). Geotechnical aspects of coal waste embankments. *Canadian Geotechnical Journal,* 13(1)**,** 27-39.

Huijgen, W. J. J. and Comans, R. N. J. (2005). Mineral CO2 Sequestration by Steel Slag Carbonation. *Environmental Science & Technology,* 39(24)**,** 9676-9682.

Imam, S. M. R., Morgenstern, N. R., Robertson, P. K. and Chan, D. H. (2005). A critical-state constitutive model for liquefiable sand. *Canadian Geotechnical Journal,* 42(3)**,** 830-855.

Indraratna, B. (1994a). Geotechnical Characterization of Blended Coal Tailings for Construction and Rehabilitation Work. *Quarterly Journal of Engineering Geology and Hydrogeology,* 27(4)**,** 353-361.

Indraratna, B., Gasson, I. and Chowdhury, R. N. (1994b). Utilization of Compacted Coal Tailings as a Structural Fill. *Canadian Geotechnical Journal,* 31(5)**,** 614-623.

Indraratna, B., Ionescu, D. and Christie, H. D. (1998). Shear Behavior of Railway Ballast Based on Large-Scale Triaxial Tests. *Journal of Geotechnical and Geoenvironmental Engineering,* 124(5)**,** 439-449.

Indraratna, B., Lackenby, J. and Christie, D. (2005). Effect of confining pressure on the degradation of ballast under cyclic loading. *Géotechnique,* 55(4)**,** 325-328.

Indraratna, B., Rujikiatkamjorn, C. and Chiaro, G. (2012). Characterization of Compacted Coal Wash As Structural Fill Material. *GeoCongress 2012.* American Society of Civil Engineers, 3826-3834.

Indraratna, B., Rujikiatkamjorn, C. and Chiaro, G. (2013a). Compaction of coal wash as reclamation fill. *In:* Leung., C., Goh., S. and Shen., R. (eds.) *18th Southeast Asian Geotechnical Conference (18SEAGC) cum Inaugural AGSSEA Conference (1AGSSEA).* Singapore: Research Publishing, 165-170.

Indraratna, B., Tennakoon, N., Nimbalkar, S. and Rujikiatkamjorn, C. (2013b). Behaviour of clay-fouled ballast under drained triaxial testing. *Géotechnique,* 63(5)**,** 410-419.

Jefferies, M. G. (1993). Nor-Sand: a simle critical state model for sand. *Géotechnique,* 43(1), 91-103.

Johnson, D. C., Macleod, C. L., Carey, P. J. and Hills, C. D. (2003). Solidification of stainless steel slag by accelerated carbonation. *Environmental Technology,* 24(6)**,** 671-678.

Juckes, L. M. (2003). The volume stability of modern steelmaking slags. *Mineral Processing and Extractive Metallurgy (Transactions of the Institution of Mining and Metallurgy, Section C),* 112(3)**,** 177-197.

Koutsoftas, D. C. and Kiefer, M. L. (1990). Improvement of mine spoils in Southern Illinois. *ASTM Special Technical Publication***,** 1070, 153-167.

La Rochelle, P., Leroueil, S., Trak, B., Blais-Leroux, L. and Tavenas, F. (1988). Observational approach to membrane and area corrections in triaxial tests, *Proc Symposium on Advanced Triaxial Testing of Soil and Rock*, Louisville, Publ Philadelphia: ASTM Special Technical Publication 977*,* 28(2-3)**,** 715-731.

Lai, Z., His, J., Rheinberger, T. and Andrews, T. (2011). Geotechnical offshore site investigation and reclamation design at Port Kembla. *Proceedings of Australian Geomechanics Society - Sydney Symposium, Coastal and Marine Geotechnics: Foundations and Trade.* Sydney, Australia, 61-72.

Lee, A. R. (1974). *Blastfurnace and steel slag: production, properties and uses*, Edward Arnold Ltd,. London.

Leventhal, A. (1996). Coal washery Reject as an Engineered Material. *National Symposium on the Use of Recycled Materials in Engineering Construction.* Sydney, NSW, 54-59.

Leventhal, A. R. and De Ambrosis, L. P. (1985). Waste disposal in coal mining—a geotechnical analysis. *Engineering Geology,* 22(1)**,** 83-96.

Li, X. S. and Dafalias, Y. F. (2000). Dilatancy for cohesionless soils. *Géotechnique,* 51(8)**,** 729-730.

Lim, T.-T. and Chu, J. (2006). Assessment of the use of spent copper slag for land reclamation. *Waste Management & Research,* 24(1)**,** 67-73.

Ling, H. and Liu, H. (2003). Pressure-Level Dependency and Densification Behavior of Sand Through Generalized Plasticity Model. *Journal of Engineering Mechanics,* 129(8)**,** 851-860.

Ling, H. and Yang, S. (2006). Unified Sand Model Based on the Critical State and Generalized Plasticity. *Journal of Engineering Mechanics,* 132(12)**,** 1380-1391.

Look, B. (2007). *Handbook of Geotechnical Investigation and Design Tables*, Taylor & Francis.

Lu, G. Q. and Do, D. D. (1992). Physical structure and adsorption properties of coal washery reject. *Fuel,* 71(7)**,** 809-813.

Mackinnon, W. and Swanson, A. (2010). Strategies for washing Australian coals. *International Coal Preparation Congress,* Society for Mining, Metallurgy & Exploration, Incorporated, 9-17.

Malasavage, N., Jagupilla, S., Grubb, D., Wazne, M. and Coon, W. (2012). Geotechnical Performance of Dredged Material—Steel Slag Fines Blends: Laboratory and Field Evaluation. *Journal of Geotechnical and Geoenvironmental Engineering,* 138(8)**,** 981-991.

Manzanal, D., Fernández Merodo, J. A. and Pastor, M. (2011). Generalized plasticity state parameter-based model for saturated and unsaturated soils. Part 1: Saturated state. *International Journal for Numerical and Analytical Methods in Geomechanics,* 35(12)**,** 1347-1362.

Manzari, M. T. and Dafalias, Y. F. (1997). A critical state two-surface plasticity model for sands. *Géotechnique*, 47(2), 255-272.

Maslehuddin, M., Sharif, A. M., Shameem, M., Ibrahim, M. and Barry, M. S. (2003). Comparison of properties of steel slag and crushed limestone aggregate concretes. *Construction and Building Materials,* 17(2)**,** 105-112.

Massarsch, K. R. (1991). Deep Soil Compaction Using Vibratory Probes. *In:* Melvin, I., Esrig and Robert, C., eds. *Deep Foundation Improvement: Design, Construction, and Testing, ASTM STP 1089*, Philadelphia. American Society for Testing and Materials, 297-319.

Mccallum, D. A. (2005). The hydrochemistry of steel and iron blast furnace slags. Part1: Characterisation. CSIRO Minerals.

Mitchell, J. K. and Soga, K. (2005). *Fundamentals of soil behavior*, John Wiley & Sons.

Modoni, G. and Gazzellone, A. (2011). Experimental Observations on the Critical State of Granular Materials. *International Symposium on Deformation Characteristics of Geomaterials, September 1~3, 2011, Seoul, Korea*, 850-857.

Modoni, G., Koseki, J. and Anh Dan, L. Q. (2011). Cyclic stress-strain response of compacted gravel. *Géotechnique*, 61(6), 473-485.

Montenegro, J., Celemín-Matachana, M., Cañizal, J. and Setién, J. (2012). Ladle Furnace Slag in the Construction of Embankments: Expansive Behavior. *Journal of Materials in Civil Engineering,* 25(8)**,** 972-979.

Morris, P. H. and Williams, D. J. (1997). Results of field trials of co-disposal of coarse and fine coal wastes. *Transactions of the Institution of Mining and Metallurgy Section A-Mining Technology,* 106**,** A38-A41.

Motz, H. and Geiseler, J. (2001). Products of steel slags an opportunity to save natural resources. *Waste Management,* 21(3)**,** 285-293.

Mroz, Z. and Zienkiewicz, O. C. (1984). Uniform formulation of constitutive equations for clay and sand. *Mechanics and Engineering Materials, New York, USA*, 415-450.

Nagaraj, H. B., Nagaraj, H. B., Munnas, M. M. and Sridharan, A. (2009). Critical evaluation of determining swelling pressure by swell-load method and constant volume method. *Geotechnical testing journal,* 32(4), 305-314.

Nguyen, Q. S. (1977). On the elastic plastic initial-boundary value problem and its numerical integration. *International journal for numerical methods in engineering,* 11(5), 817-832.

Ni, Q., Powrie, W., Zhang, X. and Harkness, R. (2000). Effect of Particle Properties on Soil Behavior: 3-D Numerical Modeling of Shearbox Tests. *Numerical Methods in Geotechnical Engineering.* American Society of Civil Engineers, 58-70.

Nik Hisyamudin, B. M. N., Nik Hisyamudin, B. M. N., Yokoyama, S. and Umemoto, M. (2009). Absorption of CO 2 in EAF reducing slag from stainless steel making process by wet grinding. *World academy of science, engineering and technology,* 56, 611-615.

Nova, R. and Wood, D. M. (1979). A constitutive model for sand in triaxial compression. *International Journal for Numerical and Analytical Methods in Geomechanics,* 3(3), 255-278.

Okagbue, C. O. and Ochulor, O. H. (2007). The potential of cement-stabilized coal-reject as a construction material. *Bulletin of Engineering Geology and the Environment,* 66(2), 143-151.

Okogbue, C. O. and Ezeajugh, C. L. (1991). The potentials of Nigerian coal-reject as a construction material. *Engineering Geology,* 30(3-4), 337-356.

Ortiz, N., Pires, M. a. F. and Bressiani, J. C. (2001). Use of steel converter slag as nickel adsorber to wastewater treatment. *Waste Management,* 21(7), 631-635.

Oweis, I. S. and Khera, R. P. (1990). *Geotechnology of waste management*, PWS Publishing.

Pappu, A., Saxena, M. and Asolekar, S. R. (2007). Solid wastes generation in India and their recycling potential in building materials. *Building and Environment,* 42(6), 2311-2320.

Pastor, M., Zienkiewicz, O. C. and Chan, A. H. C. (1990). Generalized plasticity and the modelling of soil behaviour. *International Journal for Numerical and Analytical Methods in Geomechanics,* 14(3), 151-190.

Poulus, H. G. and Davis, E. H. (1974). *Elastic solutions for soil and rock mechanics*, John Wiley & Sons, Inc. (ed.), Sydney.

Proctor, D. M., Fehling, K. A., Shay, E. C., Wittenborn, J. L., Green, J. J., Avent, C., Bigham, R. D., Connolly, M., Lee, B., Shepker, T. O. and Zak, M. A. (2000). Physical and Chemical Characteristics of Blast Furnace, Basic Oxygen Furnace, and Electric Arc Furnace Steel Industry Slags. *Environmental Science & Technology,* 34(8)**,** 1576-1582.

Pusadkar, S. S. and Ramasamy, G. (2005). Collapse behavior of compacted coal ash fills. *Geotechnical Testing Journal,* 28(3)**,** 297-304.

Qiu, Y. and Sego, D. C. (2001). Laboratory properties of mine tailings. *Canadian Geotechnical Journal,* 38(1)**,** 183-190.

Rai, A., Prabakar, J., Raju, C. B. and Morchalle, R. K. (2002). Metallurgical slag as a component in blended cement. *Construction and Building Materials,* 16(8)**,** 489-494.

Reyad, M. M. (1990). Comparison between two methods for swelling pressure determination. *Proceedings of the 1st Alexandria Conference on Structures and Geotechnical Engineering*, Alexandria, Egypt. 53-61.

Rohde, L., Peres Náñez, W. and Augusto Pereira Ceratti, J. (2003). Electric Arc Furnace Steel Slag: Base Material for Low-Volume Roads. *Transportation Research Record: Journal of the Transportation Research Board,* 2**,** 201-207.

Roscoe, K. H., Schofield, A. N. and Thurairajah, A. (1963). Yielding of clays in states wetter than critical. *Géotechnique,* 13(3)**,** 211-240.

Roscoe, K. H., Schofield, A. N. and Wroth, C. P. (1958). On the yielding of soils. *Geotechnique,* 8(1)**,** 22-53.

Roth, L. H., Cesare, J. A. and Allison, G. A. (1977). Rapid monitoring of coal refuse embankments. *Proceeding Conference on Geotechnical Practice for Disposal of Solid Waste Materials, University of Michigan, Ann Arbor*, ASCE, 428-443.

Rowe, P. W. (1962). The Stress-Dilatancy Relation for Static Equilibrium of an Assembly of Particles in Contact. *Proceedings of the Royal Society of London. Series A, Mathematical and physical sciences,* 269(1339)**,** 500-527.

Rujikiatkamjorn, C., Indraratna, B. and Chiaro, G. (2013). Compaction of coal wash to optimise its utilisation as water-front reclamation fill. *Geomechanics and Geoengineering,* 8(1)**,** 36-45.

Rujikiatkamjorn, C., Indraratna, B., Chiaro, G., Naeeni, S. and Tasalloti, S. M. A. (2012). Compaction and strength testing of industrial waste blends as

potential port reclamation fill. *In:* Narsilio, G. A., Arulrajah, A. and Kodikara, J. (eds.) *11th Australia - New Zealand Conference on Geomechanics: Ground Engineering in a Changing World.* Melbourne, Australia, 973-978.

Russell, A. R. and Khalili, N. (2004). A bounding surface plasticity model for sands exhibiting particle crushing. *Canadian Geotechnical Journal,* 41(6)**,** 1179-1192.

Safiuddin, M., Jumaat, M. Z., Salam, M. A., Islam, M. S. and Hashim, R. (2010). Utilization of solid wastes in construction materials. *International journal of physical sciences,* 5(13)**,** 1952-1963.

Saxena, S., Lourie, D. and Rao, J. (1984). Compaction Criteria for Eastern Coal Waste Embankments. *Journal of Geotechnical Engineering,* 110(2)**,** 262-284.

Schofield, A. N. and Wroth, C. P. (1968). *Critical state soil mechanics*, McGraw-Hill Book Co., London.

Schreyer, H. L., Kulak, R. F. and Kramer, J. M. (1979). Accurate Numerical Solutions for Elastic-Plastic Models. *Journal of Pressure Vessel Technology,* 101(3)**,** 226-234.

Selig, E. T., Chaney, R. C., Stevens, E. and Sheth, N. (1979). Suggested Test Method for Determination of Degree of Saturation of Soil Samples by B Value Measurement. *Geotechnical testing journal,* 2(3)**,** 158-162.

Setién, J., Hernández, D. and González, J. J. (2009). Characterization of ladle furnace basic slag for use as a construction material. *Construction and Building Materials,* 23(5)**,** 1788-1794.

Shen, H. and Forssberg, E. (2003). An overview of recovery of metals from slags. *Waste Management,* 23(10)**,** 933-949.

Shi, C. (2002). Characteristics and cementitious properties of ladle slag fines from steel production. *Cement and Concrete Research,* 32(3)**,** 459-462.

Shi, C. (2004). Steel Slag-Its Production, Processing, Characteristics, and Cementitious Properties. *Journal of Materials in Civil Engineering,* 16(3)**,** 230-236.

Shi, C. and Qian, J. (2000). High performance cementing materials from industrial slags — a review. *Resources, Conservation and Recycling,* 29(3)**,** 195-207.

Skempton, A. W. (1954). The Pore-Pressure Coefficients A and B. *Géotechnique,* 4**,** 143-147.

Sloan, S. W. (1987). Substepping schemes for the numerical integration of elastoplastic stress–strain relations. *International Journal for Numerical Methods in Engineering,* 24(5)**,** 893-911.

Sridharan, A., Rao, A. S. and Sivapullaiah, P. V. (1986). Swelling Pressure of Clays. *Geotechnical testing journal,* 9(1)**,** 24-33.

Suiker, A., Selig, E. and Frenkel, R. (2005). Static and Cyclic Triaxial Testing of Ballast and Subballast. *Journal of Geotechnical and Geoenvironmental Engineering,* 131(6)**,** 771-782.

Taylor, D. W. (1948). *Fundamentals of soil mechanics*, Wiley, New York.

Thompson, R., Perko, H. and Rethamel, W. (2006). Comparison of Constant Volume Swell Pressure and Oedometer Load-Back Pressure. *Unsaturated Soils 2006.* American Society of Civil Engineers, 1787-1798.

Thomson, G. M. K. and Rodin, S. (1972). *Colliery spoil tips - after Aberfan*, Institution Civil Engineers.

Vesic, A. S. and Clough, G. W. (1968). Behavior of granular materials under high stresses. *Journal of the Soil Mechanics and Foundation Division,* 94(3), 661-688.

Wachsmuth, F., Geiseler, J., Fix, W., Koch, K. and Schwerdtfeger, K. (1981). Contribution to the Structure of BOF-Slags and its Influence on Their Volume Stability. *Canadian Metallurgical Quarterly,* 20(3)**,** 279-284.

Wang, G. (1992). *Properties and utilization of steel slag in engineering applications.* PhD thesis, University of Wollongong.

Wang, G. (2010). Determination of the expansion force of coarse steel slag aggregate. *Construction and Building Materials*, 24(10), 1961-1966.

Wang, G., Wang, Y. and Gao, Z. (2010). Use of Steel Slag as a Granular Material: Volume Expansion Prediction and Usability Criteria. *Journal of Hazardous Materials,* 184(1-3)**,** 555-560.

Watts, K. S. and Cooper, A. (2011). Compaction of Fills in Land Reclamation by Rapid Impact. *ICE-Geotechnical Engineering,* 164(3)**,** 181-193.

Wei, M.-S. and Huang, K.-H. (2001). Recycling and reuse of industrial wastes in Taiwan. *Waste Management,* 21(1)**,** 93-97.

Williams, D. J. and Morris, P. H. (1990). Engineering properties of Australian coal mine tailings relevant to their disposal and rehabilitation. *In:* Rainbow, A. K. M., ed. *Reclamation, treatment and utilization of coal mining wastes*, Balkema, Rotterdam, The Netherlands. 49-56.

Yildirim, I. Z. and Prezzi, M. (2009). Use of steel slag in subgrade application. *Publication FHWA/IN/JTRP-2009/32, Joint Transportation Research Program, Indiana Department of Transportation and Purdue University, West Lafayette, Indiana.*

Yildirim, I. Z. and Prezzi, M. (2011). Chemical, mineralogical, and morphological properties of steel slag. *Advances in civil engineering*.

Zekkos, D. and Flanagan, M. (2011). Case Histories-based Evaluation of the Deep Dynamic Compaction Technique on Municipal Solid Waste Sites. *Geo-Frontiers 2011*, Dallas, Texas. ASCE, 529-538.

Zhu, G., Sun, S., Wu, G. and Hu, J. (1989). Quality of steel slag and assessing method for its cementing property. *2nd Int. Symp. on Cement and Concrete*, Beijing. 295-302.

Zienkiewicz, O. C. and Taylor, R. L. (2000). *The Finite Element Method: Solid mechanics*, Butterworth-Heinemann.

APPENDIX A. MATLAB CODE FOR THE CW-SFS CONSTITUTIVE MODEL

```
%Generalised Elasto-Plastic Model
%Material: Coal Wash and Steel Furnace Slag Mixtures
%Program Developer: S.M.Ali Tasalloti, University of
Wollongong



clear all;

%% Display Code Name, Author
    display(' ');
    display('Matlab code for Simulation of CW-SFS
Constitutive Model');
    display('S.M.Ali TASALLOTI, University of
Wollongong');


%% Input Parameters
    display(' ');
    display('Input Parameters for CW-SFS Constitutive
Model:');

    Fcw=input('Enter the Coal Wash Percentage
(eg., 50)       = ');
    pc=input('Enter the inital Consolidation pressure
(kPa) (eg., 150 kPa)  = ');
```

```
    v0=input( 'Enter the value of Initial Specific Volume
(eg., 1.2)      = ');
    nu=input('Enter the value of poissons ratio
(eg., 0.25)     = ');


%% Material Parameter
nu=nu;                          %Poisson's Ratio

Mcs=1.5446-0.097*Fcw/100;    %Critical State Stress Ratio

k=0.0027+0.0024*Fcw/100;      %Unloading Slope (kappa)

%Dilatancy
kesig=1.25;                      %Dilatancy Material
Constant
miug=2;                          %Dilatancy Material
Constant

%Loading Direction
kesif=1.45;         %Material Parameter for Loading Vector
miuf=5;             %Material Parameter for Loading Vector

%Hardening
hzero=200000;                %Hardening Material Constant
miupk=14;                    %Hardening Material Constant
etaf=0.9*Mcs;                %Hardening Material Constant
```

```
%%Critical State Line

%Slope of CSL in v-lnp' Space
lCSL=0.019+0.144*Fcw/100-0.1*(Fcw/100).^2;

%Specific Volume Corresponding to p'=1 kPa
gamaCSL=1.7091+0.521*Fcw/100-0.548*(Fcw/100).^2;


%% Test Condition
pc=pc;                                  %Confining Pressure
v0=v0;                                %Initial Specific Volume
dEq=0.0001;                                %Strain increment


%% Initialization
q(1)=0;
p(1)=pc;
v(1)=v0;
Evol(1)=0;
Eq(1)=0;

%% Stress and Strain Calculation
for j=1:3000


    %Stress Ratio
    eta(j)=q(j)/p(j);

    %Critical State Line
    vc(j)=gamaCSL-lCSL*log(p(j));
```

```
    %Vertical distance from current void ratio to CSL
    si(j)=v(j)-vc(j);

    %Elastic Matrix
    K(j)=v(j)*p(j)/k;
    G(j)=3*(1-2*nu)*K(j)/(2*(1+nu));
    De=[K(j),0;0,3*G(j)];

    %Loading Direction Vector
    A(j)=kesif*(etaf*exp(miuf*si(j))-eta(j));
    np(j)=A(j)/sqrt(1+A(j)*A(j));
    nq(j)=1/sqrt(1+A(j)*A(j));
    n=[np(j);nq(j)];

    %Plastic Flow Vector
    dg(j)=kesig*(Mcs*exp(miug*si(j))-eta(j));
    mp(j)=dg(j)/sqrt(1+dg(j)*dg(j));
    mq(j)=1/sqrt(1+dg(j)*dg(j));

        if q(j)==0,m=[1;0];
        else m=[mp(j);mq(j)];
        end

    %Hardening Modulus
    etapk(j)=Mcs*exp(-miupk*si(j));
    H(j)=hzero*((etapk(j)/eta(j))-1)*(1-((kesif-
1)*eta(j)/(kesif)/etaf))^(4)*sqrt(p(j)/100);

    %Elasto-Plastic Matrix
    Dep=De-(De*m*n'*De/(H(j)+n'*De*m));
```

```
    %Stress, Strain and void ratio increments
    dq(j)=((Dep(2,2)-Dep(2,1)*Dep(1,2)/Dep(1,1))/(1-
Dep(2,1)/3/Dep(1,1)))*dEq;
    dp(j)=dq(j)/3;
    dEvol(j)=(dp(j)-Dep(1,2)*dEq)/Dep(1,1);
    dv(j)=-(v(j))*dEvol(j);

    %Total Stress, Strain and Void ratio
    q(j+1)=q(j)+dq(j);
    p(j+1)=p(j)+dp(j);
    Evol(j+1)=Evol(j)+dEvol(j);
    Eq(j+1)=Eq(j)+dEq;
    v(j+1)=v(j)+dv(j);

end

subplot (2,2,1)%
plot(Eq,q)
xlabel ('Shear Strain, \epsilon_q')
ylabel ('Deviatoric Stress, q(kPa)')

subplot (2,2,2)%
plot(p,q)
xlabel ('Mean Stress, p(kPa)')
ylabel ('Deviatoric Stress, q(kPa)')

subplot (2,2,3)%
plot(Eq,Evol)
xlabel ('Shear Strain, \epsilon_q')
ylabel ('Volumetric Strain, \epsilon_v')

subplot (2,2,4)%
```

```
plot(p,v)
xlabel ('Mean Stress, p(kPa)')
ylabel ('Specific Volume, \nu')
```

APPENDIX B. UMAT SUBROUTINE FOR THE CW-SFS CONSTITUTIVE MODEL

```
SUBROUTINE UMAT(STRESS,STATEV,DDSDDE,SSE,SPD,SCD,
1       RPL, DDSDDT, DRPLDE, DRPLDT, TRAN, DSTRAN, TIME, DTIME,
2       TEMP, DTEMP, PREDEF, DPRED, CMNAME, NDI, NSHR, NTENS,
3       NSTATV, PROPS, NPROPS, COORDS, DROT, PNEWDT, CELENT,
4       DFGRD0, DFGRD1, NOEL, NPT, LAYER, KSPT, KSTEP, KINC)
C
        INCLUDE 'ABA_PARAM.INC'
C
        CHARACTER*80 CMNAME
C
        DIMENSION  STRESS(NTENS), STATEV(NSTATV),
2       DDSDDE(NTENS,NTENS), DDSDDT(NTENS),DRPLDE(NTENS),
3       STRAN(NTENS), DSTRAN(NTENS), TIME(2), PREDEF(1), DPRED(1),
4       PROPS(NPROPS), COORDS(3), DROT(3,3), DFGRD0(3,3), DFGRD1(3,3),
5       IS(4), JS(4), DEP(4), DEE(4)

C**********************
C    LOCAL ARRAYS    *
C**********************

        DIMENSION DEL(4,4), PS(3), DPLASTIC(4,4), STRESSB(4), DV(4),
1       DP(4), DV1(4), DV2(4), DV3(4,4), DLOADING(4), STRESSC(4),
2       STRK(4), STRESSCORECTOR (4), DR(4), ZDELSTRESSONE(4),
3       STRESSTWO(4), ZDELSTRESSTWO(4), ERROR(4), STRESSTRIAL (4),
4       DSTRESSTRIAL(4),  DPSTRESSONE(4), STRESSONE(4),
5       DLOADINGONE(4)

C

        DOUBLE PRECISION  VOID, ELKAPA, ELNU, ELBULK, ELG,
1       ELLAMDA, MEAN, KESIG, MIUG, KESIF, MIUF, DILATE, JTWO,
2       DEVIATOR, SICSL,  GAMMACSL, MCSL, LAMDACSL, DV4, HZERO,
3       MIUPK, ETAF, HARDENING, DRR, VOLUMESTRAIN, YIELD,
4       PLASTICMULT, VOLUMEPLASTIC, DV5, MAGNITUDEDP, DELTAT,
5       MAGNITUDEERROR
C
        INTEGER KEY
C
```

```
      PARAMETER (ZERO=0.D0, ONE=1.D0, TWO=2.D0, THREE=3.D0,
1     FOUR=4.D0, SIX=6.D0, NINE=9.D0, EIGHT=8.D0, HALF=5.D-1,
2     TOLER=1.D-4, NNEWTON=100)

C

C*****************************
C     ELASTIC PROPERTIES      *
C*****************************
      ELKAPA=PROPS(1)
      ELNU=PROPS(2)
      VOID=PROPS(3)

C*****************************
C     DILATANCY PROPERTIES    *
C*****************************
      KESIG=PROPS(4)
      MIUG=PROPS(5)

C************************
C     CSL PROPERTIES     *
C************************
      MCSL=PROPS(6)
      GAMACSL=PROPS(7)
      LAMDACSL=PROPS(8)

C***************************************
C     LOADING DIRECTION PROPERTIES     *
C***************************************
      KESIF=PROPS(9)
      MIUF=PROPS(10)

C************************************
C     PLASTIC MODULUS PROPERTIES    *
C************************************
      HZERO=PROPS(11)
      MIUPK=PROPS(12)
      ETAF=PROPS(13)



C*****************************
C     ZERO MATRICES           *
C*****************************

      DO K1=1,4
      DO K2=1,4
```

```
            DEL(K1,K2)=ZERO
        END DO
        END DO
C
        DO K1=1,4
        DO K2=1,4
            DPLASTIC(K1,K2)=ZERO
        END DO
        END DO

        YIELD=ZERO

C
C       VOID=STATEV(1)
C       WRITE (7,*) "NOEL=",NOEL
C       WRITE (7,*) "NPT=",NPT

C**************************************************************
C TRANFER STRESS AND STRAIN TO CONVENTIONAL DEFINITION       *
C IN SOIL MECHANICS. (COMPRESSION IS POSITIVE)               *
C**************************************************************

        DO N=1,4
        STRESS(N) = -STRESS(N)
        STRAN(N)  = -STRAN(N)
        DSTRAN(N) = -DSTRAN(N)
        END DO

C*********************************
C       SET UP ELASTICITY MATRIX   *
C*********************************
        VOLUMESTRAIN=EXP(STRAN(1)+STRAN(2)+STRAN(3))-1
C       WRITE(7,*) "VOLUMETRIC STRAIN=", VOLUMESTRAIN
        STATEV(2)=VOLUMESTRAIN

        VOID=VOID-VOLUMESTRAIN*(ONE+VOID)
C       WRITE (7,*) "VOID=",VOID
        STATEV(1)=VOID

        MEAN=ONE/THREE*(STRESS(1)+STRESS(2)+STRESS(3))
C       WRITE(7,*) "MEAN STRESS=",MEAN
        JTWO=ONE/SIX*((STRESS(1)-STRESS(2))**2+(STRESS(2)-
1       STRESS(3))**2+(STRESS(3)-STRESS(1))**2)+STRESS(4)*STRESS(4)
C       WRITE(7,*) "JTWO=", JTWO

        DEVIATOR=SQRT(THREE*JTWO)
C       WRITE(7,*) "DEVIATOR=",DEVIATOR
```

```
      SICSL=(ONE+VOID)-GAMACSL+LAMDACSL*LOG(MEAN)
C     WRITE(7,*) "SICSL=", SICSL

      ELBULK=(ONE+VOID)*MEAN/ELKAPA
C     WRITE(7,*) "BULK MODULUS=",ELBULK

      ELG=THREE*(ONE-TWO*ELNU)*ELBULK/TWO/(ONE+ELNU)
C     WRITE(7,*) "SHEAR MODULUS=",ELG

      ELLAMDA=(ONE+VOID)*MEAN/ELKAPA-TWO*ELG/THREE
C     WRITE (7,*) "ELLAMDA=", ELLAMDA

      DO K1=1,3
      DO K2=1,3
            DEL(K2,K1)=ELLAMDA
      END DO
        DEL(K1,K1)=ELG*TWO+ELLAMDA
      END DO
        DEL(4,4)=ELG
C       WRITE(7,*) "DEL=",DEL


C*****************************************************
C     STRESS INCREMENT BASED ON ELASTIC MATRIX    *
C*****************************************************
C     WRITE (7,*) "STRESS=",STRESS
C     WRITE (7,*) "DSTRAN=",DSTRAN
C     WRITE (7,*) "STRAN=",STRAN
      CALL KMLT1(DEL,DSTRAN,DSTRESSTRIAL,NTENS)
C     WRITE (7,*) "DV=",DV
      DO K1=1,4
            STRESSTRIAL(K1)=STRESS(K1)+DSTRESSTRIAL(K1)
      END DO
C     WRITE (7,*) "STRESSB=",STRESSB
C
      CALL SPRINC(STRESSB,PS,1,3,1)
C     WRITE (7,*) "PS=",PS

      DO K1=1,4
            STRESSONE(K1)=STRESS(K1)
      END DO

C*****************
C     ITERATION   *
C*****************
C     DO 666 TITERATION=0,1
```

```
      DELTAT=0.001
      DO K2=1,1000
      MEAN=ONE/THREE*(STRESSONE(1)+STRESSONE(2)+
     1 STRESSONE(3))

      JTWO=ONE/SIX*((STRESSONE(1)-STRESSONE(2))**2+
     2 (STRESSONE(2)-STRESSONE(3))**2
     3 +(STRESSONE(3)-TRESSONE(1))**2)+STRESSONE(4)*STRESSONE(4)

      DEVIATOR=SQRT(THREE*JTWO)

      SICSL=(ONE+VOID)-GAMACSL+LAMDACSL*LOG(MEAN)

      CALL PLASTICFLOW (STRESSONE, KESIG, MIUG, MCSL, SICSL,
     1 DEVIATOR, MEAN, JTWO, DPSTRESSONE)

      CALL KMLT1(DEL,DP,DV1,NTENS)

      CALL LOADINGDIRECTION (STRESSONE, KESIF, MIUF, ETAF,
     1 SICSL, DEVIATOR,MEAN,JTWO,DLOADINGONE)

      CALL DOTPROD(DLOADINGONE,DV1,DV4,NTENS)

      CALL HARDENINGFUNC(HZERO,MCSL,MIUPK,SICSL,MEAN,
     1 DEVIATOR,KESIF,ETAF,HARDENING)

      CALL DOTPROD(DLOADINGONE,DSTRESSTRIAL,DV5,NTENS)

      PLASTICMULT=DV5*DELTAT/(DV4+HARDENING)
      PLASTICMULT=MAX(PLASTICMULT,ZERO)

      DO K1=1,4
            ZDELSTRESSONE(K1)=DSTRESSTRIAL(K1)*DELTAT-
            PLASTICMULT*DV1(K1)
      END DO

      DO K1=1,4
            STRESSTWO(K1)=STRESSONE(K1)+ZDELSTRESSONE(K1)
      END DO

      MEAN=ONE/THREE*(STRESSTWO(1)+STRESSTWO(2)+
     1 STRESSTWO(3))

      JTWO=ONE/SIX*((STRESSTWO(1)-STRESSTWO(2))**2+
     1 (STRESSTWO(2)-STRESSTWO(3))**2+(STRESSTWO(3)-
     2 STRESSTWO(1))**2)+ STRESSTWO(4)*STRESSTWO(4)
```

```
      DEVIATOR=SQRT(THREE*JTWO)

      SICSL=(ONE+VOID)-GAMACSL+LAMDACSL*LOG(MEAN)

      CALL PLASTICFLOW(STRESSTWO, KESIG, MIUG, MCSL, SICSL,
     2 DEVIATOR, MEAN, JTWO, DP)

      CALL KMLT1(DEL,DP,DV1,NTENS)

      CALL LOADINGDIRECTION (STRESSTWO,KESIF,MIUF,ETAF,SICSL,
     1 DEVIATOR,MEAN,JTWO,DLOADING)

      CALL DOTPROD(DLOADING,DV1,DV4,NTENS)

      CALL HARDENINGFUNC(HZERO,MCSL,MIUPK,SICSL,MEAN,
     1 DEVIATOR,KESIF,ETAF,HARDENING)

      CALL DOTPROD(DLOADING,DSTRESSTRIAL,DV5,NTENS)

      PLASTICMULT=DV5*DELTAT/(DV4+HARDENING)
      PLASTICMULT=MAX(PLASTICMULT,ZERO)

C     WRITE (7,*) "PLASTIC MULTIPLIER=", PLASTICMULT

      DO K1=1,4
            ZDELSTRESSTWO(K1)=DSTRESSTRIAL(K1)*DELTAT-
     1      PLASTICMULT*DV1(K1)
      END DO

      DO K1=1,4
             ERROR(K1)=5.0D-1*(-ZDELSTRESSONE(K1)+
     1      ZDELSTRESSTWO(K1))/(STRESS(K1)+5.0D-*
     2      (ZDELSTRESSTWO(K1)+ ZDELSTRESSONE(K1)))
      END DO

      MAGNITUDEERROR=SQRT(ERROR(1)**2+ERROR(2)**2+ERROR(3)*
     1 *2+ERROR(4)**2)

      STATEV(4)=MAGNITUDEERROR


      DO K1=1,4
             STRESSONE(K1)=STRESSONE(K1)+5.0D-1*
     1      (ZDELSTRESSTWO(K1)+ZDELSTRESSONE(K1))
      END DO

      END DO
```

```
      DO K1=1,4
            STRESS(K1)=STRESSONE(K1)
      END DO

      MEAN=ONE/THREE*(STRESS(1)+STRESS(2)+STRESS(3))
C     WRITE(7,*) "MEANB=", MEAN

      JTWO=ONE/SIX*((STRESS(1)-STRESS(2))**2+(STRESS(2)-
1     STRESS(3))**2+(STRESS(3)-STRESS(1))**2)+STRESS(4)*STRESS(4)
C     WRITE(7,*) "JTWOB=", JTWO

      DEVIATOR=SQRT(THREE*JTWO)
C     WRITE(7,*) "DEVIATORB=",DEVIATOR

      SICSL=(ONE+VOID)-GAMACSL+LAMDACSL*LOG(MEAN)

      CALL PLASTICFLOW(STRESSTWO, KESIG, MIUG, MCSL, SICSL,
2     DEVIATOR, MEAN, JTWO, DP)
C     WRITE(7,*) "DP=", DP

      CALL KMLT1(DEL,DP,DV1,NTENS)
C     WRITE (7,*) "DV1=", DV1

      CALL LOADINGDIRECTION (STRESS,KESIF,MIUF,ETAF,SICSL,
1     DEVIATOR,MEAN,JTWO,DLOADING)
C     WRITE(7,*) "DLOADING=", DLOADING

      CALL KMLT2(DLOADING,DEL,DV2,NTENS)
C     WRITE (7,*) "DV2=", DV2

      CALL DYADICPROD(DV1,DV2,DV3,NTENS)
C     WRITE (7,*) "DV3=", DV3

      CALL DOTPROD(DLOADING,DV1,DV4,NTENS)
C     WRITE(7,*) "DV4=", DV4

      CALL HARDENINGFUNC(HZERO,MCSL,MIUPK,SICSL,MEAN,
1     DEVIATOR,KESIF,ETAF,HARDENING)
      WRITE(7,*) "HARDENING=", HARDENING
      STATEV(3)=HARDENING
      DO K1=1,4
            STRESS(K1)=-STRESS(K1)
      END DO

C     WRITE(7,*) "STRESS=", STRESS
```

```
      DO K1=1,4
      DO K2=1,4
        DPLASTIC(K2,K1)=DV3(K2,K1)/(DV4+HARDENING)
      END DO
      END DO
C     WRITE(7,*) "DPLASTIC=",DPLASTIC

      DO K1=1,4
      DO K2=1,4
            DDSDDE(K2,K1)=DEL(K2,K1)-DPLASTIC(K2,K1)
      END DO
      END DO


      RETURN
      END

C**************************************
C**       PLASTIC FLOW DIRECTION       *
C**************************************
*USER SUBROUTINE
      SUBROUTINE PLASTICFLOW(STR,DKESIG,DMIUG,DMCSL,DSICSL,
1     DDEVIATOR,DMEAN,DJTWO,DP)
C
      INCLUDE 'ABA_PARAM.INC'
      PARAMETER (ZERO=0.D0, ONE=1.D0, TWO=2.D0, THREE=3.D0,
2     FOUR=4.D0, EIGHT=8.D0, NINE=9.D0)

      DIMENSION STR(4), DP(4)

      DOUBLE PRECISION MMCSL, MDILATE, MKESIG, MMIUG, DSICSL,
1     DMEAN, DDEVIATOR,DJTWO, MAGNITUDEDP

      IF (DJTWO.EQ.ZERO) THEN
      DJTWO=1.0D-10
      ELSE
      DJTWO=DJTWO
      END IF


      DILATE=DKESIG*(DMCSL*EXP(DMIUG*DSICSL)-
1     DDEVIATOR/DMEAN)

      DO K=1,3
            DP(K)=DILATE/THREE+SQRT(THREE)/TWO*(STR(K)-
1           DMEAN)/SQRT(DJTWO)
```

```
      END DO

      DP(4)=SQRT(THREE/DJTWO)*STR(4)

      RETURN
      END

C*********************************
C**       LOADING DIRECTION         *
C*********************************
*USER SUBROUTINE
      SUBROUTINE LOADINGDIRECTION(STR, DKESIF, DMIUF, DETAF,
1     DSICSL, DDEVIATOR,DMEAN,DJTWO,DLOADING)
C
      INCLUDE 'ABA_PARAM.INC'
      PARAMETER (ZERO=0.D0,  ONE=1.D0, TWO=2.D0, THREE=3.D0,
1     FOUR=4.D0, EIGHT=8.D0, NINE=9.D0)

      DIMENSION STR(4), DLOADING(4), STRK(4)

      DOUBLE PRECISION ZARIB, DMCSL, DJTWO, DBETA


C     WRITE (7,*) "DSICSL=", DSICSL
C     WRITE (7,*) "DMEAN=", DMEAN
C     WRITE (7,*) "DDEVIATOR=", DDEVIATOR
C     WRITE (7,*) "DJTWO=", DJTWO

      ZARIB=DKESIF*(DETAF*EXP(DMIUF*DSICSL)-
DDEVIATOR/DMEAN)
C     WRITE(7,*) "ZARIB=", ZARIB

      DO K=1,3
        DLOADING(K)=ZARIB/THREE+SQRT(THREE)/TWO*(STR(K)-
DMEAN)/SQRT(DJTWO)
      END DO

      DLOADING(4)=SQRT(THREE/DJTWO)*STR(4)

      RETURN
      END
C************************
C**       HARDENING         *
C************************
*USER SUBROUTINE
      SUBROUTINE HARDENINGFUNC(DHZERO, DMCSL, DMIUPK,
1     DSICSL, DMEAN, DDEVIATOR,DKESIF,DETAF,HARDENING)
```

```
C
      INCLUDE 'ABA_PARAM.INC'
      PARAMETER (ZERO=0.D0,  ONE=1.D0, TWO=2.D0, THREE=3.D0,
1     FOUR=4.D0, EIGHT=8.D0,NINE=9.D0,HUNDRED=100.D0)

      DOUBLE PRECISION DHZERO,DMCSL,DMIUPK,DSICSL,DMEAN,
1     DDEVIATOR,DKESIF,DETAF,DETAPK,HARDENING


      DETAPK=DMCSL*EXP(-DMIUPK*DSICSL)

      HARDENING=DHZERO*((DETAPK/(DDEVIATOR/DMEAN))-ONE)*
1     ((ONE-(DKESIF-ONE)*DDEVIATOR/DMEAN/DETAF/(DKESIF))**4)*
2     SQRT(DMEAN/100.D0)

      RETURN
      END

C**************************************************
C**       MULTIPLY 4X4 MATRIX WITH 4X1 VECTOR    *
C**************************************************
*USER SUBROUTINE
      SUBROUTINE KMLT1(DM1,DM2,DM,NTENS)
C
      INCLUDE 'ABA_PARAM.INC'
C
      PARAMETER (M=4)
C
      DIMENSION DM1(M,M),DM2(M),DM(M)
C
      DO 10 I=1,4
            X=0.0
      DO 20 K=1,4
            Y=DM1(I,K)*DM2(K)
            X=X+Y
20    CONTINUE
            DM(I)=X
10    CONTINUE

      RETURN
      END

**************************************************
**       MULTIPLY 1X4 MATRIX WITH 4X4 VECTOR    *
**************************************************
      SUBROUTINE KMLT2(DM1,DM2,DM,NTENS)
C
```

```
      INCLUDE 'ABA_PARAM.INC'
C
      PARAMETER (M=4)
C
      DIMENSION DM1(M),DM2(M,M),DM(M)
C
      DO 10 I=1,NTENS
            X=0.0
      DO 20 K=1,NTENS
            Y=DM1(K)*DM2(K,I)
            X=X+Y
20    CONTINUE
            DM(I)=X
10    CONTINUE

      RETURN
      END

**********************************************
**       MULTIPLY 4X1 VECTOR WITH 1X4 VECTOR    *
**********************************************

      SUBROUTINE DYADICPROD(DM1,DM2,DM3,NTENS)
C
      INCLUDE 'ABA_PARAM.INC'
C
      PARAMETER (M=4)
C
      DIMENSION DM1(4),DM2(4),DM3(4,4)
C
      DO I=1,4
      DO J=1,4
      DM3(I,J) = DM1(I)*DM2(J)
      END DO
      END DO
C
   RETURN
   END



**********************************************
**       MULTIPLY 4X4 MATRIX WITH 4X4 MATRIX     *
**********************************************
*USER SUBROUTINE
      SUBROUTINE KMLT3(DM1,DM2,DM,NTENS)
C
```

```
      INCLUDE 'ABA_PARAM.INC'
C
      PARAMETER (M=4,ZERO=0.0)
C
      DIMENSION DM1(M,M),DM2(M,M),DM(M,M)
C
      DO 10 I=1,NTENS
      DO 10 J=1,NTENS
            DM(I,J)=ZERO
      DO 20 K=1,NTENS
            DM(I,J)=DM(I,J)+DM1(I,K)*DM2(K,J)
20    CONTINUE
10    CONTINUE

      RETURN
      END

*****************************************
**       DOT PRODUCT OF TWO VECTORS      *
*****************************************
*USER SUBROUTINE
      SUBROUTINE DOTPROD(DM1,DM2,DM,NTENS)
C
      INCLUDE 'ABA_PARAM.INC'
C
      DIMENSION DM1(NTENS),DM2(NTENS)
C
      Y=0.D0
      DO 20 K=1,NTENS
            X=DM1(K)*DM2(K)
            Y=X+Y
20    CONTINUE
            DM=Y

      RETURN
       END




C*****************************************
**     CALCULATE INVERSE OF A MATRIX      *
*****************************************
      SUBROUTINE INVERSE(EAA,L,IS,JS)
C
      INCLUDE 'ABA_PARAM.INC'
```

```
C
      PARAMETER (ZERO=0.D0, ONE=1.D0, TWO=2.D0, THREE=3.D0,
     1  FOUR=4.D0, EIGHT=8.D0, NINE=9.D0)
C
      DIMENSION EAA(4,4),IS(4),JS(4)
      DOUBLE PRECISION EAA
      L=1
      DO 100 K=1,4
            EDD=ZERO
      DO 10 I=K,4
      DO 10 J=K,4
            IF (ABS(EAA(I,J)).GT.EDD) THEN
                  EDD=ABS(EAA(I,J))
                  IS(K)=I
                  JS(K)=J
            END IF
10    CONTINUE
C
            IF (EDD+ONE.EQ.ONE) THEN
                  L=0
                  WRITE(*,20)
            RETURN
            END IF
20    FORMAT (1X,'ERROR*****NOT INV')
C
      DO 30 J=1,4
            ETT=EAA(K,J)
            EAA(K,J)=EAA(IS(K),J)
            EAA(IS(K),J)=ETT
30    CONTINUE
C
      DO 40 I=1,4
            ETT=EAA(I,K)
            EAA(I,K)=EAA(I,JS(K))
            EAA(I,JS(K))=ETT
40    CONTINUE
C
      EAA(K,K)=ONE/EAA(K,K)
      DO 50 J=1,4
            IF (J.NE.K) THEN
                  EAA(K,J)=EAA(K,J)*EAA(K,K)
            END IF
50    CONTINUE
C
      DO 70 I=1,4
            IF (I.NE.K)THEN
                  DO 60 J=1,4
```

```
                        IF (J.NE.K) THEN
                            EAA(I,J)=EAA(I,J)-EAA(I,K)*EAA(K,J)
                        END IF
60          CONTINUE
            END IF
70      CONTINUE
C
        DO 80 I=1,4
            IF (I.NE.K) THEN
                EAA(I,K)=-EAA(I,K)*EAA(K,K)
            END IF
80      CONTINUE
100     CONTINUE
C
        DO 130 K=4,1,-1
        DO 110 J=1,4
            ETT=EAA(K,J)
            EAA(K,J)=EAA(JS(K),J)
            EAA(JS(K),J)=ETT
110     CONTINUE
        DO 120 I=1,4
            ETT=EAA(I,K)
            EAA(I,K)=EAA(I,IS(K))
            EAA(I,IS(K))=ETT
120     CONTINUE
130     CONTINUE

        RETURN
        END
```